NEAR-SURFACE DAMAGE OF ALLOY 617 WITH AND WITHOUT BARRIER LAYERS DURING STATIC AND CYCLIC CREEP DEFORMATION AT 800°C

by

Alfred Ogola Okello

A dissertation submitted in partial fulfillment
of the requirements for the degree of
Doctor of Philosophy
(Materials Science and Engineering)
in The University of Michigan
2015

Doctoral Committee:

Professor J. Wayne Jones, Chair
Professor John Edmond Allison
Associate Professor Emmanuelle Marquis
Professor Gary S. Was

ACKNOWLEDGEMENTS

The author expresses sincere gratitude to Professor J. Wayne Jones, for his guidance, patience, and rigor towards both in my professional and personal growth during this time. I also thank my committee members, Professor Gary Was, Professor John Allison, and Professor Emmanuelle Marquis for their insightful comments and contributions towards my dissertation.

It would have been difficult to conduct the creep experiments without Chris Torbet of the University of California Santa Barbara, who assisted in designing and building the retort, and who was always available to offer technical support. I am also grateful to Harald Eberhart for fabricating the quartz parts for my setup. The conversations with Professor Tresa Pollock of the University of California Santa Barbara, Dr. Richard Wright, Dr. Laura Carroll and Dr. Dave Swank both of Idaho National Laboratory were helpful in the provision of the alloy, designing of experiments, and troubleshooting of experimental setup. Also, the help from Dr. Anne Campbell and Dr. Ovidui Toader with the vacuum setup, Alexander Fink with Labview programming, Dr. Zhongrui Li with AES, and Dr. Ying Qi with XRD is acknowledged.

I am grateful for my research colleagues, past and present – Dr. Deepak Kumar, Dr. Gokce Gulsoy, Dr. Raghavendra Adharapurapu, Dr. Liu Liu, Dr. Clinique Brundidge, Dr. Jessica Terbush, Dr. McLean Echlin, Dr. Jason Van Sluytman, Dr. Anish Kumar, Dr. Tracy Berman, Luke Rettberg, Jason Geathers, Patrick Milligan, Victoria Miller, Garret Huff, Vir Nirankari – whose encouragement, assistance, and camaraderie helped ease the pressure and challenges during this long endeavor.

I recognize my parents and parents-in-law for their support, love and encouragement, and also my siblings and siblings-in-law for their prayers and thoughts.

I am also thankful to my wife who has been a constant source of love and support during the happy and challenging moments during this journey. I agree with what you always say, “We are a great team!”

Finally I acknowledge the funding of this work by the U.S. Department of Energy under NEUP Award Number 87993, Project Number 09768 and NEUP Contract 102215, Project 10-963. This journey gave me a great opportunity to collaborate with Professor Carlos Levi of the University of California Santa Barbara, and Dr. Elizabeth Clark, who coated the creep specimens and were part of insightful discussions during a significant part of this project. I am very thankful.

TABLE OF CONTENTS

LIST OF FIGURES

LIST OF TABLES

ABSTRACT

NEAR-SURFACE DAMAGE OF ALLOY 617 WITH AND WITHOUT BARRIER LAYERS DURING STATIC AND CYCLIC CREEP DEFORMATION AT 800°C

by

Alfred Ogola Okello

Chair: J. Wayne Jones

Alloy 617 – a Cr_2O_3-former – is the leading candidate material for heat exchangers of the Next Generation Nuclear Plants with high outlet temperatures (750-850°C). The first objective of this work was to understand the effect of oxidizing (He-≤0.1ppm O_2) and carburizing/oxidizing (He-CO/CO_2=1320) environments on creep deformation under static and cyclic stresses (σ_{max}=50MPa and 75MPa), and specifically on damage in surface and near-surface regions of Alloy 617 at 800°C. Secondly, the work investigated the mitigation of environmental attack on Alloy 617 by using combinations of Al_2O_3-forming coatings, NiAl and FeCrAlY. Interrupted creep studies in the two environments were conducted on uncoated 617, aluminized 617 (NiAl/617), clad-aluminized 617 (FeCrAlY/NiAl/617), aluminized 617 with FIB micro-notches, and clad-aluminized 617 having undergone extra heat treatment (>24h). In these test conditions, the environmental attack was limited to the surface of the uncoated alloy without affecting the bulk creep behavior, with cyclic stress accelerating the surface damage. Uncoated 617 suffered surface and internal oxidation in both environments, with thin/less

porous Cr_2O_3 scales, and porous/extensive grain boundary Cr_2O_3 intrusions characterizing surface damage in He-$\leq$0.1ppm O_2 and He-CO/CO_2=1320, respectively. The existence in unstressed specimens of different Cr_2O_3 growth rates due to Cr interstitials or Cr vacancies primary mobile species as a result of low or high oxygen partial pressures, respectively, was confirmed during the application of stress in this work. Also, the carburizing nature of the environment caused embrittlement of the near-surface regions of the alloy, hence exposing fresher alloy surfaces for inward oxidation to take place. In contrast, slow growing alumina scale on NiAl and FeCrAlY coating layers protected underlying 617 from environmental attack. Surface undulation, characteristic of NiAl layers under cyclic stresses, was absent on NiAl and hence no surface cracking was observed, nor were cracks initiated or propagated from FIB-notches planted to simulate defects in the layer. The NiAl layer was, however, vulnerable to cracking when a FeCrAlY cladding overlay was employed. In general, these coatings prevented environmentally-induced damage on the substrate. However, further investigations are needed to study the long-term implications of creep damage accumulation in both the underlying substrate and coating layers in non-accelerated tests.

CHAPTER 1
INTRODUCTION

For quite some time now, nuclear power has been considered as an alternative non-greenhouse-gas-emitting energy source to meet growing electricity consumption. With the current fleet of reactors expected to be retired in the near future, there is a growing need to replace them with new nuclear reactor concepts. To this end, considerable efforts have been made to further the research and development of more efficient, more sustainable, more cost effective, and safer reactor designs referred to as Generation IV nuclear energy systems [1].

The Very High Temperature Gas-cooled Reactor (VHTR) is one of the advanced reactor concepts with near future commercial viability that has been considered. Its appeal is derived from the fact that the heat from the reactor can be used for the co-generation of steam for power and process heat for hydrogen production [2]. In this reactor design, helium gas is used as a coolant because of its chemical inertness and high heat transfer coefficient [1]. A critical component in the VHTR system is the Intermediate Heat Exchanger (IHX) [3], which is expected to play an important role in transferring heat from the primary coolant in the nuclear reactor core to the electricity generation and hydrogen production units. The IHX is characterized by service conditions of high outlet temperatures (>950°C), a helium cooling gas containing low levels of residual impurities, and high lifetime expectancy (>60 years) [3, 4]. These stringent conditions require that the alloy used for the IHX have excellent oxidation resistance, microstructural stability, and accompanied with good creep strength within the service temperature range.

Of the potential candidate alloys considered for the IHX application, Alloy 617 has received more attention. It is an austenitic alloy based on Ni-Cr with solid solution strengthening offered by cobalt and molybdenum, while chromium and aluminum provide oxidation resistance. The presence of intergranular and intragranular $M_{23}C_6$ and

M_6C (where M is mainly Cr and Mo respectively) carbides provides creep strength and microstructure stability by inhibiting grain boundary sliding and grain growth at elevated temperatures.

At elevated temperatures the IHX alloys may experience steady loading, cyclic loading (due to startup, shutdown and power changes), or even a combination of both [5]. Creep and cyclic creep deformation are, therefore, expected to be the primary damage modes for the IHX occurring under steady loading and cyclic loading respectively. Alloy 617 has demonstrated competitive creep and cyclic creep properties compared to other Ni-based superalloys at these high temperatures [6, 7] . Unfortunately, its application in the IHX is affected by its poor compatibility with the CO, CO_2, H_2, and H_2O impurities in helium. Low oxygen and carbon potentials arise from the low concentration levels of impurities, which actively corrode the metallic surfaces. Depending on the temperature, impurity levels, and composition of alloys, attack by the reactor environment in the form of surface or internal oxidation, carburization, and decarburization of the alloy are expected to occur with deleterious effects on the creep strength [8-12]. The creep strength is expected to be affected as a result of the grain boundaries being exposed to environmental attack under static and cyclic loading. Even though a chromia scale is formed upon exposure to the helium environments, these environmental attacks show that this scale is not protective enough and is permeable to molecular oxidants [13]. Environmental attack is expected to be more severe in the presence of static and cyclic stress during creep, and hence the need to explore methods to reduce the ingress of corrosive molecular (which dissociate and diffuse inward) oxidants. A less permeable surface scale that is more protective than chromia and offers a barrier against oxidation and corrosion in nickel and iron alloys is alpha alumina [14]. Since Alloy 617 is a chromia former, coatings that allow the preferential formation of more stable alpha alumina have been reported widely in the past [14-17] and more recently [18].

There are two objectives in this research work. First, the studies here seek to understand the effect of oxidizing and carburizing/oxidizing environments on creep deformation under static and cyclic stresses, and specifically on surface and near-surface regions of Cr_2O_3-forming 617 at 800°C. Second, investigations will be conducted on the mitigation of environmental attack on Alloy 617 by using combinations of Al_2O_3-forming

barrier layers - NiAl and FeCrAlY – developed at the University of California Santa Barbara [18].

Chapter 2 provides a review of the literature that is relevant to the present work, including previous studies of the effects of impure He environments on alloy 617 at elevated temperatures, and known differences in behavior in these environments under creep conditions. A review of the work by Clark on the efficacy of barrier layers on alloy 617 will also be highlighted. In Chapter 3, the experimental approach taken in terms of the procedure and the apparatus used in this research is described. A detailed description of near-surface environmental damage during creep deformation of uncoated 617 at 800°C with respect to the mechanisms responsible for this behavior is presented in Chapter 4. The role of NiAl barrier coatings and the special role of FeCrAlY clad overlayers on environmental damage, along with results on the mechanical integrity of these coatings at significant creep strains are presented in Chapter 5. Finally, conclusions and recommendations for future work are detailed in Chapter 6.

CHAPTER 2
LITERATURE REVIEW

In this chapter, a review of the literature relevant to understanding the objectives, the approach, and the results of the study in this dissertation is provided. Section 2.1 describes the microstructure of Alloy 617 used in this dissertation. The nuclear reactor environments expected during service, and which are simulated in this dissertation, will be described in section 2.2. Section 2.3 outlines the types of environmental attack on nickel alloys, in general, and Alloy 617, in particular. The presentations in sections 2.2 and 2.3 are a summary of prior research in Professor Gary Was's group at the University of Michigan [19, 20]. Section 2.4 reviews the synergy that exists between this attack and the mechanical behavior of the alloy. Section 2.5 provides a summary of the development of barrier layers used to mitigate environmental attack in Ni alloys as described in Clark's work [18, 21]. The final section states the objectives and the approach taken to meet them.

2.1 Microstructure and thermal stability of Alloy 617

Alloy 617 was introduced by Hosier and Tilack [22] and developed initially as a material for high-temperature applications above 800°C for use in aircraft and land-based gas turbines, chemical manufacturing components, and power generation structures. Since the early 1980s, this alloy has been considered for use in high temperature gas-cooled reactors [23]. It is a face centered cubic wrought alloy – nominal composition is shown in Table 2-1 – with a favorable combination of high temperature creep strength (Co, Cr and Mo) and oxidation resistance (Al and Cr) [24]. The Ni-Cr alloy, with solid solution strengthening offered by Co and Mo, is predominantly used in the solution annealed condition consisting of annealing at a minimum of 1175°C followed by water quenching or rapid cooling by other means. Aluminum can also form the intermetallic compound γ' over a range of temperatures, which results in precipitation strengthening. The accepted grain size for the alloy is ASTM No. 6 (45μm) or coarser for high creep-

rupture strength but finer when fatigue resistance is preferred [23]. Depending on the level and success of the solid solution, intergranular and intragranular precipitates can occur along the rolling direction, as shown in Figure 2-1.

Mankins et al performed ageing studies to determine the effects of long exposure (up to 10,000h) on the thermal stability of alloy 617 in the temperature range of 649°C-1093°C [25]. The major phase present in the alloy after exposure was Mo and Cr rich $M_{23}C_6$, which was present along the grain boundaries and interior of the grains as discrete precipitate, and remained stable at all temperatures. X-ray diffraction (XRD) studies did not conclusively identify M(C,N) and M_6C carbides in any sample, neither were topological close-packed phases such as sigma identified. Approximately 0.6 wt% of γ' was precipitated in this alloy in the temperature range of 649-760°C thanks to the presence of Al. The findings in this study were similar to that of Takahashi et al [26] who determined the exact compositions of the carbides as $Cr_{21}Mo_2C_6$ and $Mo_3Cr_2(Ni,Co)_1C$ and confirmed that both precipitates formed at grain boundaries when aged at 1000°C. Kihara et al observed the difference between the two types of carbides: bright and massive Mo-rich M_6C and small, dark Cr-rich $M_{23}C_6$ particles [27].

Figure 2-2 shows time-temperature-precipitation (TTP) diagrams recently constructed by Ren et al [23] to summarize the data on long term stability of precipitates ($M_{23}C_6$ and M_6C) in alloy 617. According to Figure 2-3, THERMOCALC® predicts the equilibrium precipitates in alloy 617 to be M(C,N), $M_{23}C_6$, M_6C, and Ni_3Al (γ') in the temperature range of 600-1400°C.

In summary, Cr-rich $M_{23}C_6$ (discrete particles), Mo-rich M_6C, and γ' (Ni_3Al) are the main precipitates in alloy 617 in order of decreasing abundance. γ' is a low temperature phase which is stable only at temperatures below 800°C. Strengthening is derived from precipitates ($M_{23}C_6$, M_6C, Ti(C,N)) and solid solution strengthening by Co and Mo.

2.2 Environments used during high temperature mechanical testing

In the VHTRs, helium is the coolant gas of choice because of its chemical inertness and attractive thermal properties. The helium coolant in an operating VHTR makes a complete circuit from the graphite core to the heat exchangers and back to the core. The sources of the impurities are air (from fuel element charge/discharge

operations), H_2O (from degassing of the graphite and the thermal insulation), carbon dioxide (from degreasing or from direct leakage), and H_2 (from proton diffusion through heat exchangers) [28, 29]. The reactions to produce the impurities are as follows. First, the hot graphite core removes virtually all free oxygen to form CO. Partial reactions of water vapor with the core produces H_2 and CO. Some of this H_2 reacts with the graphite core to produce CH_4. The main impurities in the helium circuit are, therefore, CO, CO_2, H_2O, H_2, and CH_4 [30]. A purification unit plays a significant role in reducing the level of these impurities, but the remaining low levels of impurities are transported to the heat exchangers where they can lead to environmental degradation of the high temperature alloys. The concentration levels of impurities in heat exchangers reported in the helium coolant during steady-state operation of some experimental reactors are shown in Table 2-2 [31, 32]. As observed in the table, helium contains impurities in the parts-per-million range. Although these concentrations are low, it is expected that the environment will bear a low oxidizing potential (low oxygen concentration) while the carbon activity, set by carbon bearing species CO and CH_4, could be significant. The typical oxidation behavior observed are surface or internal oxidation, surface or bulk carburization, and bulk decarburization.

Several researchers have described the gas/metal reactions and the corrosion behavior of Ni-Cr alloys in VHTR environments [11, 29, 33-37]. The following is a summary of the proposed reactions that describe the oxidation behavior of Ni-Cr alloys in VHTR environments:

Oxidation by H_2O, CO, and CO_2:

$$2Cr_{solution} + 3H_2O \rightarrow Cr_2O_3 + 3H_2 \quad (2.1)$$

$$2Cr_{solution} + 3CO_2 \rightarrow Cr_2O_3 + 3CO \quad (2.2)$$

$$9Cr_{solution} + 3CO \rightarrow Cr_2O_3 + C_{solution} \quad (2.3)$$

Decarburization by H_2O and CO_2:

$$3C_{solution} + H_2O \rightarrow CO_{(g)} + H_2 \quad (2.4)$$

Carburization by CH_4:

$$7Cr_{solution} + 3CH_4 \rightarrow Cr_7C_3 + 6H_2 \quad (2.5)$$

First, the oxidation of Cr by water vapor and carbon dioxide is possible under favorable thermodynamic and kinetic conditions to form Cr_2O_3 layers that help prevent further carburization and decarburization. The progress of Equation (2.3) depends on whether the temperature is above or below the critical value (T_{cr}) as described by Brenner [37], Quaddakers [33], and Christ [38]. The forward direction of the equation is favored below the critical temperature and oxidation and carburization occur. Above the critical temperature, the reverse direction of the equation is favored resulting in the formation of Cr metal and CO gas. Second, decarburization of the alloy takes place by oxidation of the carbon in solution to CO, which in turn leads to the dissociation of internal carbides (necessary for creep strength). There is also release of two gases from the metal surface. Lastly, carburization of the alloy is made possible by CO and CH_4. Methane thermally cracks at high temperature, forming carbides within the alloy.

Based on the reactions shown by Equations (2.1) - (2.5), the impurities in helium can be grouped into two categories: carburizing/decarburizing gases (CO and CH_4), which establish carbon potential at the metal surface, and oxidizing gases (CO_2 and H_2O), which establish an oxygen potential at the metal surface. Quaddakers et al. proposed a theoretical model for determining the combined effect of the oxidizing and carburizing/decarburizing gases in a Ni-Cr alloy system [11, 33, 39]. By superimposing the kinetics of Equations (2.1) - (2.5) on a Cr-stability diagram, stability regimes of metal, oxide, and carbide are delineated. Figure 2-4 [19] shows a modified Ellingham diagram to display results of the Ni-Cr alloy's stability calculations. The boundaries and triple point shown on the stability diagram are governed by the following reactions:

Boundary QA: $$4Cr_{solution} + 3O_2 \rightarrow 2Cr_2O_3 \quad (2.6)$$

Boundary QB: $$23Cr_{solution} + 6C_{solution} \rightarrow Cr_{23}C_6 \quad (2.7)$$

Boundary QC: $$Cr_{23}C_6 + 69O_2 \rightarrow 46Cr_2O_3 + 24C_{solution} \quad (2.8)$$

Triple Point Q: $$2Cr_2O_3 + Cr_{23}C_6 \rightarrow 27Cr_{solution} + 6CO \quad (2.9)$$

The oxidation behavior of a Ni-Cr alloy can be predicted by comparing the oxygen and carbon potentials at the metal surface [11, 33] established by the impurities with the critical parameters $P^*_{O_2}, a^*_C,$ and P^*_{CO}. A simplistic breakdown of the different

environmental responses at different carbon and oxygen potentials at the metal surface are identified in the stability diagram. The four environments, labeled 1, 2, 3, and 4, have the following characteristics: Cr metal is stable and no corrosion takes place (Zone 1); decarburization of the alloy is expected (Zone 2); oxidation and slow carburization of Cr-rich alloy is expected (Zone 3); and carburization is expected in Zone 4. During the steady-state operation of the VHTR, the materials are expected to be in the area of highest stability, Zone 3 (oxidizing and slightly carburizing environment). In the current research, therefore, the environment of interest will be oxidizing and slowly carburizing.

Cabet et al. [40] suggested that there is a critical temperature (900-1000°C), above which chromium oxide is reduced by carbon from the alloy and the surface oxide layer is unstable, hence Equation (2.3) proceeds to the left. The deleterious reaction of chromia and carbon thus fixes the operating temperature of the reactor, which determines the temperature at which the experiments in this research are conducted. The critical temperature is also a function of the partial pressure of carbon monoxide. Figure 2-4 shows that the relationship between the critical temperature and the level of CO. It is observed that the temperature increases with the increase in CO level.

The presence of CH_4, H_2, CO, CO_2, and H_2O in the VHTR helium makes for complex gas-metal interactions. For this reason, the experiments conducted in this research use a simplified binary gas mixture (helium gas containing only CO and CO_2 as impurities) as proposed by Kumar [10]. In the He + CO + CO_2 gas mixture, the oxygen potential and carbon potential are given by the reactions:

$$2CO + O_2 \rightarrow 2CO_2 \tag{2.10}$$

$$P_{O_2} = \frac{(P_{CO_2})^2}{K_{(2.10)}(P_{CO})^2} \tag{2.11}$$

$$C + CO_2 \rightarrow 2CO \tag{2.12}$$

$$a_C = \frac{(P_{CO})^2}{K_{(2.12)}(P_{CO_2})} \tag{2.13}$$

As shown, the oxygen potential in the environment depends only on the CO/CO_2 ratio, whereas the carbon potential depends on both the CO/CO_2 ratio and the CO

concentration in the gas. This means that a low CO/CO_2 ratio has high oxygen and low carbon potentials, whereas a high CO/CO_2 ratio has low oxygen and high carbon potentials.

2.3 Environmental attack of nickel alloys at high temperature

The types of environmental attack outlined in the previous section are manifested in the form of oxidation, carburization and decarburization. The behavior that takes place will depend on the alloy composition, temperature, and helium composition. These processes can degrade the mechanical strength of the material. Cracks can nucleate from internal oxides [41]; low temperature embrittlement [9] and loss of creep ductility can take place as a result of bulk carburization and [42]; decarburization can reduce creep rupture strength [12, 43, 44].

Since the alloys used in the VHTR, as stated previously, are expected to operate in Zone 3 of the stability diagram, this research will focus on the oxidation and carburization degradation modes of Alloy 617. Decarburization is not expected to occur at 800°C [40] and so will not be considered here. Several studies have been conducted to evaluate the corrosion performance of Ni-Cr alloys [10, 28, 33, 40, 45-49].

2.3.1 Oxidation

Chromium is the only major alloying element which would be expected to oxidize in the environment together with other elements present at much lower levels such as aluminum, silicon, manganese, and titanium [28].

The main microstructural observation made is formation of a slow-growing Cr_2O_3 surface scale. This scale can be enriched with Mn on the outer surface and grain boundary oxides rich in Al, Ti and Si [33, 50] as observed for temperatures 800-1000°C for Alloy 617. Elements with a higher oxygen affinity than Cr can form oxides below the chromia scale (Si and Al). Spinel formations can also form at the outer region of the chromia scale. An example is $Mn_xCr_yO_4$ [40, 47] as seen for W-containing Alloy 230. It is important to note also that Cr depletion, caused by preferential oxidation of Cr, can be observed beneath the scale. Figure 2-5 shows the microstructure of Alloy 230 after oxidation [47].

2.3.2 Carburization

Carburization is a high temperature corrosion phenomenon caused by the ingress of carbon from the environment into the alloy, leading to internal carbide precipitation and changes to mechanical properties of the alloy [45]. It has been proved that the solubility and diffusivity of carbon in Fe-Ni-Cr alloys are relatively high so that inward diffusion of carbon prevails and the outward diffusion of carbide-forming elements is much slower. This criterion [51] leads to the well-known appearance of carbide-containing materials in the matrix of the alloy.

Depending on the oxygen partial pressure, two cases of carburization can be considered [8]. On the one hand, if the oxygen partial pressure is lower than the equilibrium partial pressure for the formation of Cr_2O_3, protective chromia scales cannot be formed and carbon can penetrate into the alloy with no inhibition. In this case, the ingress of carbon is diffusion-controlled (rate of carburization depends on the carbon diffusion and solubility into the material). Two zones of carbides are formed: an outer zone with M_7C_3 and an inner zone with $M_{23}C_6$, where M is Cr and/or Mo, as seen in Figure 2-6. At this lower oxygen level, an increase in the content of aluminum in the alloy could be used to form a protective scale. On the other hand, if the oxygen partial pressure is higher than the equilibrium partial pressure for chromium oxide formation, a protective chromia scale is formed. Carburization of chromia-forming alloys should not take place under these conditions since there is virtually no solid solubility of carbon in oxides as shown by Wolf and Grabke [49]. However, carburization may occur if there is permeation of carbon through oxide layers by transport of carbon-bearing molecules along the grain boundary cracks and voids of the oxide scale into the material [46] or if spallation of the oxide scale occurs [48]. Here the ingress of carbon is said to be phase boundary-controlled. This second case is a slow carburization process and is what is expected in the VHTR environments and so will be considered in this research.

Was et al [20] presented the results of experiments in two He + x ppm CO + 1.5 ppm CO_2 (where x = 13.5 and 1980) environments for durations up to 500 h at 850°C on Alloy 617. The corresponding CO/CO_2 ratios are 9 and 1320 respectively. As has been mentioned previously, the low CO/CO_2 ratio of 9 has high oxygen and low carbon potentials, whereas the high CO/CO_2 ratio of 1320 has low oxygen and high carbon potentials. Figure 2-7 and Figure 2-8 show cross-sections revealing the surface

microstructure of the samples exposed to these environments. The exposed specimens were characterized by SEM where the key microstructural features were identified as surface Cr_2O_3, carbide-free zone confined to the grain boundary regions, and Al_2O_3 scales [20]. The dimensions of these features were summarized [20] as shown in Table 2-3, Table 2-4, and Table 2-5. The average dimensions of the features increased with the increase in the carbon potential from environments 9 to 1320 and with the increase in exposure time. A salient observation was that the surface scale Cr_2O_3 was thicker over the grain boundaries where they intersected the surface. It is believed that this could be attributed to higher diffusivity of Cr along the grain boundaries. Also, particles believed to be carbides (Cr_7C_3) were observed on the surface of the chromia scale but only after 500 h of exposure to the environment. Bulk carburization, where there is an increased area fraction of the carbides along the twin boundaries and grain interiors, is shown to have occurred by Kumar et al [10]. Figure 2-9 and Figure 2-10 show the bulk microstructure of Alloy 617 in these environments [10].

2.4 Interaction between mechanical deformation and environmental attack by impure helium environments

Under VHTR high temperature service conditions, the metallic components are subjected to steady loading, cyclic loadings, or even a combination of both while at the same time exposed to the helium environments. The following section describes creep deformation on Alloy 617.

2.4.1 Creep Phenomenon

According to Hooke's law, the instantaneous relationship between the load applied and the deformation of materials at room temperature is linear in the elastic regime. However, at elevated temperatures these materials deform slowly and continuously in a time-dependent manner even when subjected to stresses well below yield stress. This phenomenon is called creep and is defined as the time-dependent deformation of a material under a constant applied load. Since this process is thermally activated, the creep deformation or creep strain can be expressed in very general terms for creeping solid as:

$$\varepsilon = f(\sigma, T, t) \tag{2.14}$$

Additionally, since creep is a thermally activated process, the steady state creep rate can be written in terms of an Arrhenius-type equation and is usually expressed as:

$$\dot{\varepsilon} = Ke^{-\frac{Q_c}{RT}} \tag{2.15}$$

where $\dot{\varepsilon}$ is the creep rate, Q_C is the activation energy for creep, and K is the creep constant. The creep constant is a combined factor that depends on stress, the elastic modulus, and the grain size. For high temperature creep (generally above 0.4 T_m where T_m is the absolute melting temperature of the materials), this activation energy, Q_C, has been shown to be equivalent to the activation energy for self-diffusion, Q_{SD}. This means, therefore, that high temperature creep is controlled by diffusion [52]. High temperature creep can also occur at stresses substantially below the yield stress of the material. The shape of the resultant curve is thus stress and temperature dependent. A model creep curve is shown in Figure 2-11.

This model curve depicts the tensile deformation of a material in the high temperature creep regime and is plotted as axial strain versus temperature. The typical tensile creep curve can be discussed in terms of the initial elastic strain and the subsequent three creep stages. The instantaneous elastic strain is a result of the stress being applied to the specimen suddenly. Thereafter, the first part of the creep curve is a region of increasing strain but at a decreasing rate. This is known as the primary creep of the logarithmic region. The second stage of the creep curve is known as the steady-state or secondary creep and is linear with time. This stage represents a balance between work hardening and recovery processes. This steady-state creep rate ($\dot{\varepsilon}_{ss}$) has a power-law dependence on stress and varies exponentially with the temperature. The relationship is typically expressed as:

$$\dot{\varepsilon}_{ss} = K\sigma^n e^{-\frac{Q_c}{RT}} \tag{2.16}$$

where the creep stress exponent, n, varies from 3 to 8. The final region or the tertiary creep region is the result of internal cavities linking up to form cracks, which ultimately lead to creep rupture. In this region, the creep rate increases at an increasing rate due to a reduction in the net effective specimen section; hence, as the crack grows and the net effective section is reduced, the stress is elevated.

The deformation mode for high temperature creep can be presented in the form of deformation mechanism maps [53]. These maps provide information on the creep mechanisms of materials and make it possible to infer the mechanism that will determine the creep rate under the given conditions. No such maps are available yet for Alloy 617, but an example is shown in Figure 2-12 for pure nickel. From this map, it can be determined that the dislocation creep begins above 0.2 T_m and above $10^{-4}\sigma/E$ depending on the strain rate.

If the material is loaded for sufficiently long times at high temperature, creep deformation will terminate in rupture. Creep rupture can be defined as the end result of the accumulation of creep damage. The first indication of eventual rupture is usually the acceleration in creep rate marking the onset of the tertiary stage as seen in Figure 2-11. According to Ashby and Dyson [54], creep rupture is the result of two or more of the four broad mechanisms. The mechanisms are categorized as: (a) damage by **loss of external section** (necking), (b) damage by **loss of internal section** (formation of cavities at lower stresses and grain boundary cracks at higher stresses), (c) damage by **microstructural degradation** (overageing of second phase particles needed for strengthening), and (d) damage by **gaseous-environmental attack** (internal and external oxidation). Although, several processes can cause or contribute to the acceleration of creep rate during the tertiary stage, it is usually the development of microcracks that leads to creep fracture. These microcracks, at high temperatures, normally form and grow along grain boundaries (intergranular cracks). Two forms of intergranular cracking are observed. At high stresses, wedge or triple-point cracks are formed, while intergranular cracks develop at low stresses by nucleation, growth and link-up of grain boundary cavities.

2.4.2 Creep of Alloy 617 in Air and impure He environments

High-temperature mechanical deformation behavior of Alloy 617 has been characterized and this sub-section summarizes the most important findings.

Studies have shown that the creep behavior of Alloy 617 depends on the test temperature. In a review by Shubert et al [55], they identified Alloy 617 as having superior creep qualities compared to other high-temperature alloys (Hastelloy-S, Hastelloy-X, Nimonic-86, IN-519, and Incoloy 800H). They observed that creep curves at 850°C showed the more or less classical form of creep curve with recognizable primary, secondary, and tertiary creep regimes. However, at 950°C the 617 curves showed an increasing creep rate from the start of the test with no recognizable secondary creep regime. This disappearance of the secondary creep regime is consistent with the observation made by Roy where increasing the level of stress or temperature decreased the length of steady-state regime [56]. In contrast, Chomette noted non-classical creep behavior of Alloy 617 between 850-950°C, where a strain rate drop at the beginning of the test preceded a creep rate increase to a plateau before the onset of tertiary creep..

Creep mechanisms of Alloy 617 have been defined in the literature. Kihara studied the evolution of carbides during creep and their effects on the creep properties of Inconel 617 at 1000°C and 24.5 MPa [27]. He identified a correlation of creep regime with evolution of carbides and determined that the grain boundary migration started in the steady state region. Cook went further and pointed out that decarburization at 1000°C reduced creep strength as grain boundary migration took place [57]. While these final creep stages exhibited grain boundary sliding due to migration of carbides, other researchers (Sharma [58] and Kim[59]) have identified dislocation climb as the rate-limiting creep deformation mechanism for Alloy 617.

2.4.3 Simultaneous action of stress and environmental attack at high temperature

Under service conditions, it is most often not high-temperature corrosion alone that causes failure of components, but the interaction with simultaneous mechanical stresses. It is important to point out the difficulty of separating the effects of these two factors at high temperatures since there seems to be a synergistic effect of both stress and environmental attack. In this section, the effect of corrosion on the mechanical behavior

and the effect of applied loads on the corrosion behavior of high temperature alloys are discussed.

Studies have been conducted in an effort to understand the effect of mechanical deformation on the high temperature environmental attack. First, Rahmel and Grabke in their review [60] have shown that the chromia scale formed at high temperature can undergo rupture and spallation as a result of creep. Due to the repetitive exposition and oxidation of the base alloy surface, the analysis of the environmental attack could be misleading to suggest a scale growing following a linear-rate law while in effect the growth is a repetition of the initial parabolic phase. Second, Schnass [42] added that the rupture of the scale could increase internal corrosion of the alloy. Under an oxidizing and carburizing H_2O-CO-H_2 environment and mechanical stress, he demonstrated how a Ni-Cr-Fe alloy suffered preferential grain boundary attack as a result of carbon-bearing element penetration and formation of internal carbides along the grain boundaries. These carbides can subsequently be selectively oxidized. Attention was also brought to the fact that this enhanced corrosion took place at high and not low strain rates.

It also is evident from several studies that the environmental attack has a bearing on the mechanical deformation of the alloys at high temperature. Conflicting observations of the effect on the creep resistance have been made. Precipitation hardening of carbides at 900°C showed an increase in creep resistance, but the creep strength was reduced after thermal ageing at 1000°C since the coarsening of the carbides became less effective dislocation barriers [61]. The reduction of creep strength has also been reported to occur as a result of chromia scale growth. This growth occurs by formation of vacancies at the metal/scale interface when metal ions and electrons migrate outwards during corrosion [61, 62]. The gas environment composition has been shown to influence the type of creep failure. In a study to investigate the effect of trace impurities in helium on creep behavior, Shankar and Natesan [12] observed that a carburizing environment exhibited the lowest rupture strain and longest life, while an oxidizing environment exhibited shorter life. These different results on creep behavior of Alloy 617 in different helium environments point to a complex behavior that is not completely understood. There is general agreement, however, that the creep behavior of Alloy 617 is affected significantly by the

type of environment. This has been shown by results of creep-rupture strength in air and in HTR helium occurring within the same scatter band [44, 63].

Studies have also been conducted on the synergy between environmental attack and cycling. Balanced cycles of equal strain rates in tension and compression were subjected on stainless steel (304) at elevated temperature in air. It was observed that as the frequency of the cycles was decreased, the fatigue life was reduced. This was demonstrated by the change from slip-band-induced transgranular initiation to oxidation-induced initiation and further propagation of cracks [64]. Sadanada [65] has shown the effect of fatigue processes of Alloy 718 at 425°C on the environmental effect at the crack tip by favoring oxygen transport ahead of the crack tip during fatigue [66].

It is apparent that most of the studies conducted so far sought to understand the synergy existing between stress and environmental attack on alloys that were tested for longer times and sometimes to failure. The observations made in these tests have shown how difficult it is to separate the effects of temperature, cycling, strain rate, and environment during high-temperature deformation studies. Yun [67], for instance, concluded that the rupture of a specimen at high temperature was not caused by oxidation-induced surface cracks alone, but also by the formation of creep pores and cracks that were not dependent on the test atmosphere. For this reason, it is believed that extra work needs to be done to clarify the near-surface damage in the absence of bulk degradation during static and cyclic deformation at high temperature. In this way, the study of the change of microstructure around the oxidation-induced surface cracks could be simplified and reduced to near-surface damage analysis and the surface response in different environments could be studied. Viskari [68, 69] gives an example of this approach by describing the course of events that takes place during the intergranular crack tip oxidation of Alloy 718. Krupp et al have also shown that there is a change of oxidation products within the cracks formed at high temperature by comparing the sharp tip of wedge-type specimens during isothermal exposure and thermal-cycling conditions.

2.5 Development and characterization of barrier layers proposed for protection of Alloy 617 in impure helium environments

The NEUP 10-963 Final Report [21] provided a comprehensive summary of the characterization of coating layers developed by Clark [18], which is presented in this section.

Chromia formed on Alloy 617 is incapable of developing a protective surface oxide scale in impure helium environments at higher temperatures (> 800°C) and cannot prevent further environmental attack in the form of oxidation, carburization and decarburization compared to alloys capable of developing the more stable alumina scale [44, 70]. The formation of chromia on 617 has two consequences. First, it induces Cr-depleted and carbide-depleted zones [61, 71] under the surface oxide layer. The loss of chromium from the matrix reduces the degree of solid solution strengthening and also leads to a dissolution of chromium carbides as the chromium activity decreases [61]. Second, the formation of internal alumina oxides is known to act as initiation sites for surface cracks [72], and also, when coupled with mechanical cycling, as an aid in crack propagation [73]. To improve the corrosion and oxidation resistance of Alloy 617, the formation of alpha alumina scale instead of chromia should be promoted, and also grain boundary oxides that affect the mechanical performance of the alloy should be eliminated or reduced.

Even though alpha alumina has more attractive properties (slow growth and superior stability) relative to chromia, its formation is preceded by metastable phases (gamma and theta) at intermediate temperatures. Two barrier concepts developed on Alloy 617 and characterized at the University of California Santa Barbara were used in this dissertation. The concepts are based on alpha alumina as a primary surface barrier, provided by one or more chemically distinct alloy layers that would promote and sustain the formation of the protective scale. One approach relied on aluminizing as a path to form an Al reservoir on the alloy surface that can enable and sustain the formation of thermally-grown alpha alumina. The second approach involved cladding the aluminized surface with a thin layer of FeCrAl(Y/RE), an alloy well known to form alpha alumina at lower temperatures much more readily than diffusion aluminide or MCrAlY coatings typically used for oxidation protection in Ni-base superalloys. The following sections

summarize the suitability of these coatings to protect Alloy 617 in the absence of mechanical stress as described by Clark [18, 21].

A high-activity/low temperature pack cementation aluminizing process was performed using a powder mixture of $4Al/4(CrCl_3 \cdot 6H_2O)/ 92Al_2O_3$ (in weight percent). After being wrapped in alumina paper, the specimens were embedded in the pack, sealed in an alumina crucible, and placed in a tube furnace under flowing high purity Ar ($X_O \leq 10^{-5}$). Depending on the desired aluminizing thickness, the pack was heated for a prescribed temperature (700-850°C) and time (4-10 h). Subsequently, annealing was done at 1000°C in flowing, gettered Ar to complete the development of the surface layers before the surface was polished down to an 800-grit finish to eliminate residual oxide. Two generations of materials with different aluminized layers were prepared, namely: Generation I and Generation II. Generation I (Gen I) specimens were made by aluminizing at 700°C/9.6h and subsequently heat treating (1000°C/16h) to develop the NiAl layer by interdiffusion with the substrate. A carbide + sigma phase was formed. Aluminizing for Generation II (Gen II) specimens was done at 850°C/4h and heat treated at 1000°C for 1h. This became the preferred aluminizing process with the advantage of minimizing the scale to be removed after heat treatment, preserving a thicker aluminized layer, and also developing a more stable sigma phase.

A subset of aluminized specimens was clad with FeCrAlY by diffusion bonding using a high vacuum hot press (1000°C/1h/20MPa). Gen II aluminized creep specimens were clad only on the wider surfaces of the gauge length and the excess cladding trimmed using a femto-second laser.

All specimens to be used for subsequent environmental exposures and creep were pre-oxidized (1000°C/2h) in gettered Ar ($X_O \leq 10^{-13}$) to form a thin, continuous alpha alumina scale prior to testing.

2.5.1 Baseline oxidation and interdiffusion properties

In order to provide a baseline for subsequent characterization of creep behavior in impure Helium environments, Clark evaluated the microstructure evolution of the synthesized barrier layers in benign environments without applied load. Long-term effectiveness of the barrier layers requires that the Al reservoir be stable against depletion by subsequent oxidation and interdiffusion with the 617 substrate, and the protective

scale needs to be regenerated in case of cracking or spalling. The following subsections provide a summary of the characterization of oxidation and interdiffusion properties as described by Clark [18].

2.5.1.1 Oxidation

Clark observed that smoother, thin, dense, and adherent α-alumina was formed on the NiAl and FeCrAlY layers upon pre-oxidation in low pO_2, thereby suppressing the plate-like or whisker-like morphologies associated with the transient alumina growth. However, the transient alumina phases persisted longer in the aluminized surfaces than on those clad with FeCrAlY, and the difference was accentuated at lower temperatures, as shown in Figure 2-13 and Figure 2-14. Even though this step demonstrated that the alumina formed was sufficiently adherent and durable, creep studies in impure He environments are required to verify whether a protective alumina scale will be regenerated in the event of local damage (cracking/spallation).

2.5.1.2 Interdiffusion - Aluminized systems

Aluminizing at low-temperature and high-activity produced a top layer comprising primarily Ni_2Al_3 with discrete second phases darker in BSE contrast, Figure 2-15(a,e). Figure 2-16(a) shows an Al:Ni ratio higher than 3:2, presumably because of substitution of other elements, e.g. Co, in the Ni_2Al_3. Clark surmised that the darker low-Z phases in Figure 2-15(a,e) and Figure 2-16(a) were likely carbides of the elements with lower solubility in Ni_2Al_3 that precipitate in situ as the aluminizing front advances rapidly into the 617 substrate. After the lower aluminizing temperature for Gen I, Clark observed no layers of intermediate phases at the interface with the substrate, Figure 2-15(a), but she observed an incipient layer of sigma phase, corresponding to the spike in the Mo and Cr concentrations in Figure 2-16(a), at the similar interface after the higher temperature process (Gen II). This layer was interpenetrated by metal that eventually allowed outward Ni diffusion to convert the Ni_2Al_3 layer into NiAl.

A more desirable NiAl was formed from transformation of Ni_2Al_3 following the heat treatment. During this process, two distinct layers developed at the interface with the substrate, consisting primarily of $M_{23}C_6$ carbide, closer to the NiAl, and sigma phase, closer to the substrate. Even though these layers were interpenetrated by a small fraction

of metallic phases, they acted as effective barriers to slow down interdiffusion with the substrate at longer times. The carbide and sigma layers are suspected to be brittle phases, and it is not clear if they could be potential crack initiation/propagation zones after strain accumulation during static or cyclic creep. Clark noted that a layer of Ni-rich NiAl that lacked second phases evolved between the original aluminized thickness marked by Cr-rich precipitates, and the *in-situ* diffusion barriers, as shown in Figure 2-16(b). This layer had a noticeably lower Cr content than the outer NiAl layer, as shown in Figure 2-17. Figure 2-19(a) indicates that the addition of Al to the original 617 composition moves the system into regions where the FCC and B2 systems can be in equilibrium with the $M_{23}C_6$ and sigma phases.

Slow growth of the carbide and sigma interphases resulting from the additional heat treatment at 1000°C are shown in Figure 2-15 and Figure 2-17. The sigma layer became destabilized after ~100h and was replaced by a less continuous layer of M_6C that was believed to be less effective as a diffusion barrier in Gen I specimens (Figure 2-15(a-d)). Close to the carbide layers, there was a region with small amounts of the $L1_2$ phase, Figure 2-19(a). In contrast, Clark observed that the higher aluminizing temperature used for Gen II resulted in a much more stable sigma layer over time that was retained even after 500h at 1000°C as shown in Figure 2-15(e-h) and Figure 2-17(a,b). The surface layers evolved much slower at 800°C, as shown by comparisons of Figure 2-17 and Figure 2-18. This was assumed to be the current temperature of interest for the IHX in the VHTR.

2.5.1.3 Interdiffusion – Clad/Aluminized systems

Clark also showed that cladding of the aluminized surface generated a combination of an Al-lean outer layer more favorable to the rapid formation of alpha alumina, with an Al-rich reservoir under it. As the FeCrAlY layer was slowly oxidized, the underlying aluminide layer was expected to replenish the Al. Additionally, it also served as a diffusion barrier between FeCrAlY and 617. In this section, the diffusional interactions of the cladding/reservoir system and their long-term durability, as observed by Clark are presented.

Figure 2-20 shows microstructures of Gen I and Gen II aluminized systems with FeCrAlY cladding, where Gen II specimens showed residual porosity at the interface

between the cladding and the aluminide layer, Figure 2-20(e). Clark could not identify the origin of this porosity, but surmised the possibility of asymmetric interdiffusion or insufficient creep deformation during bonding. It is worth noting, however, that the Gen I specimens were heat treated for 16h at 1000°C to develop the aluminized layer structure prior to cladding, whereas the Gen II specimens were clad in the as-aluminized condition because the sigma layer was already present. The outer surface was Ni-rich NiAl in Gen I and Ni_2Al_3 evolving into Al-rich NiAl during the process, as suggested by the presence of Cr-rich precipitates in Figure 2-20(e). Clark hypothesized that the chemical differences resulted in variations in the interdiffusion and creep behavior occurring during the diffusion bonding process, leading to porosity in Gen II but not in Gen I. Subsequent diffusion eliminated the pores at 1000°C (Figure 2-20f-h), but much more slowly at 800°C (Figure 2-21). It remains to be verified whether the presence or absence of precipitates in the NiAl layer of the clad systems could have an effect on the mechanical integrity of the system during creep.

According to Clark, cladding of aluminized specimens rendered the carbide+sigma diffusion barrier layers less stable than the un-clad aluminized layers at 1000°C (Figure 2-15 and Figure 2-20). In general, the sigma layer was disrupted and largely eliminated in the presence of the cladding although it was slightly more durable in the Gen II specimens. Figure 2-20(b,f) shows that the sigma layer was still continuous after 24h at 1000°C in the Gen II specimen, but was discontinuous for the Gen I materials. The evolution of the sigma layer composition in Gen I aluminized+clad specimens at 1000°C after 16h and 168h is compared in Figure 2-22. The composition of the sigma layer was modified by the inward diffusion of Fe from the cladding, thereby reducing the content of Mo, Ni and Co, which Clark supposed was responsible for reducing the stability of the sigma layer since Mo is a stronger stabilizer for sigma than Fe. The released Mo would then favor the formation of M_6C, seen after 24h in Figure 2-20(b).

However, heat treatment at 800°C retained the diffusion barrier layers, Figure 2-21, with concomitant evolution of carbides within the matrix (Figure 2-18). The Cr precipitates within the NiAl layer persisted after the treatment at 800°C, but were largely eliminated after 500h at 1000°C, especially for the Gen II specimens. Conversely, Clark

did not observe $L1_2$ phases develop within the B2 layer in the Gen I or II specimens, in contrast with the behavior observed for Gen I without cladding, Figure 2-15(d).

Clark noted two important changes in the microstructure of the clad layer as interdiffusion proceeded. First, a fine dispersion of precipitates evolved near the interface with the aluminized layer, which receded gradually, as illustrated in Figure 2-23(a,b). TEM analysis in Figure 2-23(c) revealed these precipitates to be B2-(Fe,Ni)Al, 100-200 nm in size, coherent with the matrix. Atom probe tomography (ATP) identified at least two additional distinct populations of Ni-bearing second phases, one in the 10-20nm range and the other comprising nanoclusters under 10 nm in diameter, Figure 2-23(d). The strength of the FeCrAlY cladding has been shown to be improved by the presence of these precipitates – of relevance to the initiation of creep-fatigue damage. However, they tend to coarsen and re-dissolve as the matrix transforms from the b.c.c. (A2) structure, characteristic of FeCrAlY to f.c.c. (A1), with continued Ni diffusion. At the longer times, the cladding consisted of a A2/B2 outer layer, denoted by β/β' in Figure 2-20, and a region of f.c.c. (A1) solid solution next to the remaining NiAl layer. The evolution was delayed in Gen II specimens relative to Gen I, with no A1 layer present after 168h at 1000°C in the former, Figure 2-20(g), while about half of the clad layer transformed to A1 in the latter, Figure 2-20(c). No evolution of an f.c.c. layer was observed by Clark upon heat treatment at 800°C, even after 375 h, Figure 2-21(d). B2 precipitates evolved in a finer scale than at 1000°C, but they re-dissolved near the interface with the aluminide layer, as shown in Figure 2-24.

Clark prepared diffusion couples between FeCrAlY foils and two NiAl alloy plates with compositions $Ni_{50}Al_{50}$ and $Ni_{60}Al_{40}$ in an effort to understand the interdiffusion phenomena when secondary alloying elements are absent. The results in Figure 2-25 show the critical role of the Ni:Al ratio on the evolution of the FeCrAlY microstructure. Interdiffusion with the stoichiometric NiAl, Figure 2-25(a), resulted in a relatively thin (20μm) layer depleted in Ni and Al and enriched in Fe and, to a lesser extent, in Cr. The FeCrAlY, however, appeared uniform in composition, with a microstructure consisting of fine B2 precipitates in the A2 matrix (β/β'). In contrast, the FeCrAlY/$Ni_{60}Al_{40}$ couple showed a much larger diffusion-affected region in the B2 region (>100μm), and a large fraction of the FeCrAlY transformed to a face-centered

cubic structure, Figure 2-25(b). She observed an abrupt change in the composition profiles within the FeCrAlY layer, with the f.c.c. region containing a much larger Ni:Al ratio than the β/β', which was enriched in Cr. The conversion of the FeCrAlY clad layer from its conventional A2 structure into A1 was shown by Clark to have implications to its oxidation behavior, as discussed in the next section.

2.5.2 Exposure to impure helium environments

In this section, the effectiveness of the alpha alumina barrier relative to the chromia scale typical of uncoated 617 in simulated exposures to impure He without applied load is summarized. The specimens were all pre-oxidized prior to exposure at temperatures of 800-1000°C for times up to 500 h. The impure He environments were decarburizing (CO/CO_2 ~9 and $CO+CO_2$ ~15 ppm, with $X_O \approx 10^{-21}$) and carburizing (CO/CO_2 ~1272 and $CO+CO_2$ ~1910 ppm, with $X_O \approx 10^{-24}$). This work described in Clark's thesis [18] was performed at the University of Michigan, Ann Arbor.

Figure 2-26 shows the weight changes per unit area during exposure to impure He for uncoated, aluminized, and aluminized+clad 617. Clark observed that the aluminized samples showed superior environmental resistance in both carburizing and decarburizing environments relative to uncoated 617. The scale in the aluminized specimens, shown in Figure 2-27(a,b), had grown over time but remained similar to that produced during the pre-oxidation treatment, i.e. dense, continuous alpha alumina, whereas the scale in the uncoated 617 was chromia, which is less stable in similar environments as reported elsewhere [10, 74].

Clark observed that the behavior of aluminized+clad samples was generally worse than the uncoated 617 in both the carburizing and decarburizing environments. She originally ascribed this behavior to damage associated with trimming of the excess cladding. The mechanical shearing approach had been used for the first trimming and was found to result in significant edge damage with increased environmental interaction. The external appearance of the specimen suggested substantial reaction of the overhang cladding surface and neighboring region, as shown by the darkened region in Figure 2-28(a). The center of the specimen, however, appeared much less affected by the exposure, retaining the alumina scale and a similar evolution of A2 into A1 and A2/B2 observed in the oxidation in gettered Ar – see Figure 2-29.

In a second approach, Clark trimmed the excess cladding using a pulsed femtosecond laser known to yield minimal thermal distortions that could initiate delamination from the substrate. This time there was improved carburization, as shown by comparison of Figure 2-28(a and b). The structure of the scale was similar to that evolving on the aluminized-only specimens after 500h (cf. Figure 2-27c,d), and the cross section was similar to that in Figure 2-29.

To explore the possibility of the mechanical shearing being the reason for the difference in behavior of the over-hang portion of the cladding, Clark conducted two different tests. In one case, she exposed pre-oxidized FeCrAlY coupons of similar dimensions to both carburizing and decarburizing environments to evaluate the intrinsic resistance of the cladding to these environments. These tests yielded maximum weight gains $\leq$ 1.6 mg/mm^2, comparable to those of the aluminized 617 specimens in Figure 2-26. In a second test, she explored the possibility that the excessive weight gain was associated with damage to the original scale. She did this by indenting the surface of the pre-oxidized specimens to crack the scale, and the specimen was then exposed to the carburizing environment. Figure 2-30, revealed that the FeCrAlY was sufficiently robust to regenerate the alumina scale in the damaged areas before any significant carburization could take place. The morphology of the oxide in Figure 2-30(c,d) suggests some transient alumina formation prior to the conversion to alpha. According to Clark, it was unlikely that the excess weight gain was due to poor resistance of FeCrAlY against carburization as the diffusion of C through alpha alumina is very slow.

Cross sections of the corners of specimens corresponding to the two different trimming approaches are shown in Figure 2-31. Clark showed that the damage was quite severe in the mechanically trimmed samples, Figure 2-31(a,b), and proceeded from the corner along the boundary between the cladding and the NiAl layer. The penetration in Figure 2-31(b) was consistent with the damage observed in Figure 2-28(a). Figure 2-32 shows that both the cladding and the aluminized layer have been substantially affected, with extensive oxidation and carburization. The cladding seemed to have incorporated a major fraction of Ni and reduced the Cr so it is likely to have transformed completely into f.c.c. (A1) and the aluminized layer has also been depleted in Al presumably due to the severe oxidation (darker areas in Figure 2-32). Clark was surprised to observe that the

edges of the 617 substrate, which were aluminized but not clad, showed little change after 100h but severe degradation after 500h, Figure 2-31(a,b), even though the surfaces of the aluminized-only specimens experienced no significant damage.

The laser-trimmed specimens showed significantly reduced damage, as shown in Figure 2-31(c,d). Clark observed interdiffusion between the cladding and the aluminized layer, as well as some oxidation and possibly some carburization, but only a small crack at the corner that did not seem to advance significantly between 100 and 500h. Details from the 100h exposure are given in Figure 2-33. In this region the FeCrAlY still retained largely the ferritic structure with B2 precipitates (β/β'). Some initial transformation to f.c.c was observed at the interface away from the corner in Figure 2-33(a). After 100h, there was no degradation at the un-clad edges, which preserved the aluminized structure, although some blemishes in the equivalent region were seen after 500h (Figure 2-31(d)).

Figure 2-36 shows the possible effects of interdiffusion on the degradation behavior of the clad specimens when the environment has access to the interface. A sample initially exposed for 100h/1000°C to the decarburizing He environment, experiencing some formation of A1 solid solution at the interface between the NiAl and FeCrAlY, was sectioned and subsequently exposed to a short oxidation treatment for 1h at 1000°C in gettered Ar. Clark observed a remarkable difference in oxidation behavior, with the f.c.c. forming a chromia scale and the β/β' structure in the upper part of the FeCrAlY forming alumina, which also evolved on the sectioned NiAl surface. She proposed that this observation implied that when a carburizing environment accesses a region of the interface that has transformed to f.c.c., through an edge crack, the subsequent oxidation may not be protective as it is on the NiAl or even the ferritic FeCrAlY. There is a need to investigate the potential of degradation at edges during creep in impure He environments.

Clark also designed experiments (that were conducted at the University of Michigan, Ann Arbor) on aluminized-only specimens at 800°C, primarily in the carburization environment that proved to be the more aggressive for these systems. Figure 2-35 shows the evolution of the microstructure as a function of time. The Cr-rich precipitates within the NiAl were still retained, although there was some indication of carbide evolution (the regions intermediate in brightness between the NiAl matrix and the

Cr precipitates). Clark could not conclusively determine if this was a result of some C ingress from the environment, which was not observed at higher temperatures and would be hindered by the presence of the original alumina barrier. Evolution of carbides under the sigma layer, shown in greater detail in Figure 2-36, was also observed. TEM analysis revealed the presence of both $M_{23}C_6$ and M_6C carbides, as well as discrete sigma precipitates and incipient formation of $L1_2$, the latter also found in greater proportions at higher temperatures. There is a need to evaluate the robustness of the aluminized layer against carburization during creep.

2.6 Research Objectives

The objectives of this research are two-fold. First, is to characterize the near-surface damage accumulation on Alloy 617 during static and cyclic creep. In order to do this, the effect of different controlled helium environments on the damage on Alloy 617 is analyzed by studying the extent and mechanism of the different types of damage. The thesis will therefore focus on oxidizing environment (O potential), carburizing environments (C potential), and both environments (O and C potentials). Second, is to evaluate the efficacy of the different coating concepts (aluminizing by NiAl, and cladding by FeCrAlY) in protecting Alloy 617 against the environmental attack during static and cyclic creep. In order to do this, this dissertation will explore both the microstructural stability and the mechanical integrity of the different coating layers.

Table 2-1 Nominal chemical composition (wt.%) of Alloy 617. Adapted from [75].

Ni	Cr	Co	Mo	Al	Fe	Mn	Ti	Si	C	Cu	B	S
Bal.	22.0	12.5	9.0	1.2	1.0	1.0	0.4	0.1	0.1	0.5	0.006	0.015

Table 2-2 Impurity content in the helium experimental reactors [31, 32].

	H_2O	**H_2**	**CO**	**CO_2**	**CH_4**	**O_2**	**N_2**
PB	0.5	10	0.5	<0.05	1	-	0.5
FSV	1	7	3	1	0.1	-	-
AVR	0.15	9	45	0.25	1	-	22
Dragon	0.1	0.1	0.05	0.02	0.1	0.1	0.05
THTR	<0.01	0.8	0.4	0.2	0.1	-	0.1

Table 2-3 Dimensions of microstructural features observed in the cross-sections of Alloy 617 samples exposed to He-CO/CO_2=9 and 1320 at 850°C for 75h. Adapted from [20].

75 h	Surface Cr_2O_3 thickness		intergranular Al_2O_3 depth		transgranular Al_2O_3 depth	
	Env. 9	Env. 1320	Env. 9	Env. 1320	Env. 9	Env. 1320
# of data	50	72	108	109	62	97
Max. value (μm)	1.32	1.24	5.61	7.86	3.63	4.41
Min value (μm)	0.50	0.69	1.36	2.96	0.97	0.82
Mean value (μm)	**0.82**	**0.93**	**3.53**	**5.15**	**1.83**	**1.98**
Standard Dev.	**0.21**	**0.11**	**0.95**	**1.13**	**0.47**	**0.73**
% Error	26.0%	11.8%	26.9%	21.9%	25.9%	36.8

Table 2-4 Dimensions of microstructural features observed in the cross-sections of Alloy 617 samples exposed to He-CO/CO_2=9 and 1320 at 850°C for 225h. Adapted from [20]

225 h	Surface Cr_2O_3 thickness		intergranular Al_2O_3 depth		transgranular Al_2O_3 depth	
	Env. 9	Env. 1320	Env. 9	Env. 1320	Env. 9	Env. 1320
# of data	90	57	171	93	200	200
Max. value (μm)	2.13	1.78	14.09	12.54	5.45	6.01
Min value (μm)	0.28	0.91	2.28	2.32	0.63	0.80
Mean value (μm)	**1.31**	**1.46**	**5.85**	**6.91**	**2.40**	**2.73**
Standard Dev.	**0.39**	**0.15**	**2.11**	**2.31**	**0.98**	**1.07**
% Error	29.5%	10.2%	36.1%	33.4%	40.8%	39.2%

Table 2-5 Dimensions of microstructural features observed in the cross-sections of Alloy 617 samples exposed to He-CO/CO_2=9 and 1320 at 850°C for 500h. Adapted from [20]

500 h	Surface Cr_2O_3 thickness		intergranular Al_2O_3 depth		transgranular Al_2O_3 depth	
	Env. 9	Env. 1320	Env. 9	Env. 1320	Env. 9	Env. 1320
# of data	75	90	153	150	136	137
Max. value (µm)	4.01	2.01	22.00	19.63	8.17	6.53
Min value (µm)	2.42	1.05	7.50	4.44	3.31	1.51
Mean value (µm)	**3.09**	**1.53**	**14.16**	**10.41**	**6.01**	**3.45**
Standard Dev.	**0.32**	**0.21**	**3.03**	**2.42**	**0.98**	**1.16**
% Error	10.4%	13.4%	21.4%	23.3%	16.2%	33.6%

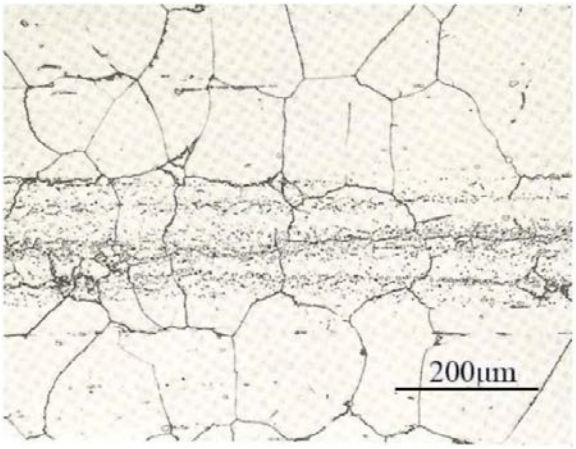

Figure 2-1 Typical microstructure for a mill-annealed Alloy 617 [76].

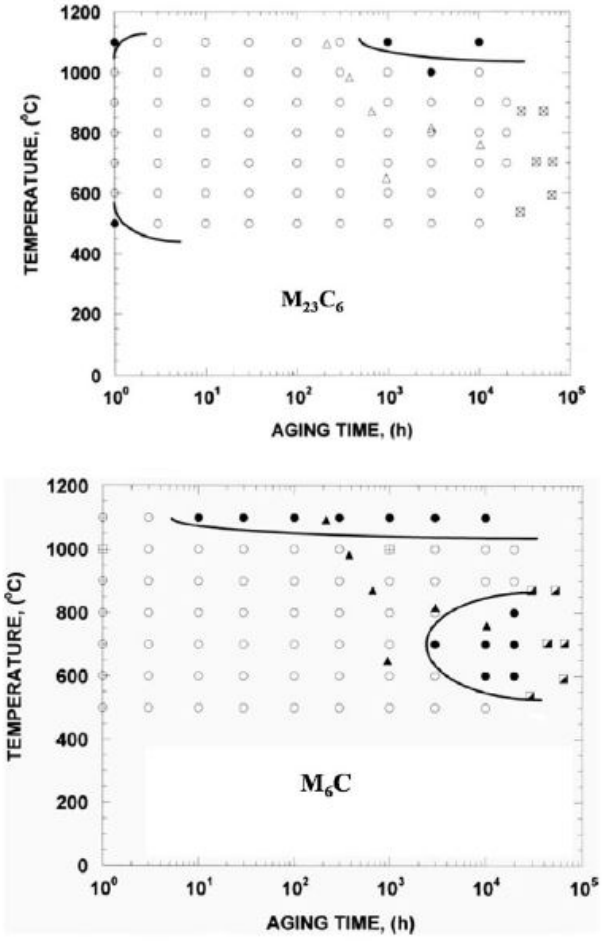

Figure 2-2 Time-temperature-precipitation diagrams for chromium carbides in Alloy 617 [23].

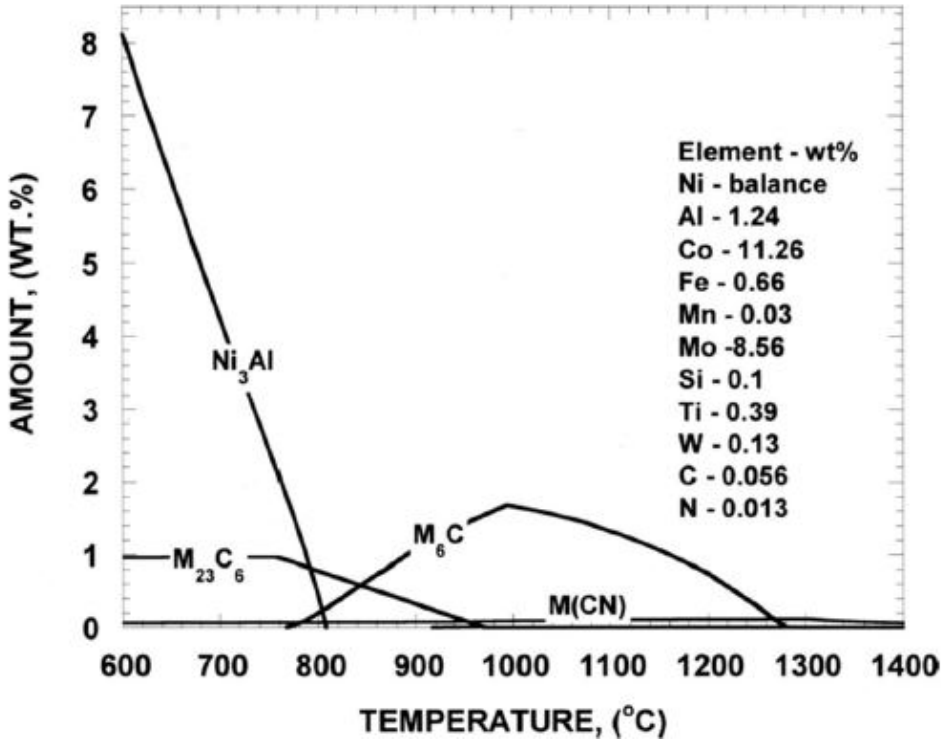

Figure 2-3 Amount of precipitates in Alloy 617 calculated by THEROCALC® [23].

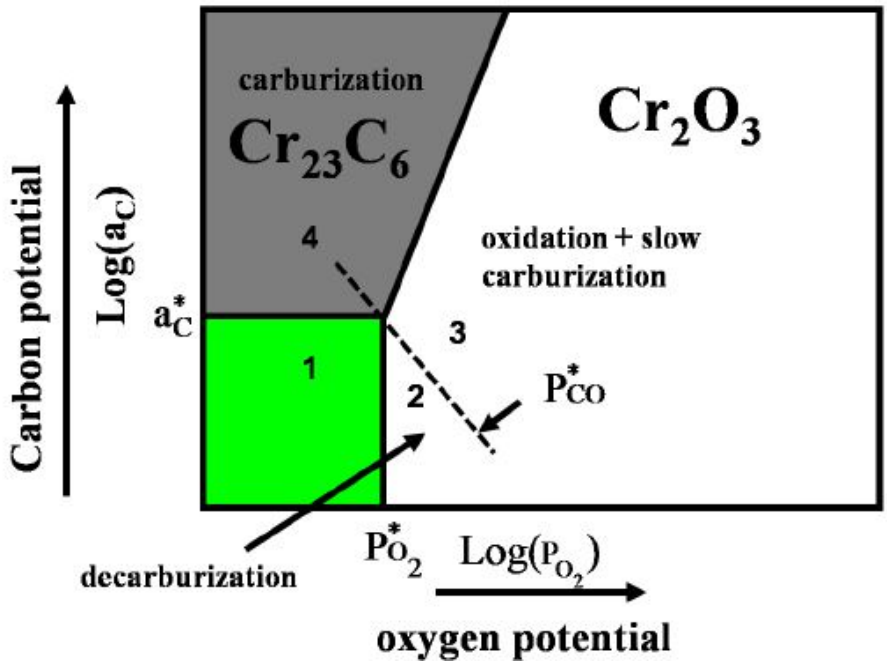

Figure 2-4 Oxidation behavior of a Ni-Cr alloy based on Cr-stability diagram. Adapted from [19].

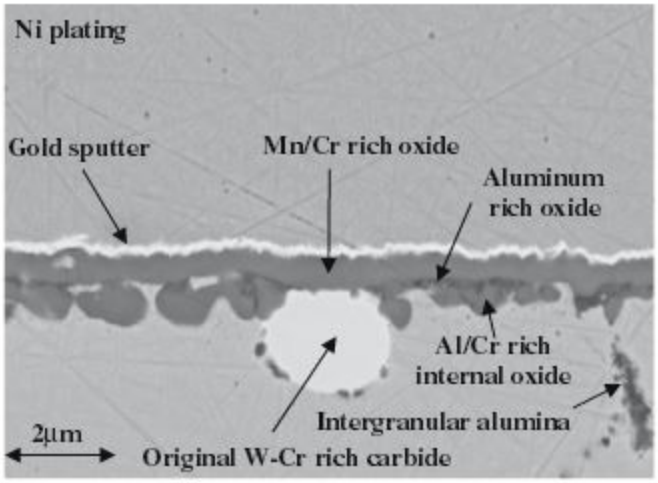

Figure 2-5 Microstructure of Alloy 230 after oxidation at 900°C [47].

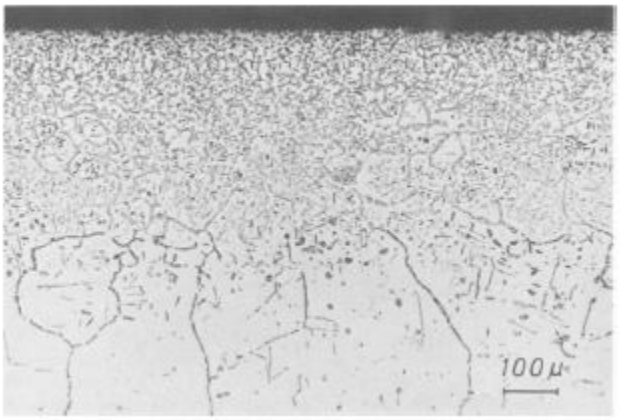

Figure 2-6 Internal carbide formation in alloy 800 with outer and inner carbide zones [42].

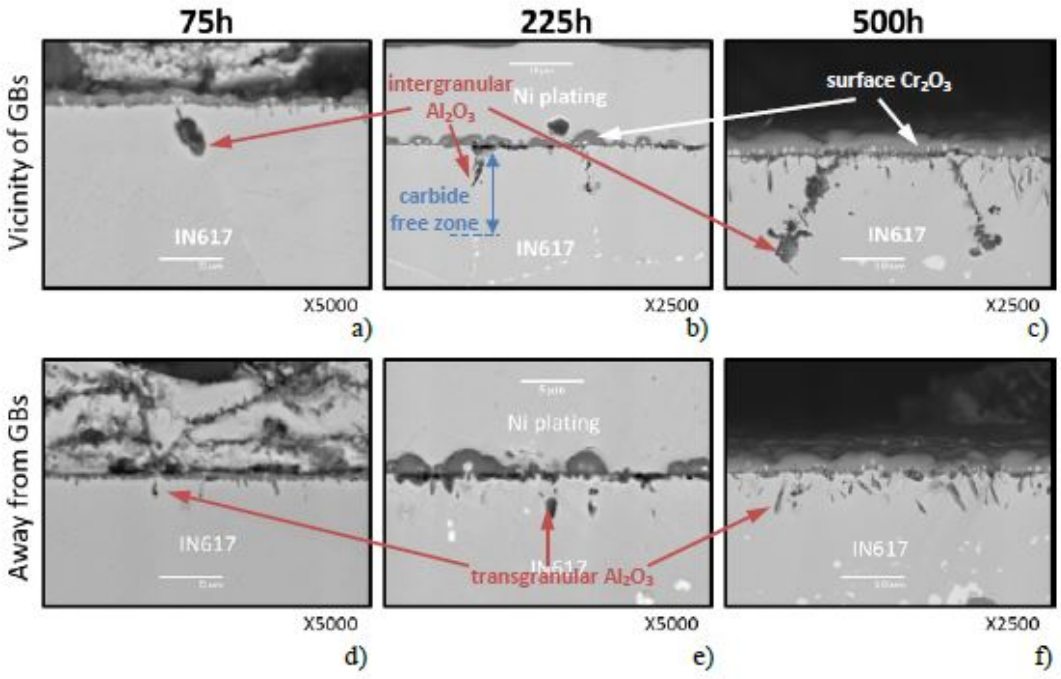

Figure 2-7 IN617 samples exposed to He-CO/CO_2 = 9 at 850°C. Adapted from [20].

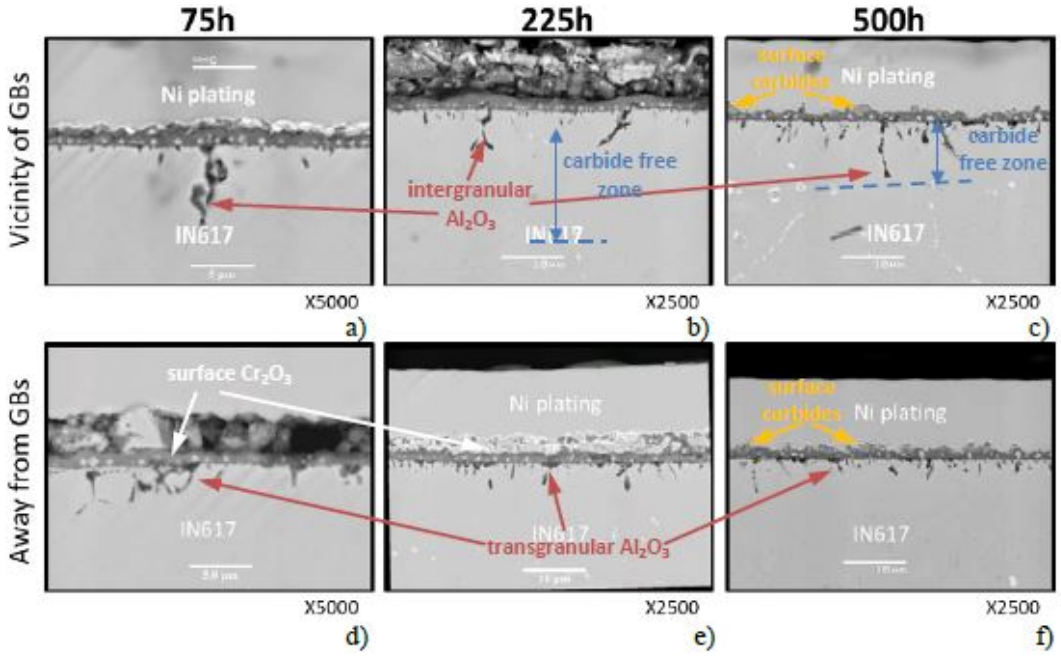

Figure 2-8 IN617 samples exposed to He-CO/CO_2 = 1320 at 850°C. Adapted from [20].

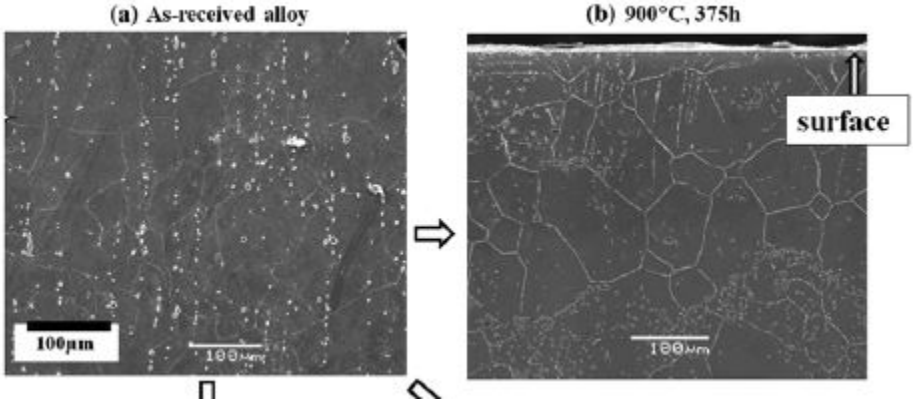

Figure 2-9 Bulk microstructure of IN617 exposed in He-CO/CO_2 = 9 at 900°C. Adapted from [19].

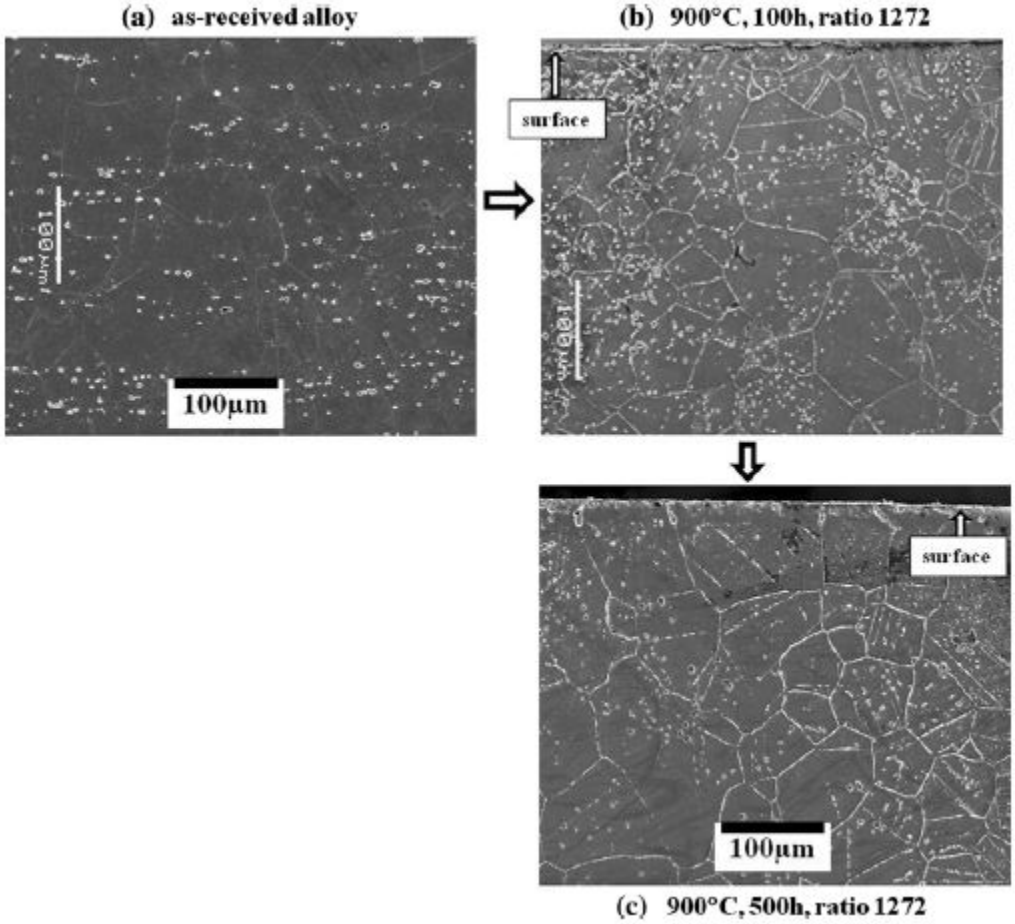

Figure 2-10 Bulk microstructure of IN617 exposed in He-CO/CO_2 = 1272 at 900°C. Adapted from [19]

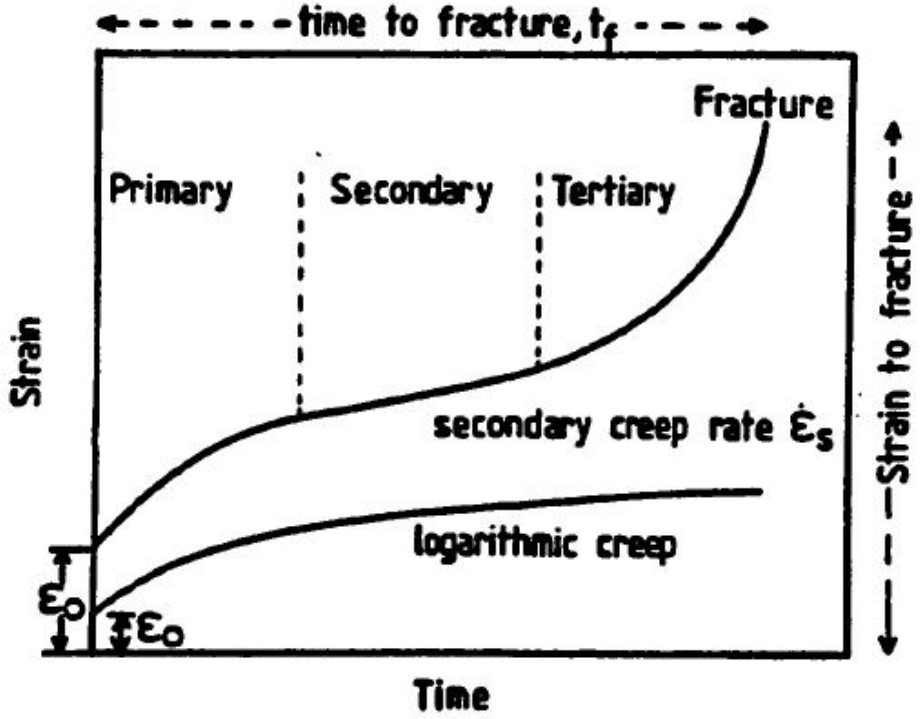

Figure 2-11 A model creep curve showing the three stages of creep.

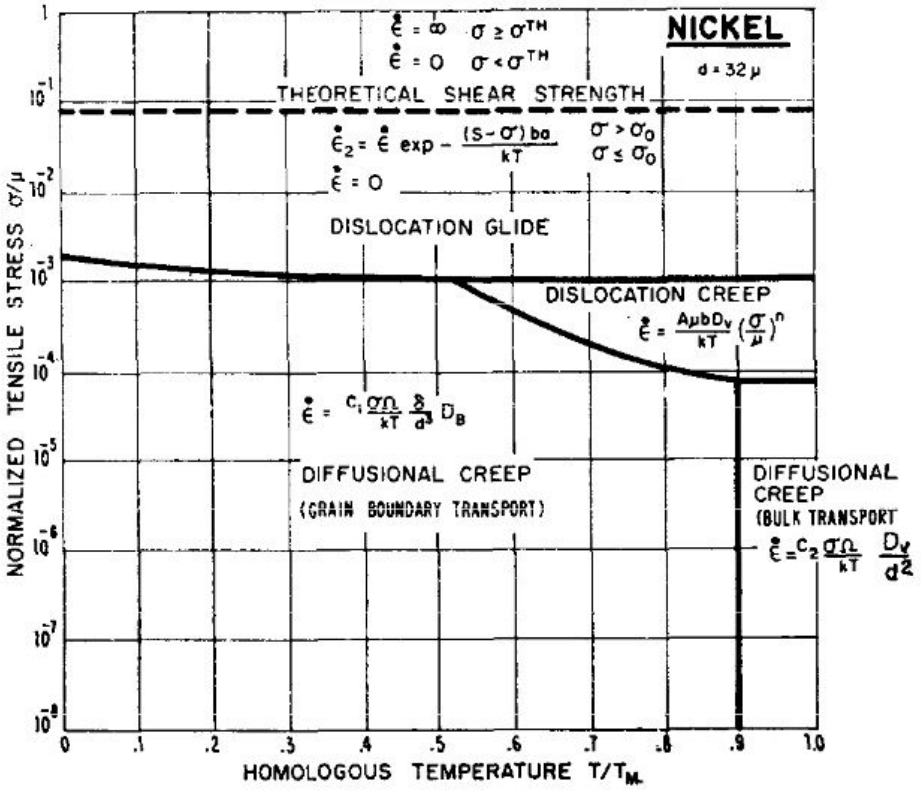

Figure 2-12 Deformation mechanism map for pure Ni with a grain size of 32 μm [53].

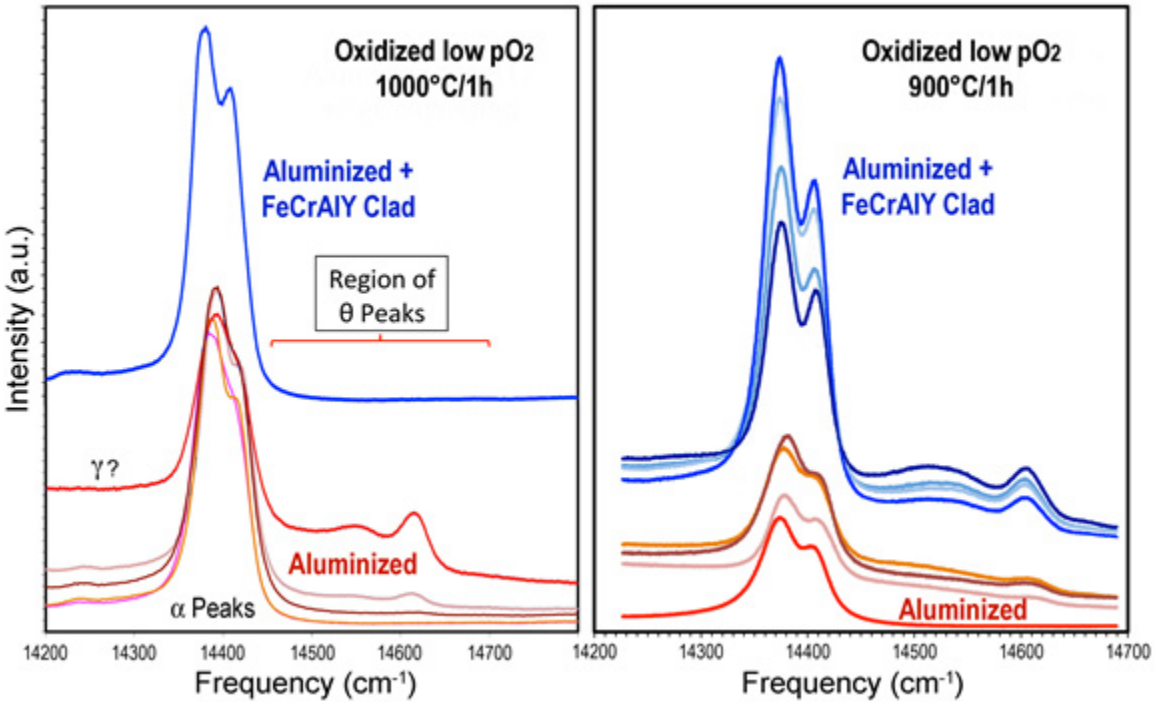

Figure 2-13 Photostimulated luminescence peaks for alumina formed on the surfaces of aluminized 617 with and without FeCrAlY cladding, after 1h oxidation in low pO_2 at 1000°C and 900°C. Adapted from [21]

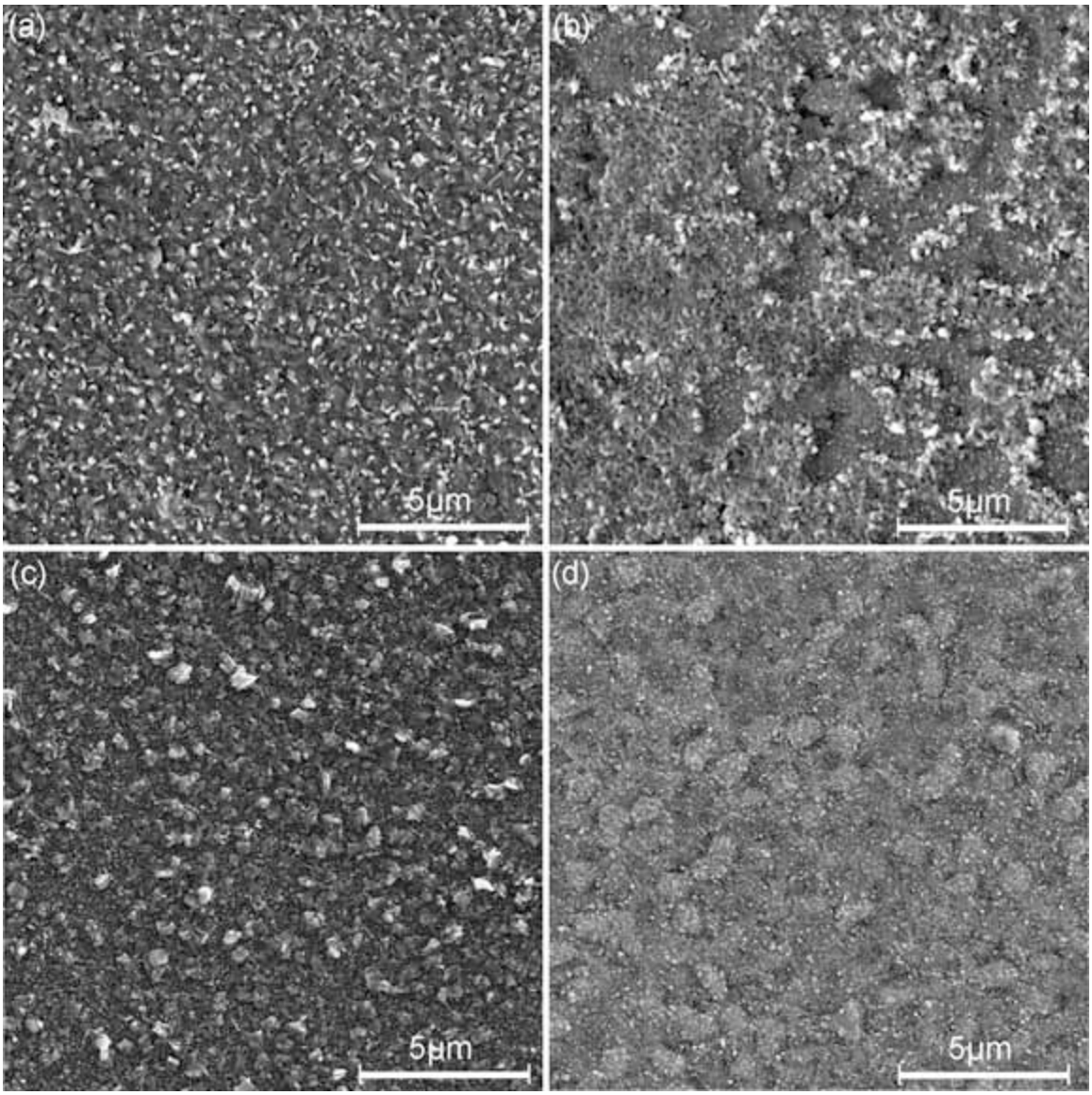

Figure 2-14 Surface scales for (a,c) FeCrAlY and (b,d) Aluminized 617, after 1h oxidation in low pO_2 at (a,b) 1000°C and (c,d) 900°C. There are transient alumina phases in (b-d), as shown in Figure 2-13. Adapted from [21].

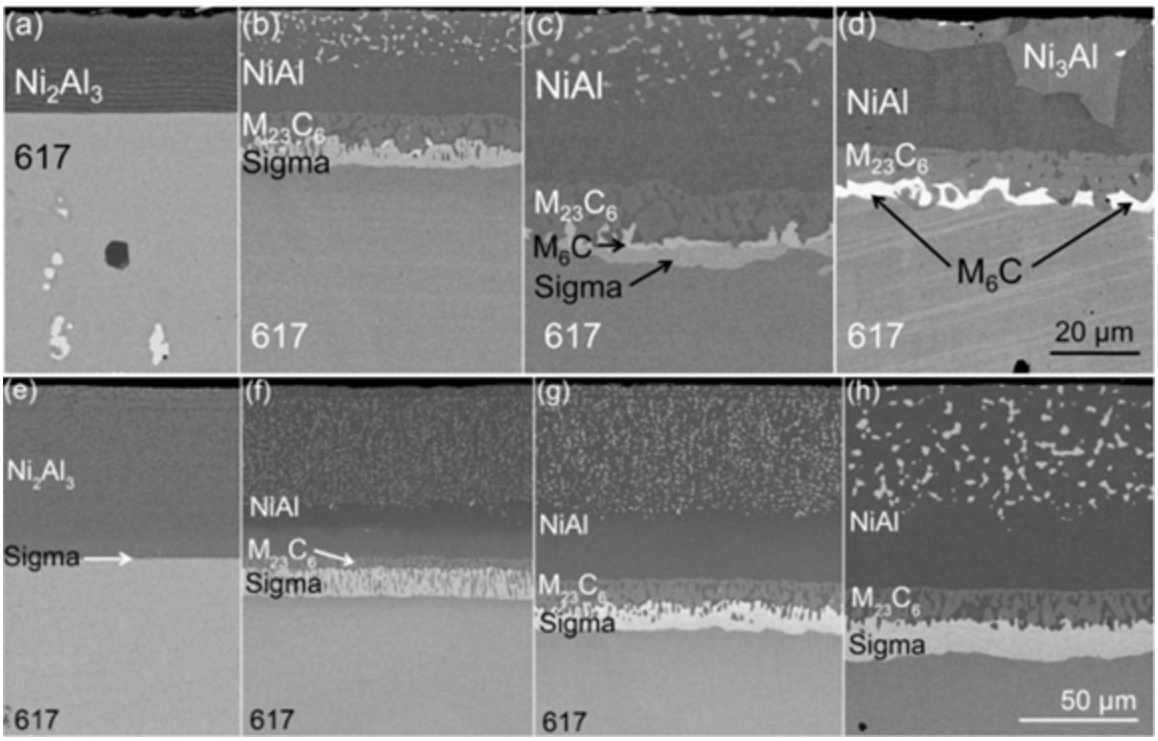

Figure 2-15 Microstructures of the Gen-I and Gen-II coating layers on 617, produced by aluminizing at 700°C (a) and 850°C (e), respectively. In both cases the bulk of the aluminized layer is Ni_2Al_3; an incipient sigma layer is found to form during the higher temperature process but not at the lower temperature. The evolution of the microstructure upon subsequent heat treatment at 1000°C and (b,f) 16h, (c,g) 100h and (d,h) 500h, is shown on the corresponding row of images for each variant of the process. The continuous sigma layer that develops initially after aluminizing at 700°C in (a) evolves to a discontinuous M_6C layer after 500h (d), but is retained at 500h when the original coating is deposited at 850°C. The NiAl layer in the latter is also richer in Al (graded from the surface to the interface) as shown by the presence of Ni_3Al after 500h in (d) but not in (h). Adapted from [21].

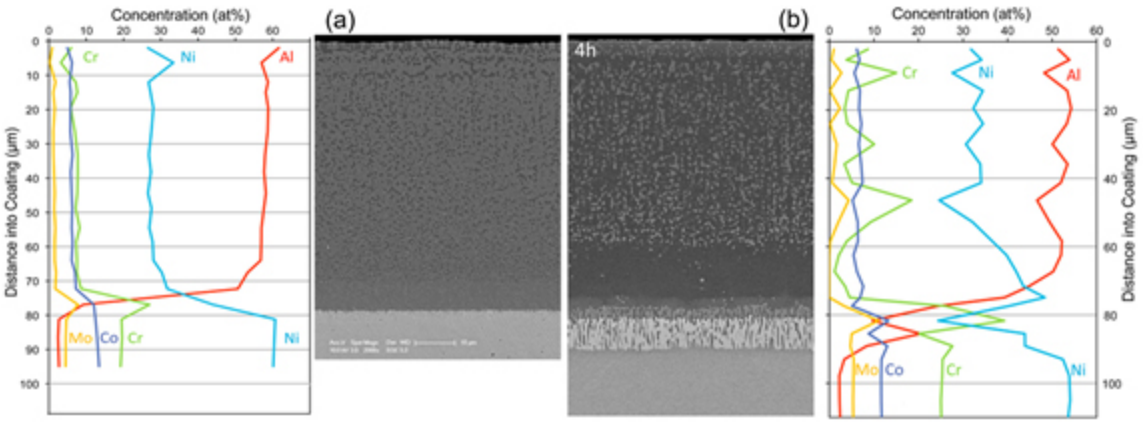

Figure 2-16 EDX line scans and microstructures of the coating layer taken on Gen II samples (a) as-aluminized and (b) after 4h/1000°C heat treatment. Ni upward diffusion transforms the original Ni_2Al_3 layer to NiAl, but it slows down as the carbide+sigma phase diffusion barrier develops *in-situ*. Adapted from [21].

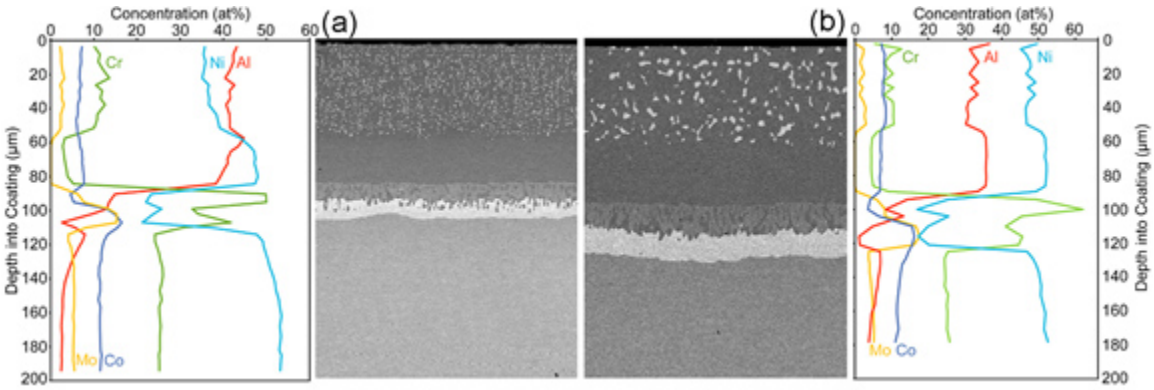

Figure 2-17 EDX line scans and microstructures of the coating layer from Gen II samples heat-treated at 1000°C for (a) 100h and (b) 500h. The carbide, sigma phase and the precipitate-free NiAl increase over time. The bulk of the NiAl layer is still B2 even after 500h. Adapted from [21].

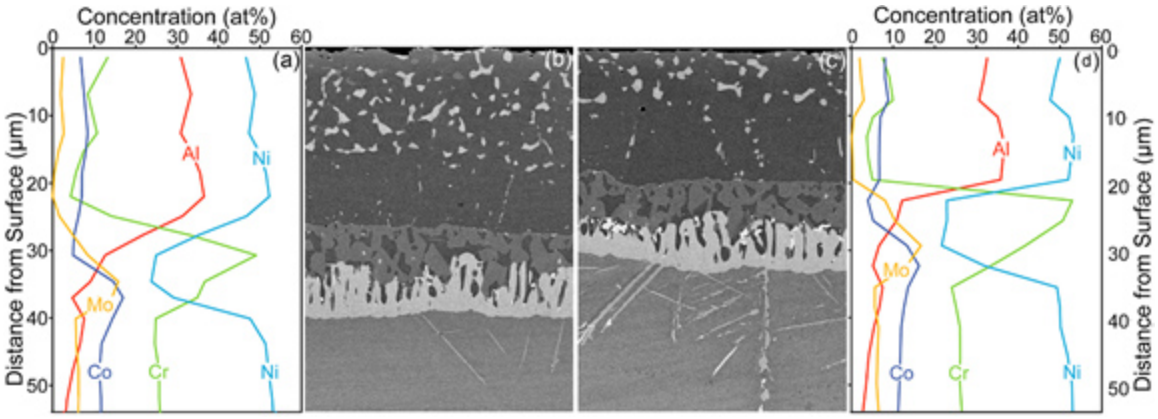

Figure 2-18 EDS line scans (a,d) microstructural regions (b,c) from which they were acquired after (a,b) 100h and (c,d) 500h at 800°C. Note that the concentration profiles are not significantly changed over time, although minor changes are observed in the microstructures, especially the increase in precipitation within the substrate next to the modified layer at the longer times. The differences in thickness of the aluminized layer are associated with the surface polishing process after aluminizing. Adapted from [21].

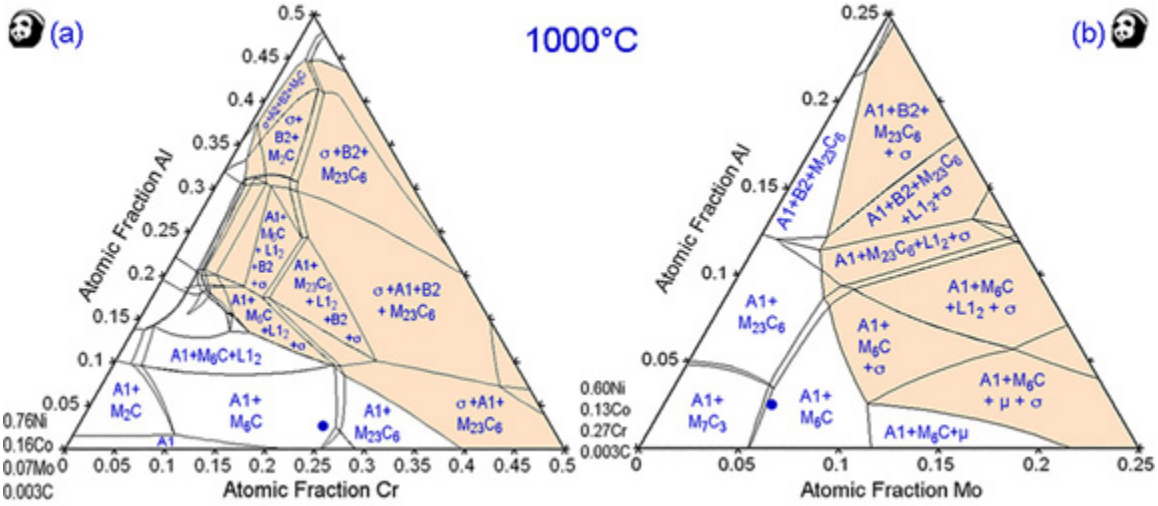

Figure 2-19 Phase equilibria for a simplified version of Alloy 617 with (a) Ni, Co, Mo and C in the right proportions, and varying Al and Cr, or (b) Ni, Co, Cr and C as a base and varying Al and Mo. The circles represent the composition of 617 in each diagram, and the shaded area the fields containing the sigma phase, usually in combination with carbides and other metallic phases. Note that the scale on (b) is enlarged by a factor of two relative to that in (a). (Calculations using the CompuTherm PanNi8 database.) as adapted from [21].

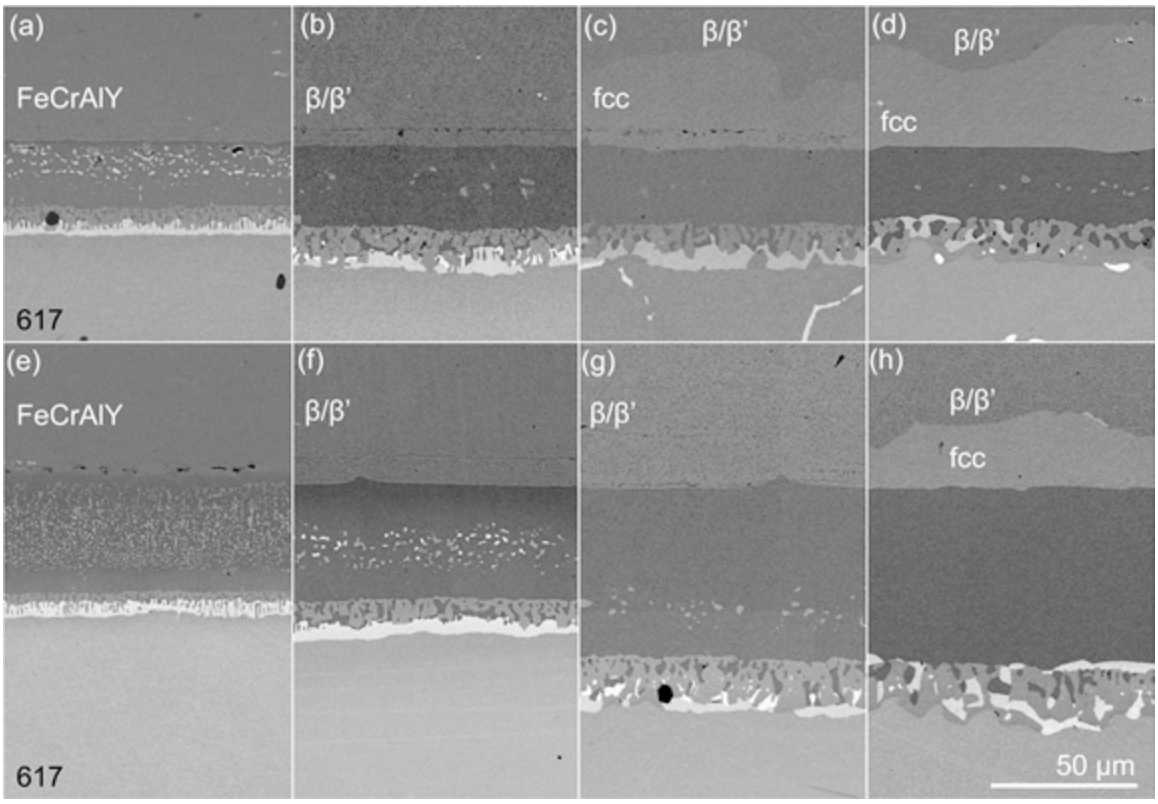

Figure 2-20 SEM images of clad + aluminized 617 Gen I (a-d) and Gen II (e-h) samples in the as-clad (a,e) and after 1000°C heat treatment for 24 h (b,f), 168 h (c,g), and 500 h (d,h). Adapted from [21].

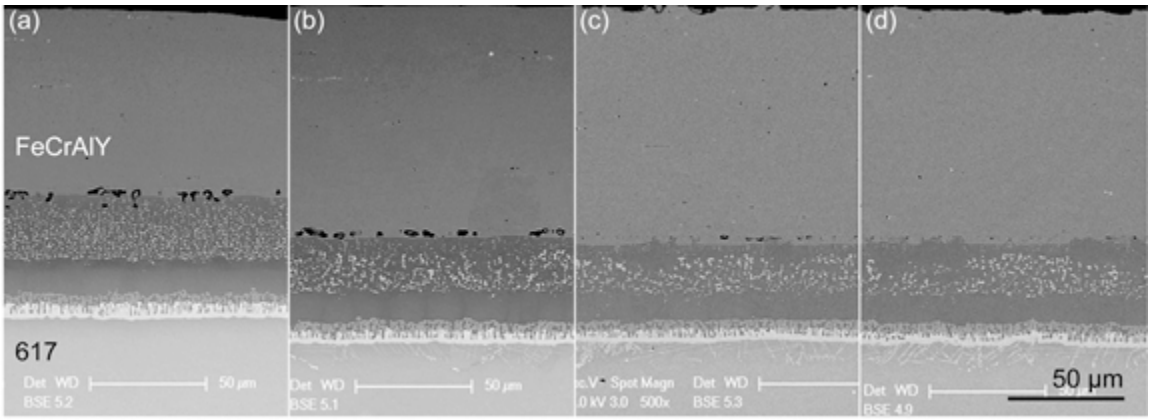

Figure 2-21 SEM images of Gen II clad + aluminized 617 (a) after 1000°C/2h pre-oxidation treatment and after 800°C exposure for (b) 100h, (c) 225h, and (d) 375h. Adapted from [21].

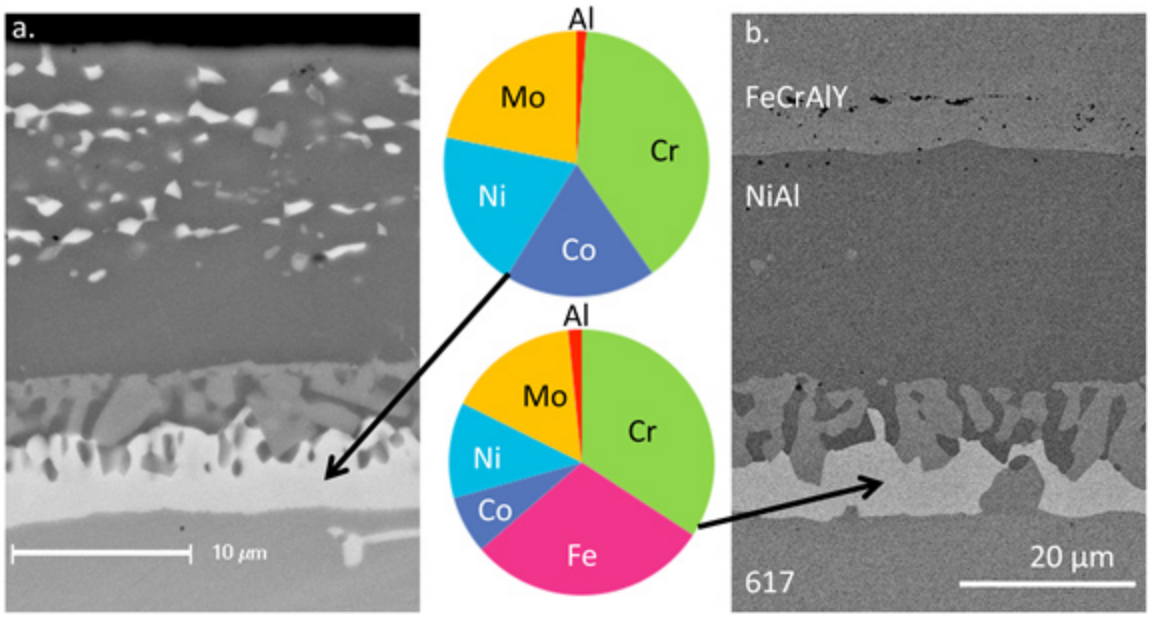

Figure 2-22 Average composition of sigma layer at NiAl/617 interface in a, aluminized 617 after 16h/1000°C heat treatment and b, clad+aluminized 617 after 168h/1000°C heat treatment. The sigma layer increases in Fe content at the expense of Ni and Co in the clad sample relative to the original layer formed after aluminizing. Adapted from [21].

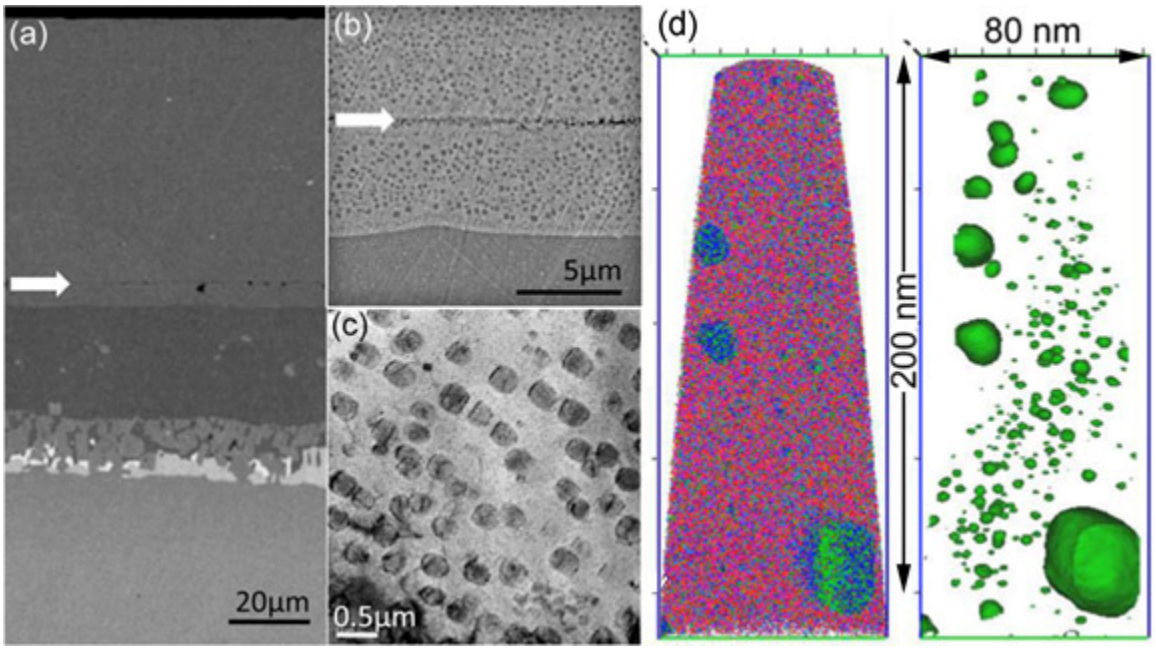

Figure 2-23 SEM (a,b) and TEM (c) of B2 precipitates that form in clad + aluminized 617 after 24h/1000°C. The arrow in (a,b) denotes the position of the original interface. (d) Atom probe tomography reveals a bimodal distribution of precipitates. The 3-D reconstruction shows all the atoms wherein the color code is: Fe-pink, Cr-orange, Ni-green, Al-blue. The precipitates are highlighted by the isoconcentration profiles at Ni=10at% where the larger precipitates correspond to those visible in (c) and (d), with smaller nanoclusters dispersed in the matrix. Adapted from [21].

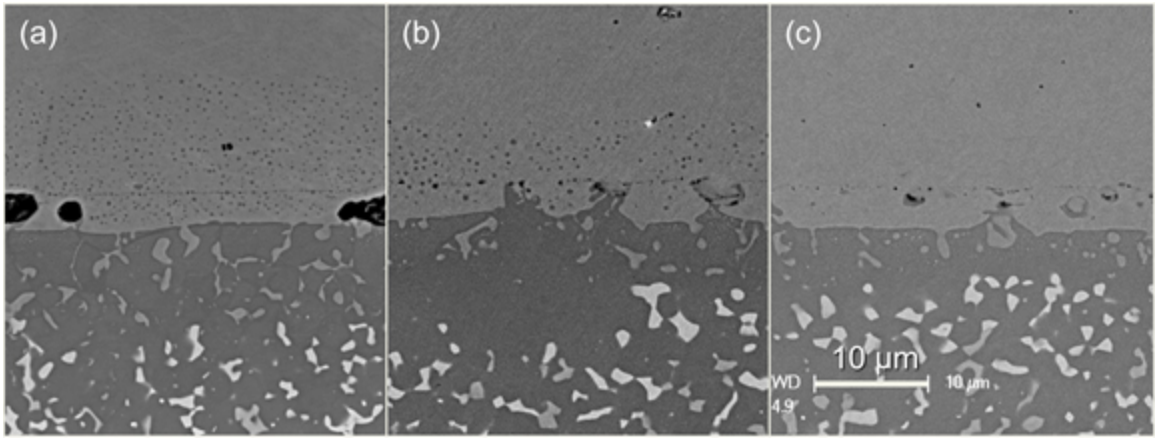

Figure 2-24 SEM images of Gen II clad + aluminized 617 after 800°C heat treatment for (a) 100h, (b) 225h and (c) 375h. The β/β' precipitates that form in the FeCrAlY as Ni diffuses into this layer dissolve with time and are no longer present by 375h. Adapted from [21].

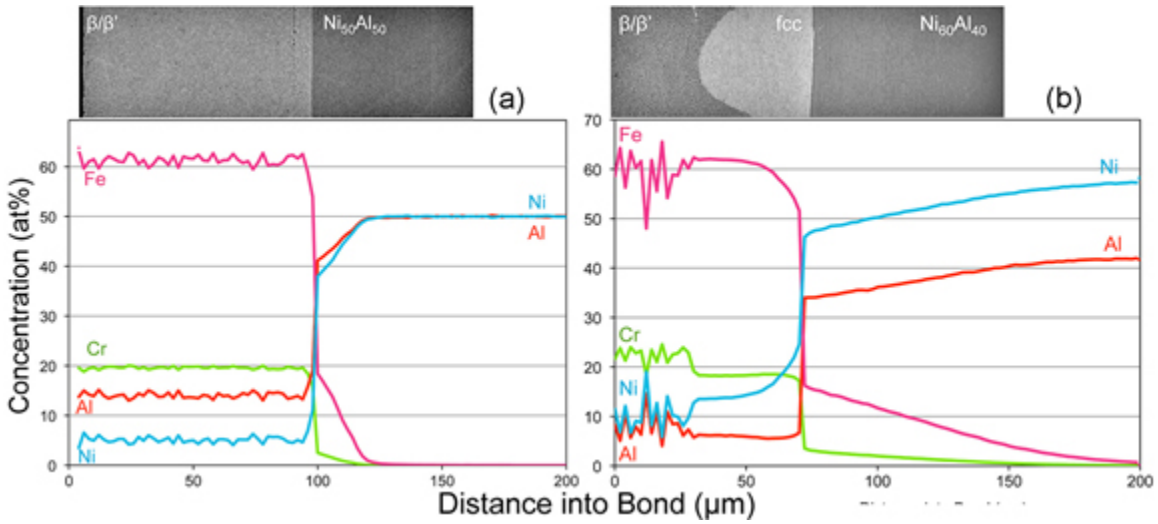

Figure 2-25 EPMA composition profiles for diffusion couples of 100 µm FeCrAlY layers with 1mm (a) $Ni_{50}Al_{50}$ and (b) $Ni_{60}Al_{40}$ after heat treatments at1000°C/168h in gettered Ar. Adapted from [21].

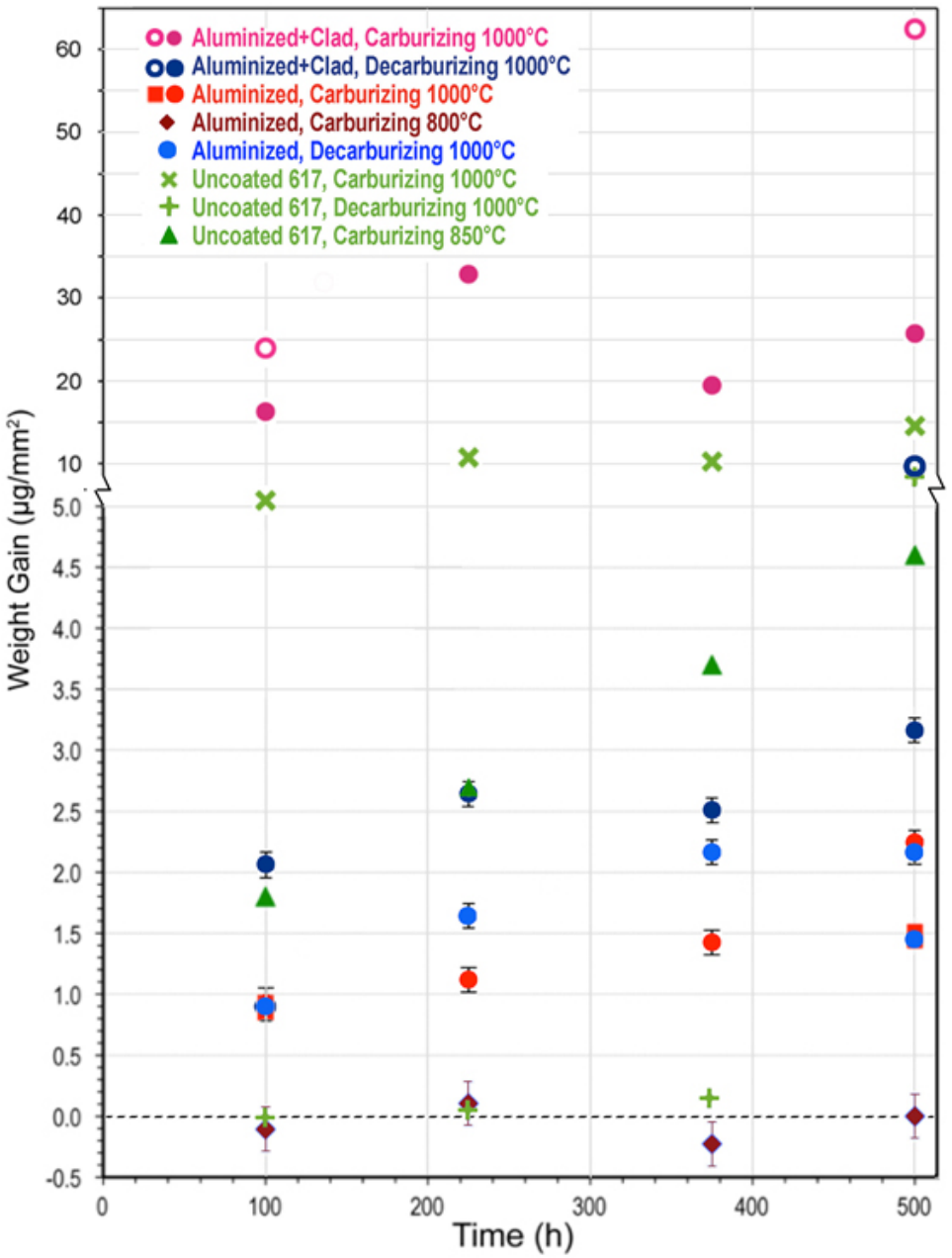

Figure 2-26 Normalized weight gains for uncoated, aluminized and aluminized+FeCrAlY clad specimens of 617, exposed to impure He environments at different temperatures and for different times. Note the change in scale between 5 and 10 mg/mm^2. All the coated samples were pre-oxidized prior to exposure. The environments are He with $CO:CO_2 \approx 1272$ (carburizing) or $CO:CO_2 \approx 9$ (decarburizing). The FeCrAlY in the aluminized+clad specimens covered only the broad sides of the aluminized specimen. Empty circles in the clad specimens correspond to those in which the cladding was trimmed mechanically, whereas solid circles are for laser-trimmed specimens. Adapted from [21].

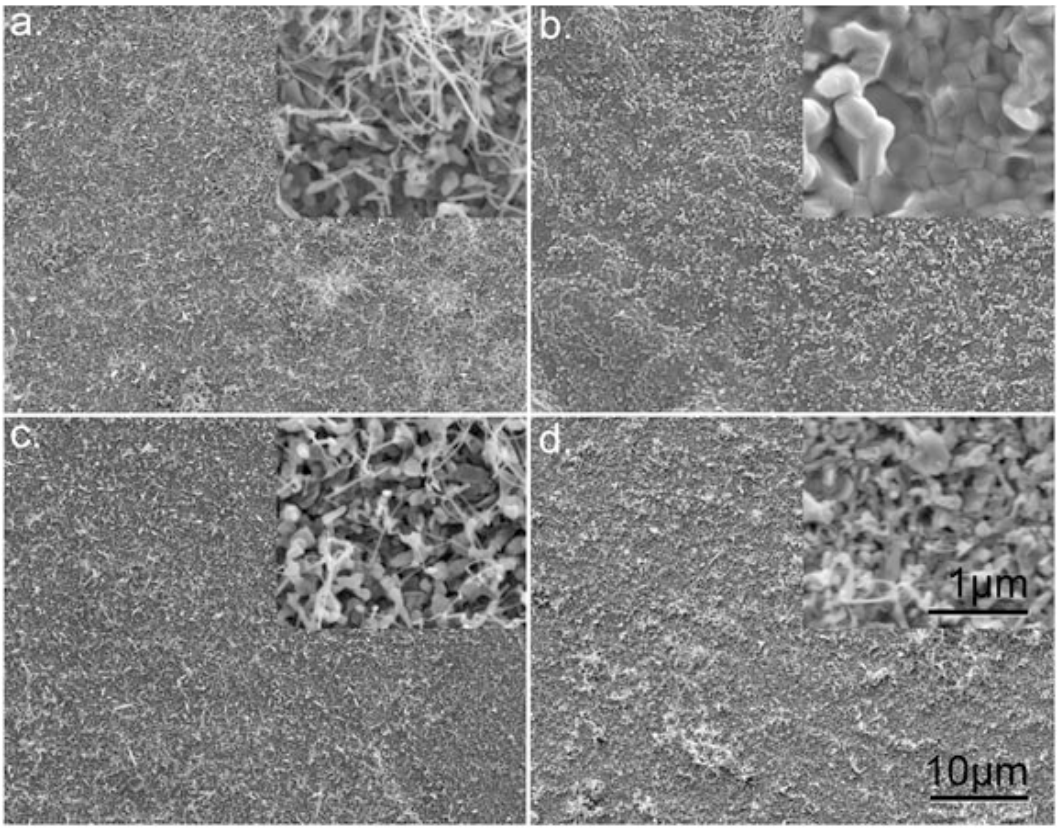

Figure 2-27 SEM images of the oxide morphology after 1000°C/500h exposure to impure He of aluminized 617 in (a), carburizing and (b), decarburizing conditions and clad + aluminized 617 in (c), carburizing and (d), decarburizing conditions. Adapted from [21].

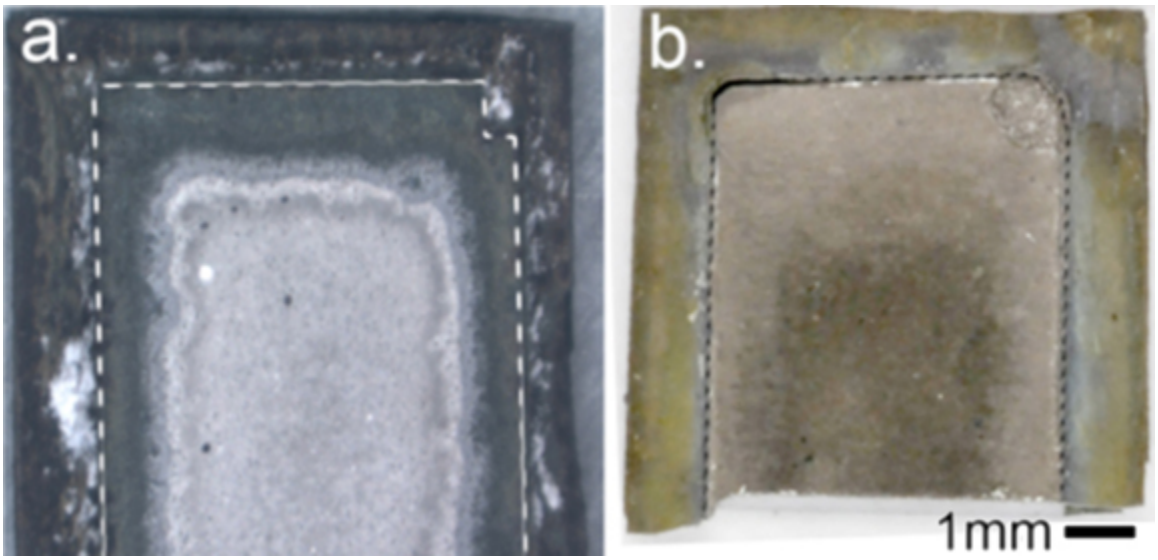

Figure 2-28 Optical images of clad + aluminized 617 specimen surfaces after exposure to 500h/1000°C/ carburizing He. The dashed line denotes the profile of the aluminized 617 substrate underneath, with the cladding overhang around it. The specimen in (a) had the excess cladding mechanically trimmed whereas (b) was laser-trimmed. Adapted from [21].

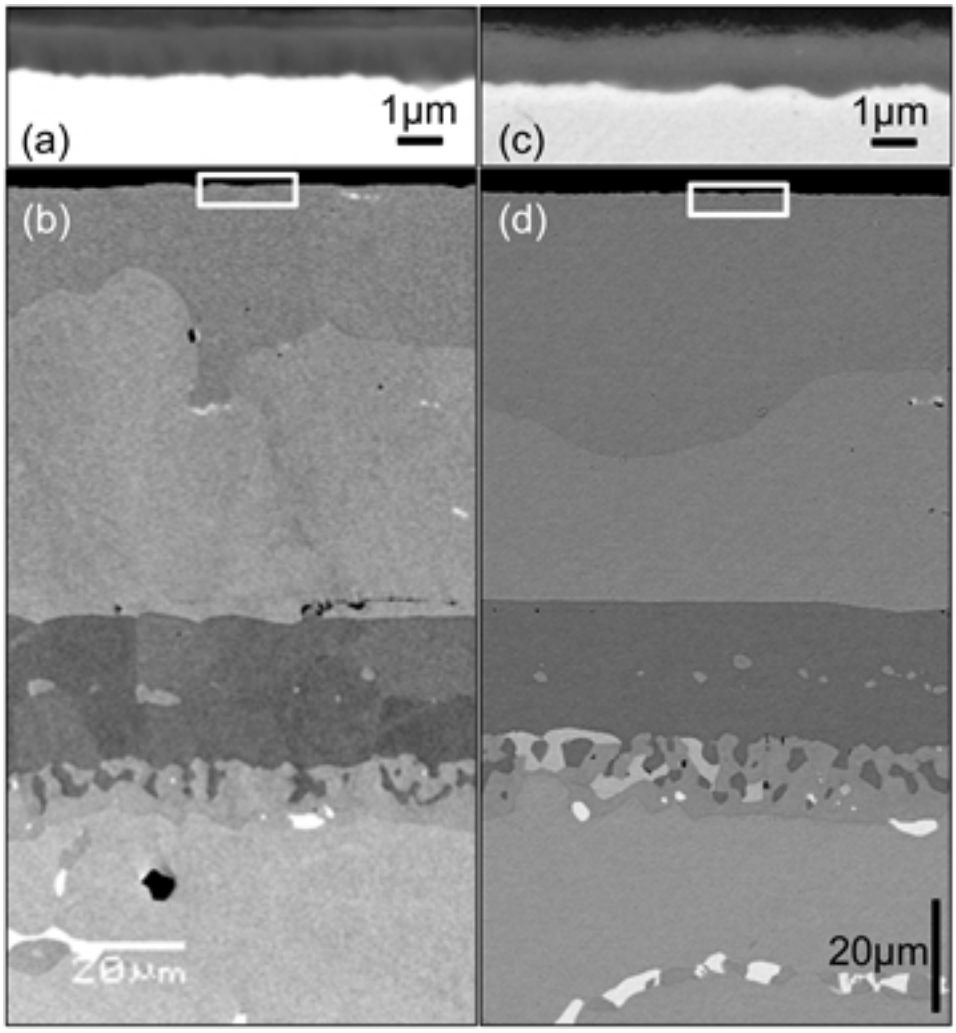

Figure 2-29 SEM images of clad + aluminized 617 after 500h exposures in (a,b) decarburizing and (c,d) carburizing environments. Though the edges suffered some damage, the central area of the exposed surface maintained a protective alpha alumina scale. Adapted from [21].

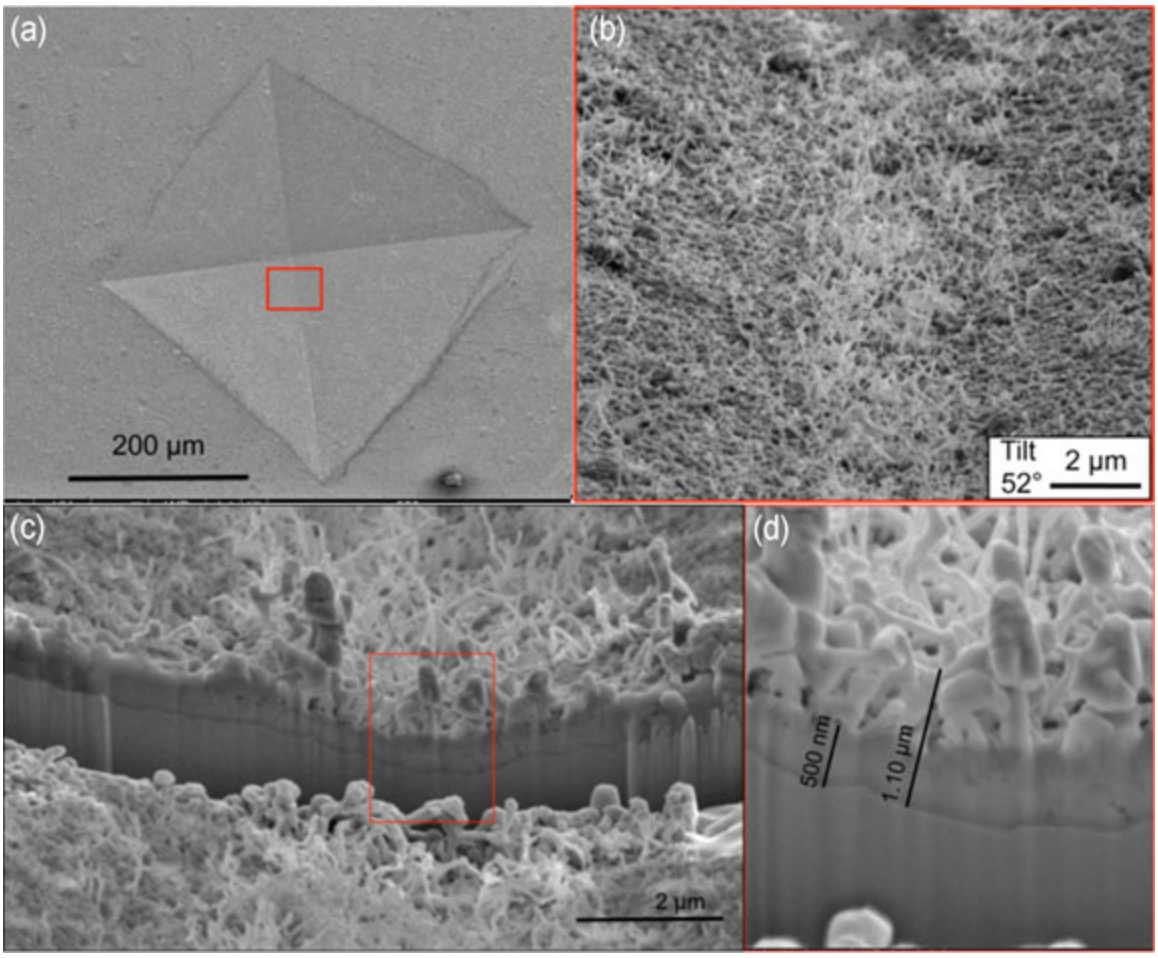

Figure 2-30 Images of indented FeCrAlY after exposure to a carburizing environment for 100h at 1000°C. (a) overview of the indent after exposure. (b) close-up of the oxide scale that reformed along the diagonal of the indent during exposure. The area of the detail is marked in the left image by the red rectangle in (a). (c) SEM image of a FIB cross section made through diagonal of indented region in (b) wherein the damaged oxide exposed the underlying alloy to a carburizing environment. (d) detail of the regenerated alumina scale, wherein the alloy and interface show no evidence of carbide formation upon exposure. Adapted from [21].

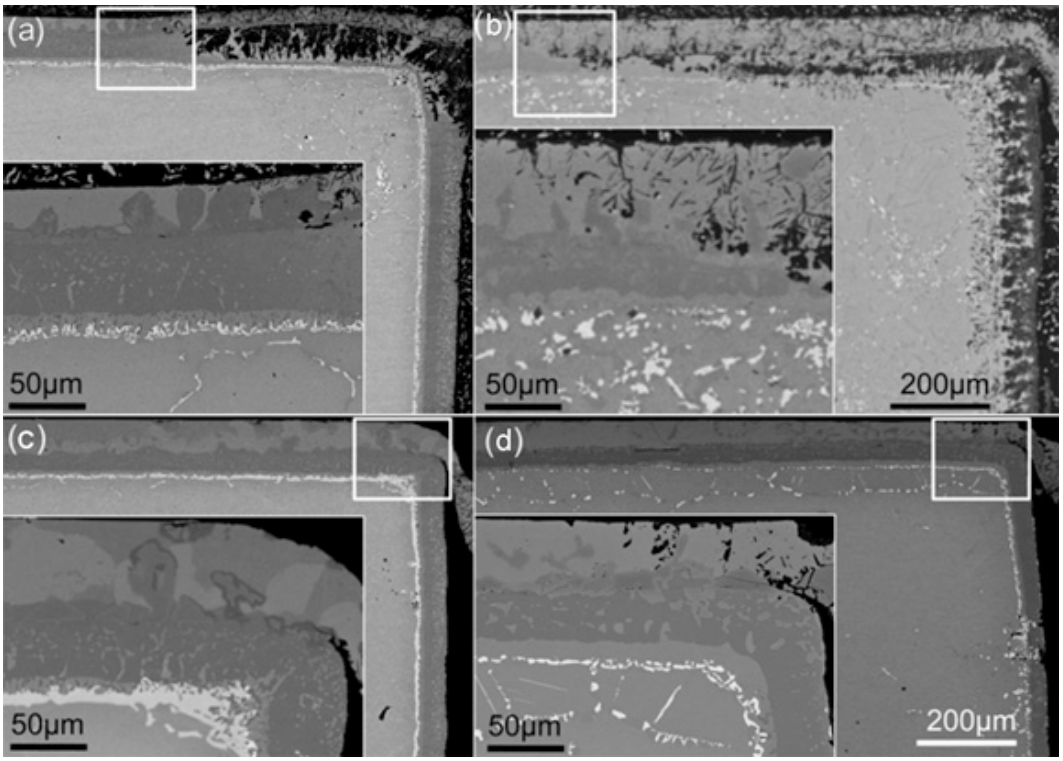

Figure 2-31 SEM images of clad + aluminized samples exposed to a carburizing He environment at 1000°C for (a,c) 100h and (b,d) 500h. Samples that were laser trimmed (c,d) showed less attack than samples that suffered more evident damage during mechanical trimming (a,b) prior to exposure. Adapted from [21].

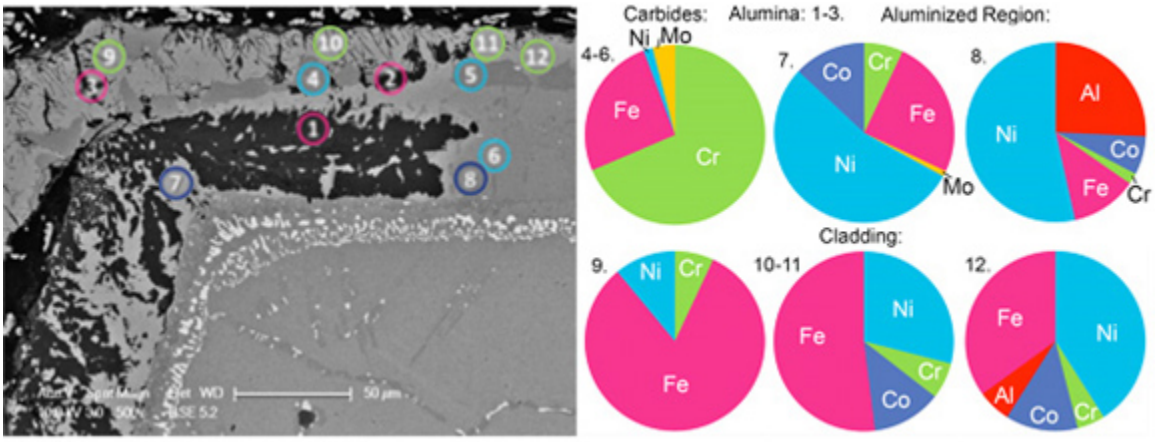

Figure 2-32 Cross section of a corner of a mechanically trimmed clad + aluminized 617 sample after exposure to a carburizing He/1000°C/100h. The spots in the micrograph correspond to EDX compositions shown on below the image. Damage to the sample prior to exposure resulted in severe oxidation (1-3) and carburization (4-6). The aluminized (7-8) and clad (9-12) regions were depleted in aluminum and also chromium in the case of the cladding. Adapted from [21].

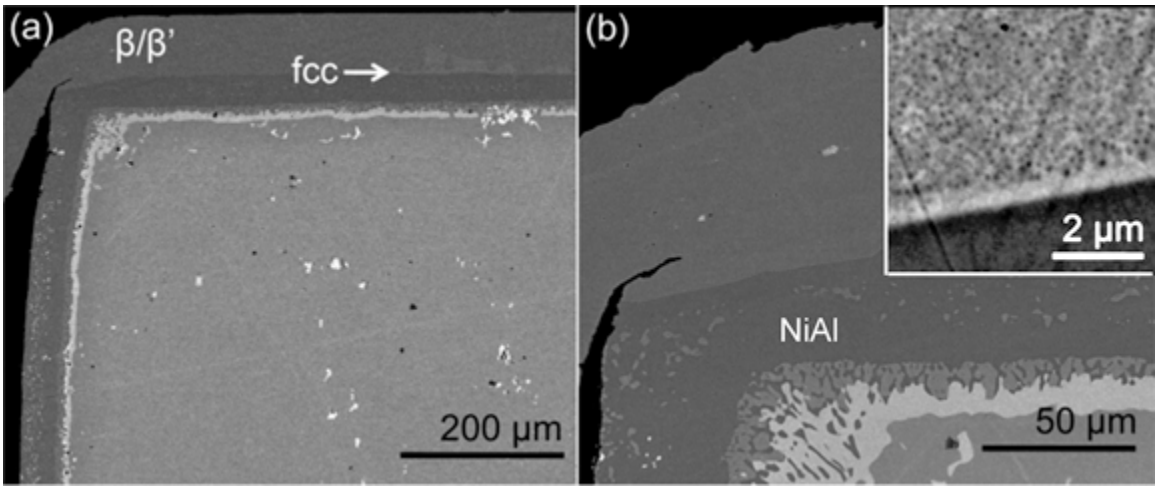

Figure 2-33 SEM images of a clad + aluminized sample that was laser-trimmed prior to exposure to a carburizing He environment at 1000°C/100h. Away from the edge, the FeCrAlY cladding has begun to transform to fcc (a), but the edge, which is free from carbides (b) still retains the β/β' microstructure seen at higher magnifications in the inset. Adapted from [21].

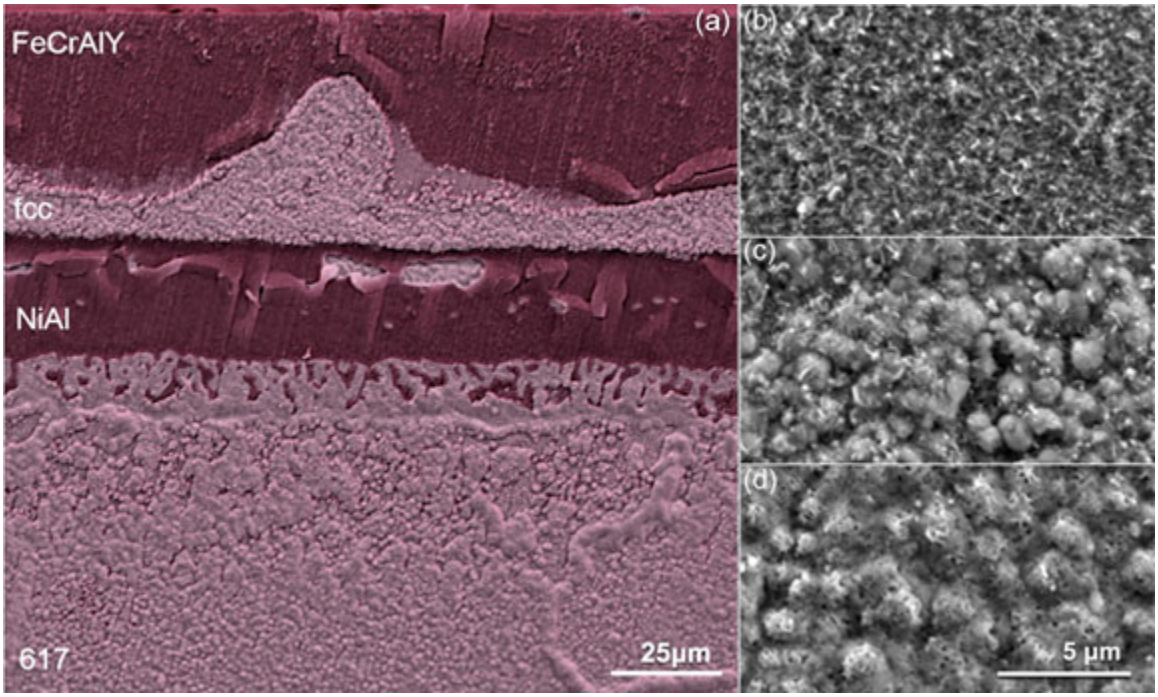

Figure 2-34 SEM images of the cross section of a Gen I clad + aluminized 617 sample that had undergone 100h/1000°C/decarburizing He prior to cross-sectioning and oxidation for 1h/1000°C/gettered Ar. The β/β' microstructure and NiAl layer formed alumina, shown at higher magnification in (b). The region where the original FeCrAlY layer had been replaced by γ (A1) formed chromia, and its morphology (c) was similar to the chromia formed by alloy 617 (d). Adapted from [21].

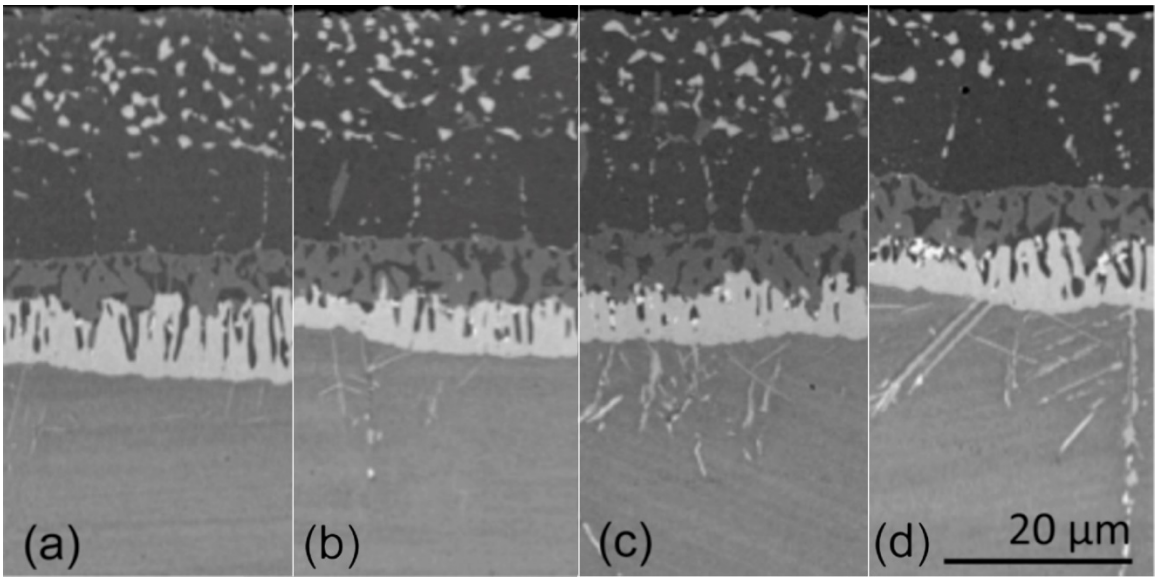

Figure 2-35 SEM images of the coating cross-section after 800°C exposure to impure He (CO:CO2 ≈ 1272) for (a) 100h, (b) 225h, (c) 375h, and (d) 500h. Adapted from [21].

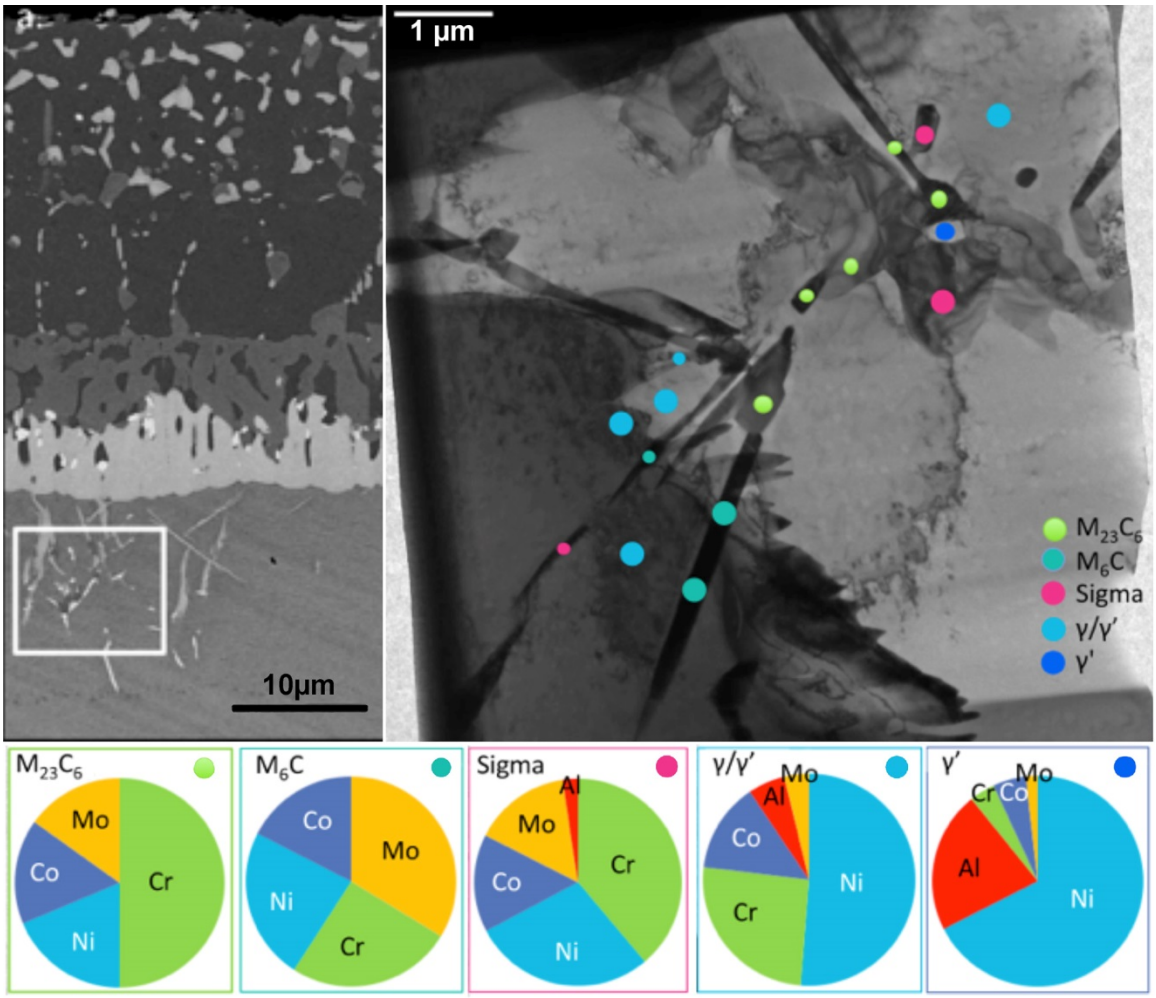

Figure 2-36 TEM image of the DAZ of aluminized 617 after 800°C/375h/carburizing He exposure showing EDS measurements and expected phase based on composition, cf. Figure 2-34(c). Adapted from [21].

CHAPTER 3
EXPERIMENTAL APPROACH

This chapter describes the Alloy 617 used for the environmental creep (Chapter 4), as well as the coatings of NiAl and NiAl+FeCrAlY cladding that were used for a major component of the research (Chapter 5). The experimental tests and procedures employed are also described. Section 3.1 describes Alloy 617; Section 3.2 presents the preparation of the creep test specimens; and Section 3.3 describes the process for coating the alloy. The design and the characterization of the facility used for the conduction of the static and cyclic creep tests in controlled helium environments are described in Section 3.4. The procedure used for conducting the tests and a summary of the experiments and analyses are provided in Sections 3.5 and 3.6.

3.1 Microstructure of Alloy 617 and Coatings

Alloy 617 was supplied by Idaho National Laboratory in the form of a 38-mm-thick plate (Heat #314626, Lot #103374422, ThyssenKrupp VDM USA, Inc.) that had been solution-annealed at 1175°C and water-quenched. The as-received microstructure (Figure 3-1) had a grain size of 139 ± 13 μm and contained $M_{23}C_6$ carbides distributed along the grain boundaries and in the grain interiors. The composition of this heat of Alloy 617 is given in Table 3-1.

3.2 Specimen Design and Preparation

A flat rectangular “dog-bone” creep specimen was chosen to obtain high surface area-to-volume ratios compared to cylindrical specimens. Creep specimens, Figure 3-2, were fabricated by electrical discharge machining and had a gauge cross section of 3 x 2 mm and a gauge length of 15 mm. Small rectangular block specimens of the same alloy with dimensions of 4.0mm x 9.85mm x 1.5mm were used for exposure-only testing. Figure 3-3 shows the results of a finite element model analysis of uniform tensile loading and indicates that the maximum strain is evenly distributed in the gauge section and is not severe in the pin-loading region. Photographs of uncoated and coated specimens are

shown in Figure 3-4. Uncoated specimens were machined by electrical discharge machining (EDM), mechanically ground starting with a grit 400 SiC paper and polished down to 1μm diamond finish until an optically scratch-free surface was obtained. The preparation was finalized by cleaning and degreasing ultrasonically in an ethanol-acetone mixture for 15 minutes with a subsequent cleaning in distilled water for another 15 minutes.

3.3 Processes for Aluminizing and Cladding

For the coating studies, some specimens received an aluminized coating while others received a cladding layer (FeCrAlY) after aluminization. All coatings were applied at the University of California Santa Barbara in Professor Carlos Levi's research group. The NiAl coatings used Al powder (<44μm, 99.5% purity, Alfa Aesar, Ward Hill, MA) as the source, Al_2O_3 powder (500 grit, Norton Co, Worcester, MA) as the filler, and $CrCl_3.6H_2O$ (>99.5% purity, Alfa Aesar) as an activator. Cladding used 50 and 100 μm foils of Fecralloy™ procured from Goodfellow, Oakland, PA. Composition of the cladding is provided in Table 3-1. The aluminization and cladding processes are described in detail by Clark [18], and are briefly described here.

Aluminization involved a high-activity, low-temperature process by pack cementation using a powder mixture of $4Al/4(CrCl_3.6H_2O)/92Al_2O_3$ (in weight percent). The specimens were wrapped in alumina fabric and embedded in the pack, which was subsequently sealed in an alumina crucible and placed in a tube furnace under flowing high purity Ar ($X_O \leq 10^{-5}$). The pack was heated to 700°C and held for 9.6 hours. After aluminizing, the specimens were annealed (heat treated) at 1000°C in flowing and gettered Ar for 16 hours to fully develop the structure of the surface layers. A measured oxygen content of $X_O \leq 10^{-13}$ was achieved by passing the high purity Ar through a Centorr 2A Inert Gas Purifier. The oxide layer on the coating produced by the heat treatment was removed using a surface grinder. Further pre-oxidation of the specimens to develop a thin, continuous layer of alpha alumina was done in flowing gettered Ar ($X_O \leq 10^{-13}$) at 1000°C for 2 hours. Two sets of aluminized specimens were made. The first one underwent a longer period of aluminizing and heat treatment (700°C/9.6h, 1000°C/16h, 1000°C/2h), while the heat treatment time for a second set was shortened by increasing

the temperature (850°C/4.5h, 1000°C/1h, 1000°C/2h). They are referred to as Generation I (Gen I) and Generation II (Gen II) aluminized specimens, respectively.

FeCrAlY foil was used to clad a subset of the aluminized specimens by diffusion bonding in a high vacuum hot press for 1 hour at 1000°C under a pressure of 20 MPa. Clad specimens consisted of aluminized 617 coupons sandwiched between two 100 μm thick sheets of FeCrAlY foil. The cladding was applied only to the faces of the creep specimens and not to the edges as illustrated in Figure 3-5. The thermal history for the clad specimens was 850°C/4.5h for aluminizing, 1000°C/1h for heat treatment, 1000°C/1h for cladding and 1000°C/2h for pre-oxidation (850°C/4.5h, 1000°C/1h, 1000°C/1h, 1000°C/2h). For both aluminized samples and aluminized plus clad specimens, polishing to 800 grit finish was conducted before the pre-oxidation step.

Microstructure of the as-aluminized substrate is shown in Figure 3-6. An overview of the NiAl layer and the 617 substrate is shown in (Figure 3-6a). Precipitates rich in Cr and Mo are situated close to the surface of the NiAl layer (Figure 3-6b), where there is also a thin and dense Al_2O_3 scale formed during the pre-oxidation stage of the coating process. Farther from the coating surface, there are Cr-rich precipitate regions (Figure 3-6d-e) and a region that is free of precipitates (Figure 3-6f), which is near the interdiffusion zone (IDZ). This interdiffusion zone is constituted of Cr and Mo interlayers (Figure 3-6g), beyond which lies the substrate (Figure 3-6h). The grain size of the substrate following this coating procedure was determined to be 139 ± 33 μm that appears to be close to that of the uncoated substrate. A similar image for the aluminized + clad coating is shown in Figure 3-7. An overview of the aluminized and clad structure is shown in (Figure 3-7a). The FeCrAlY cladding (Figure 3-7b) is intended to act as the Al reservoir for formation of Al_2O_3 scale (Figure 3-7c). There is a precipitate-free FeCrAlY/NiAl junction (Figure 3-7d), beyond which there are precipitate-rich and precipitate-free regions of NiAl (Figure 3-7e-g), Cr and Mo interlayers of IDZ (Figure 3-7h) near the underlying 617 substrate (Figure 3-7i). The grain size of the substrate following the aluminization and cladding procedure is close to that of the aluminized substrate, since the thermal treatments required for either coating process were similar as described earlier.

In a subset of aluminized 617 specimens, Focused Ion Beam (FIB) micro-notches were placed on the coating to examine the role of pre-existing defects on damage processes. In a subset of clad/aluminized 617 specimens, an additional 24h and 100h at 1000°C heat treatment was performed to investigate the role of precipitates on damage processes. These procedures are described in more detail in Chapter 5.

3.4 Experimental Setup: Controlled Impurity Helium Flow Creep System

High temperature exposures in controlled impurity helium environments have been conducted previously in our laboratory [19, 77, 78]. Building on the knowledge and success of this previous system that had been designed for exposure tests only, the controlled impurity helium flow creep system was constructed to allow for the studies of exposure tests in impurities such as CH_4, CO and CO_2 in the presence of static or cyclic stresses. The controlled impurity helium flow creep system is composed of different sections as shown in the schematic (Figure 3-8) and the photograph (Figure 3-9): helium purification, gas mixing, exposure-mechanical testing, and gas analysis. The helium purification system consists of filtering cartridges for further removal of impurities present in the initial helium stream of 99.9995% purity. The helium stream is thereafter supplied to the gas mixing section to be mixed with controlled amounts of CH_4, CO and CO_2 to establish the target chemistry of test environment. The mixture is then fed to the exposure-mechanical testing section where the test specimen is subjected to static or cyclic stresses and the furnace provides the required test temperature. The inlet and outlet gas ports in the tube in the exposure-mechanical system are connected to a discharge ionization detector gas chromatograph (DIDGC) for gas analysis. DIDGC can analyze the CH_4, CO and CO_2 concentrations in the helium stream both at the inlet and outlet of the creep retort and therefore enables precise control of the inlet and outlet concentrations established during the creep test. Each section is described in more detail hereafter.

3.4.1 Helium purification system

This unit is composed of a Perkin Elmer Three-Cartridge Gas Purification System and a manual gas stream changeover system connected to two $8m^3$ pure helium cylinders (99.9995%). Helium from the cylinders is further purified by passing through a series of moisture, hydrocarbon and oxygen removal cartridges. A manual gas stream changeover

system enables switching the flow from a cylinder nearing depletion to a full cylinder without flow interruption. This arrangement enables a continuous supply of pure helium to the creep retort.

3.4.2 Gas mixing section

The gas mixing section is comprised of 3 pre-mixed gas bottles and 3 electronic mass-flow controllers manufactured by Omega ®. The electronic mass flow controllers used for gas mixing have an accuracy of ±1 ml/min with a full scale operation range of 0 to 200 ml/min, and are capable of withstanding pressure up to 500 PSIG (3.45 MPa). With 3 mass flow controllers, it is possible to adjust the flow rates of the gas supplied to achieve the target chemistry. For the He-CO-CO_2 environment, one mass flow controller is assigned to each of the helium, carbon monoxide, and carbon dioxide gas cylinders. For the He-CH_4 environment, two mass flow controllers are used to supply helium while the third one supplies methane gas for mixing. Lastly, for the He-O_2 environment, only helium is supplied using the three mass flow controllers, and the composition of oxygen is determined by the detection limit of the gas chromatograph (seen in the next section). Finally, the mixed environments are fed to the exposure-mechanical testing system through 316 stainless steel tubing.

3.4.3 Exposure-mechanical testing system

The creep experiments are conducted in a creep retort that consists of a vertical split-tube furnace (rated for temperatures up to 1100°C), flowing helium containing varying levels of the named impurities, and a static or cyclic load applied via the load train. The main components of this system are the creep frame, the specimen chamber, the servomotor and the servo-controller unit (Figure 3-9 and Figure 3-10). The creep frame is constructed of stainless steel columns and a base for mounting the load train, the furnace, and the servomotor unit. The specimen chamber has a minimum volume (38 mm internal diameter, 42 mm external diameter, 660.4 mm long) necessary to house the specimen, the thermocouple wires, the load train, and the porous alumina within the hot zone. Silicone O-rings in the chamber end seals are protected from direct heat by use of porous alumina barriers situated at the chamber ends and chilled water circulated around the end seals (made of stainless steel 304). Three K-type thermocouples are inserted into

the quartz tube from the bottom end seal and are placed within the quartz tube to monitor temperatures at the middle and both ends of the gauge section of the specimen. The load train components in the hot zone are made of high-temperature molybdenum alloy (TZM), which exhibits high strength at 1000°C. The specimen grips are designed using creep-resistant Mar-M-247 alloys. In order to protect these components from corrosion in impure helium, the TZM cylindrical load train components are coated with high temperature boron nitride lubricant and encased in 99.99% pure alumina tubes with almost negligible clearance. Since the thermal expansion coefficient of TZM is very low, the components do not exhibit sufficient thermal stresses to crack the alumina casings.

Strain measurement is accomplished by measuring the load-line displacement as shown in Figure 3-10. It was demonstrated that strain can be measured from two different locations – with similar results (Figure 3-11). Usually, the strains are measured directly from the gauge section in the hot zone. However, if the strains are determined via the load line displacement instead of the gauge length deformation, the creep system is simplified since extra components near the specimen and, which are exposed to gaseous environment, are reduced. This precludes any error in estimating the gas consumptions during the corrosion-creep testing. In this dissertation, the strains were determined using the load line displacement measurements and the verification was done by comparing the lengths of the specimens before and after the tests.

Mechanical experiments in impure He environments are conducted by subjecting the specimens to static and cyclic stresses. A digitally controlled closed-loop servomotor (Figure 3-9) enabled the application of both static and cyclic loads. A servomotor was used instead of conventional dead-weight loading and is capable of operating in either load or displacement control. The motor is controlled via the servo-controller unit (control panel) from where one can manually or remotely configure the control of the load and displacement in real-time. A built-in waveform generator can be programmed to cycle or ramp the control point for the duration of the creep tests. Since the servomotor contains a closed loop digital PID controller, the control point was accurately manipulated in real time. The control panel has an RS-232 serial port enabling a computer to have full control of the servomotor for even more functionality. The PC attached to it enabled, in conjunction with LabVIEW, the control of the unit's operation

and the collection of data during the experiments. A subset of specimens are only exposed to the environment either by specimens in between the grips (with no load applied) or attached on the top grip.

3.4.4 Gas analysis section

This section is composed of the DIDGC and the PC (Figure 3-8 and Figure 3-9). The DIDGC is used to continuously analyze the gas mixture both at the inlet and outlet of the creep retort. The PC is used to control the DIDGC and for collection of gas composition data. The details of the functioning of the gas chromatograph have been extensively described elsewhere [19, 77, 78].

3.4.5 Validation of the mechanical system.

3.4.5.1 Determination of the accuracy of load applied

The servomotor is an electrical actuator that is used to convert analog signals from the controller into a positional change or change in velocity to apply a desired load via the load train. It is important to verify the accuracy of both continuous and cyclic signals sent from the servomotor. The accuracy of the signals can be controlled by two parameters of the servomotor: actuator rate and digital filter. The actuator rate determines how fast the setpoint or target load is attained. Slower actuator rates are used to improve accuracy of the controller, but minimizing the controller error quick would require faster rates. A low pass filter can be programmed to filter out any analog noise in the signal. Setting a high filter value (e.g. 40 Hz) allows the controller to respond quickly to variations but can become susceptible to analog noise. On the other hand, lowering the filter value (e.g. 5 Hz or lower) reduces the noise but the system can become sluggish to change. In general, slower actuator rates along with an aggressive filter can produce very stable and accurate load control. The servomotor actuator was monitored for a different set of rates and filter frequencies (Table 3-2) to determine what combination would give a more accurate response of cycling a load from 6.43N/11MPa – 643N/110MPa (the domain of load expected to be applied in this work). The response shown in Figure 3-12 shows that the optimal settings used for static and cyclic loading from the servomotor were 0.05 in/min and 0.3125 Hz as actuator rate and digital filter frequency respectively.

3.4.5.2 Determination of deformation during creep

Creep behavior of materials is usually presented in the form of a strain-time curve. Strain is determined from the deformation of the material during a creep test and the measurements can be done from two different locations in the creep system. Conventionally, the deformations are measured by direct monitoring of the deformation of the specimen's gauge section in the hot zone. While this method is direct and gives a more accurate determination of deformation, it cannot be used in the current setup as there is a need to reduce the surface area of materials in contact with the helium environments at creep temperatures. A different method that was used is the monitoring of the deformation indirectly via the load line displacement. The assumption is that since the material exposed to the test temperatures has a high creep resistance, then the extension of the load line would be due to the deformation of the specimen's gauge. In this case, the creep system is simplified by reducing the number of components exposed to the environment. A conventional creep system was used to compare the deformation of the specimen using the two methods mentioned above as shown in Figure 3-13 and the strain-times curves shown in Figure 3-11. Therefore, the load-line method for strain determination that was used in all the experiments.

3.4.6 Temperature uniformity along the specimen gauge section.

The difficulty of sustaining a uniform temperature along a vertical quartz tube, makes it necessary to only focus on the temperature range along the gauge section of the specimen. For this reason, after inserting the load train in the quartz tube and mounting the assembly on the creep frame, the setup was such that the specimen in the tube was always in the central zone of the vertical furnace. Tuning of the temperature controller was done to help maintain good control of the test temperature during the experiment. This good control of temperature helped minimize overshoots, undershoots, and allowed quick response to deviations from the temperature setpoint. Figure 3-14 shows the temperature variation along the specimen gauge to be within ± 0.5°C of the setpoint temperature.

3.4.7 Analysis of inlet/outlet of the creep retort.

Quartz was chosen for the creep retort to reduce interaction with the impure helium environments investigated in this work. Exposure experiments performed elsewhere [77] indicate that for the He-CO/CO_2=1320 (one of the environments used in this work), the deviations in CO and CO_2 concentrations between the outlets and the inlets of the quartz tubes reached a steady state after ~ 40-50 hours. It is after this observation had been made that the exposure specimens were pushed into the furnace for testing. Unlike the case for exposure-only studies, creep specimens must be located within the furnace before vacuum-purging and temperature ramping procedures take place. Even though enough precaution, as stated earlier, had been taken to remove all volatiles at 200°C, it took as long as 250 hours for the outlet concentrations to reach a steady state. The likelihood that the interaction between the environment and the quartz tube or even the load-train could help explain the long times to reach stability in the environment chemistry at the outlet (Figure 3-15). Also, the larger volume of the vertical quartz tube and its vertical disposition would also make it difficult to sustain the targeted environment. In spite of these challenges, the creep retort is still able to sustain different environments that would facilitate the achievement of the objectives of this work. Since the study does not involve the need to determine the kinetics of corrosion of the alloy in the different environments, the sustained environments were still enough to help develop an understanding of the synergy between the effect of exposure in the environments and mechanical stresses. In this work, therefore, the chemistry of the target environments at the input of the creep retort were verified and sustained for all experiments.

3.5 Procedure for exposure and creep-exposure tests.

Most of the exposure and creep-exposure experiments were conducted at 800°C in the creep retort. Some select specimens were exposed to helium environments in the exposure-only setup described elsewhere [78].

For the creep-exposure experiments, the specimen was mounted on the grips attached to the load train and all the connections and fittings tightened. The creep retort was then subjected to a series of purging and evacuating steps using a mechanical vacuum pump at 200°C so as to remove any volatiles in the system, before allowing the gas mixture (of targeted chemistry) to flow through the retort at 170 ml/min. The

temperature was then ramped up to 800°C at a rate of 1°C/min until equilibrium was reached. Loading of the specimen was done after the responses from the displacement transducers were seen to have stabilized on the LabView software. Gas compositions were measured using the DIDGC throughout the experiments at the inlets and the outlets. The small rectangular specimens meant for exposure-only experiments were attached to the upper grip in the creep retort such that no load was subjected to them during normal creep tests.

Table 3-3 lists the experiments conducted in this research work. The experiments were organized around two objectives. The first goal was to study the role of different environments (carbon potential, oxygen potential and both carbon and oxygen potentials) on the near-surface damage of Alloy 617. The second objective was to understand the structural integrity and mechanics of the different coatings in the aluminized-only and the clad-aluminized 617 specimens.

3.6 Microstructural Analysis Techniques

Microstructural changes of the different specimens were characterized by electron microscopy, X-Ray Diffraction (XRD), Auger Electron Microscopy (AES), and Electron Microprobe Analysis (EMPA). In general, samples to be examined were sectioned and mounted in phenolic resin and mechanically ground and polished, with a final polish using 0.25μm diamond paste.

3.6.1 Electron Microscopy

A TESCAN Mira3 Field Emission Gun microscope equipped with an EDAX energy dispersive spectroscopy (EDS) detector, and an EDAX electron backscatter diffraction camera was used for the majority of microstructural characterization studies. A Schottky Field Emission filament FEI Nova 200 Nanolab SEM/FIB was used for making FIB notches [79][1] of a selected set of specimens. Both these instruments were capable of performing secondary electron (SE) imaging, backscattered electron (BSE) imaging, and energy dispersive X-ray spectroscopy.

[1] Damage induced by use of gallium ion beam exists as a result of FIB machining. It is possible that this may influence local compositional changes in the specimen during notching. The use of a reduced beam current of 3nA of 30 keV gallium ion penetration is expected to limit the damage to nanometer range.

Concentration profiles across the different layers of the coated specimens were analyzed using a Cameca SX100 electro-microprobe-analyzer (EMPA). The accelerating voltage and beam current used were 15kV and 15nA, respectively. Table 3-4 lists the calibration standards and the spectrometer crystals used. The standards were used to first calibrate the instrument, and verification was done by using the standards as unknown. It is reported that the electron interaction volume of the beam with the Ni-based alloy is 1-2μm [80].

3.6.2 X-Ray Diffraction (XRD)

Phase identification of the oxidation products on the specimens was performed using x-ray diffraction. A Rigaku rotating anode CuK_α X-Ray was used in the θ - 2θ mode at the operating voltage and current of 40kV and 100mA respectively. In this mode, the detector and the sample rotate simultaneously such that the incident and reflecting beam angles remain the same.

3.6.3 Auger Electron Microscopy (AES)

Selected use was made of a Physical Electronics Auger Nanoprobe 680 to characterize composition of surface features. Depth profiling and surface cleaning were performed by sputtering the sample surface with 2 keV argon at a current of 1 μA. Elemental analysis was calibrated by collecting spectra from oxide standards of Cr_2O_3 and Al_2O_3 and the as-received alloy. Spectra were collected using a 10 keV, 10nA electron beam, which yielded a spot size of about 50 nm. Depth profiling was conducted by first sputtering with argon for 10 minutes followed by a 1 second hold before collecting spectra from points selected on the surfaces.

Table 3-1 Chemical Compositions of Alloy 617 and Fecralloy® as provided by manufacturer [18].

	Alloy 617		Fecralloy®	
	ThyssenKrupp VDM		Goodfellow	
Element	wt%	at%	wt%	at%
Ni	Bal.	Bal.		
Fe	1.6	1.66	Bal.	Bal.
Cr	22.2	24.75	22	22.03
Co	11.6	11.41		
Mo	8.6	5.20		
Al	1.1	2.36	5	9.65
Ti	0.4	0.48		
Si	0.1	0.21	0.3	0.56
Mn	0.1	0.11	0.2	0.19
Cu	0.04	0.04		
C	0.05	0.24	0.02	0.09
Y			0.1	0.06
Zr			0.1	0.06

Table 3-2 Digital frequencies and actuator rates used to determine the optimal response of the actuator from the load.

	Filter (Hz)	Actuator Rate (in/min)		
a)	0.3125	0.01	0.02	0.05
b)	0.625	0.01	0.02	0.05

Table 3-3 Matrix of experiments conducted in this research work on both uncoated and coated 617 specimens. The objectives of the research work are shown side-by-side with the experiments conducted to answer them. Experiments consisted of exposure (E), static creep (S) and cyclic creep (C) in controlled impurity helium environments with different impurity potentials at 800°C.

OBJECTIVES	**EXPERIMENTS**			
1. Determine the role of environment (C, O, and both C and O potentials), and the absence of environmental effect on the near-surface damage during creep of Alloy 617.	**Uncoated 617**			
	He-CO/CO_2=1320 (C and O potentials)[2]	E	E+S (50 MPa)	E+C (10/50 MPa)
	He- ≤0.1ppm O_2 (O potential)[3]	E	E+S (50 MPa)	E+C (10/50 MPa)
	He-600ppm CH_4 (C potential)[4]	E	E+S (50 MPa)	
	He-600ppm CH_4 (C potential) + He- ≤0.1 ppm O_2 (O potential)	E	E+S (50 MPa)	
	Coated 617			
	Gen I Aluminized 617 in He- ≤0.1ppm O_2 (O potential)	E+S (50 MPa)		E+C (10/50 MPa)
	Gen II Aluminized 617 in He-CO/CO_2=1320 (C+O potentials)	E+S (75 MPa)		E+C (15/75 MPa)
	Clad+Aluminized 617 in He-CO/CO_2=1320 (C+O potentials)	E+S (50 MPa)		E+C (10/50 MPa)
				E+C (15-75 MPa)
	Clad+Aluminized 617 in He- ≤0.1ppm O_2 (O potential)	E+S (75 MPa)		
	Cladding on 617 in He-CO/CO_2=1320 (C+O potentials)			E+C (15/75 MPa)
	Coated 617 in He-CO/CO_2=1320			
2. Understand the mechanics of aluminized and clad/aluminized 617 during cyclic creep.	Aluminized 617 with notches	100h and 500h of E+C (10/50 MPa)		
	Clad/Aluminized 617 after 24h/1000°C extra heat treatment	E+C (10/50 MPa)		
	Clad/Aluminized 617 after 100h/1000°C extra heat treatment	E + C (10-50 MPa)		

[2] In this environment, 1980ppm CO and 1.5ppm CO_2 are mixed in pure helium (99.9999%). The concentration ratio of CO:CO_2 in helium is 1320.

[3] This environment is pure helium but, since oxidation is expected to occur, 0.1ppm concentration level is given to indicate the gas chromatograph detection limit for oxygen.

[4] In this environment, 600ppm of CH_4 is contained in pure helium.

Table 3-4 Element, spectrometer crystal, and material used for calibration in EMPA analysis. The spectrometer crystals used are: Large Lithium Fluoride (LLIF), Pentaerythritol (PET), and Large Thallium Acid Phthalate (LTAP).

Element	Crystal	Calibration Standard
Ni	LLIF	NiAl
Cr	PET	pure Cr
Co	LLIF	pure Co
Mo	PET	pure Mo
Al	LTAP	NiAl
Ti	PET	pure Ti
Fe	PET	pure Fe

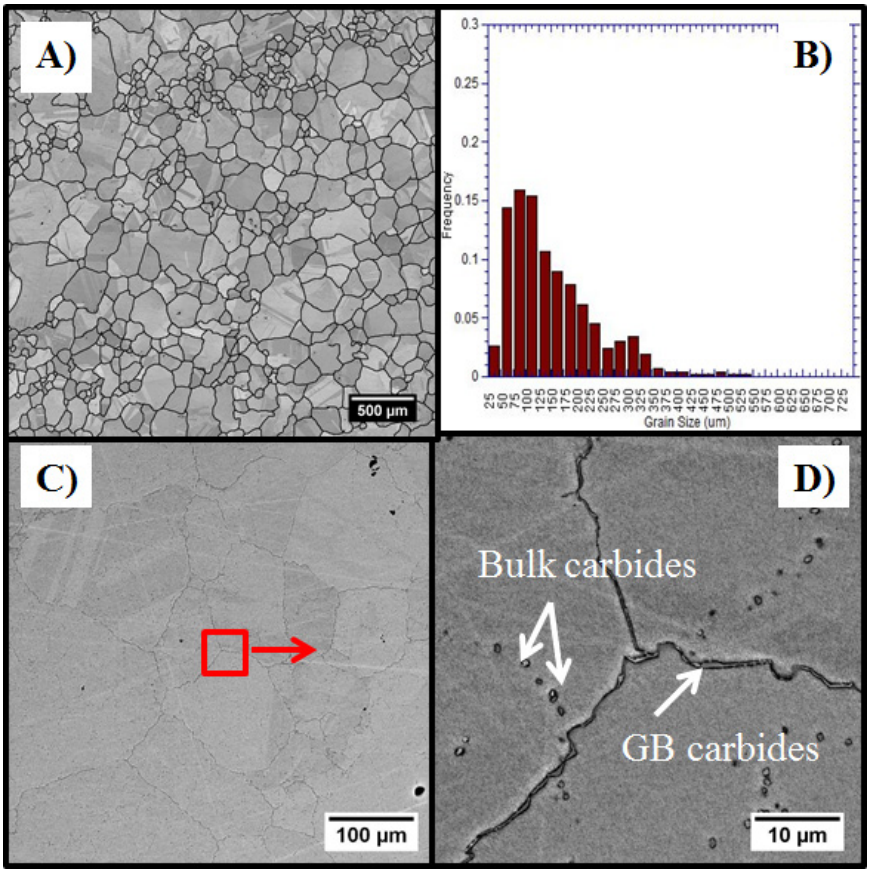

Figure 3-1 Microstructure of as-received Alloy 617 etched in Kalling's reagent (5g $CuCl_2$, 100ml ethanol and 100ml HCl). The typical polycrystalline microstructure with an average grain size of 139 µm ± 13 µm and grain size distribution are shown in (A) and (B), respectively. The $M_{23}C_6$ carbides present initially in the alloy are visible within the grain and along the grain boundaries are shown in (C) and (D), respectively.

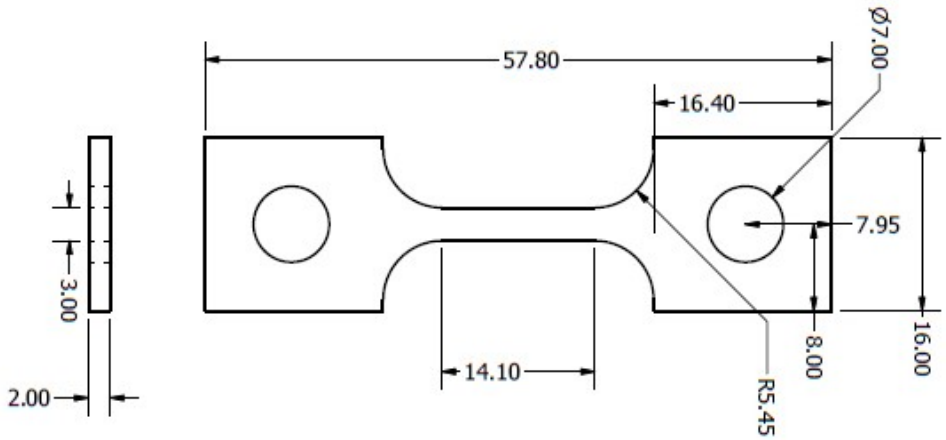

Figure 3-2 Schematic of rectangular "dog-bone" specimen designed for the static and cyclic creep experiments of Alloy 617 in controlled impurity helium environments.

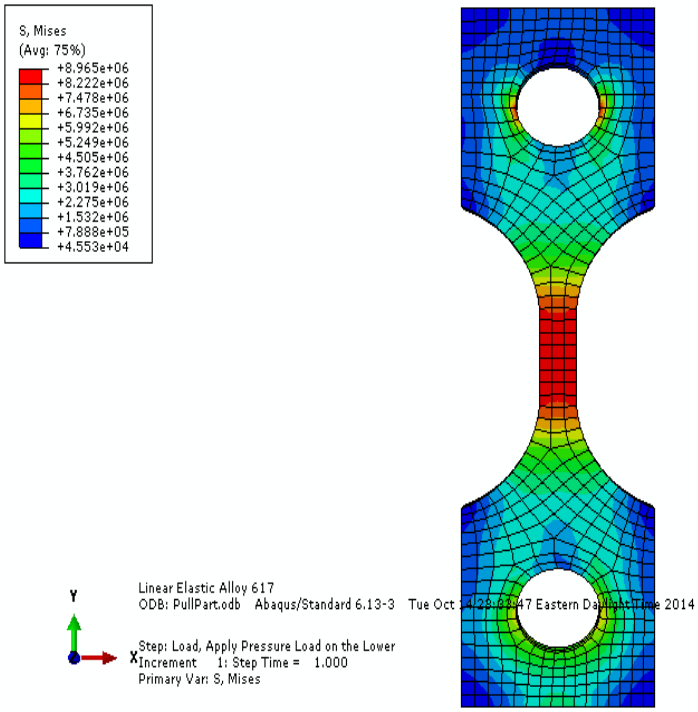

Figure 3-3 Creep specimen geometry showing tensile stress distribution by FEM modeling. Maximum stresses are uniform within the gauge section and stresses at the holes are much lower.

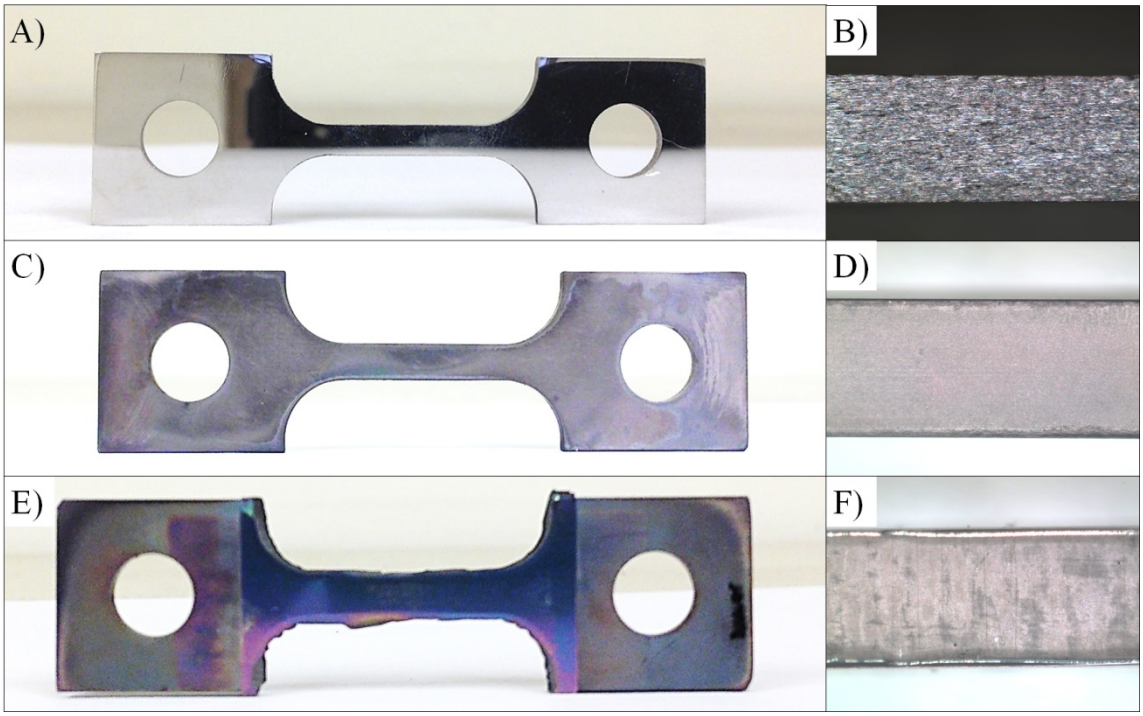

Figure 3-4 Rectangular "dog-bone" 617 specimens prepared for static and cyclic creep experiments. Three kinds of specimens used in this research work are as-polished and uncoated (A), as-aluminized (C), and as-clad/aluminized 617. (B), (D) and (F) show the

gauge faces that are perpendicular to the flat faces in (A), (C) and (E). Note that the cladding is applied on an aluminized specimen only on the flat gauge area as shown in (E), and not on the perpendicular faces of the gauge (F).

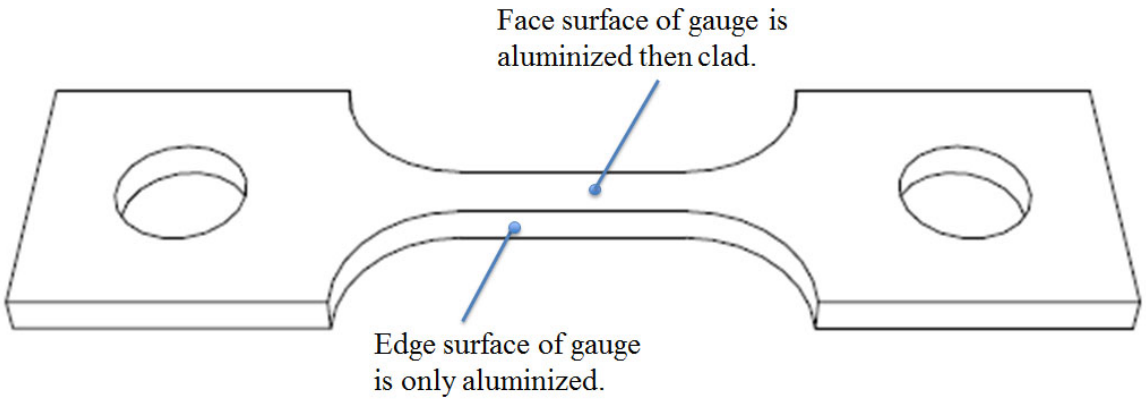

Figure 3-5 Schematic of dog-bone creep specimen indicating the face surfaces of the gauge to be clad and aluminized, while the edge surfaces are aluminized only.

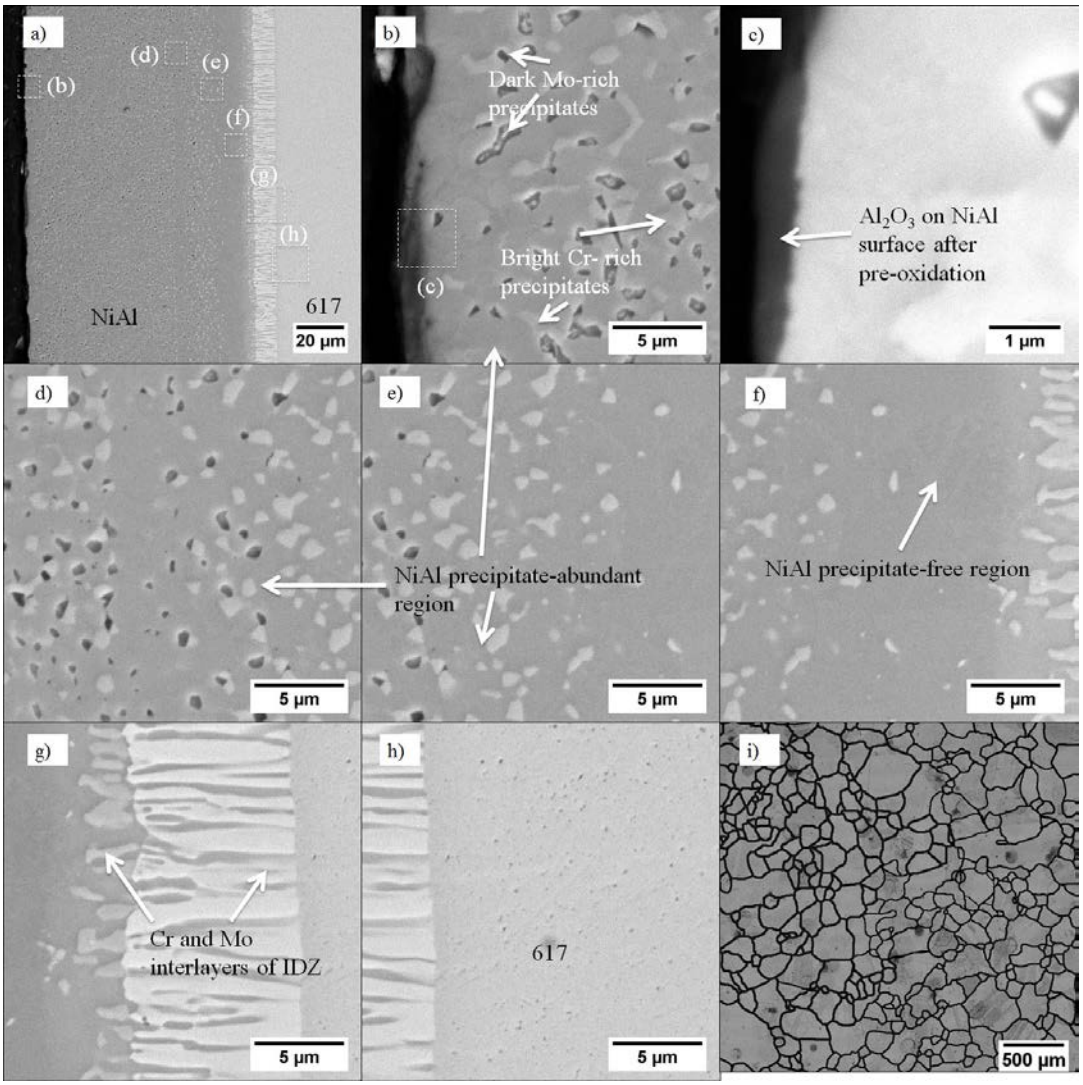

Figure 3-6 Microstructure of as-coated aluminized 617 (Gen II) showing a thick NiAl coating with chromium and molybdenum precipitates and a sigma layer (a-h), with Al_2O_3 formed on NiAl surface after pre-oxidation (c). The average grain size of the underneath 617 is 139µm and the distribution of grains is shown in (i).

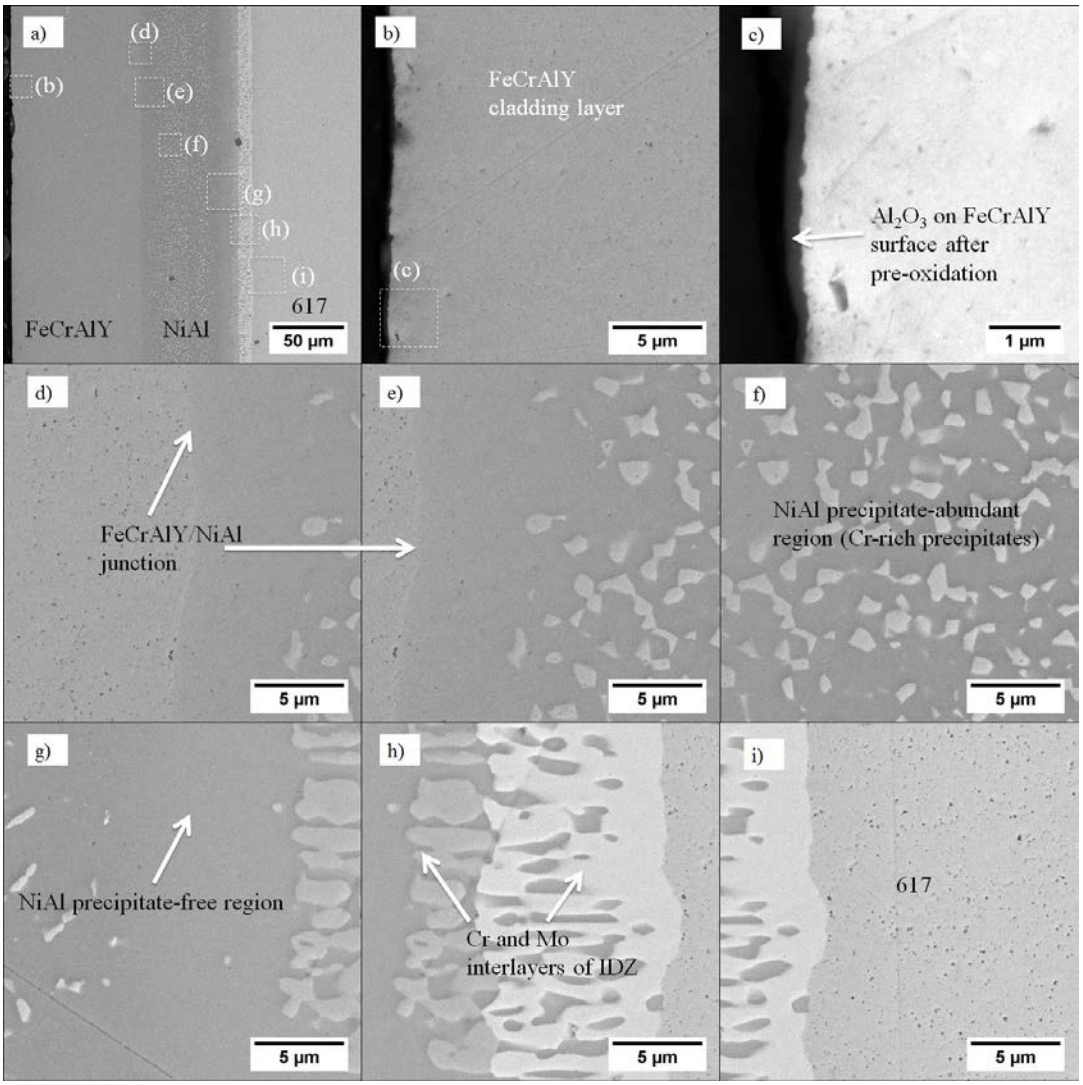

Figure 3-7 Microstructure of as-coated clad-aluminized 617 showing FeCrAlY cladding and NiAl layers with chromium precipitates and a sigma layer (a-i), with Al_2O_3 formed on FeCrAlY surface after pre-oxidation (c).

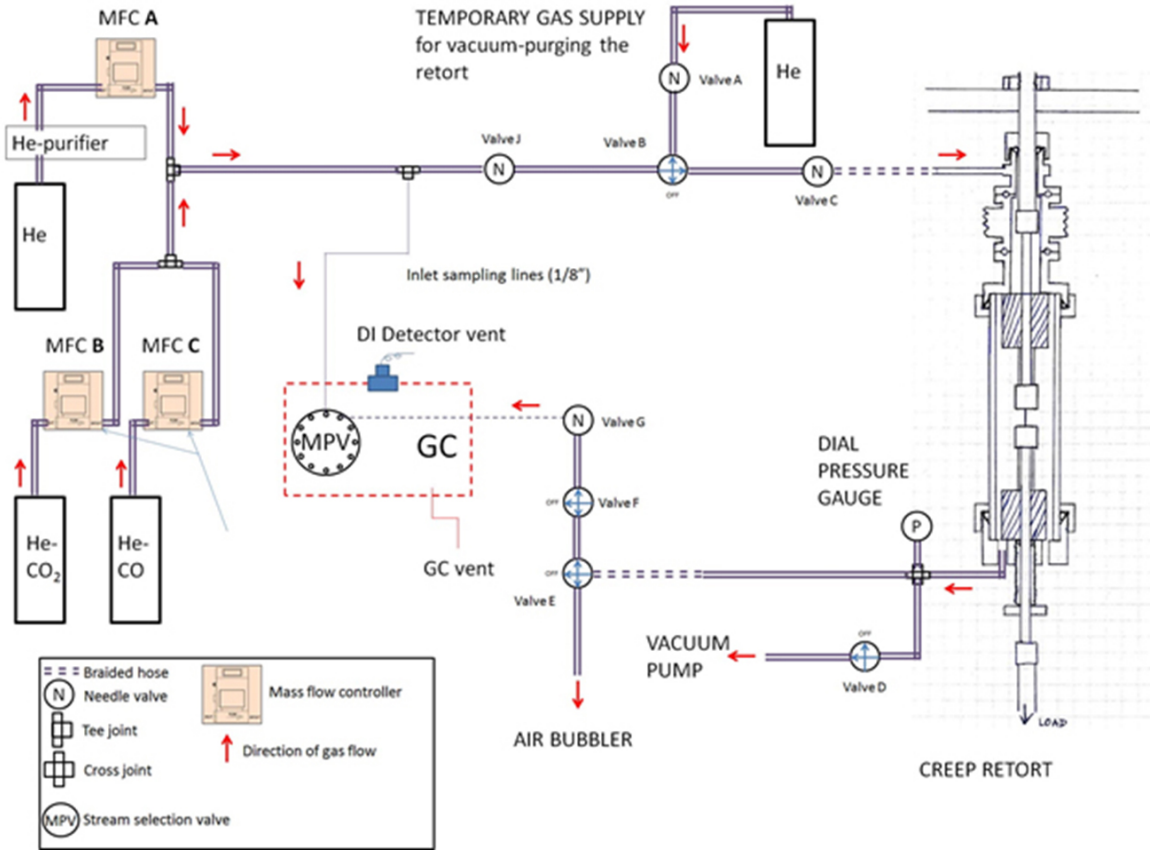

Figure 3-8 Schematic of the Controlled-Impurity-Flow Creep system. The three major sections: helium purification, gas mixing, exposure-mechanical testing, and gas analysis.

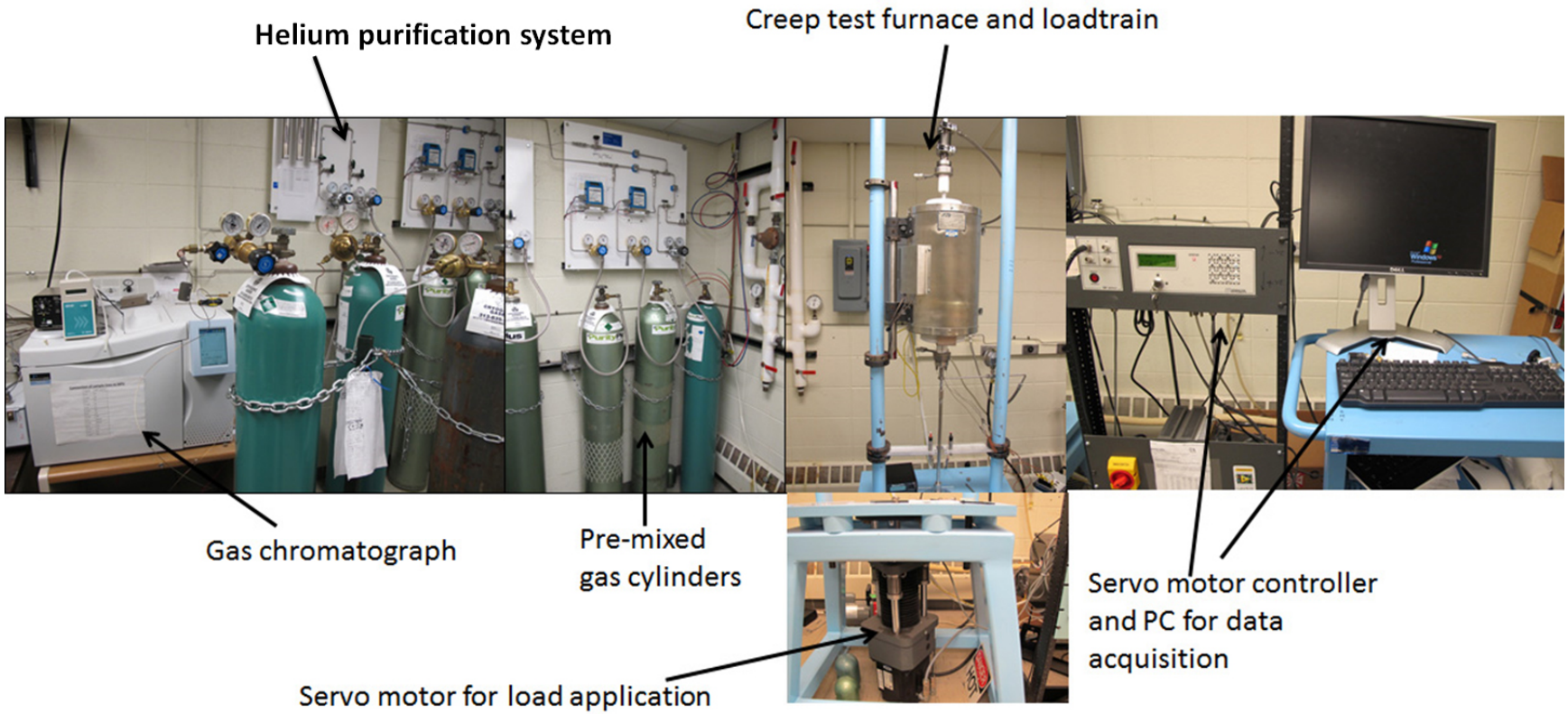

Figure 3-9 Photograph of the Controlled-Impurity-Flow Creep system. The three major sections are: helium purification, gas mixing, exposure-mechanical testing, and gas analysis.

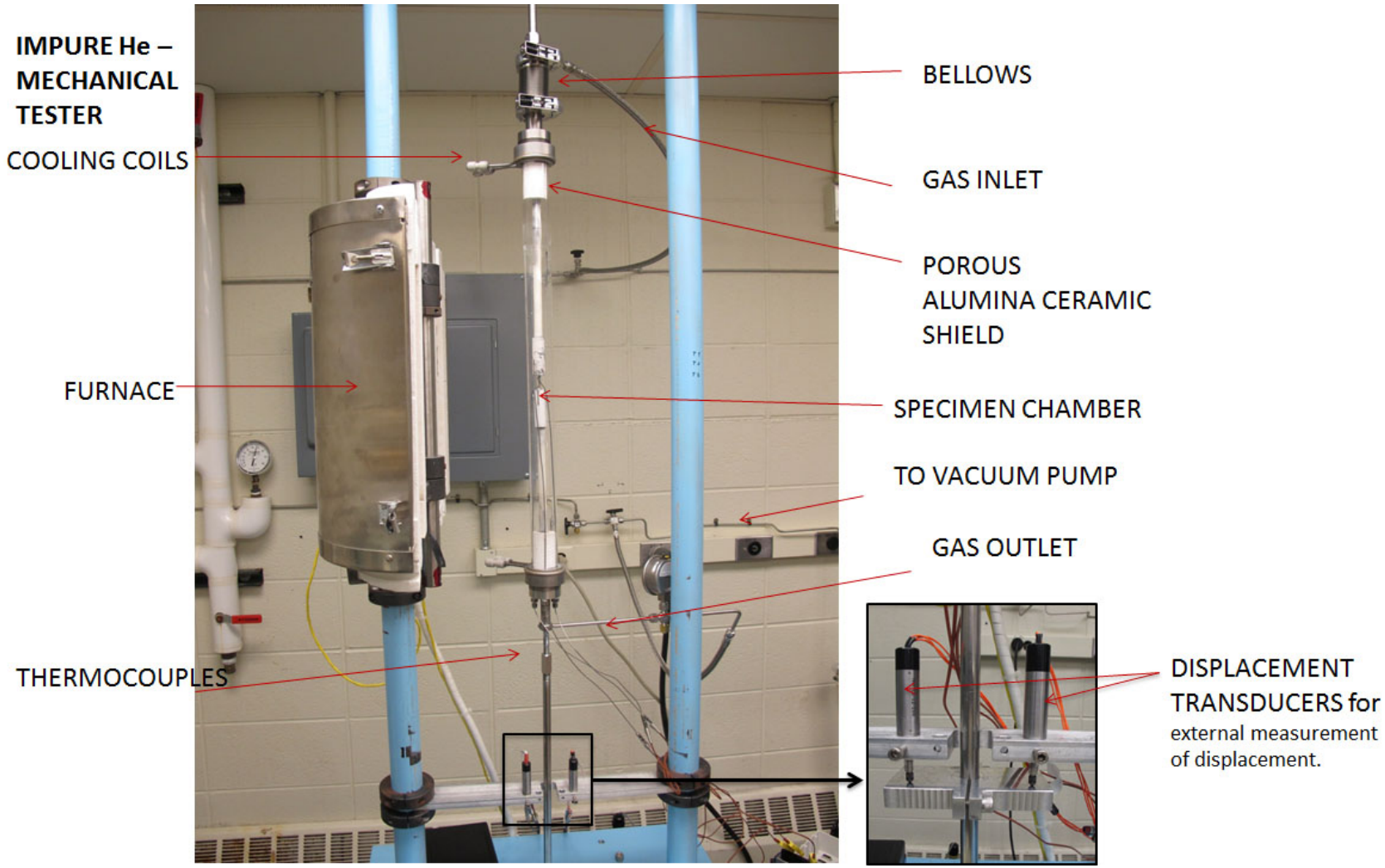

Figure 3-10 Image of the exposure-mechanical testing system showing the creep frame and the specimen chamber.

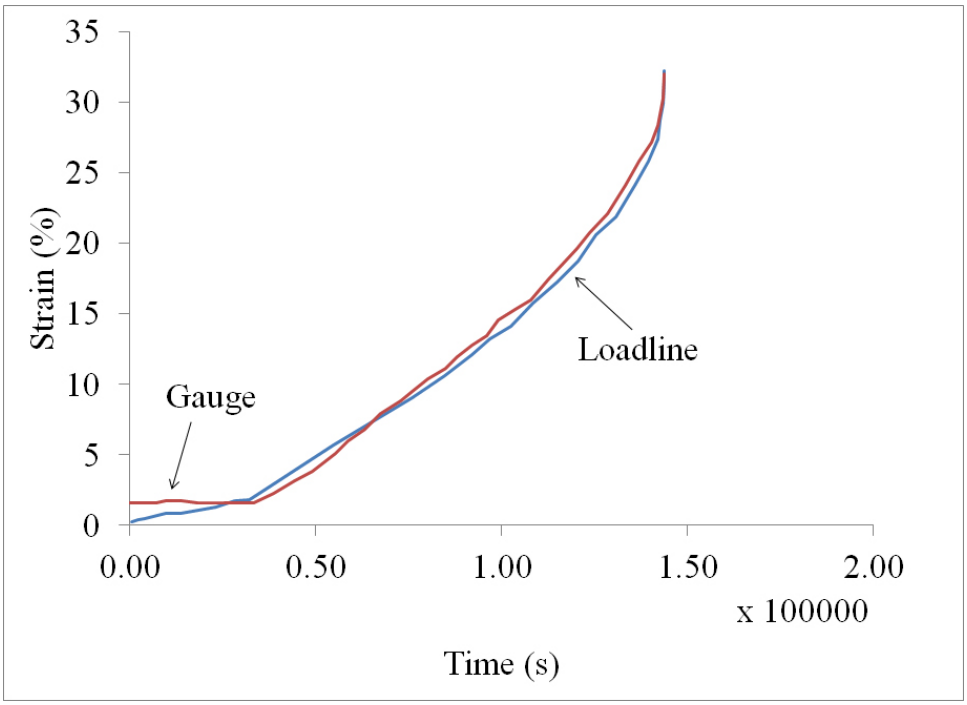

Figure 3-11 Strain versus time data for Alloy 617 showing the verifiability of strain measurements taken at two different locations: loadline and gauge.

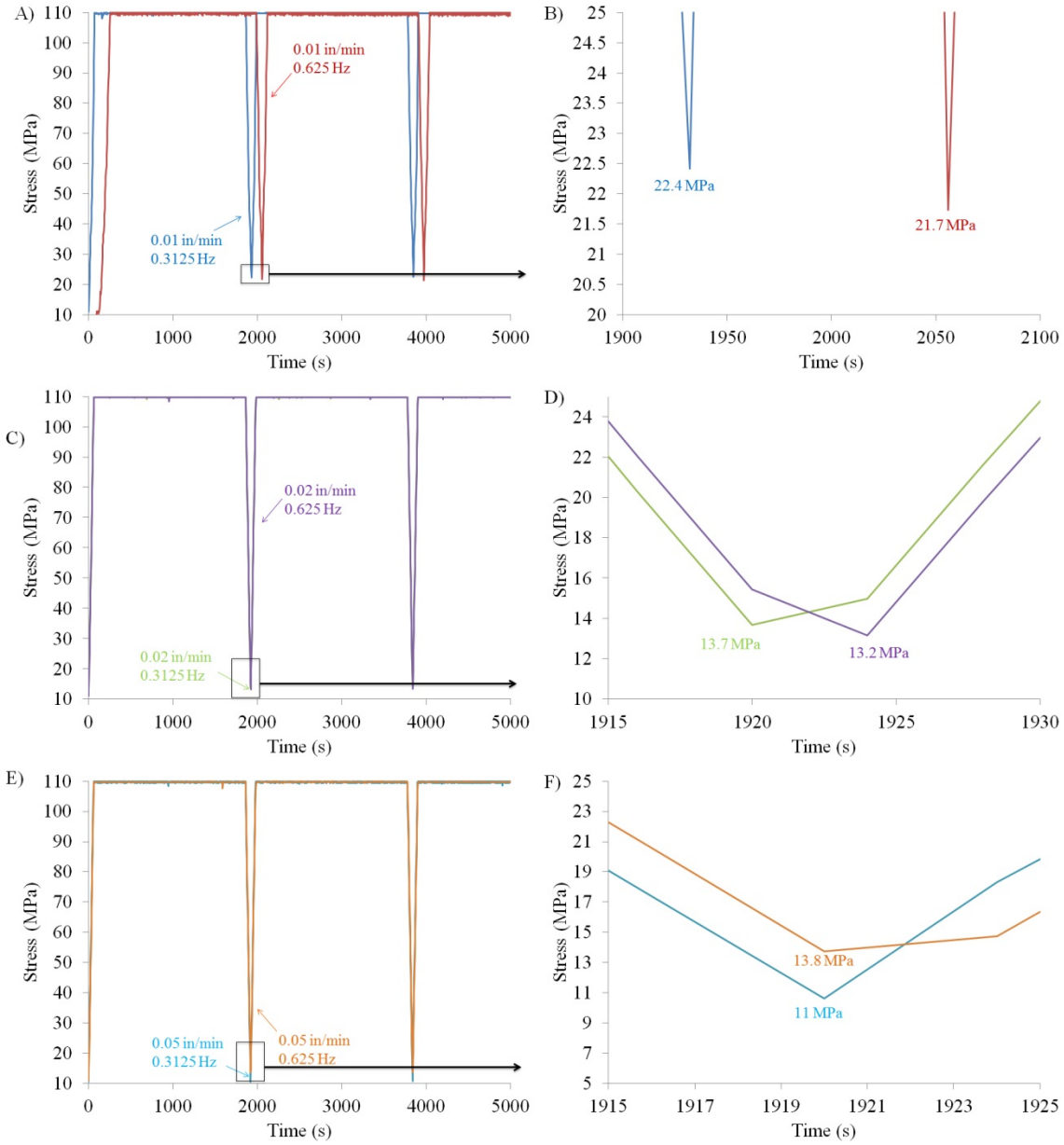

Figure 3-12 Different settings (actuator rate and digital filter frequency) used to evaluate how accurately the servomotor applied load from 11-110 MPa. For each actuator rate, two digital filter frequencies (0.3125 Hz and 0.625 Hz) were tested. The actuator rates are (A) 0.01in/min, (C) 0.02 in/min, and (E) 0.05 in/min, and their respective insets (B), (D), and (F). The optimal settings were determined to be 0.05 in/min and 0.3125 Hz.

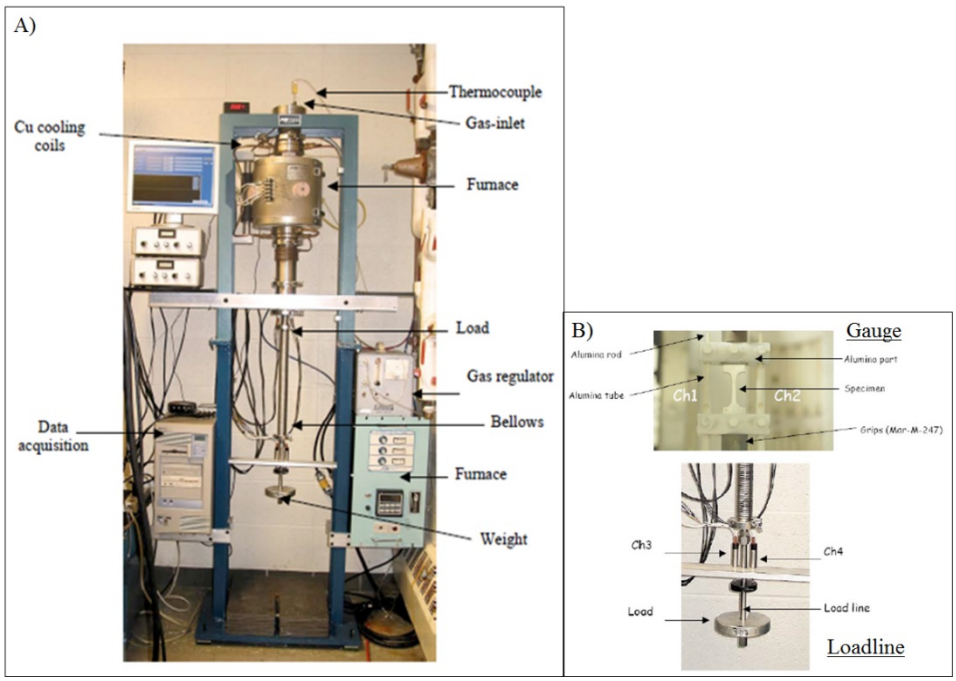

Figure 3-13 Old creep frame developed for static creep testing of Alloy 617 in controlled impure helium environments. The loading here is provided by dead-weights.

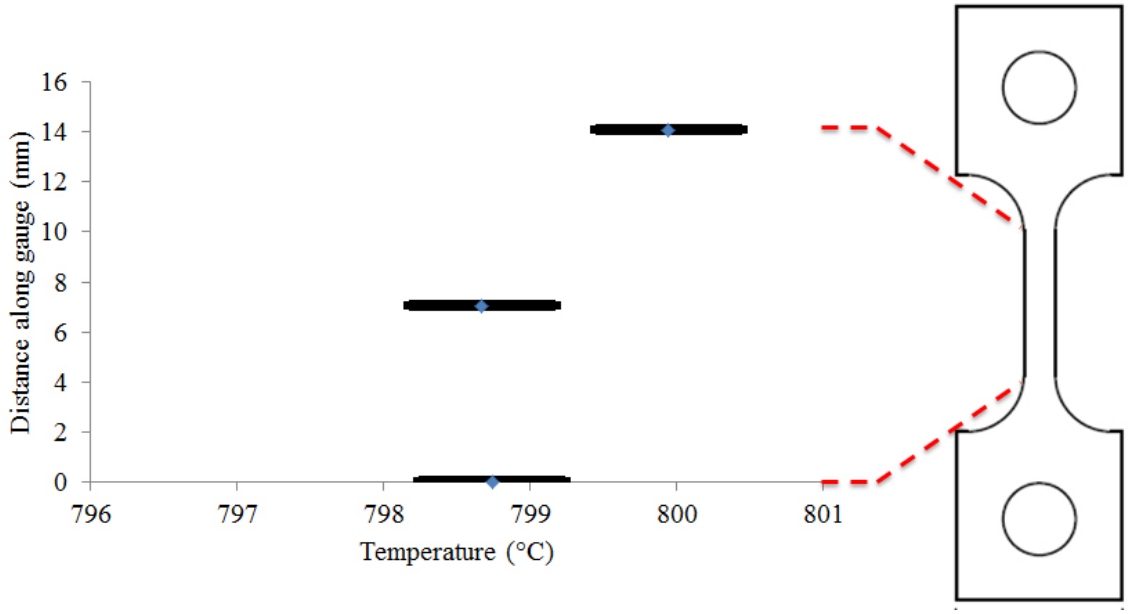

Figure 3-14 Temperature profile obtained along the gauge of the specimen for creep experiments in controlled impurity helium environments at 800°C. The error in the measurements was ±0.5°C.

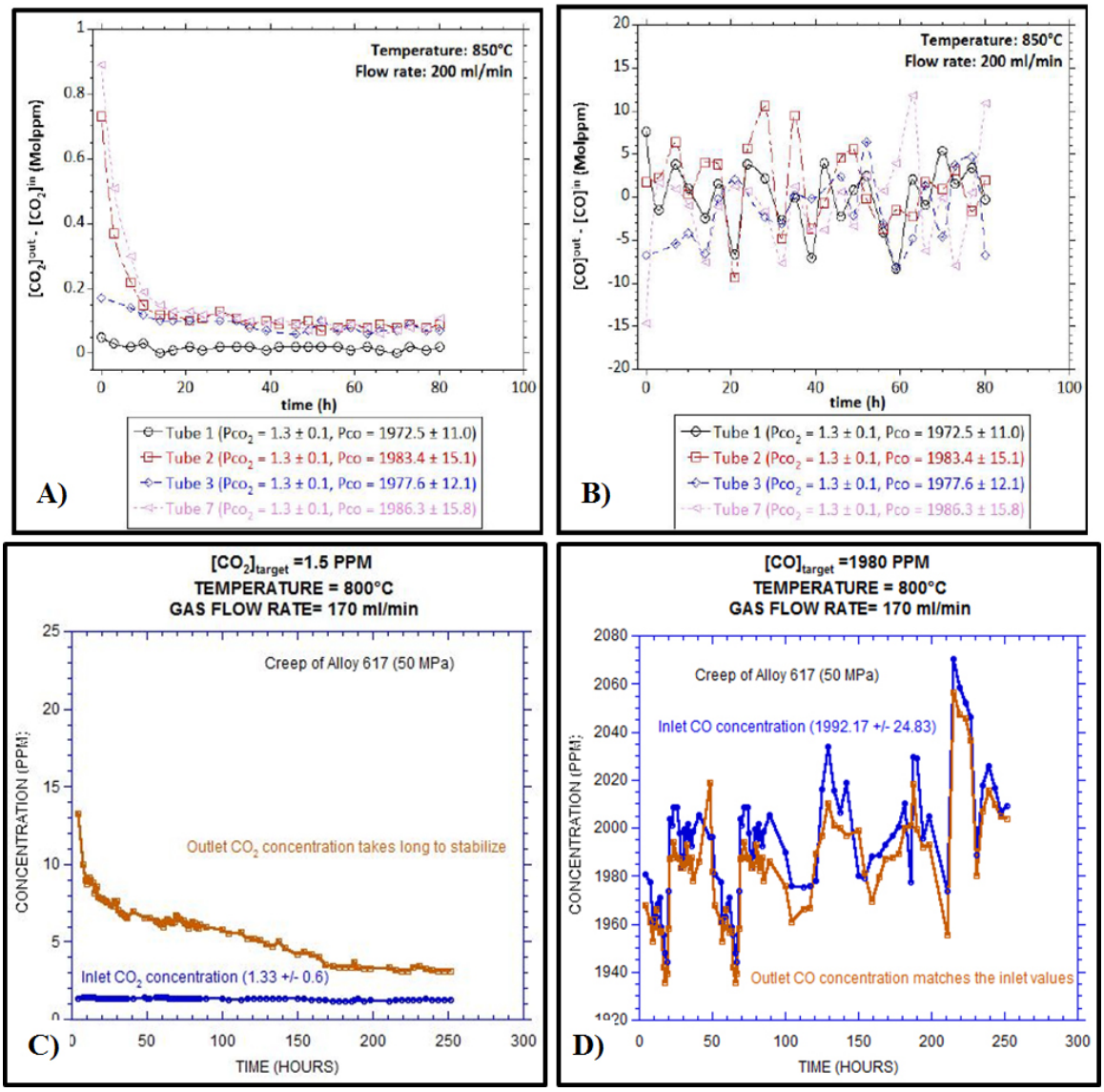

Figure 3-15 Differences in the inlet and outlet CO_2 (a,c) and CO (b,d) concentrations due to the interactions of He-CO/CO2=1320 with the quartz tubes and/or creep retort assembly. For the exposure-only experiments (a,b) [77], the concentrations between the inlet and outlet reached a steady state after ~40-50h; for the creep-exposure experiments (c,d) the times were longer (250h).

CHAPTER 4
EFFECT OF IMPURE HELIUM ENVIRONMENTS ON THE EXTENT AND MECHANISMS OF NEAR-SURFACE DAMAGE OF ALLOY 617 DURING CREEP AT 800°C

In this chapter, the role of different impure helium environments on damage accumulation in the surface and near-surface regions of uncoated Alloy 617 is examined. In particular the role of creep strain on damage accumulation is investigated, with the goal of inferring how such an attack would affect the long-term degradation of Alloy 617 under creep and cyclic creep conditions.

Studies were conducted to characterize the near-surface damage of Alloy 617 as a function of carbon and oxygen potentials in helium during static and cyclic creep at 800°C. All creep tests were interrupted at nominal strains well before failure, and the damage was limited to the near-surface region, which is of most interest in differentiating the effects of environment. Sections 4.1 to 4.5 present the effects of two environments, oxidizing (He-≤0.1ppm O_2) and carburizing/oxidizing (He-CO/CO_2=1320), on the type of near-surface damage of Alloy 617 under static (50 MPa) and cyclic (10/50 MPa) loading. The former is an environment where oxidation only is expected to occur, while in the latter environment both oxidation and carburization are expected. In these studies, surface morphologies, cross-sections, and chemical characteristics of the oxide scale are examined. The role of stress on environmental attack, the role of gas environment on creep behavior, the morphology and growth rates of Cr_2O_3, and whether chromia formation is a step-wise mechanism of formation of carbides before their oxidation, will be discussed in Section 4.6.

4.1 Creep Behavior of Alloy 617 in He-≤0.1ppm O_2 and He-CO/CO_2=1320

The creep behavior of Alloy 617 in the oxidizing and carburizing/oxidizing impure He environments is shown in Figure 4-1 for both static and cyclic creep

conditions. The details of the creep behavior (time under load, minimum creep rate and strains) are listed in Table 4-1. For the sake of comparing the creep behavior for both static and cyclic loading, the creep curves for the cyclic loading are shown as creep strain vs. time at maximum stress. Figure 4-1a shows the creep curves of Alloy 617 in the different environments and stress conditions at 800°C. Figure 4-1b-c show the static and cyclic creep behavior of the alloy in He-≤0.1ppm O_2 and He-CO/CO_2=1320 environments respectively. The tests were interrupted at approximately the same nominal strains[5] long before failure, and the creep curves show the primary and secondary stages of the creep behavior. To achieve the same strain levels, the exposure under cyclic stress was approximately twice as long as under static stress. The measured steady state (minimum) creep rates under the two environments for both static and cyclic loading were similar[6]. It is concluded, that up to the nominal strains reached in the tests, the nature of test environment and type of loading do not affect the bulk creep behavior of Alloy 617. Since environmental attack is a time-dependent phenomenon, the extra time under cyclic strain accumulation provides more information on the surface scale formation and near-surface damage.

4.2 Morphology of surface oxide

The surface scale morphologies of Alloy 617 after creep in the two environments exhibited marked differences. The nature of applied loading (static versus cyclic) did not affect the type of oxide morphology produced on the alloy surface in either environment, and so the oxide morphology for static loading (50 MPa) was shown for each environment.

Following exposure for 211 h in the oxidizing-only environment (He-≤0.1ppm O_2) and a total creep strain of 1.9% strain, the alloy formed an overall nodular-type

[5] The tests were stopped at ~2% strain for two reasons. First, these tests were designed as a feasibility study aimed to help understand the synergistic relationship between environmental and mechanical effects during creep before significant mechanical damage could take place and hence render it difficult to appreciate the environmental effects on the surface of the alloy. Second, the strain level was chosen such that the cyclic tests did not take too long to reach the same strain as in static tests and so would have made it unfeasible to conduct extra studies of creep of Alloy 617 as a function of environment composition, loading, and presence or absence of coatings.

[6] Creep strain rates, as indicated by the linear part of the creep curves, under static and cyclic loading in the two environments fall within the same scatter band, and so there seems to be no effect on creep behavior of environment composition and loading type.

surface oxide with enhanced oxidation at the grain boundaries, as shown in Figure 4-2a. The oxidation is generally uniform, but spallation of the oxide layer is observed in certain parts of the specimen surface. This localized loss of the surface oxide – possibly a result of compressive stresses of the scale, test loading, cooling from test temperature, or a combination of all these factors – exposed an underlying substrate surface with evidence of intergranular grain boundary cracking (Figure 4-2b,c). Thick oxide ridges along the grain boundaries (Figure 4-2d,e), as viewed from the surface, are indicative of enhanced grain boundary oxidation, since grain boundaries are fast diffusion paths. The nature of the oxide is similar at the grain boundary as on the grain, and is rich in Cr and O, as shown in Figure 4-3.

In contrast to the morphology of the oxide produced in the oxidizing environment, the surface oxide that developed after 206 h in the carburizing/oxidizing environment (He-CO/CO_2=1320) was smooth – not nodular (Figure 4-4a). There was no indication of thick oxide ridges along the grain boundaries, and certain areas showed the opening of grain boundaries. Spallation of the surface oxide occurred here as well and exposed needle-like features underneath the smoother part of the oxide, as shown in Figure 4-4b,c. The same needle-like features were observed in the intergranular cracking (Figure 4-4d), and cross-sections will show that they extend from the surface into the alloy.

4.3 Characterization of Damage Penetration

Here surface damage is defined as surface scale formed as a result of exposure to environment, and the presence of intrusions (cracks or internal oxidation) due to the effect of environment and stress. The nature of loading (whether static or cyclic) did not change the type of damage in either environment. However, as shown in Table 4-2, the near-surface regions of specimens subjected to cyclic loading (10/50 MPa) experienced more frequent and deeper Cr_2O_3 and/or Al_2O_3 intrusions, as well as thicker surface scales than for specimens crept at static loading (50 MPa) in the same environments. In order to attain the same nominal strains, specimens under cyclic loading were crept for twice as long as for those under static loading, and this accounted for thicker and more penetrative oxides in the former, which is presumed to be only a function of time at temperature. The carburizing/oxidizing environment was more damaging – number and extent of grains attacked than the oxidizing environment under the same type of loading. In summary,

there is an increase in the frequency of grain attack, the depth of grain boundary intrusions, and the thickness of the surface oxide in the presence of carbon and oxygen potentials (He-CO/CO_2=1320) than when only oxygen (He-$\leq$0.1ppm O_2) is present. This is also the case under cyclic loading (10/50 MPa) when compared to static loading (50 MPa). Figure 4-5 compares the combined effect of environment and stress on the surface damage of Alloy 617 at 800°C for the different test conditions, while quantification of the damage is presented in Table 4-2.

Cross-sections of Alloy 617 crept in the He-$\leq$0.1ppm O_2 are shown in Figure 4-6 and Figure 4-7. In this environment, the damage is comprised of a surface chromia scale and internal oxide (alumina) in select grain boundaries. It is worth noting that the less porous and continuous chromia, which appears to be of a fine and nodular structure, is limited to the surface and there is no substantive presence of chromia penetrating the grain boundaries. Figure 4-6a shows the surface scale and grain boundary intrusions. From Figure 4-6b it can be seen that the surface oxide at the intersection of the grain boundary with the specimen surface is thicker than elsewhere (where the scale thickness is generally uniform), indicative of the thick grain boundary oxide ridges seen earlier on the surface in Figure 4-2. Also, a closer look at the surface oxide shows the presence of a mixture of matrix and scale. The thicker grain boundary oxides and the presence of matrix within the surface scale are indicative of an outward growth of the outer scale. Cr_2O_3 scale has been shown to grow mainly outwardly [81-83]. Underneath the surface chromia scale, there is a thin alumina scale that extends internally along certain grain boundaries, as shown in Figure 4-7. The chromia surface scale and internal and sub-surface alumina oxides are identified by EDS maps in Figure 4-8. In this environment, it can be said that cracks are initiated by internal alumina oxides. The cross-section and surface morphology can both be seen in Figure 4-9 where the sample has been tilted to 45° relative to the beam.

In He-CO/CO_2=1320, the damage is comprised of a chromia scale located on the surface and extending into the matrix along the grain boundary, and internal alumina close to the surface scale and cracks (Figure 4-10a). Internal oxidation occurs below the surface scale (Figure 4-10b), and alongside the chromia-filled crack (Figure 4-10c). The surface scale is made of porous, blocky, coarse-grained, and plate-like features, with no

indication of enhanced scale ridges at the intersection of grain boundaries and the surface (Figure 4-10d). The crack tip is composed of the same corrosion product as that on the surface (chromia) and alumina around the crack (Figure 4-11b-d). Carbides have precipitated in the matrix of the alloy, and there is a carbide-free zone close to the chromia crack (Figure 4-12b). The precipitate-free zones are present near the grain boundaries and also the surface, most likely as a result of the depletion of Cr during the nucleation and growth of the Cr-rich carbides. These zones are easier to observe here than in the oxidizing environment due to the precipitation of carbides. Occasionally, alumina – dark phase – is incorporated in certain areas of the chromia-filled crack body – bright phase – and also alongside the crack, as shown in Figure 4-12c,d. The carbides near the surface are formed as a result of carburization effect of the environment. Figure 4-13 shows the presence of carbides near the surface and their diminished presence in the bulk. The chromia surface scale and crack corrosion product, and internal alumina oxides are identified by EDS maps as shown in Figure 4-14. The surface/cross-sectional features, as shown in Figure 4-15, characterize the surface and grain boundary oxides, and the continuation of the surface oxide into the matrix via the grain boundaries. Also, it is clearer here that the needle-like oxide features are below the smooth upper layer, and are exposed when spallation occurs. It is apparent that in the carburizing/oxidizing environment, the corrosion products are thicker on the surface, and penetrate deeper into the matrix along the grain boundaries than in the oxidizing environment. Another difference is that the oxide formed in He-CO/CO_2=1320 is more porous than that in He-$\leq$0.1ppm O_2. This difference in morphology of the oxides developed in the two environments points to the possibility of the two scales having different crystalline structures or different pathway of formation.

4.4 Determination of Oxide Structure by XRD Analysis

X-Ray diffractometry was used to identify the phases in the oxide films and hence determine the crystallographic structure of the different scales. Identification of phases in bulk and surface was done in the θ-2θ mode as shown in Figure 4-16, while surface-sensitive diffractometry was performed to highlight the surface corrosion products using a grazing angle of incidence of 2° with 2θ between 23° and 67° (Figure 4-17). The identified phases were γ-Ni substrate (PDF: 65-2865), Cr_2O_3 (PDF: 38-1479), and $Cr_{23}C_6$

(PDF: 65-3132), while Al_2O_3 peaks (PDF: 10-0173) were not unambiguously identified; therefore, only the expected peak positions are shown. The XRD data is normalized in order to accentuate the peaks of phases produced during corrosion compared to stronger peaks from the Ni-substrate and to facilitate comparison of different testing conditions. Since the volume of interaction of X-rays is greater for bulk compared to surface characterization, different normalization is used ($(I/I_{max})^{1/2}$ and I/I_{max} respectively).

Figure 4-16 shows the results for the bulk measurement of the corrosion products developed for Alloy 617 in the different He environments. γ-Ni substrate (peaks at 43.5° and 50.5°) is the only phase identified in the as-received alloy (Figure 4-16a), and no carbides are identified as they are in solution. Results for static and cyclic loading are compared here to show the effect of exposure time and not the effect of the type of loading, since the latter is not expected to produce different corrosion products in the same environment. In He-≤0.1ppm O_2, the main corrosion product is Cr_2O_3, and the effect of time increase from 211 h to 690 h is seen by the increased Cr_2O_3 peak intensities in (Figure 4-16b,c). The extra peak seen at 29° for the 211 h data was not identified and it is assumed to be an artifact. Cr_2O_3 and $Cr_{23}C_6$ were produced in He-CO/CO_2=1320, and here also an increase in the peak heights is seen with increase in exposure time (comparison of 206h and 553h data in Figure 4-16d and e respectively). Comparison of the effect of the two environments reveals that He-CO/CO_2=1320 produces more intense Cr_2O_3 peaks than He-≤0.1ppm O_2 for short- (Figure 4-16b,d) and long-exposure times (Figure 4-16c,e), consistent with a thicker oxide in He-CO/CO_2=1320, as summarized in Table 4-2. Also, since there is an overlap in the peaks of Cr_2O_3 and $Cr_{23}C_6$ phases (peak at 33.5°), this increase in peak height could also be due to the increased precipitation of these carbides in the He-CO/CO_2=1320. The reduction in peak intensity of γ-Ni substrate relative to Cr_2O_3 (peaks between 50°-52°) is more significant in He-CO/CO_2=1320 relative to He-≤0.1ppm O_2 (Figure 4-16d relative to Figure 4-16b, and Figure 4-16e relative to Figure 4-16c), a condition that could be attributed to reduction of the volume fraction of the matrix phase in the sampling volume as more significant oxidation occurs in He-CO/CO_2=1320.

The results for the XRD surface characterization of the corrosion products developed for Alloy 617 in the different He environments are shown in Figure 4-17. The

main phase identified is Cr_2O_3; however, the substrate was picked up as well. Once again the peak intensities of Cr_2O_3 are weaker in He-≤0.1ppm O_2 than in He-CO/CO_2=1320 (Figure 4-17a,c and Figure 4-17b,d) while the effect of time on the intensity of Cr_2O_3 peaks is not noticeable for exposures in the same environment (Figure 4-17a,b and Figure 4-17c,d). It is also noticeable that there are no carbides identified within the oxide scale.

The conclusion here is that Cr_2O_3 with the same crystallographic structure was developed in the different environments even though their morphologies were different. This difference in morphology of the grown oxides will be subsequently described in the discussion section in terms of the difference in porosity of Cr_2O_3, the effect of ambient oxygen partial pressure, and the possibility of difference in pathway of oxide formation.

4.5 Determination of Oxide Composition by Auger Analysis

Since XRD is not expected to be able to detect all the phases, Auger depth profiling was used to determine the composition of the oxides as a function of depth. The composition profiles were taken after 10 minutes of sputtering with 10 keV argon at a current of 10 nA. Figure 4-18 shows the composition of the corrosion surface products as a function of sputtering time for Alloy 617 exposed to four He-environments.

The concentration profiles show the presence of an oxide (mainly Cr_2O_3) for at least the first 50 minutes of sputtering. Since the morphology and porosity of the oxides were distinct, and therefore different depending on the environmental exposure, calibration of the sputtering distance with the time could not be determined accurately, and sputtering time is used in the data instead. Figure 4-18a shows the presence of surface Cr_2O_3 up to 200 minutes of sputtering for He-≤0.1ppm O_2, but just 70 minutes for He-CO/CO_2=1320 in Figure 4-18b.

4.6 Discussion

In this study, the type of near-surface damage of Alloy 617 at 800°C has been shown to depend on the gas chemistry represented by the two helium environments. Porous, and thick surface Cr_2O_3 together with deep grain boundary oxides and internal carbide precipitation characterized the alloy crept in He-CO/CO_2=1320, an environment with low oxygen partial pressure. A high oxygen partial pressure environment (He-≤0.1ppm O_2) produced thinner and less porous surface Cr_2O_3. In order to understand the

different surface damage mechanisms, this section will examine the role of stress, oxygen partial pressure, and carbon potential in the environment.

4.6.1 Role of stress in near-surface damage of Alloy 617

Environmental attack during creep of Ni-Cr alloys has been shown to be accelerated by the presence of mechanical stresses. Jang reported that the application of tensile loading during high-temperature oxidation of Alloy 617 in air and helium environments between 900-1100°C enhanced the thickness of the surface-oxide layer, the internal corrosion, and decarburization. He attributed this acceleration of environmental attack to the increase in diffusion of the oxidizing agent and gaseous reaction products [71]. Carbon intrusion was deeper in Alloy Hastelloy X [43] during accelerating creep than during steady state creep, and also at the rupture portion than at grip sections of the test specimen, further establishing the role of stress in accelerating environmental attack.

In this dissertation, comparison between unstressed and stressed conditions was made only for the more damaging carburizing/oxidizing environment. Even though the bulk creep behavior of Alloy 617 was not changed by varying the loading (static versus cyclic) in the two environments (Table 4-1), the alloy surface was significantly more damaged in the carburizing/oxidizing environment (Table 4-2). The creep behavior and characterization of the near-surface damage of the alloy in the oxidizing environment (He-$\leq$0.1ppm O_2) was used as a baseline for understanding the behavior in an environment with activity of carbon and low oxygen partial pressure (He-CO/CO_2=1320). To determine if the significant grain boundary attack is attributed to the application of mechanical stress during exposure in He-CO/CO_2=1320, as opposed to exposure only, Figure 4-19 compares the surface damage of stressed (50 MPa/1.7%/206h) and unstressed (0 MPa/0%/308h) specimens, and shows that the near-surface grain boundaries are attacked whether stress is applied or not. This means that stress is not responsible for the extensive damage in the He-CO/CO_2=1320 environment, and so the other possibility is the role of carburization on the damage accumulation near the surface. Tawancy et al [70] reported extensive intergranular cracking near the surface of a tensile-tested specimen that had been exposed to a carburizing environment prior to testing. This surface cracking was more likely due to the specimen surface layer being hardened by carburization, a condition in agreement with the concept of case-hardening

known to occur during carburization. It is, therefore, reasonable to conclude that stress does not, in the environmental condition here, initiate grain boundary attack, but rather there is an environmental effect by the carburizing environment that stress only accelerates.

4.6.2 Stability diagram and stability of carbides/oxides

In the current work, impurities used in the helium environments were expected to be oxidizing, in the case of He-≤0.1ppm O_2, or carburizing and oxidizing in He-CO/CO_2=1320 with respect to Alloy 617. Helium is an inert gas, but since achieving an oxygen-free environment is not feasible, the environment was designated as containing an oxygen level equal to or less than the detection limit of the gas chromatograph (0.1ppm O_2) used in the analyses of the test environments. In this regard, He-≤0.1ppm O_2 is considered to be a high oxygen potential environment (equilibrium oxygen partial pressure of 0.1ppm or 10^{-7} atm). Gas mixtures containing CO and CO_2 are usually used when it is required that the partial pressure of oxygen in a gas phase be fixed at a very low value [84]. He-CO/CO_2=1320, with equilibrium oxygen partial pressure of 2.1 x 10^{-25} atm and carbon activity of 0.4 in the gas mixture, falls in this category. Since the gas contains both CO and CO_2 impurities, carburization and/or oxidation are expected to occur.

The corrosion modes of Ni-Cr alloys in impure He environments can be understood by analyzing the stability diagram of chromium to determine the thermodynamic stability of the different phases formed in Ni-Cr alloys at a given temperature. From the Cr-C-O stability diagram, Figure 4-20, the regions where Cr, its carbide and oxide are stable can be identified as a function of equilibrium carbon activity and oxygen potential of the test environment [33, 35]. As previously explained in Chapter 2, the most stable oxide and carbide phases of the candidate alloys are Cr_2O_3 and $Cr_{23}C_6$. The oxygen and carbon activities of the He environments used in this work are within the region of stability of Cr_2O_3 and $Cr_{23}C_6$ for He-CO/CO_2=1320 (oxygen partial pressure of 2.1 x 10^{-25} atm and carbon activity of 0.4) and Cr_2O_3 for He-≤0.1ppm O_2 (oxygen partial pressure of 10^{-7} atm). It should be pointed out that equilibrium between the alloy surface and CO and CO_2 impurities in the primary coolant helium is not expected to be achieved under the fast-flowing service conditions [30]. Therefore, these calculated equilibrium

values of oxygen and carbon activities in the gas are not expected to occur. However, Gulsoy showed that the steady-state values of oxygen and carbon activities could not be calculated due to lack of data in the literature, but that the anticipated difference between the equilibrium and steady-state values was not expected to affect the diffusion and mechanism of Cr oxidation [77].

4.6.3 Effect of environmental attack on creep

The effects of chemistry of the gas environment on bulk creep behavior of chromia-forming alloys have been explored in the past. For instance, it has been reported that the precipitation of carbides could lower the creep ductility of the alloy [12, 43, 57, 85]; oxidation could lead to formation of surface cracks that would reduce the load-bearing area [67]; and decarburization could reduce the creep strength of the alloy [12, 43, 44].

The creep behavior of Alloy 617 in the He-$\leq$0.1ppm O_2 and He-CO/CO_2=1320 environments was shown in section 4.1, showing no immediately observable effect of the chemistry of the helium environments or load types on the creep strain rates. This is surprising since it would appear that the differences in the near-surface damage in the two environmental conditions would significantly affect the creep rates. The creep tests were interrupted in the secondary creep regime, and this is confirmed by the fact that features associated with the initiation of the tertiary stage (formation of voids and necking) did not occur. The environmental effect was, therefore, reduced to surface effects only. The surface effects on the alloy in the environments were short internal oxides/cracks in He-$\leq$0.1ppm O_2 and long grain boundary cracks and carbide precipitation in He-CO/CO_2=1320. Understanding the effect on the load-bearing area of the depths of these intrusions (internal oxide/cracks and grain boundary cracks) is important. Table 4-3 shows an approximation of the reduction of cross-sectional area due to oxidation and development of cracks after creep in the two environments. For simplicity, the cross-sectional area reduction due to creep elongation is not considered here. The load-bearing area is somewhat reduced (to 91-94%) in the carburizing/oxidizing environments compared to the oxidizing environments (98-99%). From this analysis, one could say that alloy 617 should creep faster in the carburizing/oxidizing compared to an oxidizing-only environment. It should not be forgotten, however, that carburization in the alloy causes

precipitation of carbides in the matrix, and so the effect of a reduced load-bearing cross-sectional area could be offset by the redistribution of carbon in the matrix to produce enhanced carbide precipitation, hence higher creep strength in the surface and core of the specimen. The first implication of deeper-attacked grain boundaries in He-CO/CO_2=1320, is that the alloy might reach tertiary stage faster and fail sooner than would be the case in He-≤0.1ppm O_2. This early onset of tertiary creep in He environments was seen by Mino [86], and he attributed it to early initiation and growth of surface cracks and resultant reduction of the effective cross-sectional area. The second possibility of the effect of the near-surface damage is that the matrix carburization could delay the initiation of the tertiary stage in He-CO/CO_2=1320, whereas failure could be rapid in the He-≤0.1ppm O_2 as observed by Shankar [12]. In this respect, the effect of environmental attack on the long-term creep behavior is complex and needs further investigation. Longer and uninterrupted creep studies of Alloy 617 in He-0.1ppmO_2 and He-CO/CO_2=1320 would be helpful to better understand the long-term effect of the environment on creep deformation.

4.6.4 Morphology and rate of growth of Cr_2O_3

Morphological differences of the surface oxides formed in the two environments were reported in the results section, supporting earlier observation that chromia scales differ in their protective abilities depending on the gas in which they are grown [87]. In this work, He-≤0.1ppm O_2 (high oxygen partial pressure) produced less porous and continuous surface oxide, while porous, and thicker Cr_2O_3 characterized the surface produced in He-CO/CO_2=1320 (low oxygen partial pressure).

The occurrence of porosity in surface Cr_2O_3 produced in a carburizing/oxidizing environment in the temperature range of 850-1000°C has been reported by Kumar [10, 19]. According to the author, the carburization of the alloy resulted in the formation of discontinuous Cr_7C_3 precipitates over a thin Cr_2O_3 film as the oxide layer kept growing. However, the surface carbide became thermodynamically unstable after the Cr activity fell below a critical value at the alloy/oxide interface, and it dissolved in the oxide to release CO and Cr, the latter of which contributed further to the oxide scale growth. The dissolution of these carbides left voids and pores in the oxide, making the alloy more vulnerable to further environmental attack. Even though no Cr_7C_3 carbides were observed

in the current work, and no carbides were observed within the chromium oxide scale (Figure 4-17), the close gas chemistry between He-CO/CO_2=1320 and that used by Kumar makes it likely that this mechanism could explain the porous nature of Cr_2O_3 formed in He-CO/CO_2=1320.

The growth rate of the oxide could therefore explain the difference in the thickness of the surface oxide scales formed in the two environments. The carburizing/oxidizing environment produced thicker Cr_2O_3 scales. It is generally agreed that Cr_2O_3 surface scale grows in the outward direction [82, 83]. The mechanism of Cr_2O_3 formation has been shown to vary, however, depending on the ambient oxygen partial pressure, which determines the species accounting for the chromium transport in the oxide scale. According to Atkinson and Taylor [88], Cr vacancies and Cr interstitials are the primary mobile species in high and low oxygen partial pressure environments, respectively. This means that Cr vacancies are expected to be the primary mobile species in the oxidizing environment (He-$\leq$0.1ppm O_2), while Cr interstitials will be dominant in the carburizing/oxidizing environment (He-CO/CO_2=1320) used in this work. Gulsoy [89] further established that the self-diffusion coefficient of Cr in Cr_2O_3 based on the measured surface oxidation rates of Alloy 617 in He-CO-CO_2 environments was greater for Cr interstitials than for Cr vacancies. The implication of this determination is that the growth rate of Cr_2O_3 is expected to be greater in low oxygen partial pressure environments (in this case, He-CO/CO2=1320) than that observed in high oxygen partial pressure environments (in this case, He-$\leq$0.1ppm O2). Another factor worth mentioning is that as established by Wagner [90] the growth rate of Cr_2O_3 has been shown to be dependent on the ambient oxygen partial pressure when vacancy diffusion is dominant, whereas it is dependent on the oxygen partial pressure at the alloy/oxide interface when interstitial diffusion is dominant. Considering that the Cr_2O_3 scale has been shown to be inherently permeable to molecular oxidants [13, 47], and, as stated above, that the growth by interstitial diffusion is a function of the oxygen partial pressure in the alloy/oxide interface, it is reasonable that Cr_2O_3 scale observed in He-CO/CO_2=1320 would be thicker.

4.6.5 Evaluation of a stepwise mechanism of oxidation of previously-formed carbides

As seen earlier, the oxidation and growth of Cr_2O_3 is a function of partial pressure of oxygen in the environment. Also, it appears that the carburizing potential of an environment causes case hardening of the alloy surface and rendered it susceptible to cracking, thereby exposing fresh surface to the oxidation potential of the environment. It also has been shown that the near-surface damage on Alloy 617 was significantly more severe (deeper intrusions and thicker surface scale) in He-CO/CO_2=1320 than in He-≤0.1ppm O_2. It is possible that the environmental damage is accelerated by the presence of carbon – in addition to oxygen – in the He-CO/CO_2=1320, compared to only oxygen in the He-≤0.1ppm O_2. The faster diffusion of carbon compared to oxygen can explain why the grain boundary intrusions are deeper in a carburizing/oxidizing environment than in an oxidizing-only environment. Schnaas [42] observed how a Ni-Cr-Fe alloy suffered preferential grain boundary attack as a result of carbon-bearing element penetration and formation of internal carbides along the grain boundaries. He posited that these carbides can subsequently be selectively oxidized. In this section, the morphology of surface corrosion product and the cross-section of Alloy 617 are characterized after creep in He-600 ppm CH_4 (expected to be only carburizing) and also after subsequent creep in He-≤0.1ppm O_2 (an oxidizing only environment), where it is hypothesized that carbides would form and be oxidized, respectively. Since it has been established earlier that the nature of loading (static vs. cyclic) did not affect the type of oxide morphology, the studies here were conducted under static loading (50 MPa). The total time after exposure (250 h) in the two environments was set to be similar to the total time under static loadings for the previous environments in Table 4-1.

The morphology of the surface corrosion product developed after 137 h of creep in He-600ppm CH_4 consisted of dark and bright isolated surface features (Figure 4-21a,b), and the surface layer was not of nodular type as seen in He-≤0.1ppm O_2 (Figure 4-2d), nor smooth (non-nodular) as seen in He-CO/CO_2=1320 (Figure 4-4a). No spallation was apparent on the surface of the alloy, and, like in the He-CO/CO_2=1320 environment, there was no indication of thick oxide ridges along the slightly-cracked grain boundaries (Figure 4-21c). However, the surface of Alloy 617 crept in He-600ppm

CH_4 for 137 h and subsequently in He-≤0.1ppm O_2 for 113 h revealed a different morphology. A survey of the surface shows clearly demarcated grain boundaries (Figure 4-22a,b), and also that the morphology of the surface corrosion product has evolved from the isolated features seen in Figure 4-21 into needle-shaped features underneath a smooth layer similarly to what was observed in He-CO/CO_2=1320. Figure 4-22c shows some openings on the surface of the alloy where one can observe development of plate-like features, but around which the layer seems to be coalescing into a relatively smoother upper layer.

FIB cross-sections of Alloy 617 crept in He-600ppm CH_4 (Figure 4-23) and in He-600ppm CH_4 + He-≤0.1ppm O_2 (Figure 4-24) are shown tilted to 45° to reveal the morphology of the surface corrosion product and the cross-sections. A deposited platinum layer protected the surface corrosion product during the FIB milling process used to reveal the cross-section. The surface oxide (revealed as rich in Cr and O by EDS) is seen in Figure 4-23b-d as a discontinuous scale. The grain boundary opening seen on the surface is shown on the cross-sectional view to penetrate into the alloy (Figure 4-23c). The grain boundary intrusion shows the beginning of development of finger-like growth of oxide on the walls of the separated grains. In this He-600ppm CH_4 environment, where carburization was expected to occur, the surface scale is rich in oxygen and not in carbon. After the introduction of an oxidizing environment, the cross-sectional surface oxide (Figure 4-24) is more continuous than in the He-600ppmCH_4. Also, the grain boundary opening on the surface penetrates deeper into the alloy than before. The grain boundary and surface oxides now appear to be porous, blocky, coarse-grained, and plate-like, similar to the observations made in He-CO/CO_2=1320 environment (Figure 4-15). These observations show the likelihood of a stepwise mechanism of carbides forming prior to their oxidation.

Bulk X-Ray diffractometry in Figure 4-16 shows that the exposure of the alloy for 137h in He-600ppm CH_4 (Figure 4-16f) forms low-intensity peaks of Cr_2O_3, and an extra 113h in He-≤0.1ppm O_2 (Figure 4-16g) doesn't change the peak heights significantly. After 137h in He-600ppm CH_4, and further 113h in He-≤0.1ppm O_2, the main corrosion product is Cr_2O_3 with peak intensities comparable to what is formed after 211h in He-≤0.1ppm O_2 (Figure 4-16b), but not to 206h in He-CO/CO_2=1320 (Figure 4-16d).

Grazing incidence X-Ray diffractometry shows that the surface corrosion product in He-600ppm CH_4 (Figure 4-17e) is Cr_2O_3, even though the signals are weaker than in He-0.1ppmO_2 (Figure 4-17a,b).

According to Auger depth profiles, the surface oxide formed after exposure to He-600ppm CH_4 and then to He-$\leq$0.1ppm O_2 (Figure 4-18c) required the same sputtering time as that one formed in He-0.1ppm O_2 (Figure 4-18a), and not as the one in He-CO/CO_2=1320 (Figure 4-18b). This is surprising since Figure 4-18b and Figure 4-18c are profiles of oxides that were shown to have similar morphologies (Figure 4-15 and Figure 4-24). Figure 4-18d shows the profile of the surface oxide in He-600ppm CH_4 where Cr_2O_3 has not developed yet.

Even though the morphology of the oxide formed here on the surface of Alloy 617 resembles slightly that formed in the He-CO/CO_2=1320, it appears that the extent of grain boundary damage is not similar to that seen in the He-CO/CO_2=1320. The environments used in the literature to provide carburizing environments are either carburizing/reducing (CH_4-H_2, [42, 91]) or carburizing (He-CH_4, [12, 85]). To understand the mechanism of formation of Cr_2O_3 in the He-CO/CO2=1320 (carburizing/oxidizing), it was deemed better to avoid a reducing environment (CH_4-H_2), which would not favor the formation of the protective Cr_2O_3 layer on the alloy surface. The He-CH_4 environment, while not reducing, did not form noticeable carbides as expected. It seems that this environment does not produce carbon easily. According to Christ [35, 92], the decay of CH_4 into C and H_2 is a very slow process, and so this could explain the difficulty of carbide precipitation. Even though the reaction is supposed to produce a high carbon activity, no carbon on the surface was detected nor any carburization observed in the matrix. This is consistent with the observations made in this dissertation, where no carburization occurred at the test conditions imposed here. For this reason, it cannot be conclusively determined whether the damage in He-CO/CO_2=1320 follows a stepwise process of carbide formation prior to their oxidation.

4.7 Summary

Exposure to oxidizing and carburizing/oxidizing helium environments during interrupted creep enhanced different modes of damage accumulation in the surface and near-surface regions of Alloy 617. While the alloy suffered surface oxidation and internal

oxidation in both environments, crack depth and frequency were more extensive in the carburizing/oxidizing environment. This damage accumulation was attributed to the synergy existing between stress and chemistry of the gas environments that affected the extent of surface damage accumulation of the alloy. It has been shown that the presence of mechanical loads enhances – but is not the cause of – grain boundary attack by the environment, and that cycling the load increases surface damage accumulation. By ensuring that bulk creep deformation was the same in both environments, it was shown that there was no effect of environment on creep deformation and that the environmental damage was limited to the near-surface regions of the alloy (surface and internal oxidation and matrix carburization).

The mechanism of the more damaging environment (He-CO/CO_2=1320) in creep damage accumulation has not been completely understood in terms of oxidation of carbides. However, the existence of different Cr_2O_3 growth rates due to Cr interstitial atoms or Cr vacancies as primary mobile species as a result of low or high oxygen partial pressures in unstressed specimens is confirmed during the application of stress in this work. Also, the carburizing nature of the environment has been shown to cause embrittlement of the near-surface regions of the alloy, which exposes new alloy surfaces and allows for inward oxidation and cracks to take place. The next chapter will examine the protective role of coating layers in mitigating the environmental attack in uncoated 617 during creep deformation.

Table 4-1 Interrupted creep behavior of Alloy 617 at 800°C in oxidizing and carburizing/slightly oxidizing helium environments.

Environment	Load	Strain (%)	Minimum Creep Rate (10^{-8}/s)	Test Time (h)
He - ≤0.1ppm O_2	Static (50 MPa)	1.9	1.7	211
	Cyclic (10-50 MPa)	2.3	0.94	690
He–CO/ CO_2=1320	Static (50 MPa)	1.7	1.3	206
	Cyclic (10-50 MPa)	2.1	1.4	553

Table 4-2 Quantification of surface damage in Alloy 617 crept at 800°C in oxidizing and carburizing/oxidizing helium environments.

Environment	Load	Test Time (h)	Strain (%)	Number of grain boundary intrusions[7]	Average intrusion depth (μm)	Average oxide thickness (μm)
He - ≤0.1ppm O_2	Static (50 MPa)	211	1.9	6	7.5 ± 2.4	1.0 ± 0.3
	Cyclic (10-50 MPa)	690	2.3	34	13.8 ± 6.4	1.3 ± 0.3
He–CO/ CO_2=1320	Static (50 MPa)	206	1.7	31	34.3 ± 21.9	2.0 ± 0.4
	Cyclic (10-50 MPa)	553	2.1	45	48.9 ± 14.1	3.5 ± 0.4

[7] Counts per 6mm of specimen gauge length.

Table 4-3 Effect of surface cracks on the load-bearing area for static and cyclic loading in He-≤0.1ppm O_2 and He-CO/CO_2=1320 environments.

		Load-Bearing Area			
	Intrusion Depth (μm)	Length (μm)	Width (μm)	Area (μm^2)	Area (%)
Original Specimen Dimensions	N/A	3000	2000	6000000	100
50 MPa He-≤0.1ppm O_2	15	2985	1985	5925225	98.8
10/50 MPa He-≤0.1ppm O_2	28	2972	1972	5860784	97.7
50 MPa He-CO/CO_2=1320	60	2932	1932	5664624	94.4
10/50 MPa He-CO/CO_2=1320	100	2900	1900	5510000	91.8

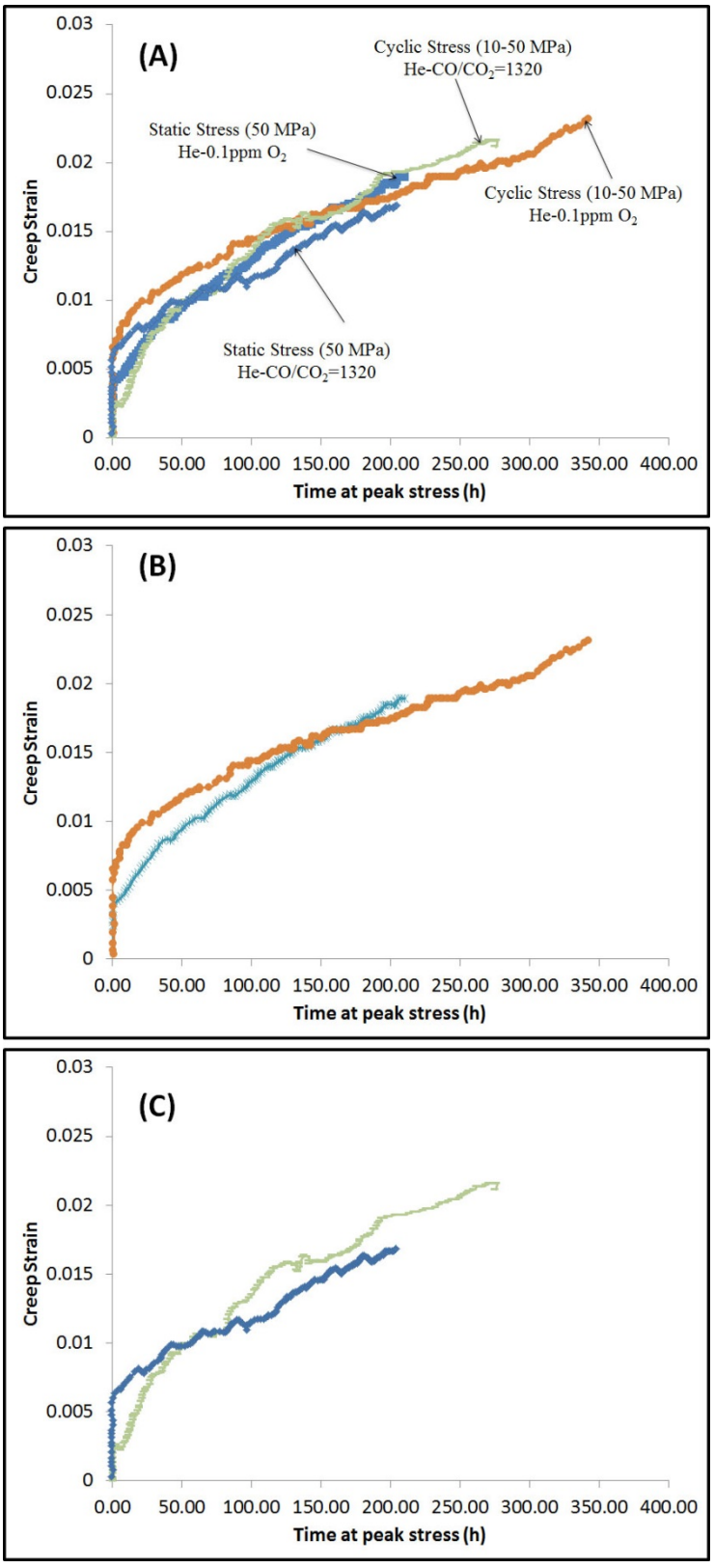

Figure 4-1 Interrupted static and cyclic creep behavior at 800°C of Alloy 617 in (A) all environments, (B) He-≤0.1ppm O_2, and (C) He-CO/CO_2=1320.

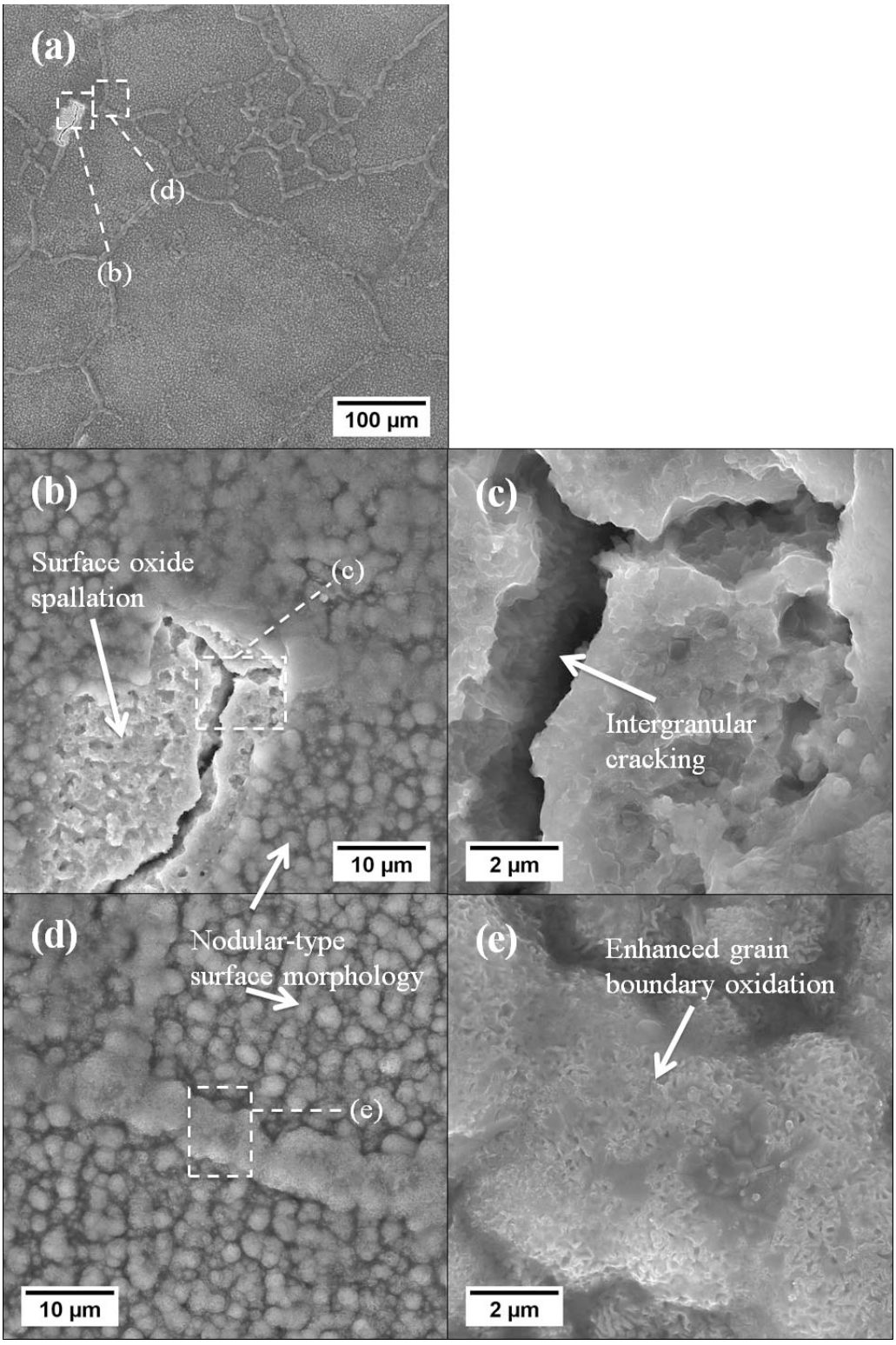

Figure 4-2 SEM micrographs of the surface morphology of Alloy 617 crept at 800°C in an oxidizing environment (He-≤0.1ppm O_2). The stress/strain/time-at-peak-stress conditions are 50MPa/1.9%/211h. The stress axis is vertical and in the plane of the page.

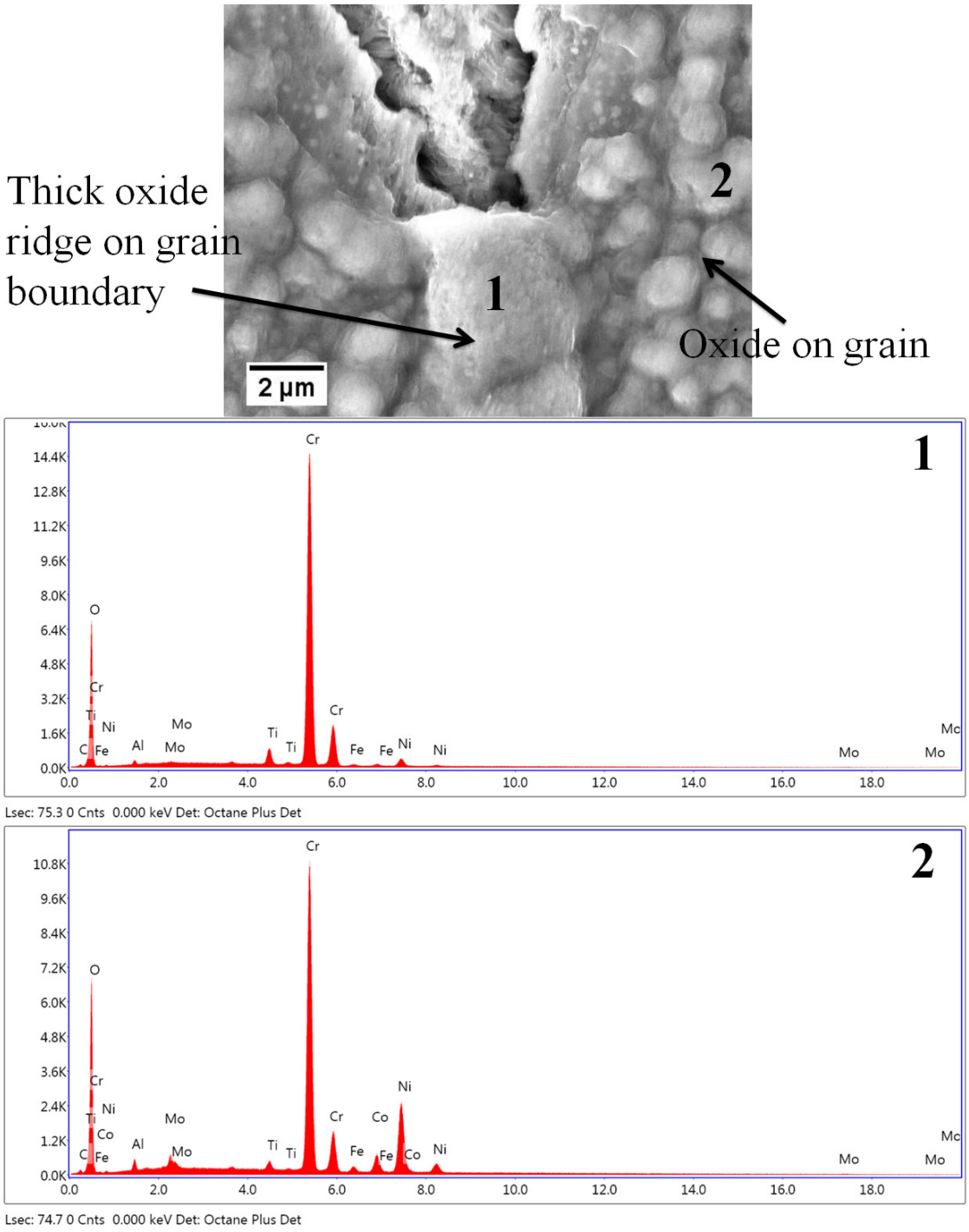

Figure 4-3 Similarity in EDS composition of oxide (rich in Cr and O) located along grain boundary and grain formed on Alloy 617 crept at 800°C in an oxidizing environment (He-≤0.1ppm O_2). The stress/strain/time-at-peak-stress conditions are 50MPa/1.9%/211h.

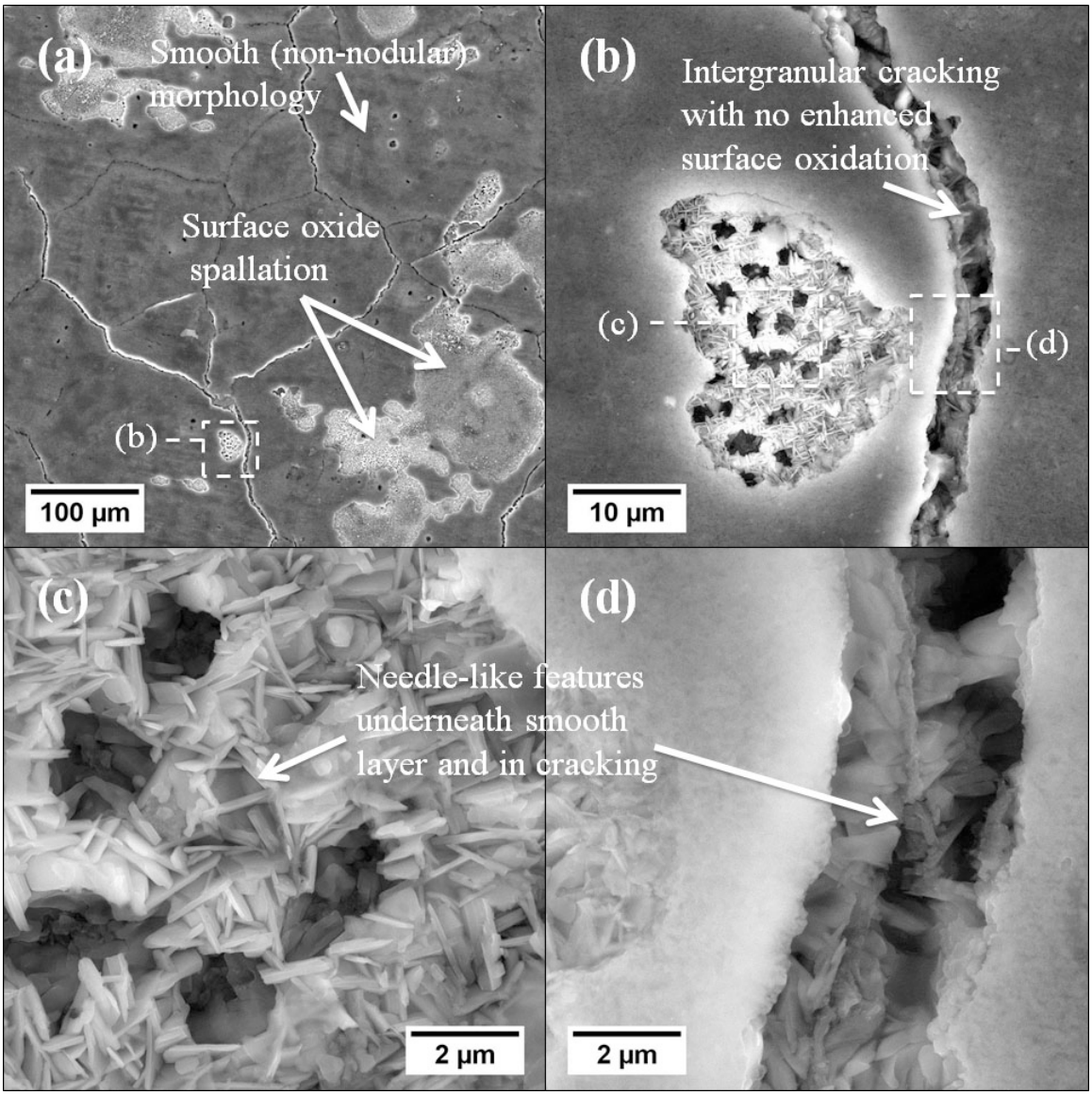

Figure 4-4 SEM micrographs of the surface morphology of Alloy 617 crept at 800°C in a carburizing/slightly oxidizing environment (He-CO/CO_2=1320). The stress/strain/time-at-peak-stress conditions are 50MPa/1.7%/206h. The stress axis is vertical and in the plane of the page.

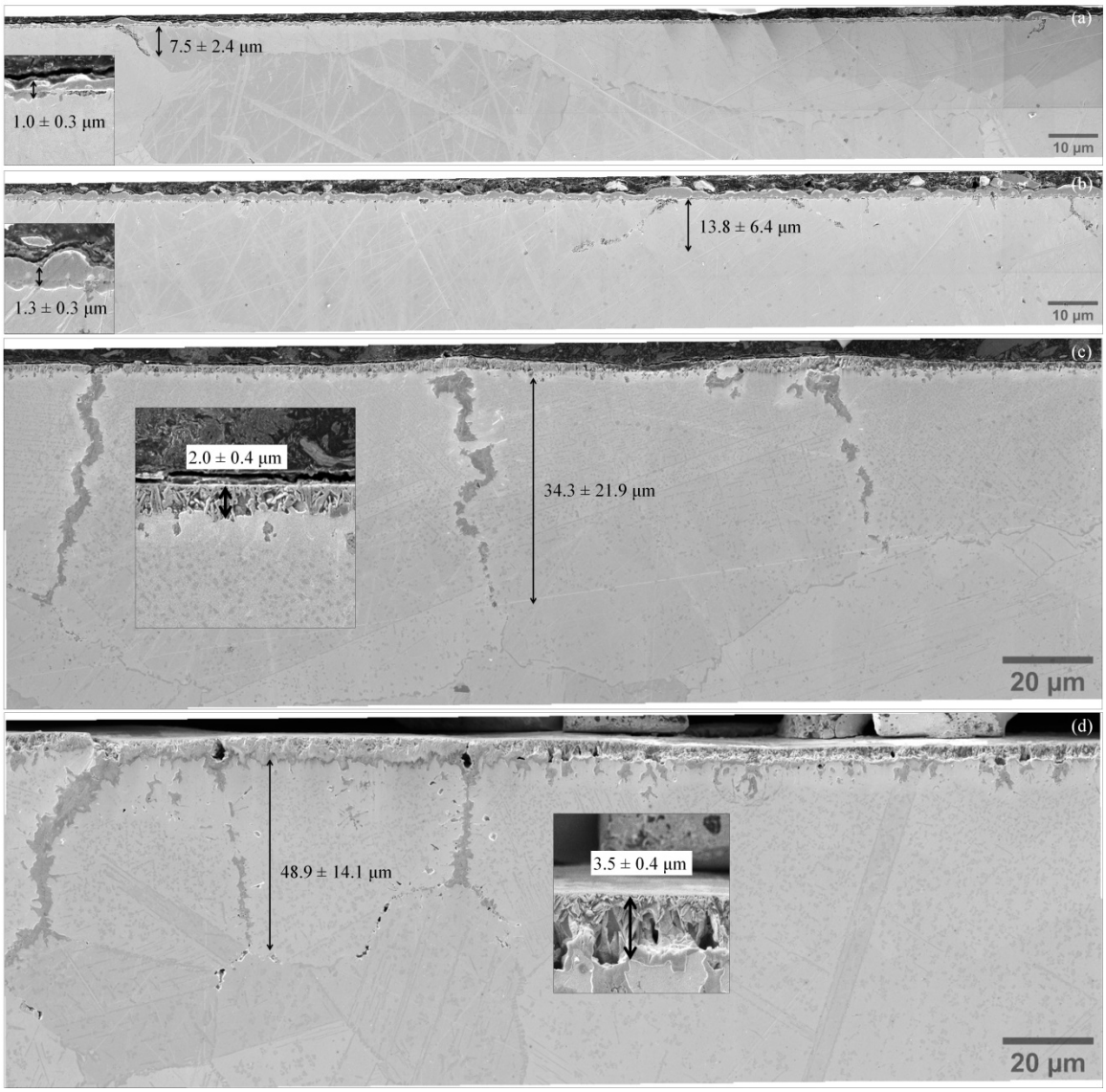

Figure 4-5 SEM images comparing the surface damage in Alloy 617 crept at 800°C in different environments and loading types. The images show the effect on the surface scale thickness and depth of intrusions of the different stress/strain/total test time conditions: (a) 50 MPa/1.9%/211 h, (b) 10/50 MPa/2.3%/690 h, (c) 50 MPa/1.7%/206 h, and (d) 10/50 MPa/2.1%/553 h. The studies were conducted in He-≤0.1ppm O_2 (a,b) and He-CO/CO_2=1320 (c,d) environments. The stress axis is horizontal and in the plane of the page.

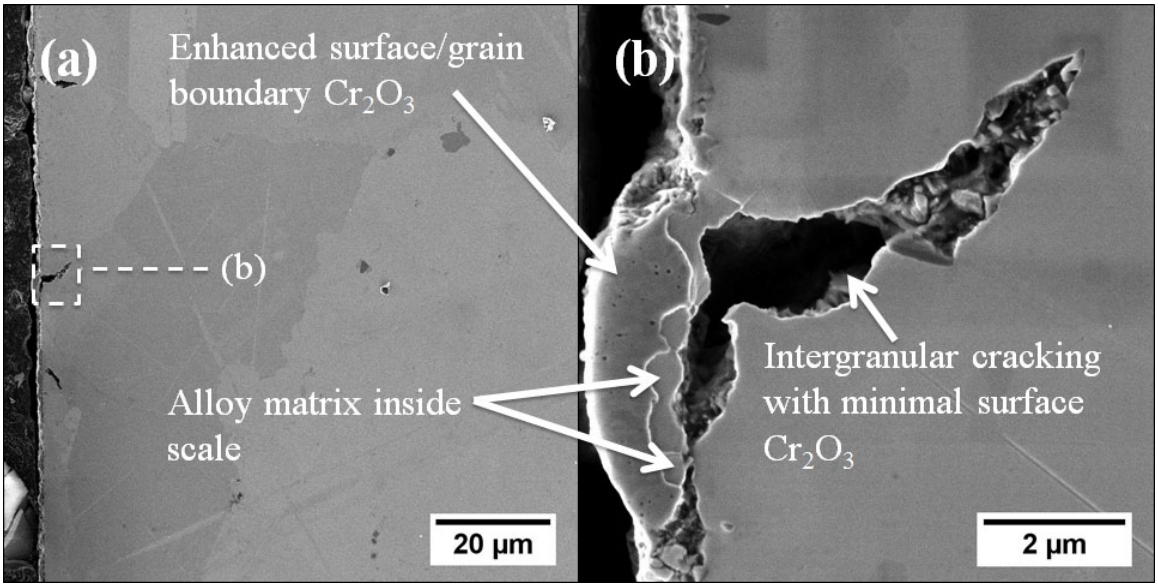

Figure 4-6 SEM micrographs of cross-sections of Alloy 617 crept at 800°C in an oxidizing environment (He-≤0.1ppm O_2), showing surface scale and grain boundary cracks. The stress/strain/time-at-peak-stress conditions are 50MPa/1.9%/211h. The stress axis is vertical and in the plane of the page.

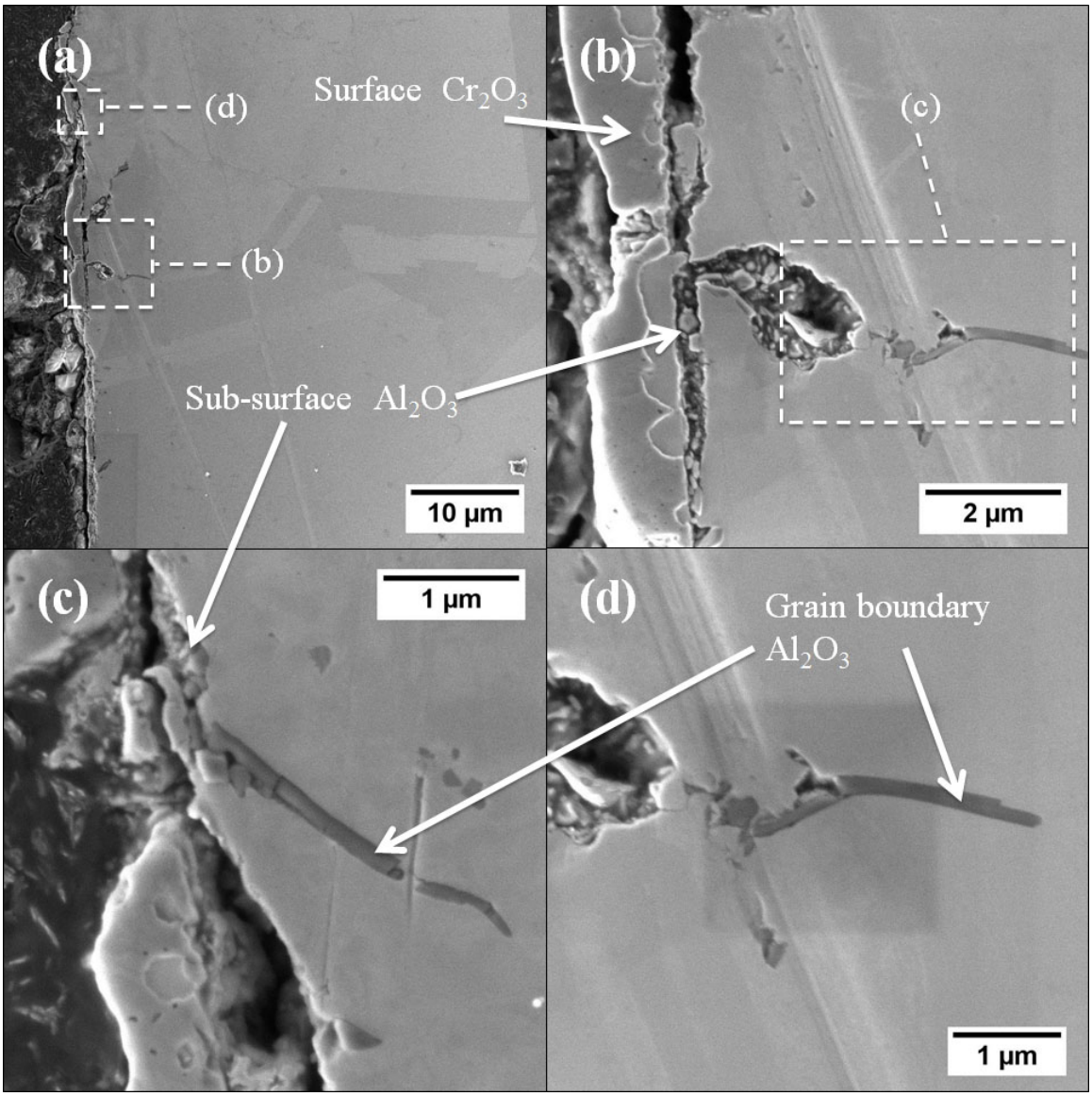

Figure 4-7 SEM micrographs of cross-sections of Alloy 617 crept at 800°C in an oxidizing environment (He-≤0.1ppm O_2), showing surface scale and internal oxidation along grain boundaries. The stress/strain/time-at-peak-stress conditions are 50MPa/1.9%/211h. The stress axis is vertical and in the plane of the page.

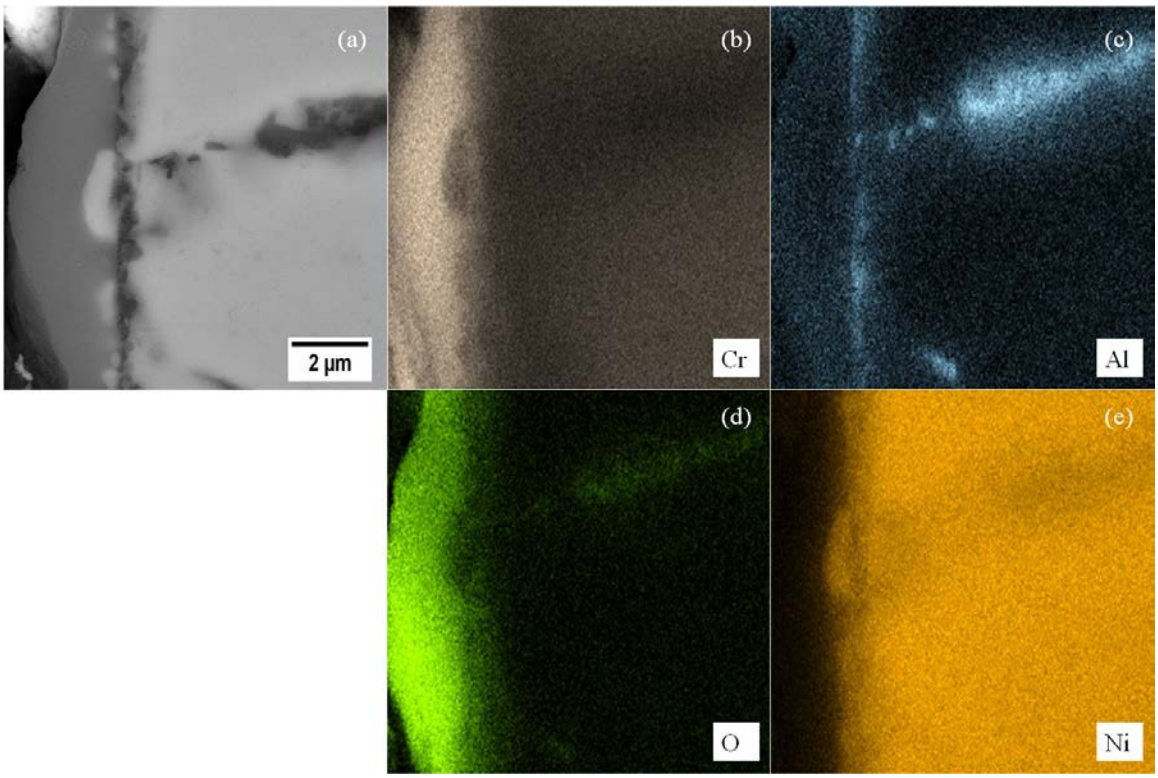

Figure 4-8 EDS maps of cross-sections of Alloy 617 crept at 800°C in an oxidizing environment (He-≤0.1ppm O_2), showing chromia surface scale and internal alumina. The stress/strain/time-at-peak-stress conditions are 50MPa/1.9%/211h. The stress axis is vertical and in the plane of the page.

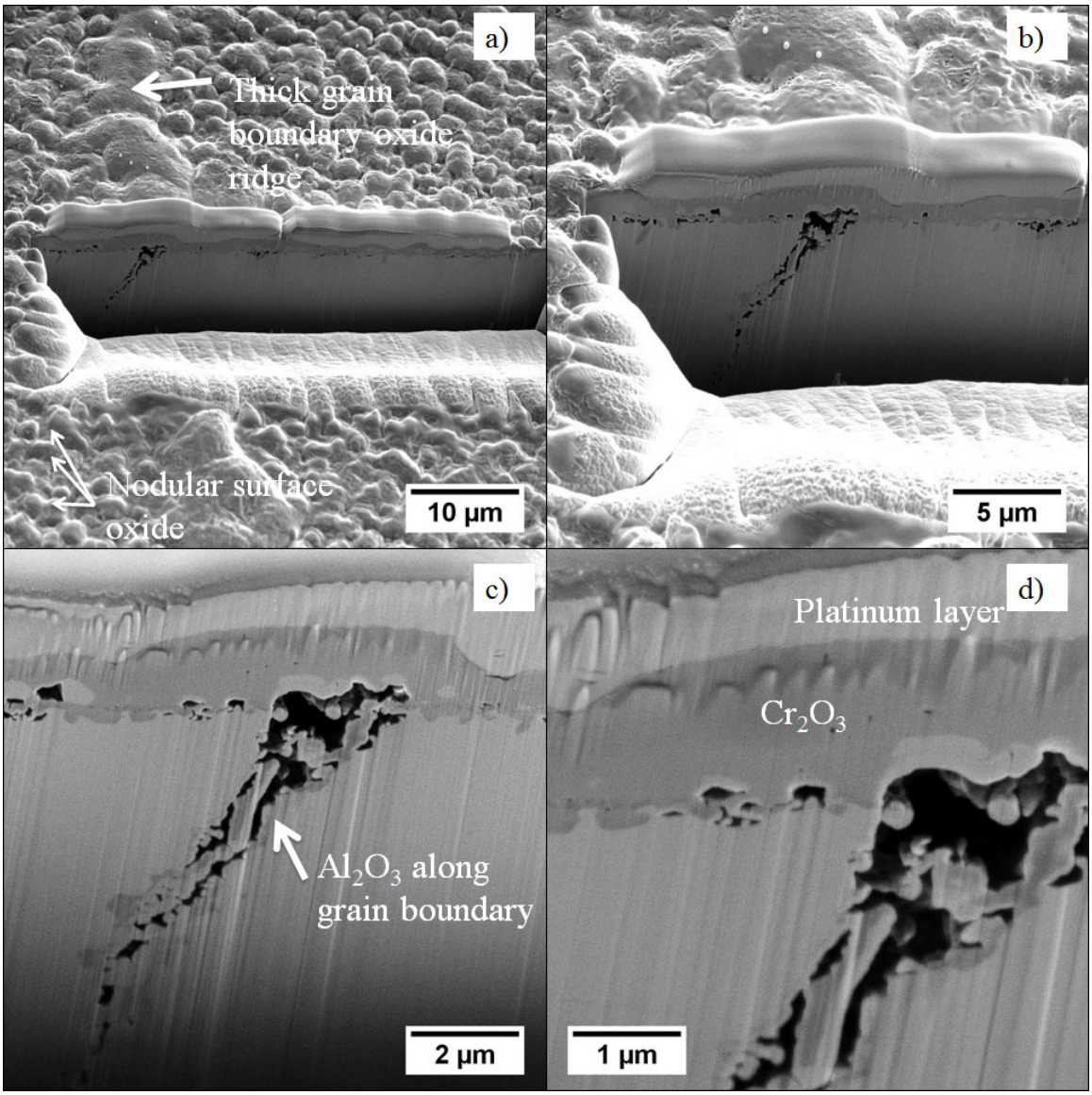

Figure 4-9 SEM images of a cross-section made in the FIB of Alloy 617 crept at 800°C in an oxidizing environment (He-≤0.1ppm O_2), showing surface scale and internal oxidation along grain boundaries. The stress/strain/time-at-peak-stress conditions are 50MPa/1.9%/211h. The stress axis is horizontal.

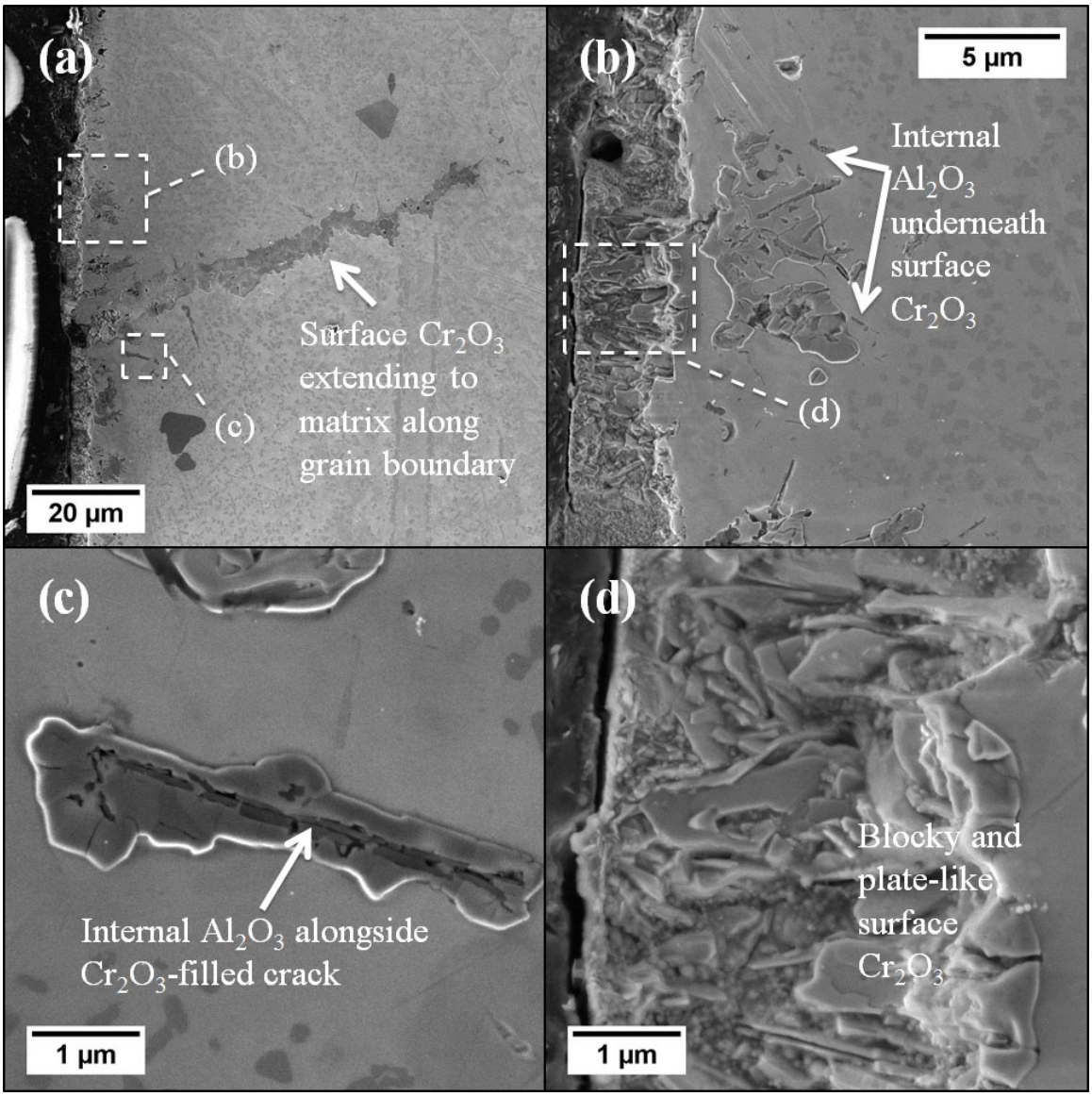

Figure 4-10 SEM micrographs of cross-sections of Alloy 617 crept at 800°C in a carburizing/slightly oxidizing environment (He-CO/CO_2=1320), showing significant crack penetration alongside alumina formation. The stress/strain/time-at-peak-stress conditions are 50MPa/1.7%/206h. The stress axis is vertical and in the plane of the page.

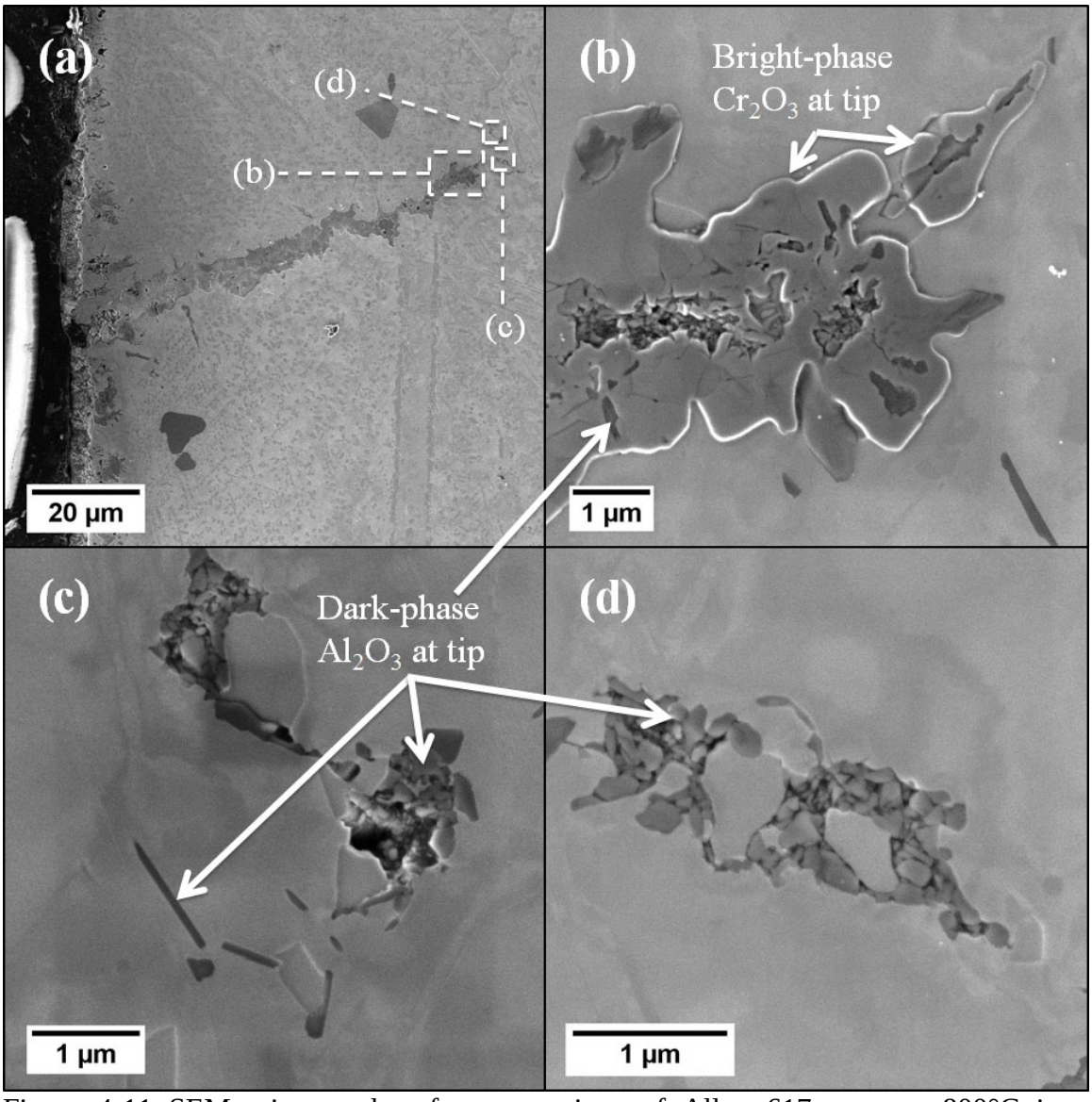

Figure 4-11 SEM micrographs of cross-sections of Alloy 617 crept at 800°C in a carburizing/slightly oxidizing environment (He-CO/CO_2=1320), showing corrosion products at the crack tip. The stress/strain/time-at-peak-stress conditions are 50MPa/1.7%/206h. The stress axis is vertical and in the plane of the page.

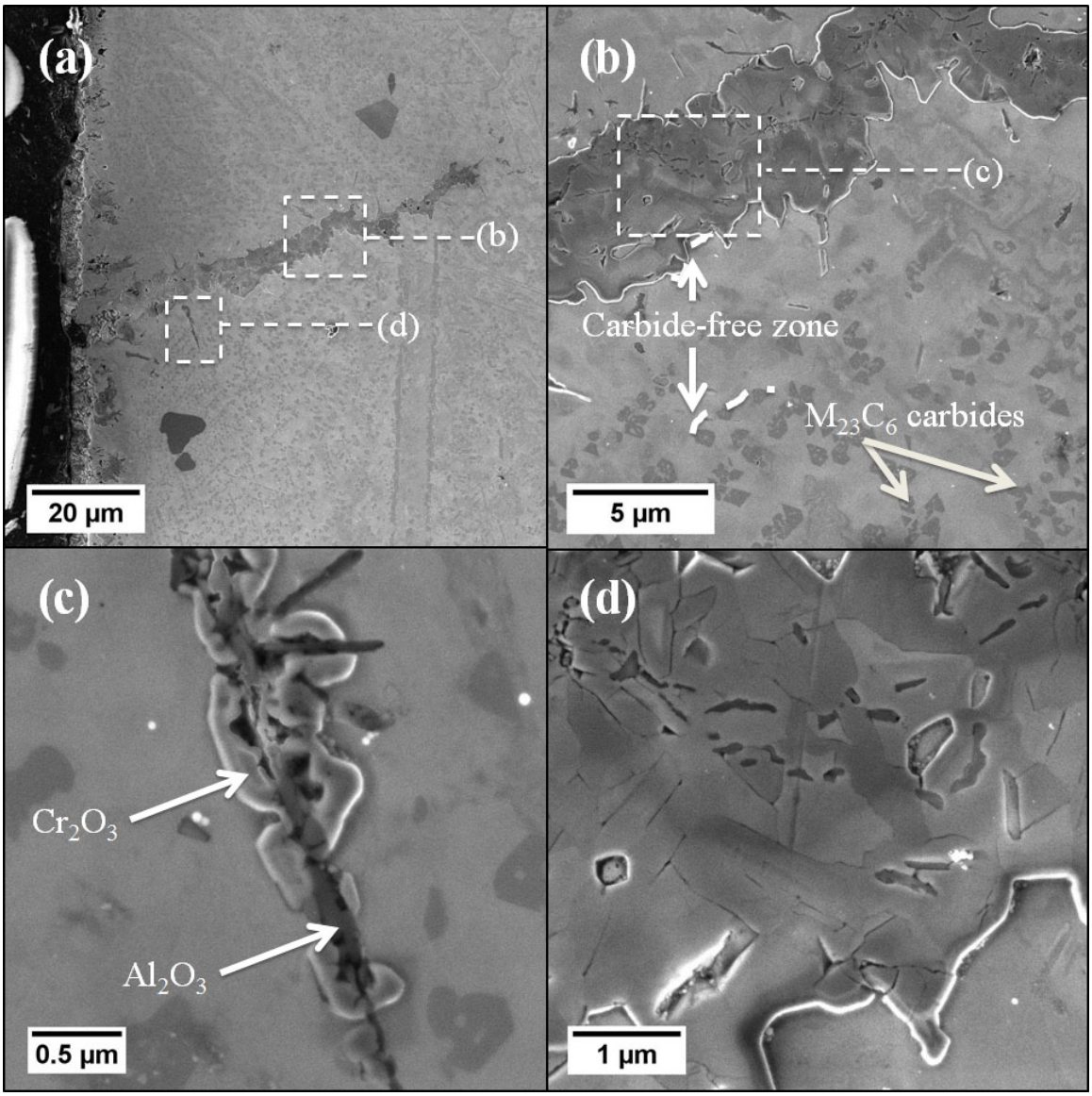

Figure 4-12 SEM micrographs of cross-sections of Alloy 617 crept at 800°C in a carburizing/slightly oxidizing environment (He-CO/CO_2=1320), showing precipitation of carbides and crack formation. The stress/strain/time-at-peak-stress conditions are 50MPa/1.7%/206h. The stress axis is vertical and in the plane of the page.

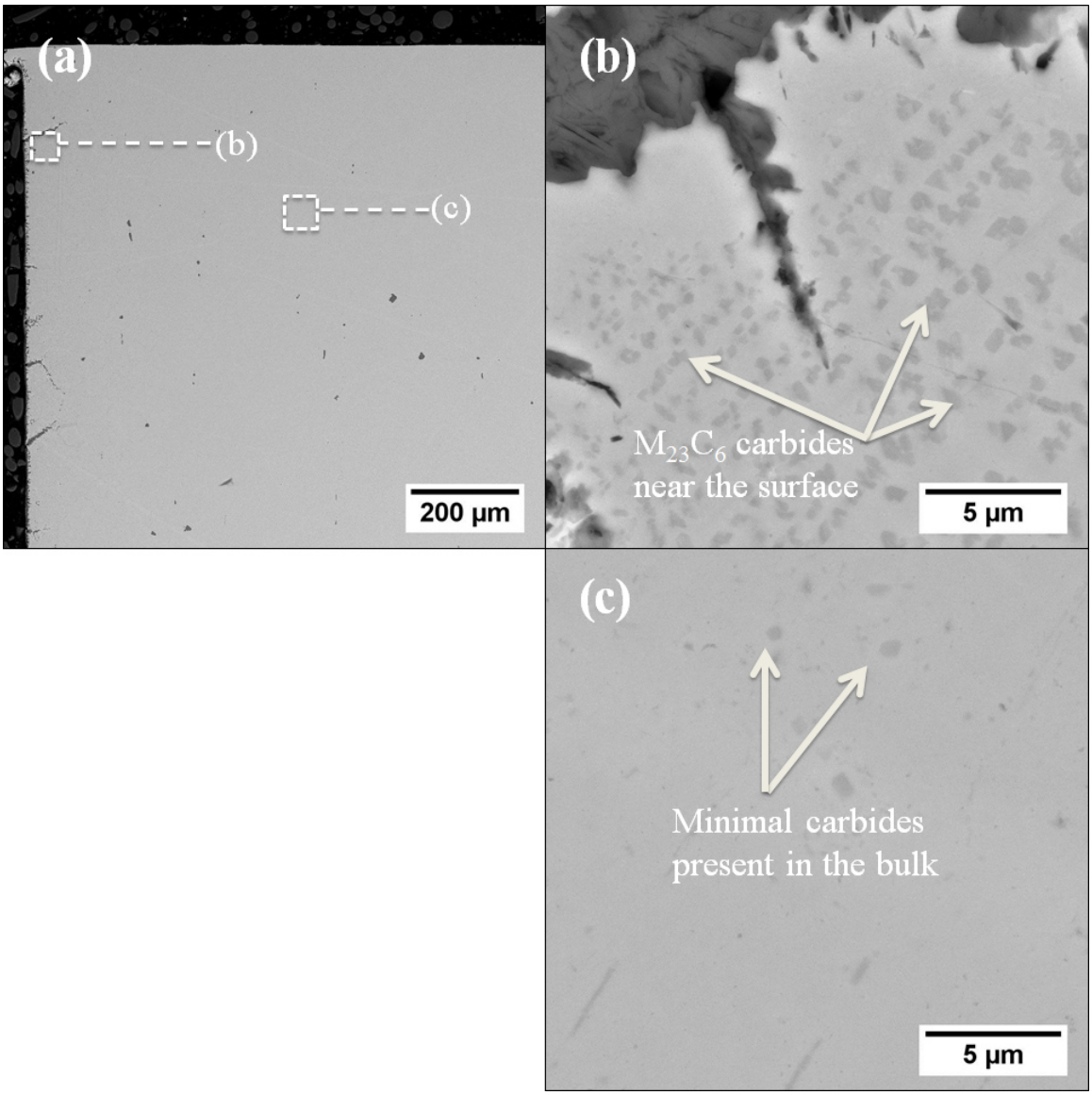

Figure 4-13 SEM micrographs of cross-sections of Alloy 617 crept at 800°C in a carburizing/slightly oxidizing environment (He-CO/CO_2=1320), showing significant carburization effect of environment on near-surface region (b), and absence of carbides in the bulk (c). The stress/strain/time-at-peak-stress conditions are 50MPa/1.7%/206h. The stress axis is vertical and in the plane of the page.

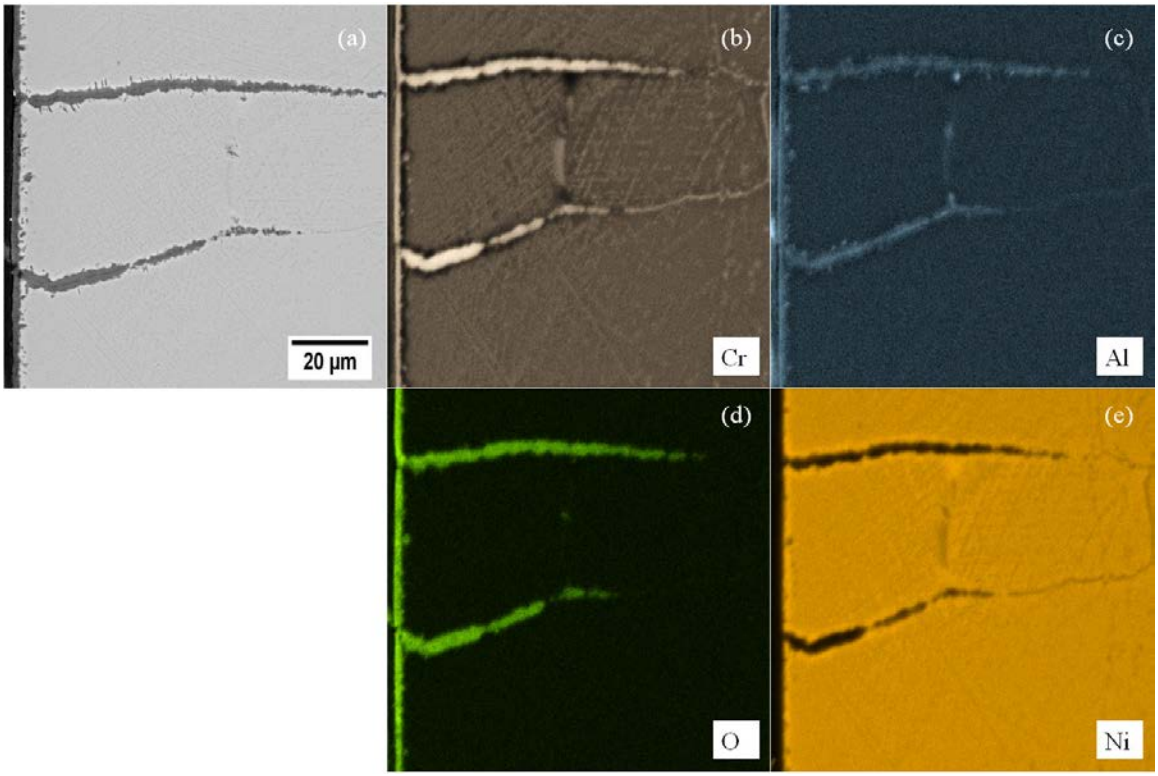

Figure 4-14 EDS maps of cross-sections of Alloy 617 crept at 800°C in a carburizing/slightly oxidizing environment (He-CO/CO_2=1320), showing chromia and alumina within the crack. The stress/strain/time-at-peak-stress conditions are 50MPa/1.7%/206h. The stress axis is vertical and in the plane of the page.

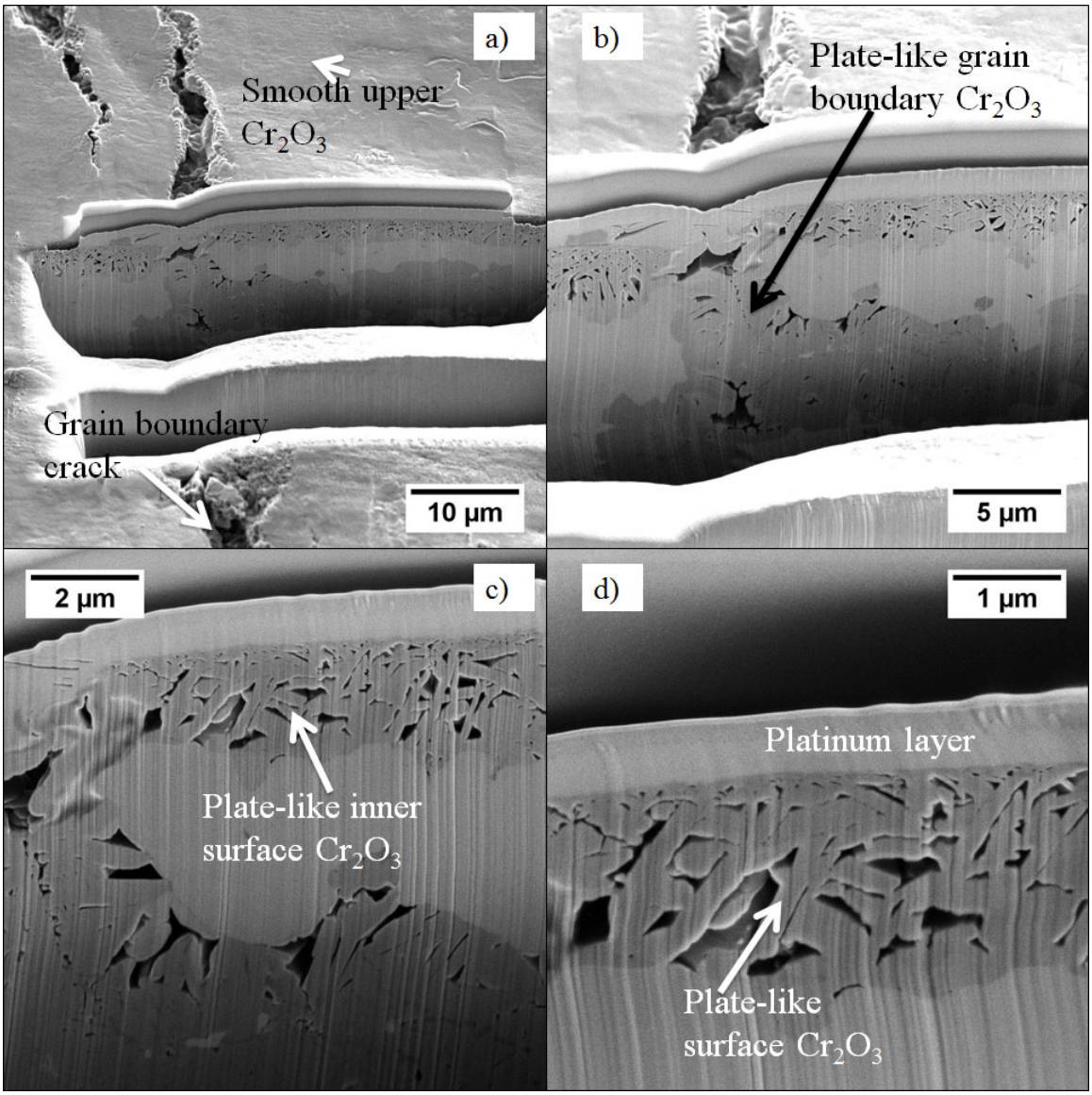

Figure 4-15 SEM images of a cross-section made in the FIB of Alloy 617 crept at 800°C in a carburizing/slightly oxidizing environment (He-CO/CO_2=1320), showing corrosion products at the crack tip. The stress/strain/time-at-peak-stress conditions are 50MPa/1.7%/206h. The stress axis is horizontal.

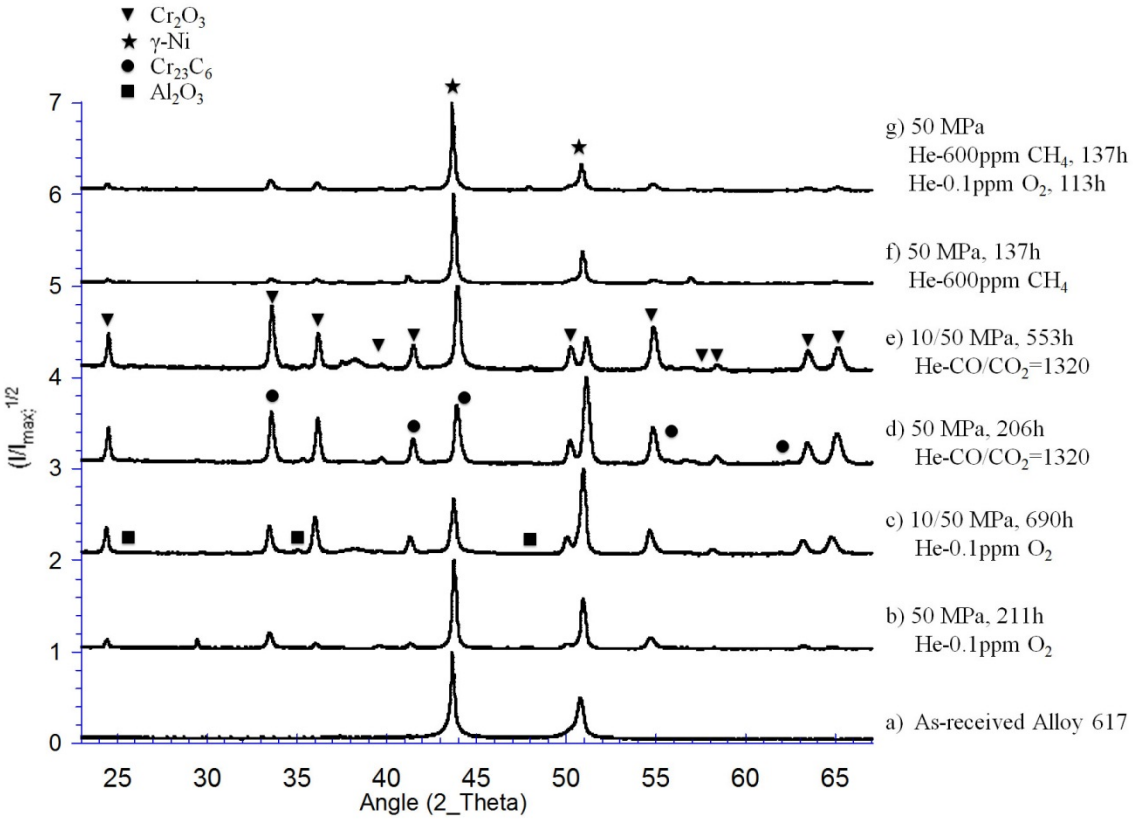

Figure 4-16 X-ray diffraction of Alloy 617 (a) compared with the alloy in different environment and loading conditions (b-g). The durations indicated are total test times.

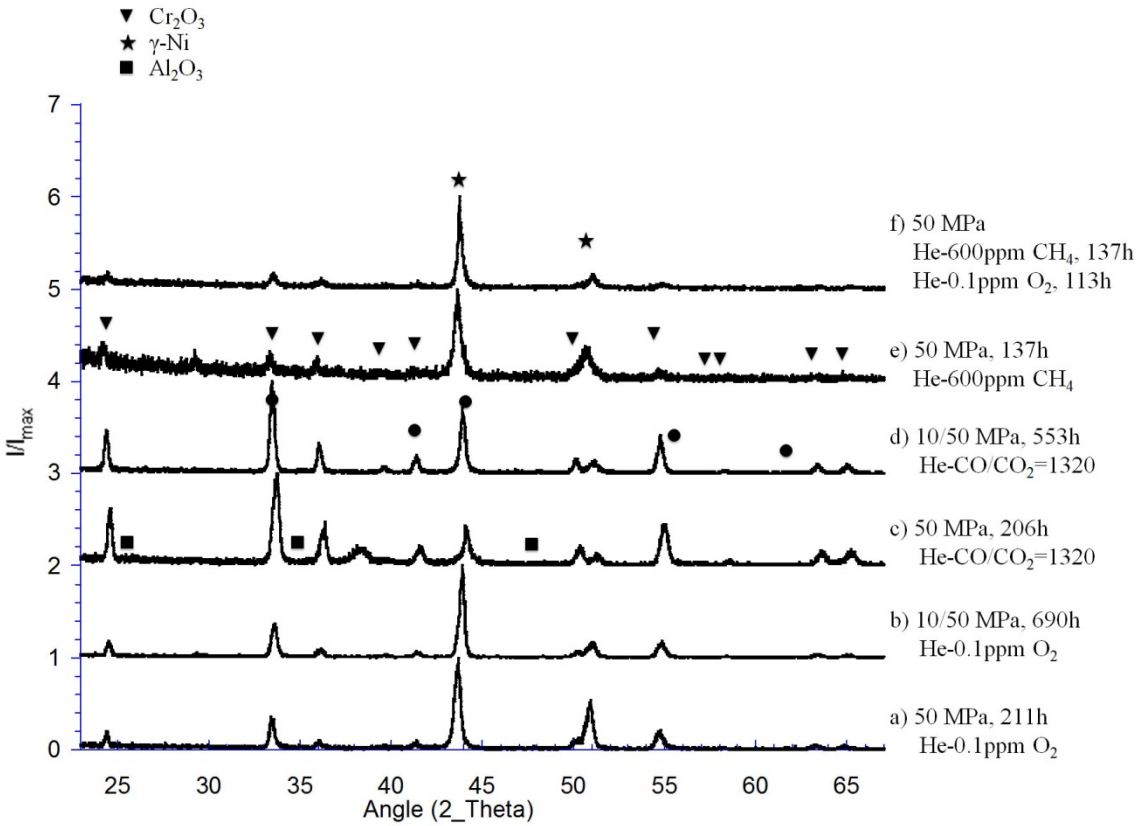

Figure 4-17 Grazing X-ray diffraction of Alloy 617 in different impure He environments and loading conditions (a-f). The incidence angle is 2°. The durations indicated are total test times.

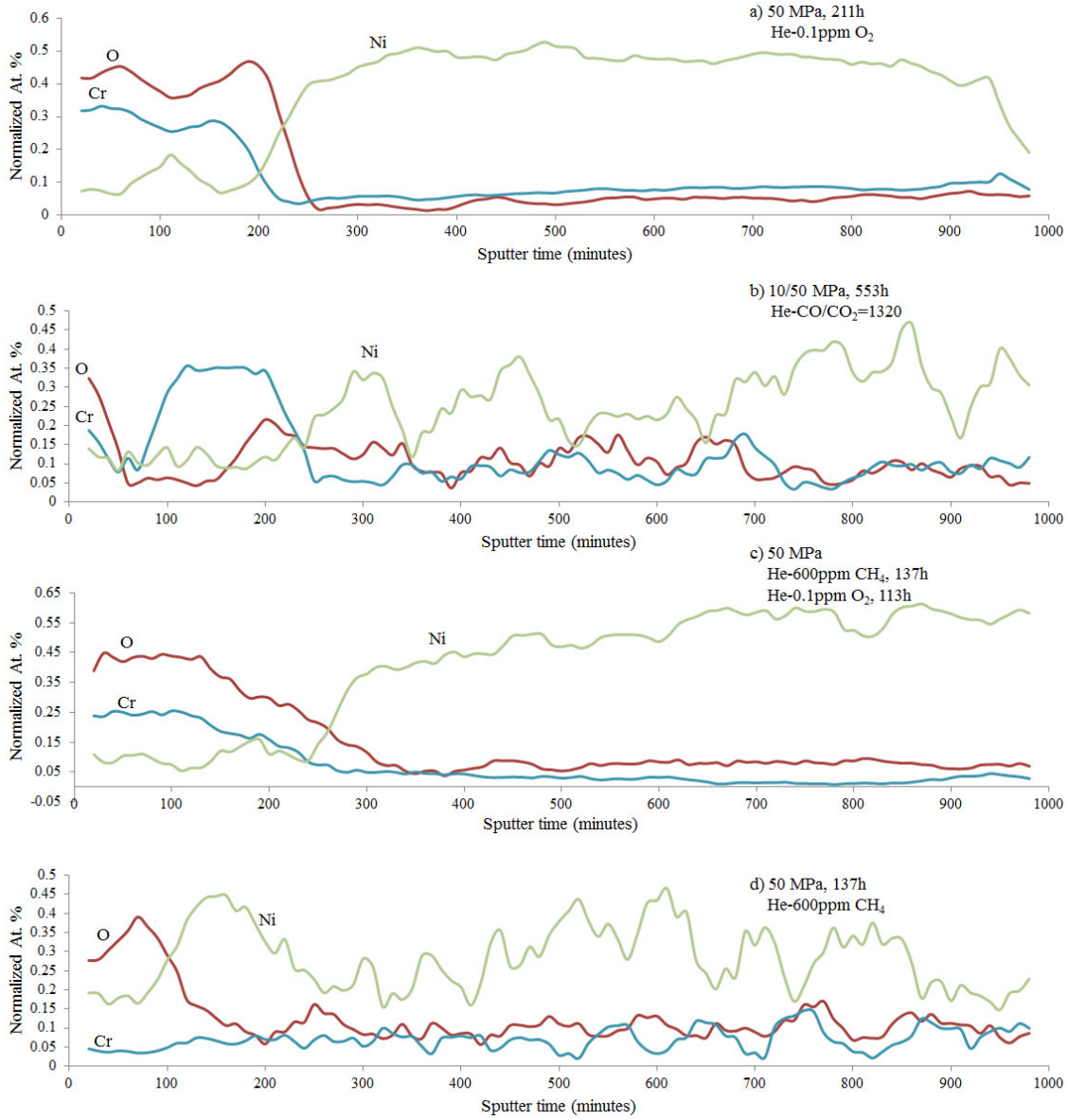

Figure 4-18 Depth profiling of surface oxide on Alloy 617 exposed to (a) oxidizing, (b) carburizing/oxidizing, (c) carburizing then oxidizing, and (d) carburizing. The durations indicated are total test times.

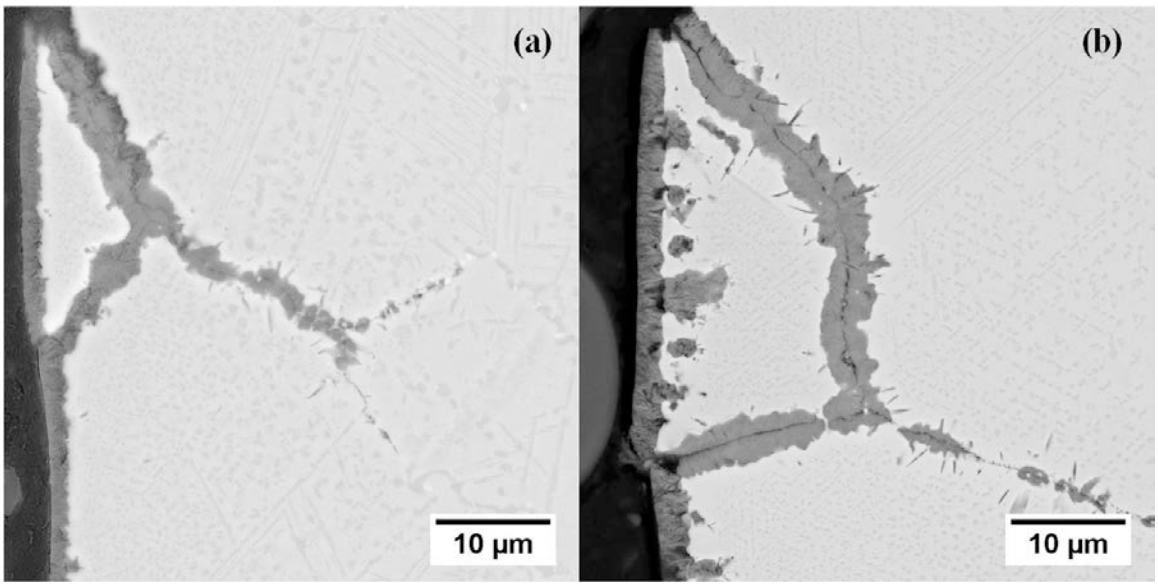

Figure 4-19 BSE micrographs comparing the near-surface damage in Alloy 617 subjected to He-CO/CO_2=1320. The stress/strain/total test time conditions are:(a) 50 MPa/1.7%/206h and (b)0 MPa/0%/308h.

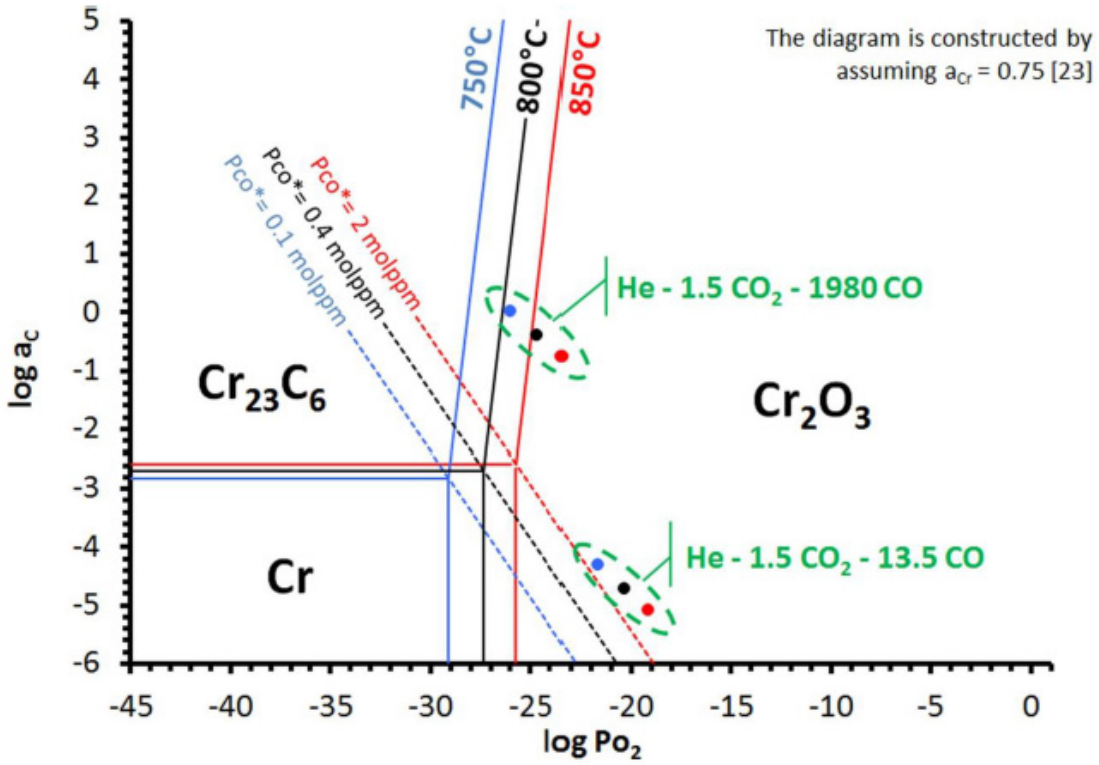

Figure 4-20 A representative Cr-C-O stability diagram taken from Gulsoy [77]. The equilibrium oxygen partial pressure and carbon activities of environments He-≤0.1ppm O_2 (oxygen partial pressure of 10^{-7} atm) and He-CO/CO_2=1320 (oxygen partial pressure of 2.1 x 10^{-25} atm and carbon activity of 0.4) at 800°C indicate the regions of stability of carbide and oxide.

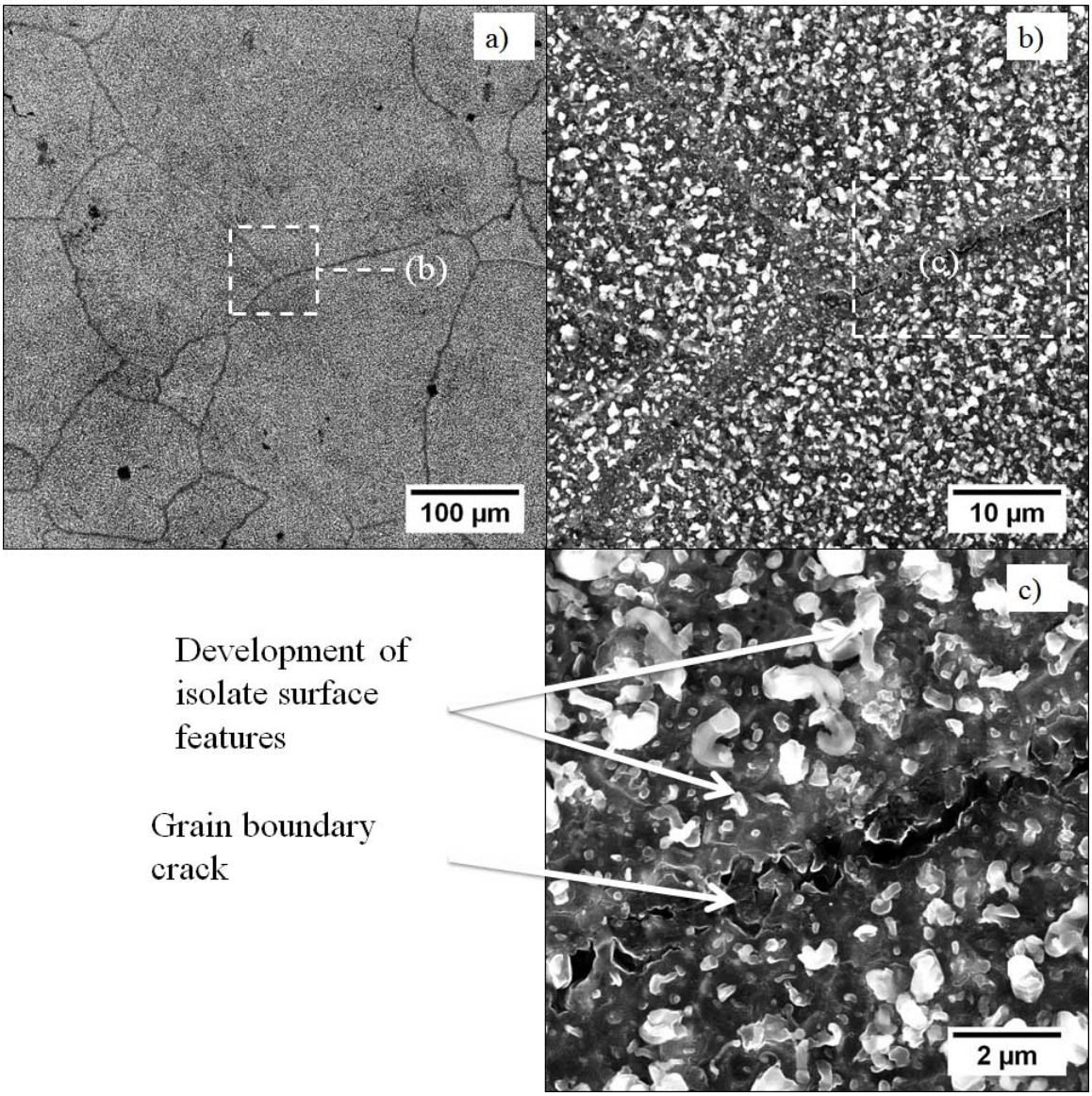

Figure 4-21 SEM micrographs of the surface morphology of Alloy 617 crept (50MPa/137h) at 800°C in He-600ppm CH_4 environment. The stress axis is vertical and in the plane of the page.

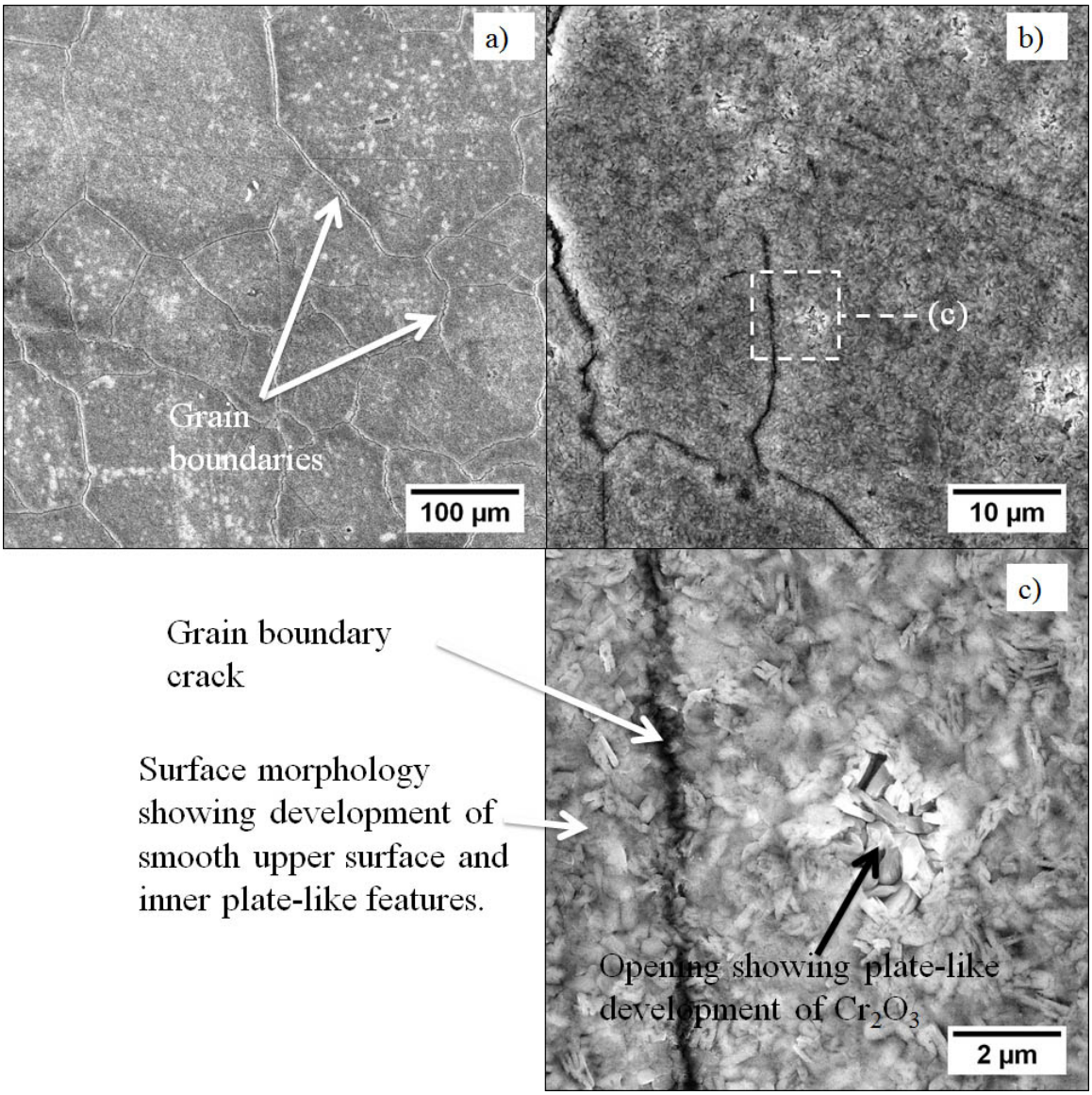

Figure 4-22 SEM micrographs of the surface morphology of Alloy 617 crept at 800°C in He-600ppm CH_4 (50MPa/137h) and subsequently in He-≤0.1ppm O_2 (50MPa/113h) environments. The stress axis is vertical and in the plane of the page.

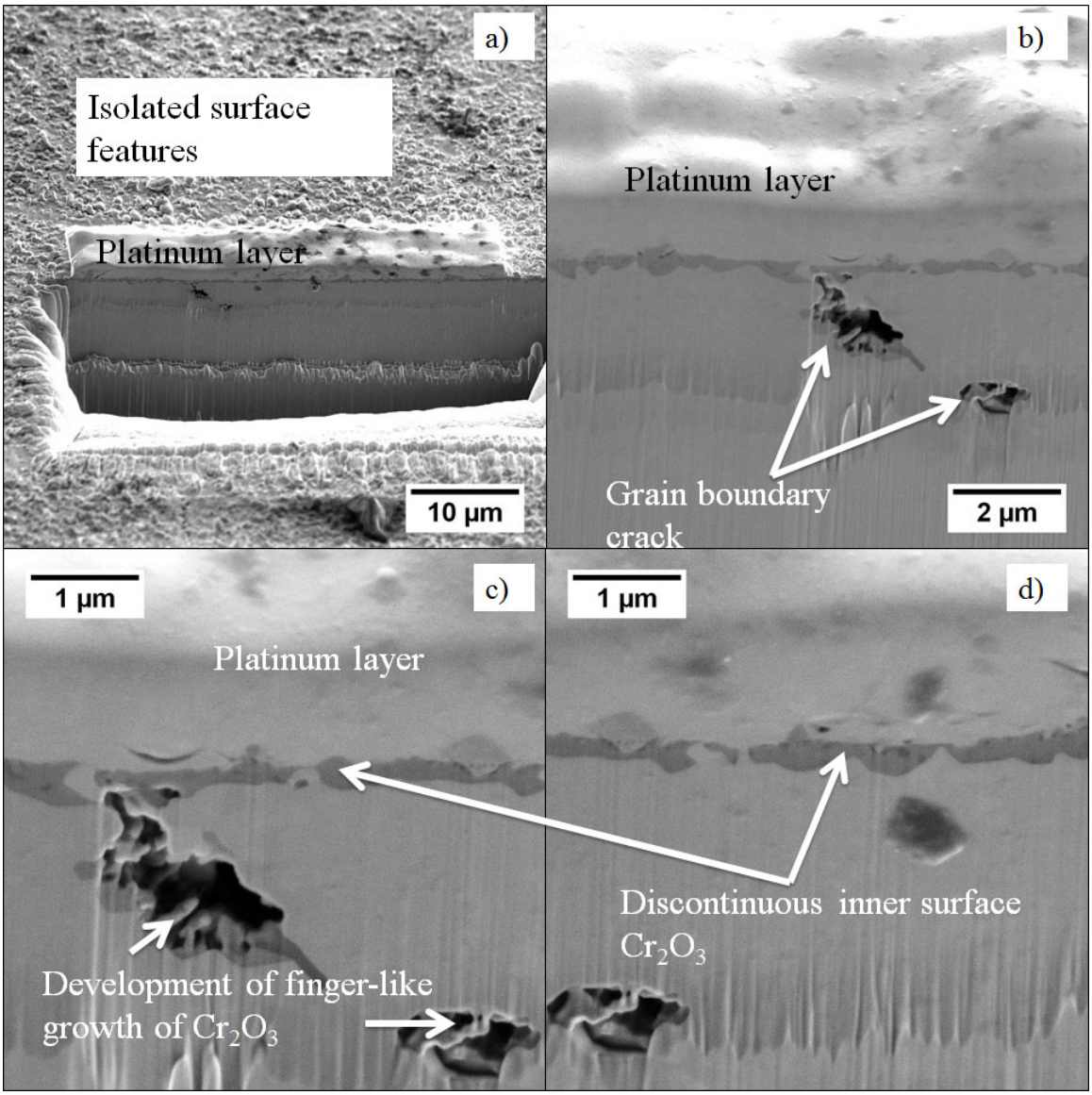

Figure 4-23 SEM images of a cross-section made in the FIB of Alloy 617 crept at 800°C in He-600ppm CH_4 (50MPa/137h) environment. Cr_2O_3 starts to develop in a finger-like manner within the crack (c), and as a discontinuous surface oxide (d).

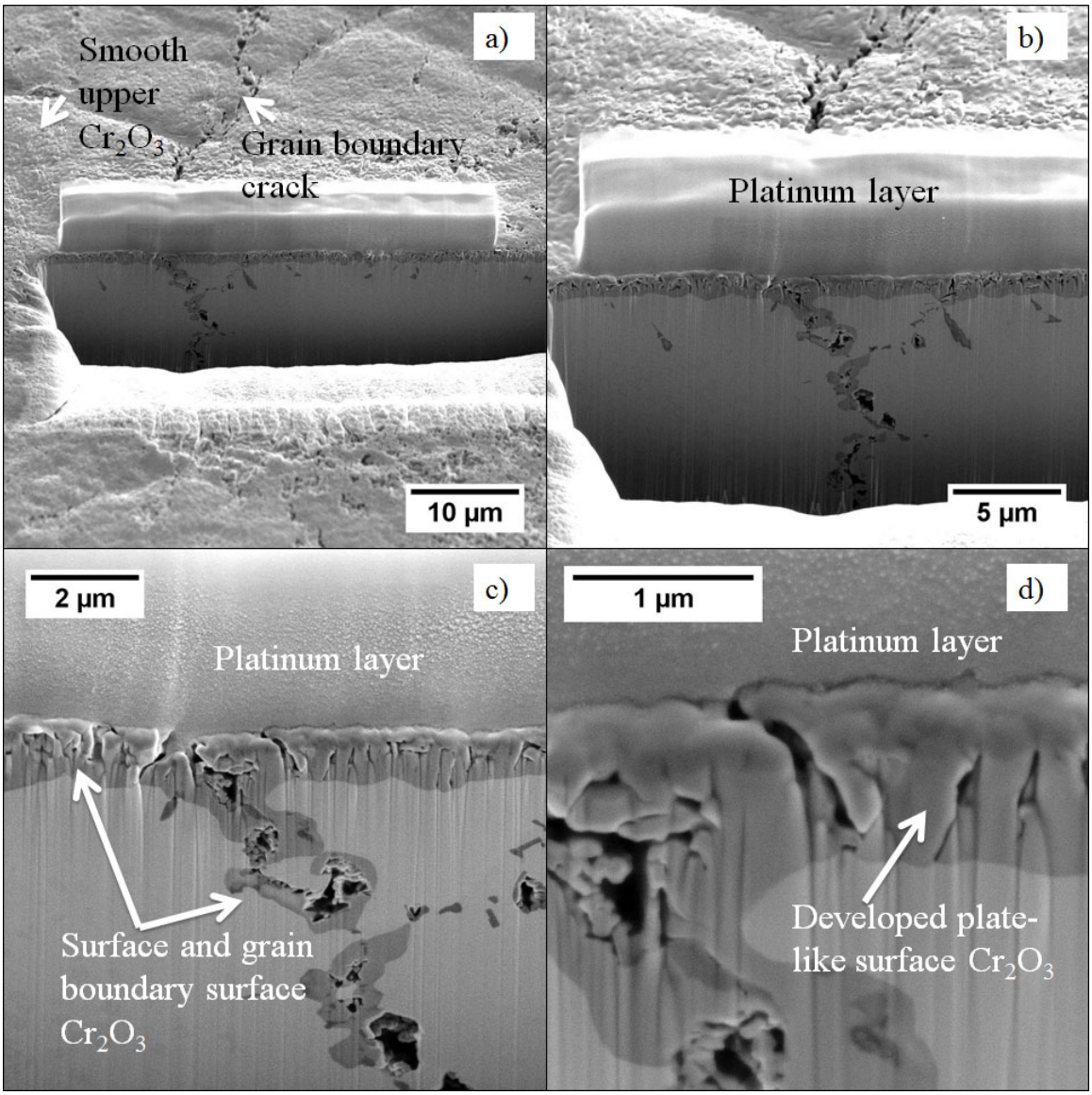

Figure 4-24 SEM images of a cross-section made in the FIB of Alloy 617 crept at 800°C in He-600ppm CH_4 (50MPa/137h) and subsequently in He-≤0.1ppm O_2 (50MPa/113h) environments. The morphology of the surface oxide and the grain boundary oxides are similar to what was seen in He-CO/CO_2=1320 environment (Figure 4-15).

CHAPTER 5
INVESTIGATION OF EFFICACY OF α-Al_2O_3 FORMING BARRIER LAYERS, NiAl AND FeCrAlY, DURING CREEP OF ALLOY 617 IN IMPURE HELIUM ENVIRONMENTS AT 800°C

In Chapter 4, surface chromia (Cr_2O_3) was shown to form naturally upon exposure of uncoated 617 to impure helium environments at 800°C. However, its formation did not protect against further internal oxidation and carburization of the substrate. Thus, in this chapter the study of coatings that favor the formation of a more protective alumina (α-Al_2O_3) is explored. The coatings were developed in a parallel research effort by Professor Carlos Levi's group at the University of California, Santa Barbara [93, 94]. Specifically, a nickel aluminide (NiAl) coating, with and without a FeCrAlY clad overlayer was developed for Alloy 617. Both coating approaches were shown to protect 617 against oxidation and carburization in impure He environments where no stress was applied. At the temperatures of interest (800-1000°C), NiAl offered a diffusionally stable coating that resisted long-term interdiffusion with 617. However, the formation of metastable γ-Al_2O_3 and θ-Al_2O_3 preceded the formation of the more protective α-Al_2O_3. In an effort to alter this occurrence, the NiAl layer was clad with FeCrAlY. At 800°C this dual layer FeCrAlY/NiAl system showed an improvement of the oxidation properties of the two coatings (compared to either layer used alone). The outer FeCrAlY cladding increased the formation of protective α-Al_2O_3, while the inner NiAl reduced interdiffusion with 617 and also provided an additional supply of Al for oxide formation.

This chapter examines the role of static and cyclic creep deformation of coated 617 at 800°C in impure He environments. Two coating systems are explored, as schematized in Figure 5-1: aluminized-only (NiAl/617) and aluminized + clad (FeCrAlY/NiAl/617). A limited study of the clad-only system (FeCrAlY/617) is presented to examine the behavior during creep without the NiAl layer. The effects of

creep deformation on potential changes in microstructure, near-surface composition, and the structural stability (cracking or delamination under stress) of the different coating layers are assessed for the as-deposited coatings. In a related experiment, artificial micronotches that were produced by FIB machining are introduced into the NiAl layer of aluminized-only creep specimens to study the role of defects on initiation and propagation of cracks during creep. Finally, the role of NiAl precipitates on accumulation of creep damage in the NiAl layer of the FeCrAlY/NiAl/617 system is examined.

5.1 Effect of stress and impure helium environments on coating/substrate systems

In this section, the bulk creep behavior at 800°C in impure helium, the effect of stress on microstructure/composition changes in the coatings, and the relative resistance of each system to environmental and mechanical degradation are examined for the aluminized-only and aluminized+clad coating/substrate systems. Table 5.1 presents environment, stress, and coating/substrate test matrix examined in this study. The impure helium environments were oxidizing (He-≤0.1ppm O_2 and He-8ppm of O_2) and carburizing/slightly oxidizing (He-CO/CO_2=1320). For NiAl/617 and FeCrAlY/NiAl/617 specimens, static creep tests at 50 MPa and 75 MPa as well as cyclic tests at 10/50 MPa and 15/75 MPa were conducted. To verify the behavior of the cladding on the substrate, cyclic creep of FeCrAlY/617 at 15/75 MPa was studied. Table 5.2 shows the process conditions used during the aluminizing and cladding processes. Two types of NiAl/617 were processed via pack cementation and are referred to as Generation I (Gen I) and Generation II (Gen II) [18]. Gen I NiAl/617 specimens were aluminized at 700°C for ~9.6h and subsequently heat treated at 1000°C for 18h. Gen II NiAl/617 specimens underwent aluminizing and heat treatment at 850°C/4h and 1000°C/3h respectively. Cladding with FeCrAlY alloy by hot pressing was done at 1000°C for 1h on selected Gen II NiAl/617 specimens. Microstructures of these as-deposited coating/617 systems are described in Chapter 3.

5.1.1 Creep behavior of coating/substrate systems

Figure 5-2 presents the creep deformation curves for the static and cyclic creep tests for the different coating/substrate systems and the uncoated 617 in the different impure helium environments, and Table 5.3 summarizes the test conditions. At 75 MPa

static or 15/75 MPa cyclic creep, strain rates in creep varied by roughly a factor of three, with the FeCrAlY/NiAl/617 showing the fastest creep rate under static loading and the FeCrAlY/617 having the slowest creep rate (only one static test was conducted). At σ_{max} = 50 MPa the creep rates and the total creep strains of the NiAl/617 and FeCrAlY/617 conditions differed only marginally. However, it is interesting to note that at the lower stress, the creep rate measured for the uncoated 617 is about a factor of 5 lower than the average creep rates for both coating systems for both loading conditions. While some differentiation of creep rates based on coating system could be inferred, it is important to note that we observed some scatter (1 - 1.7 10^{-8}/s) in the creep rates of uncoated 617 under the same test conditions, as described in Chapter 4. Thus, the variation in creep rates cannot necessarily be ascribed to the thermal history associated with coating/cladding processes or the architectural differences among the various combinations of coatings.

5.1.2 Microstructural changes and compositional evolution of coating systems

Changes in microstructure of coating and substrate.

The microstructure characterization of the coated specimens prior to creep studies was presented in Chapter 3, but will be reviewed here for the purpose of comparing them with microstructures of specimens crept at 800°C.

As presented by Clark in her exposure studies [18], the microstructure of Gen I NiAl/617 after aluminizing at 700°C for 9.6h and heat treating at 1000°C for 18h is shown in Figure 5-3a. The microstructure of this ~20μm coating after the 1000°C heat treatment and prior to creep consists of an NiAl matrix with precipitates rich in Cr and Mo near the surface, but free of precipitates closer to the interdiffusion zone (IDZ). The upper layer of this IDZ is composed of Cr-rich $M_{23}C_6$ carbides, while the lower layer closer to the substrate is sigma phase. Subsequent to exposure in a decarburizing environment at 800°C/500h, the microstructure of the initially heat-treated NiAl/617 appears as shown in Figure 5-3b. The microstructure of Gen I NiAl/617 crept in He-8ppm O_2 at 10/50 MPa cyclic stress for 513h to a 3% strain is shown in Figure 5-4. The microstructure is such that the NiAl layer and sigma phase are retained (Figure 5-4a), while the Cr-rich precipitates in the outer layer (Figure 5-4b) are still present with some of them appearing darker (probably evolving to $M_{23}C_6$ carbides). The NiAl region that

was precipitate-free after heat treatment now contains precipitates (Figure 5-4c), and the region in the 617 matrix adjacent to the sigma phase has needle-like precipitates (Figure 5-4e) after creep exposure. The underlying substrate shows no sign of oxidation (Figure 5-4f) or grain boundary cracking as was observed for crept uncoated 617 specimens (Chapter 4).

The microstructure of as-deposited Gen II NiAl/617 after aluminizing at 850°C for 4.5h and heat treating at 1000°C for 3h is shown in Figure 5-5. This higher aluminizing temperature produced thicker Gen II coatings (~60μm) than their Gen I counterparts (~20μm). The coating surface here is also mainly NiAl with precipitates rich in Cr and Mo near the surface, but it is free of precipitates closer to the interdiffusion zone (IDZ). The upper layer of this IDZ is composed of Cr-rich $M_{23}C_6$ carbides, while the lower layer consists of sigma phase. Figure 5-6 shows the evolution of the microstructure of Gen II NiAl/617 specimens subsequent to 120h of creep at 800°C/15/75 MPa and a strain accumulation of 16%. The NiAl layer and sigma phase are retained while some Cr-rich precipitates appear darker in tone in the outer NiAl layer. There is formation of precipitates in the region that was precipitate-free and also under the sigma phase in the alloy. No environmental attack is visible on the underlying substrate.

The FeCrAlY/NiAl/617 system had a thermal history of 850°C/4.5h and 1000°C/4h of aluminizing and cladding/heat treatment respectively. The as-deposited microstructure is shown in Figure 5-7. The NiAl layer contains the already-established Cr-rich precipitates, whereas there are no precipitates between the FeCrAlY/NiAl interface and the NiAl/617 interdiffusion zone. The Cr- and Mo-rich interlayers of the interdiffusion zone are also present. After 140h of creep at 800°C (Figure 5-8), the porosity still remains at the interface of the cladding with the aluminized layer. A portion of the NiAl precipitates has evolved slightly to brighter features and the needle-like precipitates typical of the interdiffusion zone is also shown with no visible environmental attack on the matrix.

Compositional evolution of coating and substrate.

Figure 5-9 to Figure 5-12 show concentration profiles (obtained by EDS or EMPA) across the coating layers of NiAl/617 and FeCrAlY/NiAl/617 coating/substrate systems prior to and following creep in impure helium environments at 800°C. The effect of stress on the composition of the coating layers after creep is evaluated in comparison with the evolution of coating composition in the unstressed systems that were investigated by Clark [18].

Clark characterized concentration profiles of Gen I NiAl/617 specimens after 1000°C/16h heat treatment in Figure 5-9a, and after 800°C/500h exposure in Figure 5-9b, and showed similar concentrations in the NiAl layer and the underlying alloy, even though precipitates had formed after exposure in a lower temperature. The crept Gen I NiAl/617 showed a similar concentration profile despite the application of cyclic (Figure 5-10a) or static (Figure 5-10b) stress. These observations indicate that the formation of precipitates after exposure in 800°C were a result of ageing and not due to interdiffusion between the NiAl and the alloy, or due to environmental effects. Also, this means that the alumina formed on the surface of the NiAl provided adequate protection against environmental attack, and that there was no effect of stress on the microstructural or compositional evolution.

Figure 5-11 shows that the coating remains as NiAl with Gen II processing, but this time it is Al-rich with the presence of precipitates in the outer NiAl region and a precipitate-free region closer to the IDZ as in Gen I NiAl/617. Even though, Gen II NiAl/617 specimens were not exposed to a lower temperature (800°C) subsequent to heat treatment at 1000°C in the absence of stress, the microstructure of the crept specimens indicate a similar evolution. Since all the concentration profiles of the Gen II NiAl/617 specimens crept under cyclic loading (σ_{max} = 75 MPa) and strains (4-16%) for times (120-286h), as shown in Figure 5-11b-e, indicate no change when compared to the unstressed condition after heat treatment (Figure 5-11a), it is also concluded here that stress does not have an effect on the coating composition of Gen II NiAl/617.

Lastly, the evolution of the microstructure and composition of unstressed FeCrAlY/NiAl/617 specimens show that there is similar diffusion of Al into the cladding and counter-diffusion of Fe in the NiAl layer after heat treatment at 1000°C/4h (Figure 5-12b) and exposure at 800°C/100h in (Figure 5-12c). Also, the NiAl layer consists of an

Al-rich outer region with precipitates and Ni-rich inner region without precipitates. A similar evolution is observed in the stressed specimens (Figure 5-12d-g); and hence it can also be concluded that stress has no effect on the composition of this system.

In summary, alloy 617 that was vulnerable to carburizing and oxidizing environments, as seen in Chapter 4, is now protected against environmental attack as a result of protection by the more effective Al_2O_3 formed on the surface of NiAl or FeCrAlY. Ageing – and not exposure to environment – is the cause for the microstructural changes in the coating layer and underlying substrate. Finally, the aluminide + clad coating layers successfully act as sufficient aluminum reservoir necessarily for the formation of protective oxide, and also act as an efficient diffusion barrier with the underlying substrate.

5.1.3 Damage characterization of coated systems

Although creep deformation did not have an effect on the composition evolution of the three coating/substrate systems, the propensity to damage accumulation under stress did depend on the type of coating system. Figure 5-13 and Figure 5-14 show the surface morphology of the Gen I and Gen II NiAl/617, respectively, subjected to static and cyclic creep deformation at stresses up to 75 MPa and strains up to 16%. Cracks develop on the surface of the NiAl layer and are perpendicular to the stress axis. Figure 5-15 and Figure 5-16 show that the corresponding cross-sections do not reveal any cracks through the coating layer or through the brittle IDZ. The absence of cracks deeper than the superficial region of the NiAl layer indicates that the cracks are limited to the thin alumina surface scale. The aluminizing conditions are not expected to be a factor in the formation of cracks in the NiAl layer, since no cracks are observed in the Gen I (Figure 5-15) and Gen II (Figure 5-16) cross-sections.

While neither face nor edge surfaces cracked below the thin Al_2O_3 on NiAl/617, cracking of the NiAl layer during creep and cyclic creep occurred the situation was dramatically different for the FeCrAlY/NiAl/617 specimens subjected to the same creep conditions. The introduction of the cladding layer above the NiAl layer (recall that edges were not clad) was associated with the development of cracks in the NiAl layer, both on the faces beneath the cladding and on the edges that were not clad. On the clad surfaces (image a of Figure 5-17 to Figure 5-20), grain boundary shifting and uplifts are observed,

and superficial cracks confined to the alumina scale run perpendicular to the stress axis across the grains. The edge surfaces of the gauge, however, which are not clad, now display cracks in the NiAl layer with depths reaching the NiAl-617 interdiffusion zone, and that also run perpendicular to the stress axis. The crack openings on the edge surfaces measure ~40um for 16% creep strain (image b of Figure 5-17 and Figure 5-18), and ~10um for 4% creep strain (image b of Figure 5-19 and Figure 5-20). The surface morphology of the cladding here displays grain boundary uplifts after creep, and cracks were observed in the aluminide layer (images c and d of Figure 5-17 to Figure 5-20) yet they were absent in the unclad NiAl layer (Figure 5-14 and Figure 5-15). Cross-sectional views of the FeCrAlY/NiAl/617 system confirm the grain boundary sliding of the cladding by the presence of necking in the cladding, whereas cracks/voids are present within the aluminized-only layer with the openings roughly proportional to the level of strain attained (4% or 16%). Voids that formed in the NiAl layer, after creep strain of 16%, are connected to the brittle layers of the interdiffusion zone and the cladding layer (image c of Figure 5-17 and Figure 5-18) or the environment (image d of Figure 5-17 and Figure 5-18) when the cladding is absent, as on the specimen edges. Pores along the junction between the cladding and NiAl, shown in Chapter 2 to characterize the process of cladding of the aluminized layer, do not seem to be associated with the formation of cracks. Under low stress (10 MPa and 10/50 MPa) and 4% strain, FeCrAlY/NiAl/617 shows the initiation of cracks in the central region of the NiAl layer in regions where pores are absent (image c of Figure 5-19 and Figure 5-20). At the lower strain level, the cracks are not long enough to link the cladding and the interdiffusion zone. Even though the cracks/voids are formed in this system, their penetration into the underlying 617 is slowed down at the interdiffusion zone. It is noteworthy that the cracks on the aluminized-only face (Figure 5-21a, edge surface of gauge) correspond well with the cross-sectional cracks seen on the aluminized layer that has cladding (Figure 5-21b, face surface of gauge), as shown in Figure 5-21. This shows that most of these cracks are continuous and wrap around the specimen gauge. Since no cracking was observed in NiAl/617, it is believed that the cladding overlay on the NiAl layer is the source of constraint that explains the cracking in this system. The wrapping of the cracks around the gauge also shows that the cracks in the sandwiched NiAl are exposed to the

environment; hence the oxidation of the crack walls to form Al_2O_3 within the coating layers, but Cr_2O_3 in the substrate (Figure 5-22 and Figure 5-23). The implication of this observation is that the capability of the coating layers to protect the underlying substrate against environmental attack is dependent on the crack depth. Therefore, it is expected that as long as the cracks do not grow beyond the interdiffusion zone, the more protective Al_2O_3 will protect the underlying substrate.

Cyclic creep of FeCrAlY/617 at 15/75 MPa and to a strain of 14% confirmed the ductile nature of the cladding layer reported above (FeCrAlY/NiAl/617). As seen before, the cladding layer was characterized by grain boundary sliding and grain uplifts (Figure 5-24a). On the surface of the cladding, grain boundaries are seen to have moved and there is presence of cracks running across the grains and perpendicular to the stress axis. According to the cross-sectional view (Figure 5-24c), the interface between the cladding and 617 did not crack, in contrast to the NiAl layer inserted between that cracked in the FeCrAlY/NiAl/617 system. Similarly to damage accumulation on 617 in He-CO/CO_2=1320, cracks occurred on the unclad edge surface (Figure 5-24b) penetrating deep beyond the chromia scale, and also precipitation of carbides was observed in the near-surface region (Figure 5-24d). While this clad/617 system was subjected to only cyclic creep stresses, results from comparisons between cyclic and static creep damage suggest that the same level of damage would have occurred under static creep tests.

In summary, the NiAl layer that was shown to be an effective diffusion barrier and which formed the protective Al_2O_3 less readily than FeCrAlY, performed well in creep and withstood stresses better without a cladding overlay. Also, upon formation of cracks in the layers, the protection of the underlying substrate could still be guaranteed as long as the cracks do not grow further.

5.2 Role of pre-existing defects on damage accumulation during creep of aluminized 617.

As shown above, the mechanical integrity (absence of crack formation) of the NiAl layer in both Gen I and Gen II aluminized systems (NiAl/617) was retained after a creep strain up to 16% in impure helium environments. Since there was no evidence of formation of cracks in the aluminide layer and in the interdiffusion zone during creep of a "defect-free" NiAl/617 system, it was of interest to evaluate the behavior of the layer

when prior damage was introduced to determine if such damage could compromise the coating integrity.

Therefore, cyclic creep experiments were conducted at 10/50 MPa for ~200h and ~600h at 800°C to investigate the behavior of FIB-notched aluminized specimens in the carburizing/oxidizing environment, as shown in Figure 5-25. Note that the time reported here is total test time, which is equivalent to twice the time at maximum stress. On the wider surface of the specimen gauge (Figure 5-25a), three sets of notches were machined in a grouping (Figure 5-25b) on one specimen face with the goal of increasing the chances of being able to reach at least one set during sample polishing after the test. Each set consisted of notches of 100 μm by 3 μm and varying depths of 10 μm, 20 μm, and 30 μm (Figure 5-25c-e). Varying notch depths were used to probe damage accumulation at different depths in the NiAl layer. The longer test duration was employed to evaluate the effect of extended exposure in the impure helium environment, and also to characterize the propagation of cracks that were expected to initiate during the shorter test.

The creep behavior of the NiAl specimens with and without notches is shown in (Figure 5-26). While the primary creep strains are somewhat different, the FIB micro-notches do not affect the global creep deformation rate after 200h and 600h. Global and local strains are defined as strains achieved for the entire specimen during creep and strains determined locally from spacing of notches, respectively. The strains local to the notched areas on the specimen are higher compared to the global strains during creep, and this difference is more significant with increased creep time. For instance, the local/global strain values for the ~200h-test specimen were 3.7%/3.5% (Figure 5-27a,b), while the ~600h test yielded 7.9%/6.4% (Figure 5-27c,d). The difference in the local versus global strains can be understood by comparing the change in the individual notch openings for the two durations, where this difference is more significant for the notch opening after ~600h (Figure 5-28). The evolution of the shape of the notch root is of interest. Figure 5-29 shows a global view of the comparison between the notch profiles of the untested coupon (Figure 5-29a) and the crept specimens (Figure 5-29b,c). It is clear that the initial sharp notch tips (Figure 5-29a) blunt with increasing creep strains (Figure 5-29b,c). It is important to note the effect of creep strain on the profile of the notches. The sharp notch tips (Figure 5-30: 1a-c) are blunted after ~200h and 3.5% strain (Figure

5-30: 2a-c). Further straining to 6.4% after ~600h (Figure 5-30: 3a-c) produces kinks in the regions immediately close to the notch root with an increase in the notch opening. Oxidation of the notch is also present. After 3.5% strain and 200 h of exposure to the carburizing/oxidizing environment, the notch tip starts to assume a round profile and is blunted, while the alumina at the tip penetrates into the aluminide layer by ~1 μm (Figure 5-31: 2a-c). However, further creep straining (6.4%) and after 600h of exposure, while producing a change in geometry of the notch tip and an increase of the notch opening, does not translate into an increase in oxide penetration or cracking at the notch root (Figure 5-31: 3a-c). This lack of significant increase in crack propagation or oxide penetration at the tip of the notch root is interesting especially considering the high local strains developed by the significant dimensional change in the notch opening, as shown in Figure 5-28c,d.

5.3 Measuring effect of NiAl precipitates on cyclic creep

In Chapter 2, it was shown that the use of both FeCrAlY and NiAl barrier layers optimized their different oxidation properties at high temperatures and in impure He environments. It was explained that a coating/substrate developed by adding FeCrAlY cladding onto aluminized 617 was ideal in that the FeCrAlY layer would readily form the protective alumina scale, while the NiAl layer would provide an additional Al reservoir and also significantly reduce interdiffusion between the coating layers and the underlying substrate. The FeCrAlY/NiAl/617 system was, however, shown in section 5.1 to be less robust and prone to local crack formation in the NiAl layer under mechanical stresses while no such damage was observed in the aluminized-only 617. Cyclic creep studies clearly showed (Figure 5-17 to Figure 5-20) that the cracking was initiated in the precipitate-rich region of the NiAl layer at low stress/strain and grew into large voids at higher stress/strains. Additionally, Clark [18] also showed that longer heat treatments (> 24h) of the FeCrAlY/NiAl/617 system at 1000°C essentially dissolved the precipitates in the NiAl precipitate-rich region, but that the interdiffusion zone was modified for times longer than 100h (Figure 5-32b,c). Therefore, an investigation was conducted to determine if the presence or absence of precipitates plays a role in the crack formation in the NiAl layer during cyclic creep of the FeCrAlY/NiAl/617 system. In order to do this, clad-aluminized specimens, developed at UCSB following the normal coating procedure

described in Chapter 2, were heat-treated at 1000°C in argon for 24h and 100h, and cyclic crept at low stress (10-50 MPa) in a carburizing/oxidizing environment. The comparison of the cyclic creep behavior at 800°C of the three clad-aluminized specimens having undergone 4h (as-coated), and extra 24h and 100h heat treatments is shown in Figure 5-33. The creep behavior of the FeCrAlY/NiAl/617 system that has been subjected to additional heat treatment at 1000°C is within the scatter seen in Figure 5-2.

Dissolution of NiAl precipitates in FeCrAlY/NiAl/617 with additional 24h and 100h heat treatments at 1000°C lowers the ease of internal damage in the form of cracking during creep. While the surface damage on the specimens in the three conditions consisted of the normal cladding behavior where grain boundary sliding and uplifts are present (Figure 5-34a-c), the frequency of cracks on the aluminized-only layer has been reduced with additional heat treatment (Figure 5-34d-f). Following the additional 100h heat treatment, only a small number of cracks are present on the aluminized-only layer. The cross-sectional views of the different layers revealed the reduced internal damage in the form of cracking the NiAl layer that has the cladding overlay (Figure 5-35a-c). However, the unclad NiAl layer is still characterized by the same type of cracking through the layer as was observed in specimens without extra heat treatment (Figure 5-35d-f). The dissolution of precipitates in the clad NiAl layer with further heat treatment is supported by EBSD characterization. Figure 5-36 shows the position of the large voids created after high stress/strain creep to coincide with the precipitate-rich NiAl region where the grains are much smaller. Cracking in the NiAl layer is shown to be localized in the precipitate-rich region of the NiAl layer having undergone low stress/strain creep, as shown in Figure 5-37. Additional heat treatment of the FeCrAlY/NiAl/617 system is associated with the dissolution of the NiAl precipitates (Figure 5-38a-c) and with the growth of grains in the region where the precipitates have been dissolved (Figure 5-38d-f). The dissolution of the NiAl precipitates is most likely the reason for grain growth since there are no more precipitates to pin down the growth.

5.4 Discussion

The barrier layers (NiAl and FeCrAlY) investigated in this work were studied to examine their protective role of Alloy 617 against environmental attack while maintaining their structural integrity over time when subjected to static and cyclic creep

deformation. This means that for the coating layers to be effective in offering protection for Alloy 617 in He environments, they need to be resistant to the effects of mechanical strains while protecting the underlying substrate from environmental attack already shown in Chapter 4. It was indeed possible for the coating systems to provide protection for the substrate, although interesting secondary cracking processes were observed in the clad + aluminized system. In this section, the capability of the coating layers to protect against environmental attack will be discussed, and the mechanical behavior of the layers assessed.

5.4.1 Environmental protection of NiAl and FeCrAlY

In the results section, it was shown that the environmental attack in the form of grain boundary intrusions (Chapter 4) does not take place in the coated 617. Comparing the near-surface regions of Alloy 617 crept in low and high oxygen partial pressure (Figure 4-4) with the region beneath the interdiffusion zone in the coated specimen (Figure 5-4e, Figure 5-6e, and Figure 5-8h), it is evident that the coating layers have protected Alloy 617 by preventing the intrusion of grain boundaries and formation of internal oxides. The formation of a dense, compact, and more protective α-Al_2O_3 compared to the "porous" Cr_2O_3 is responsible for this improvement. As shown in Chapters 2 and 4, the natural-forming Cr_2O_3 is less protective on Alloy 617, and its role of environmental protection on 617 is susceptible to the environment in which they are grown and the level of oxygen partial pressure. However, α-Al_2O_3 is believed to come close to satisfying the requirements of an ideal surface oxide layer: slow-growing, continuous and free from pores that would enhance the diffusion of oxidants from the gaseous environment. Since no microstructural changes in the coating layers or the underlying substrate could be associated with the carburizing or oxidizing nature of the environment, it was established that Al_2O_3 played a dominant and sufficient role in protecting the NiAl layer and the underlying 617.

In general, the behavior of the NiAl/617 system (Figure 5-4 and Figure 5-6) shows that aluminizing is a sufficient way of protecting 617 against carburization and oxidation. It is known that NiAl does not readily form the stable α-Al_2O_3, and so it is assumed that pre-oxidation of the coating surface at low oxygen partial pressure prior to creep provided the required phase of alumina. This environmental protection was also

confirmed in the FeCrAlY/NiAl/617 system (Figure 5-8). Even though NiAl offers the resistance to environmental attack required during creep, the FeCrAlY cladding is still considered essential as an overlay on NiAl since the resulting composite system offers a long-lasting reservoir of Al for the formation of the stable scale as well as offering a diffusion barrier between the cladding and 617.

Based on the findings of Chapter 4, where the carburizing and oxidizing environments are shown to be the initiators of near-surface damage in Alloy 617, one would expect that a similar mechanism would be observed on the surface of alumina-forming coatings. Indeed, cracking originating from the surface and that penetrate into the coating have been reported before in the presence and absence of mechanical strains. In a study by Tolpygo and Clarke [95], where the rumpling mechanism of nickel aluminide at 1150°C during cyclic oxidation was investigated, they reported that cracking of the alumina scale occurred with the development of through-thickness cracks that provided oxygen ingress to the coating surface so that the crack tips penetrated deeper into the coating with subsequent cycling. This observation shows that the conditions of environment and temperature cycling were sufficient to initiate surface cracks in the coating. It should be pointed out, however, that the main reason in their study for the development of these environmentally-induced surface cracks was due to the surface roughening/undulation of the aluminide coating or the cladding. Tolpygo noted that the undulation of the coating layer initiated separation and cracking of the coating layer and the superalloy. He also asserted that one factor causing this undulation was the presence of cyclic plastic strains in the coating driven by growth strains in the alumina surface scale. Obviously the NiAl and FeCrAlY layers used in the current research have not displayed this undulating behavior in the absence of mechanical strains as shown by Clark [18] or after static and cyclic creep as shown earlier in findings here.

5.4.2 Mechanical aspect of NiAl and FeCrAlY

The effectiveness of a coating layer depends also on whether the role of environmental protection could be affected by the application of mechanical strain. One possible role of stress would be to increase the rate of interdiffusion of elements across the coating layers. However, this was not observed in the present study since the elemental concentration profiles produced by EDS/EMPA analysis were similar before

and after creep deformation. The second effect of mechanical strains is on the propensity to cracking in the coating with increased strain accumulation. This cracking has been reported by Pollock and others [96] where, with the imposition of a constant total compressive strain range of 0.35% by sustained peak low cycle fatigue on aluminide-coated superalloy, they observed that the oxide-filled cracks penetrated the bond coat and the interdiffusion zone after approximately 80% of the cyclic life. It is intriguing that the NiAl used in this research accommodated high cyclic strains without formation of any environmentally-induced or mechanically-induced cracks. If the cracks were to form, it is surmised that they would be initiated either on the surface (environmentally-induced) or from the brittle interdiffusion zone, as seen by Shneider and Grünling [97]. Pollock also showed that the failure process due to fatigue cycling with compressive holds consisted of cracks extending from the surface through the bond coat, past the interdiffusion zone and substrate before a long crack could grow into the underlying Ni-alloy substrate [96]. There are also other reports where high temperature embrittlement of the nickel aluminide have appeared to be related to oxygen penetration along grain boundaries [98]. Furthermore, the resistance to crack initiation and propagation from the notches planted in the NiAl, consistent with the resistance to initiate cracks from the surface alumina, makes it more unlikely that cracks would form on the surface without the presence of undulations or mechanical stress. In the absence of surface cracks, the interdiffusion zone, a brittle phase formed during the aluminizing process, would be expected to initiate cracks that would then be propagated into the underlying substrate. Therefore, the absence of cracking in NiAl/617 clearly indicates that Al_2O_3 resists the ingress of oxidants; hence, no initiation of cracking on the surface, and also could point to the increased ductility of the NiAl layer because of the presence of Cr that also helps to reduce the amount of aluminum required for oxidation [99]. Additionally, the interdiffusion zone is made up of carbide and sigma layers believed to be brittle phases. However, the interpenetration of these layers by 617 (Figure 5-39) is thought to allow limited interdiffusion but also prevent cracking by breaking up the former into discontinuous layers [21].

As already established, the addition of FeCrAlY overlay on NiAl was meant to provide a composite system with enough Al for formation of Al_2O_3 more readily, but also

to provide a good diffusion barrier between the cladding and 617. While this composite system displayed protection of 617 from the environment, the mechanical integrity of the composite structure was not sustained with strain accumulation. It is important to look at the creep deformation mechanisms and the source of cracking in the system to explain the mechanical instability. Even though there is no consensus on the mode of creep deformation in NiAl and no data on FeCrAlY, the mode of creep deformation of the system could be generalized to be a combination of grain boundary sliding for FeCrAlY (based on the observation of grain shifting) and dislocation creep for 617 [52, 100, 101] and NiAl [102]. Clark in her work [18] did not observe the grain shifting of unstressed FeCrAlY alloy, but this phenomenon has been reported to occur in the absence of stress purely as a result of oxide and alloy mismatch on cooling by Nychka [103]. Therefore, it is reasonable to suspect that mechanical strains would enhance an effect of pronounced grain shifting and uplifts during creep. It is not clear, though, whether this difference in creep deformation modes in the different layers and substrate could explain the cracking in the NiAl since the EBSD maps do not show any evidence of grain-to-grain constraint from FeCrAlY to NiAl that would explain why grain upshifts in FeCrAlY would engender a constrain in NiAl.

Cracks on NiAl when clad with FeCrAlY (only the face surfaces were clad) were tracked as shown in Figure 5-21 and shown to wrap around the specimen gauge. Since NiAl by itself does not crack under stress, it is likely that the cracks initiate underneath the cladding at the FeCrAlY/NiAl interface before propagating around the specimen. There are two likely possibilities to explain this cracking phenomenon. One possibility is that there is an association between the dissolution of precipitates in the unclad NiAl and the reduced propensity to cracking in NiAl. However, the findings in Figure 5-35 show that the cracking in the NiAl was not entirely eliminated even after 100h of additional heat treatment to dissolve the NiAl precipitates. As pointed out earlier, the lack of proof that the grains in the FeCrAlY and NiAl are aligned makes it difficult to ascribe the crack initiation in the precipitate-rich region of unclad NiAl to the grain shifting in the FeCrAlY cladding. The second possibility is that cracking is caused by a change in the stress state during creep in the NiAl that is now sandwiched between the FeCrAlY cladding and the substrate, and this is an interesting topic for future work both in terms of

the stress analysis and in terms of designing a different specimen configuration or cladding process to eliminate the unclad surfaces. For example, it would be informative to study the static and cyclic creep behavior of the two coating layers when applied on a tubular substrate. The application of the cladding would need to be changed from hot pressing (not practical for cladding around the gauge of the current rectangular specimen) into an ion plasma deposition or low plasma spraying technique that would be practical for cladding around the specimen.

Finally, the higher creep rates of coated 617 compared to their uncoated counterparts need to be verified since lower creep strength of coated systems could have implications on their suitability for long-time service. It has been observed that coated substrates have lower creep strengths compared to the bare alloys (Figure 5-2h,i.j). It was initially believed that the higher creep rates could be ascribed to the additional high temperature processing that the coatings undergo, but this has been ruled out by Dryepondt [104], and can be ignored for the coatings here since there was no evidence of change in grain sizes due to the coating treatment (Sections 3.1 and 3.3). Standard estimates could be made for the properties of composite coating/substrate systems, as described by Osgerby and Dyson [105], but the estimates could be simplified by considering the coatings as non-load bearing. This way, a comparison of the creep rates and stresses could be made using the appropriate Norton law relating creep strain rate to applied stress. Figure 5-40 shows an approximation of the creep strain rate-stress dependency of the coated specimens used in this work. The exponent determined for NiAl/617 and FeCrAlY/NiAl/617 is 5.5 and 4.5 respectively. For the sake of the analysis, Equation 5.1 is used to determine by how much the stress of the NiAl/617 system changes relative to the bare alloy. If the target stress on the NiAl/617 is σ_1 and the effective stress on the 617 is σ_2, the measured strain rate is $\dot{\varepsilon}_1$, while the new strain rate based on the effective stress would be $\dot{\varepsilon}_2$. The measured NiAl thickness is ~ 43μm, and the gauge dimensions with the coating are 3.03mm x 1.98mm. Given that $\dot{\varepsilon}_1$=4x10^{-8}/s, σ_1=50 MPa, and σ_2=51.85 MPa, the new creep strain rate would be $\dot{\varepsilon}_2$=4.88x10^{-8}/s, which is an increase of 22% (compared to 200% determined in this work). This means that the application of an extra layer of coating does not significantly change the effective stress and the resulting creep strain rate. The observed jump in creep strain rate of the

coated specimens would therefore be understood more clearly given more complementary data and specifically by verifying the non-load bearing theory given in the literature.

$$\frac{\dot{\varepsilon}_1}{\dot{\varepsilon}_2} = \left(\frac{\sigma_1}{\sigma_2}\right)^{5.5} \tag{5.1}$$

5.5 Summary and conclusions.

The application of either NiAl or NiAl+FeCrAlY coatings prevented damage in the near-surface regions of the underlying 617 during exposure to oxidizing and carburizing/oxidizing helium environments and creep or cyclic creep conditions. The main reason for this was the protection against the diffusion of oxidants from the environment by the slow-growing alumina scale on NiAl and FeCrAlY. The coating layers used here also did not display surface undulation that has been reported to initiate surface cracks on the alumina scale/coating interface. The NiAl coating layer remained stable and did not display any cracking in the layer or in the interdiffusion zone after significant strain accumulation. It was also resistant to initiation and propagation of cracks from FIB-notches planted to simulate defects in the layer. Unfortunately, the NiAl layer was vulnerable to cracking in the presence of a FeCrAlY cladding overlay that was meant to provide a coating system with a sustained environmental protection role. A different cladding technique on a tubular specimen is proposed to replace the hot pressing technique on rectangular specimens. The cladding overlay on the aluminide coating using hot pressing could probably be the origin of a different stress state on the specimen that was clad only on two face surfaces. The calculated stresses were based on the total cross-sectional area of the coated specimens, while in fact the coating layers might be non-load bearing. For this reason, complementary studies are needed to verify whether NiAl and FeCrAlY layers are non-load bearing..

Table 5.1 Test matrix of static and cyclic creep experiments at 800°C conducted to evaluate the efficacy of coatings layers to offer environmental protection while ensuring mechanical integrity (no cracking).

	NiAl/617		FeCrAlY/617		FeCrAlY/NiAl/617	
Low Stress	8ppm O_2	50 MPa			CO/CO_2 = 1320	50 MPa
	8ppm O_2	10-50 MPa			CO/CO_2 = 1320	10-50 MPa
High Stress	CO/CO_2 = 1320	75 MPa			0.1ppm O_2	75 MPa
	CO/CO_2 = 1320	15-75 MPa	CO/CO_2 = 1320	15-75 MPa	CO/CO_2 = 1320	15-75 MPa

Table 5.2 Temperature and time conditions for aluminizing of 617 by pack cementation under flowing high purity Ar.

	Aluminizing Conditions		Heat Treatment Conditions	
	Temperature (°C)	Time (h)	Temperature (°C)	Time (h)
Gen I NiAl	700	9.6	1000	16
Gen II NiAl	850	4.5	1000	3
Cladding + Gen II NiAl	850	4.5	1000	4

Table 5.3 Interrupted creep behavior of uncoated 617, aluminized 617 (NiAl/617), clad-only 617 (FeCrAlY/617), and clad-aluminized 617 (FeCrAlY/NiAl/617) tested at 800°C in different helium environments.

Curve	**Specimen**	**Creep Test**	**Environment**	**Strain (%)**	**Steady-State Creep Rate (10^{-8}/s)**	**Total test time (h)**	**Cycles**
a	Clad-aluminized	Static Creep (75 MPa)	He-≤0.1ppm O_2	16	62	109	N/A
b	Clad-aluminized	Cyclic Creep (15-75 MPa)	He-CO/CO_2=1320	16	36	140	3358
c	Aluminized	Cyclic Creep (15-75 MPa)	He-CO/CO_2=1320	16	35	120	2871
d	Aluminized	Static Creep (75 MPa)	He-CO/CO_2=1320	15	30	139	N/A
e	Clad	Cyclic Creep (15-75 MPa)	He-CO/CO_2=1320	14	24	167	3992
f	Clad-aluminized	Cyclic Creep (10-50 MPa)	He-CO/CO_2=1320	4	8	213	3191
g	Clad-aluminized	Static Creep (50 MPa)	He-CO/CO_2=1320	4	8	120	N/A
h	Aluminized	Static Creep (50 MPa)	He-8ppm O_2	3	4	215	N/A
i	Aluminized	Cyclic Creep (10-50 MPa)	He-8ppm O_2	3	3	513	7691
j	Uncoated	Cyclic Creep (10-50 MPa)	He-CO/CO_2=1320	2	1	553	8294

Table 5.4 Ductile-Brittle Transition Temperatures of Diffusion and Overlay Coatings [106]. LTHA; Low Temperature High Activity; HTLA: High Temperature Low Activity.

Coating Type		**DBTT (°C)**
Diffusion Coatings	LTHA Nickel Aluminide	840
	HTLA Nickel Aluminide	600
Overlay Coatings	Co-Cr-Al-Y	235-910
	Ni-Cr-Al-Y	430

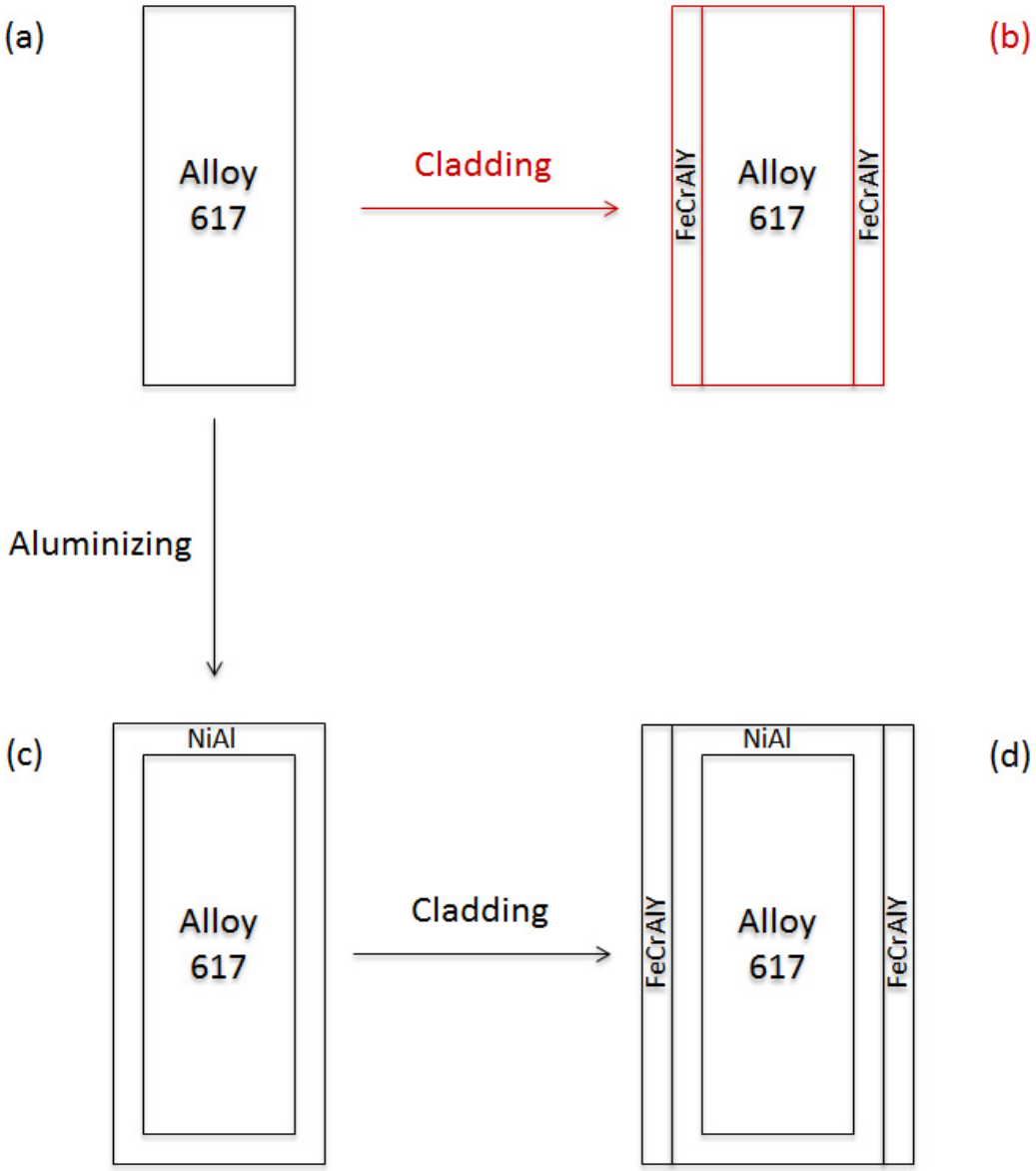

Figure 5-1 Schematic showing the cross-sections perpendicular to the stress axis of: (a) uncoated 617, explored in Chapter 4, and (c,d) coated 617 that is explored in this chapter. The study of clad 617 (b) was used to confirm the general mechanical behavior of the FeCrAlY layer on 617.

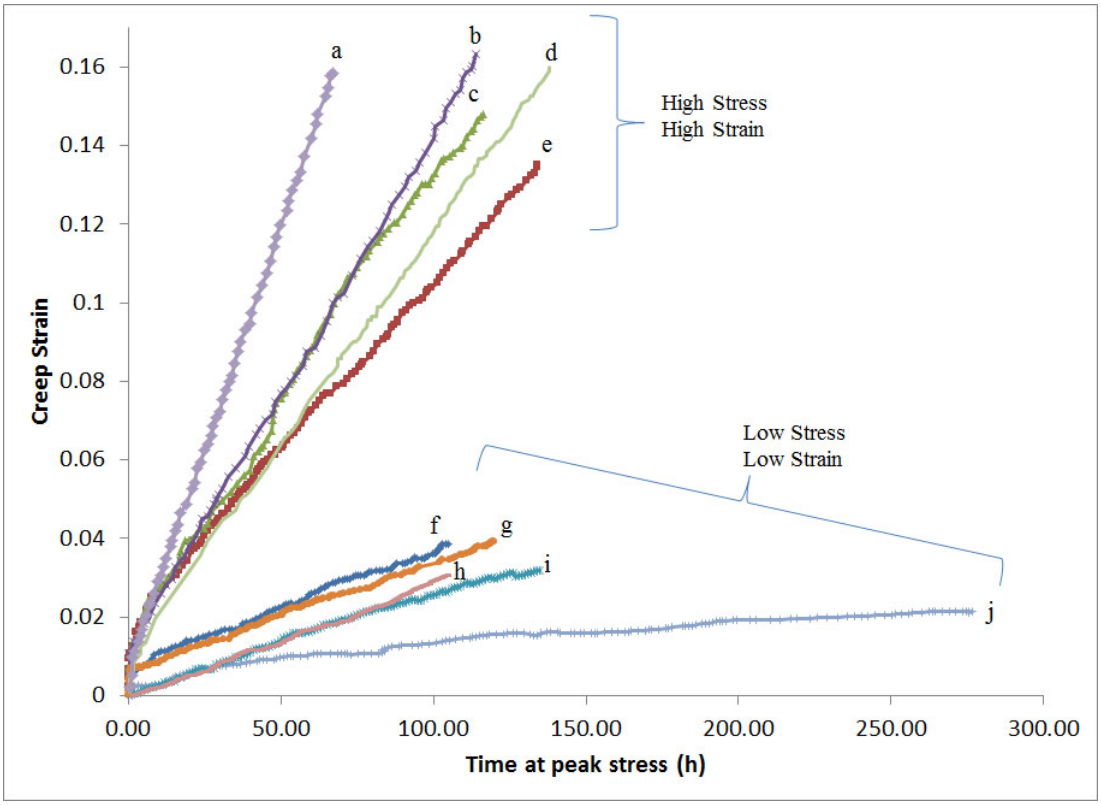

Figure 5-2 Interrupted creep behavior of uncoated 617 (j), aluminized 617 (NiAl/617, c,d,h,i), clad-only 617 (FeCrAlY/617, e), and clad-aluminized 617 (FeCrAlY/NiAl/617, a,b,f,g) tested at 800°C in different helium environments.

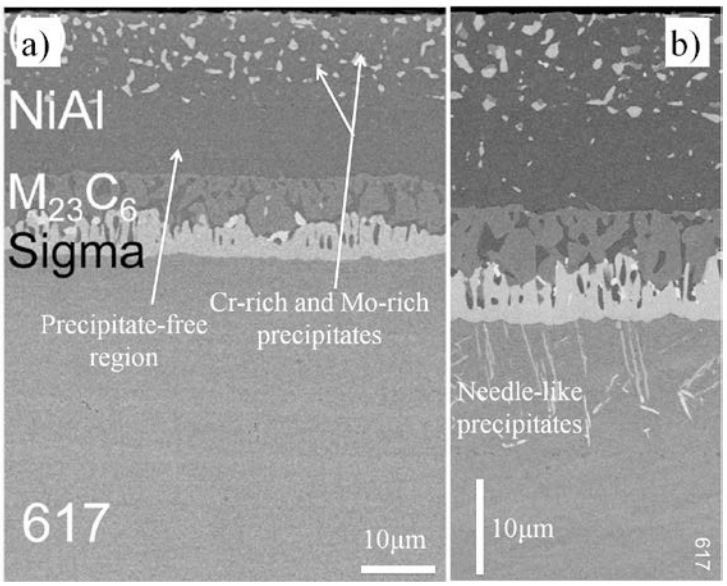

Figure 5-3 Micrograph showing the microstructural evolution of Gen I NiAl/617 showing (a) system as-aluminized at 700°C/9.6h and heat-treated at 1000°C/18h, and (b) subsequent exposure to a decarburizing environment at 800°C/500h. Adapted from reference [18].

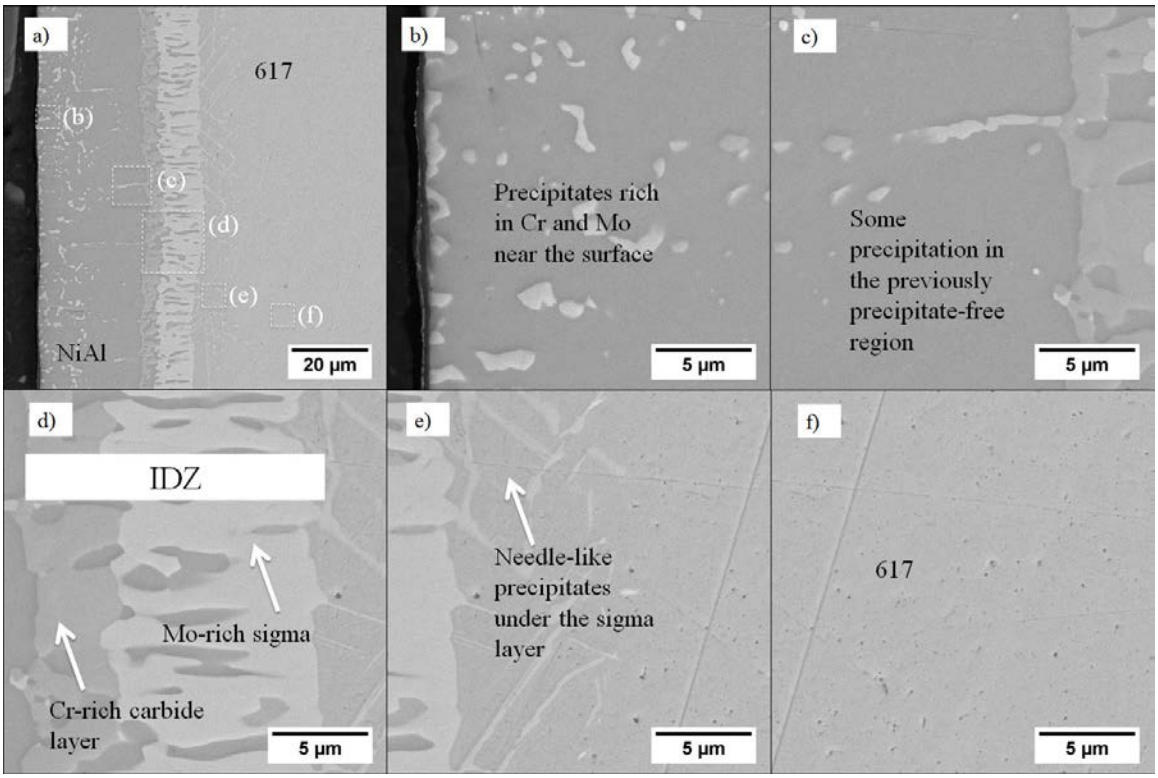

Figure 5-4 Microstructure evolution of Gen I clad-aluminized 617 after creep (10/50 MPa/513h/ε=3). The duration reported is total test time.

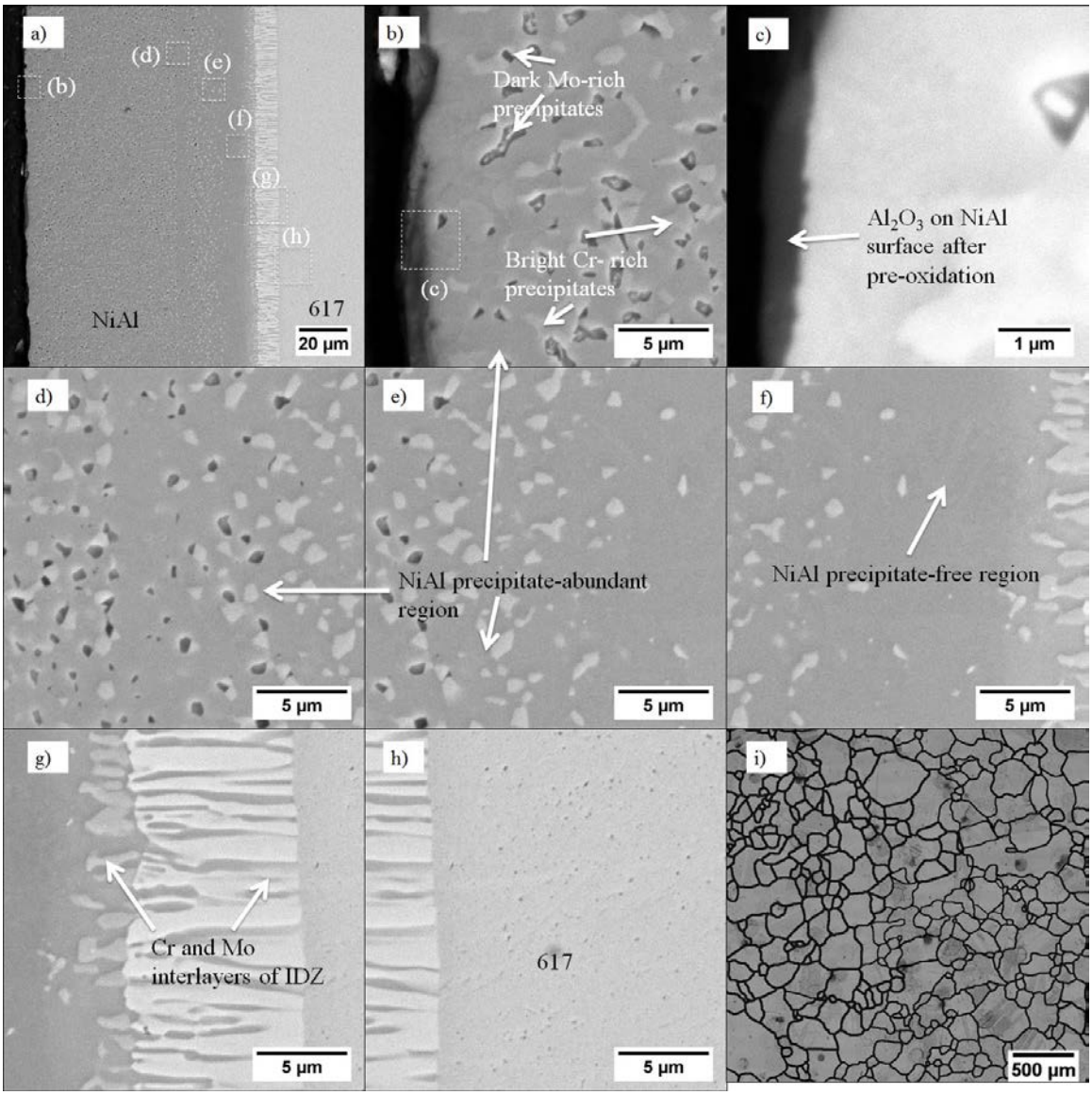

Figure 5-5 Microstructure of as-coated aluminized 617 (Gen II) showing a thick NiAl coating with chromium and molybdenum precipitates and a sigma layer (a-h), with Al_2O_3 formed on NiAl surface after pre-oxidation (c). The average grain size of the underneath 617 is 139µm and the distribution of grains is shown in (i)

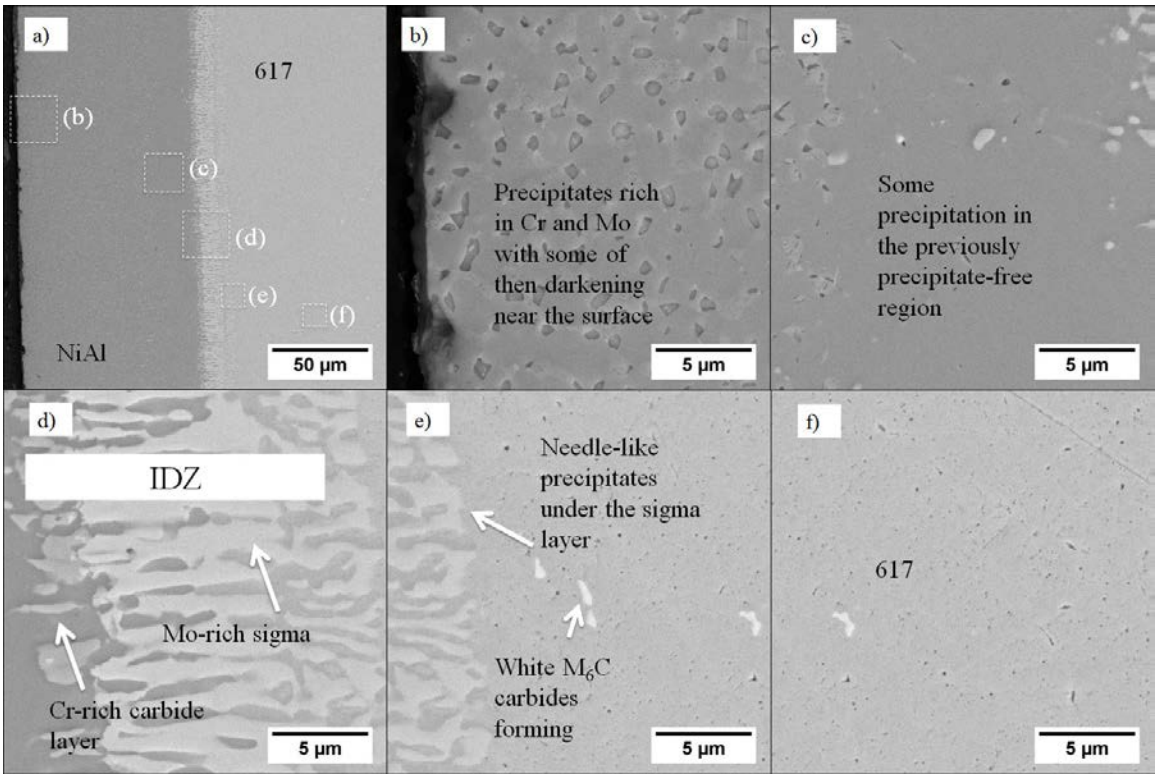

Figure 5-6 Gen 2 NiAl 617 crept Microstructure evolution of Gen II aluminized-only 617 after creep (15/75 MPa/120h/ε=16). The duration reported is total test time.

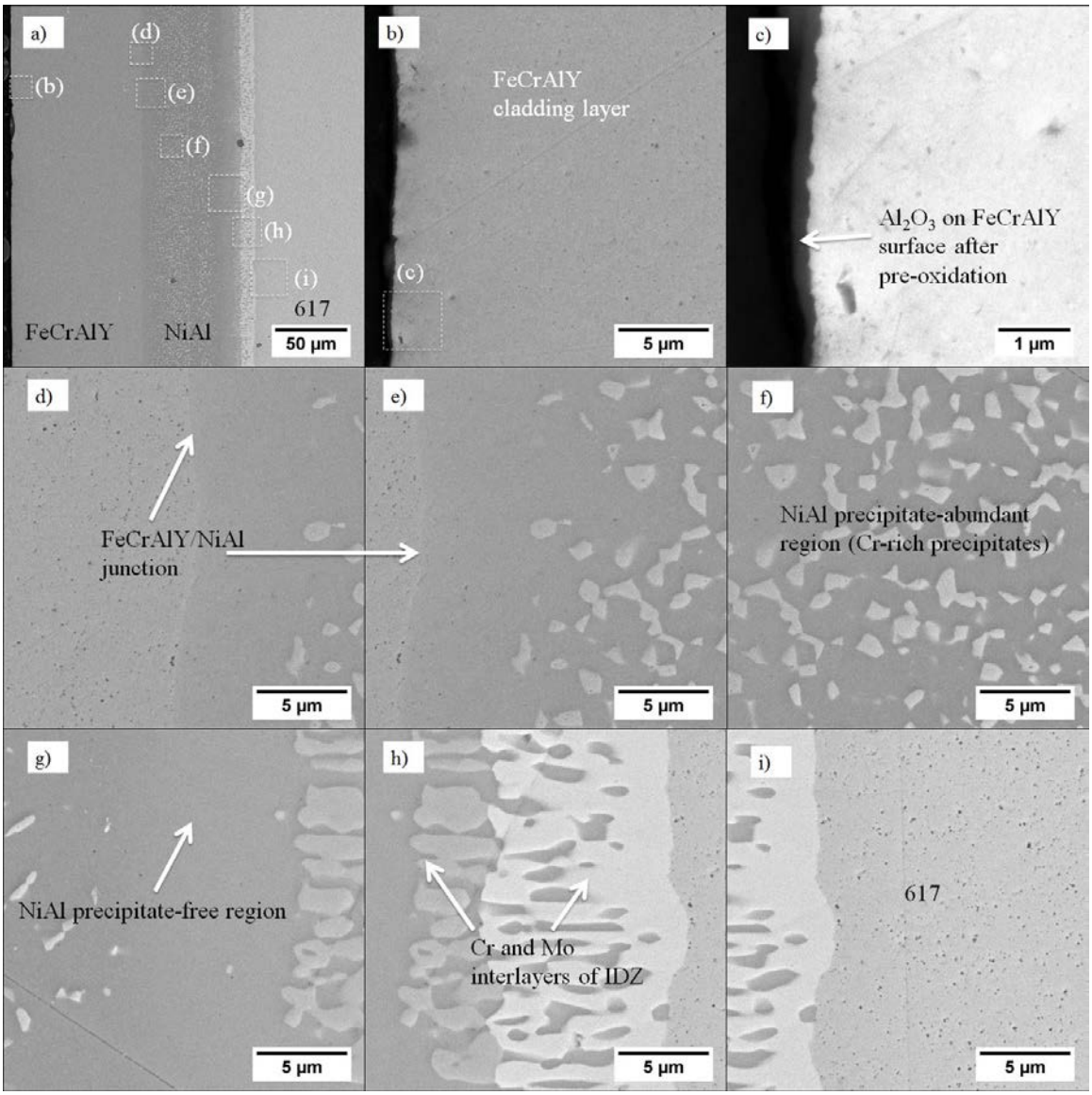

Figure 5-7 Microstructure of as-coated clad-aluminized 617 showing FeCrAlY cladding and NiAl layers with chromium precipitates and a sigma layer (a-i), with Al_2O_3 formed on FeCrAlY surface after pre-oxidation (c).

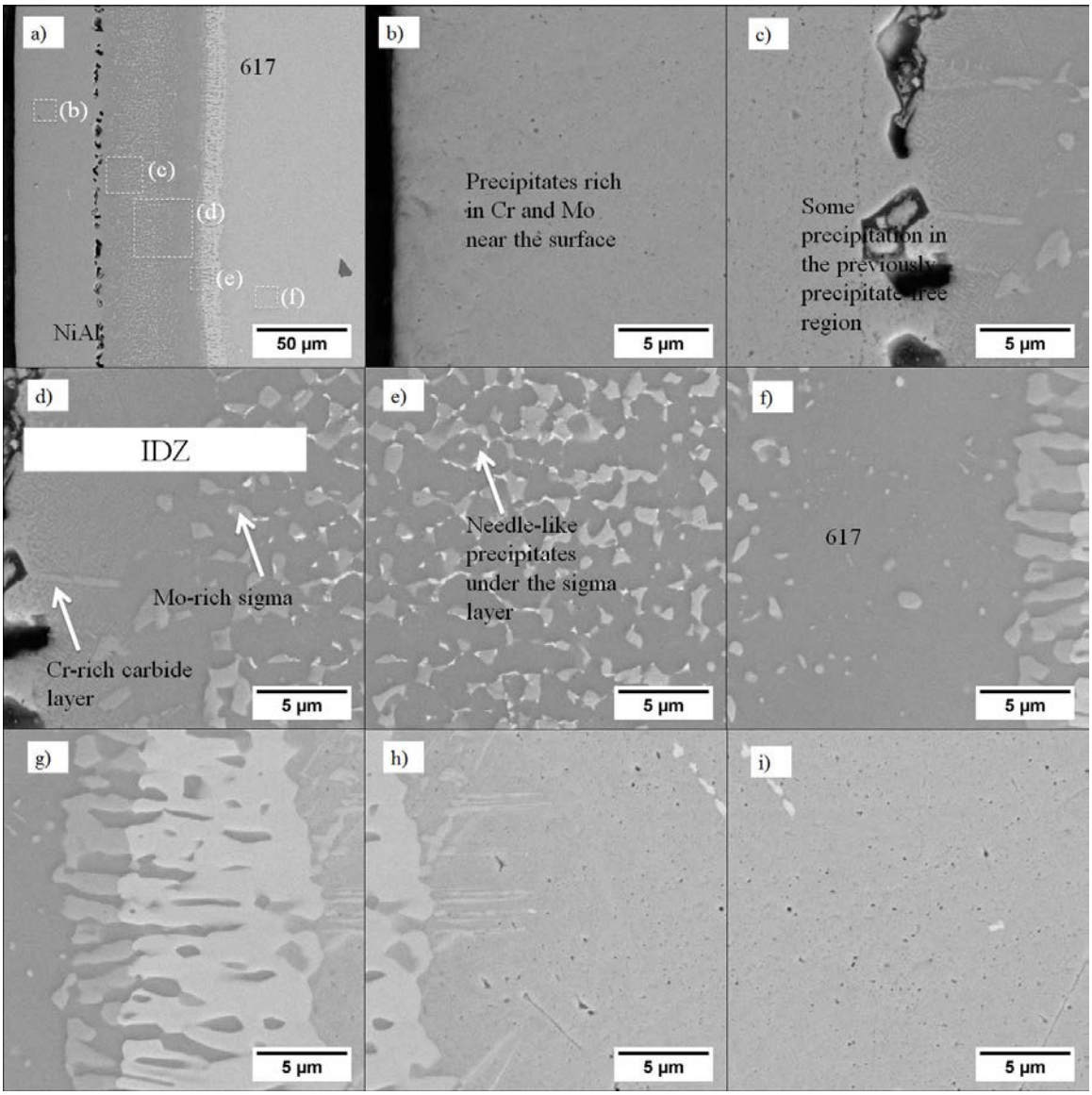

Figure 5-8 Microstructure evolution of clad-aluminized 617 after creep (15/75 MPa/140h/ε=16). The duration reported is total test time.

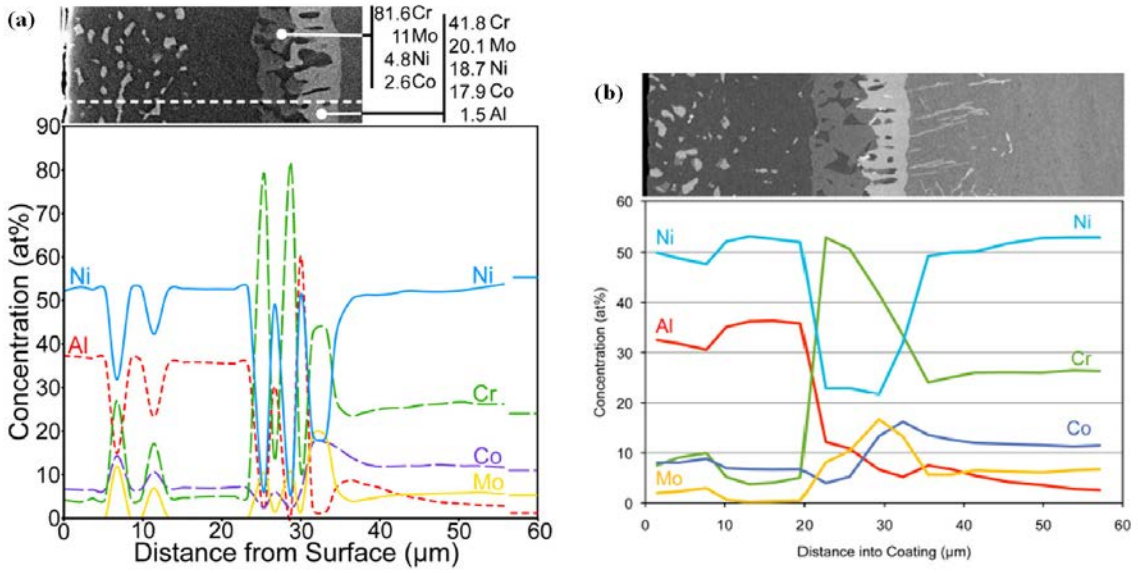

Figure 5-9 EDS concentration profiles of Gen I aluminized 617 showing the effect of ageing on compositional evolution. (a) shows the as-received 617 aluminized at 700°C/9.6h and heat treated at 1000°/18h, and (b) shows aluminized 617 exposed to a decarburizing environment at 800°C/500h. Adapted from reference [18].

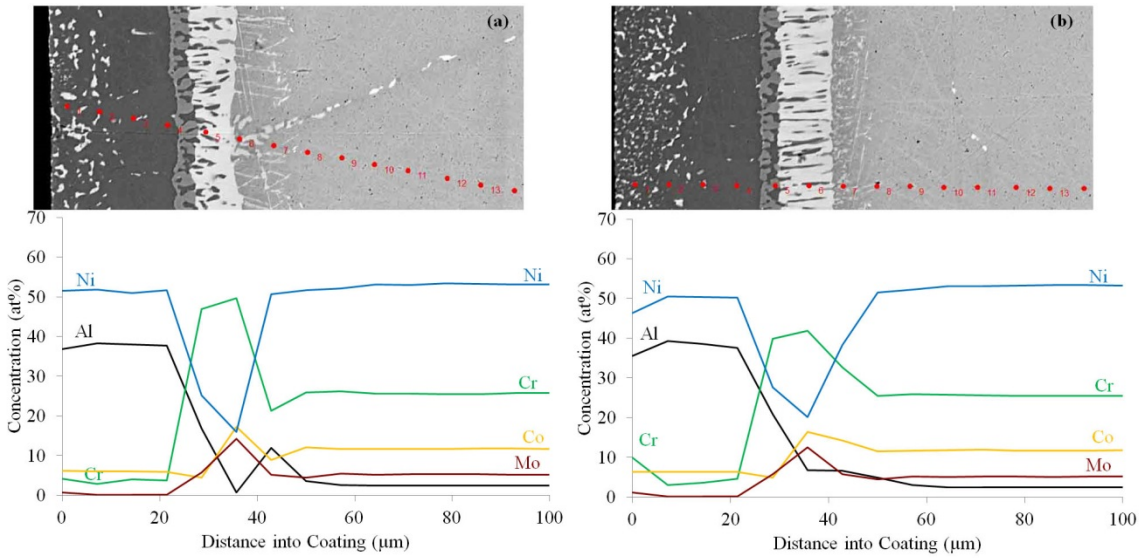

Figure 5-10 EMPA concentration profiles of Gen I aluminized 617 after (a) cyclic creep (10-50 MPa, 513h) and (b) static creep (50 MPa, 215h) at 800°C. The stress axis is vertical and in the plane of the page. The duration reported is total test time.

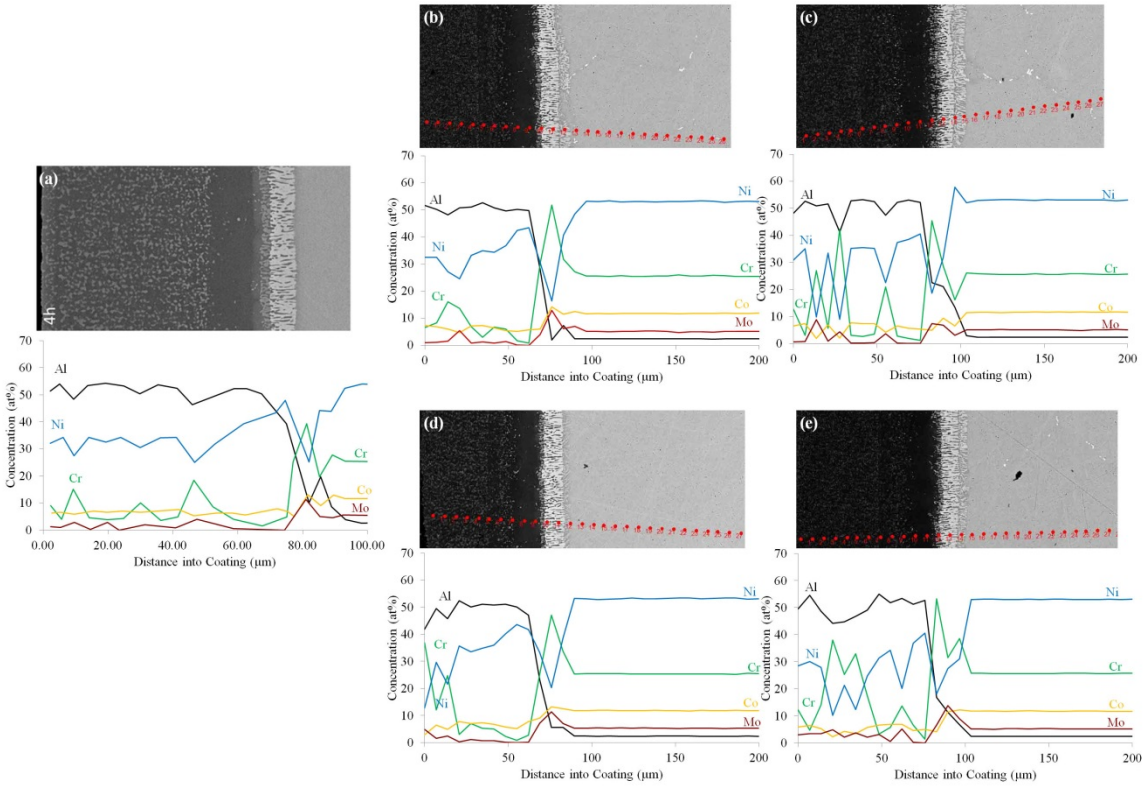

Figure 5-11 EMPA concentration profiles of Gen II aluminized 617 specimens evaluating the effect of creep deformation at 800°C on compositional evolution. The profiles shown are for: (a) as-received material after a heat treatment of 1000°C/4h; (b) static creep 50 MPa/212 h/ε=4%; (c) static creep 60 MPa/286 h/ε=10%; (d) static creep 75 MPa/139h/ε=15%; and (e) cyclic creep at 15-75 MPa/120h/ ε=16%. The fluctuations in the Cr levels are attributed to the presence of precipitates along the profile scan line. The stress axis is vertical and in the plane of the page. The duration reported is total test time.

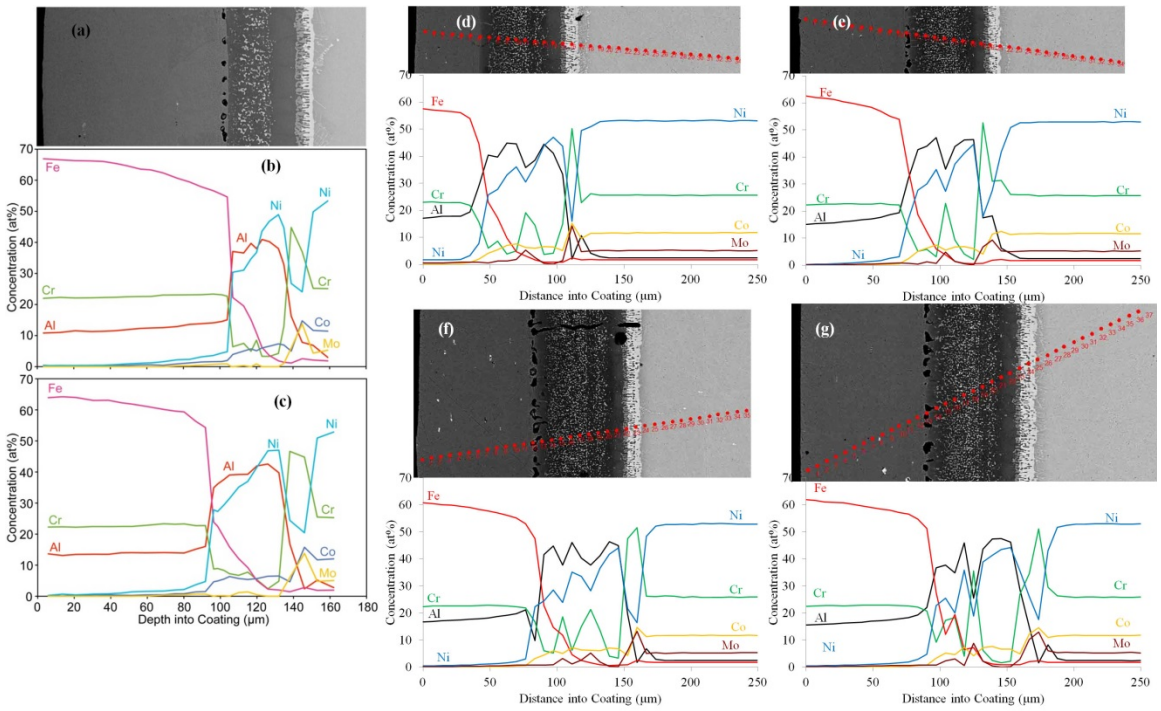

Figure 5-12 EMPA concentration profiles Gen II FeCrAlY/NiAl/617 exploring the potential effect of creep deformation at 800°C on compositional evolution. The profiles shown are for: (b) as-received specimen subjected to a heat treatment of 1000°C/4 h and clad at 1000°C/2 h, (a, c) after 800°C/100 h exposure without load, (d) cyclic creep at 15-75 MPa/117 h/ε=17%, (e) static creep at 75 MPa/109 h/ ε=16%, (f) static creep at 50 MPa/120 h/ε=4%, and (g) cyclic creep at 10-50 MPa/213 h/ε=4%. The stress axis is vertical and in the plane of the page. The duration reported is total test time.

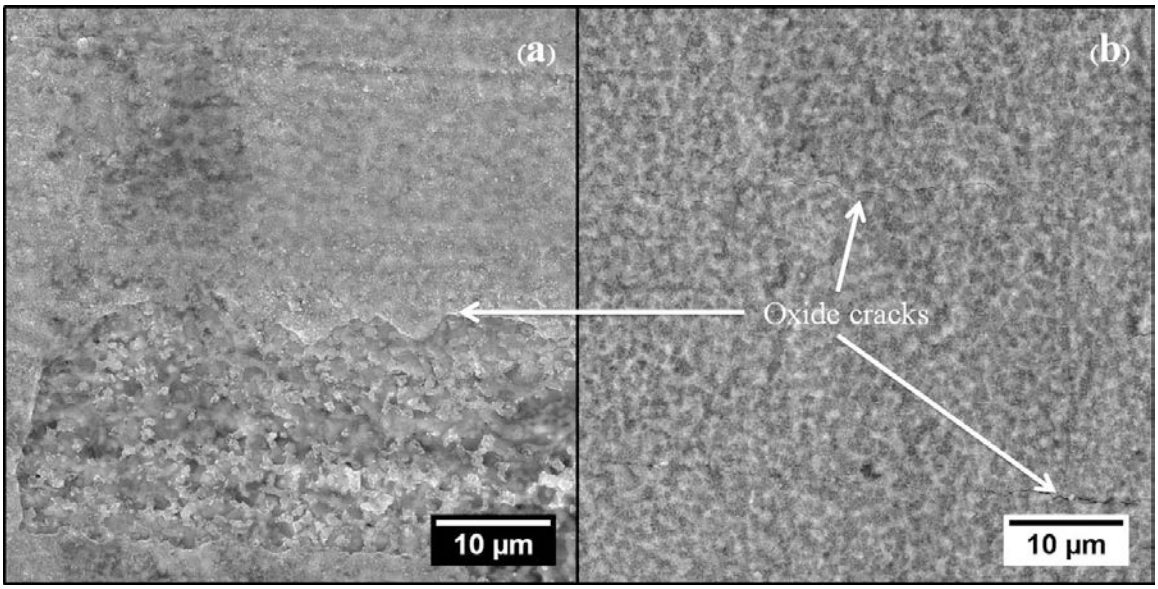

Figure 5-13 SEM images showing damage on the surface of Gen I NiAl/617 specimens after creep in He-8ppm O_2 at 800°C. The stress/strain conditions were (a) 10-50 MPa/513h/ε=3% and (b) 50 MPa/215h/ε=3%. The stress axis is vertical and in the plane of the page. The duration reported is total test time.

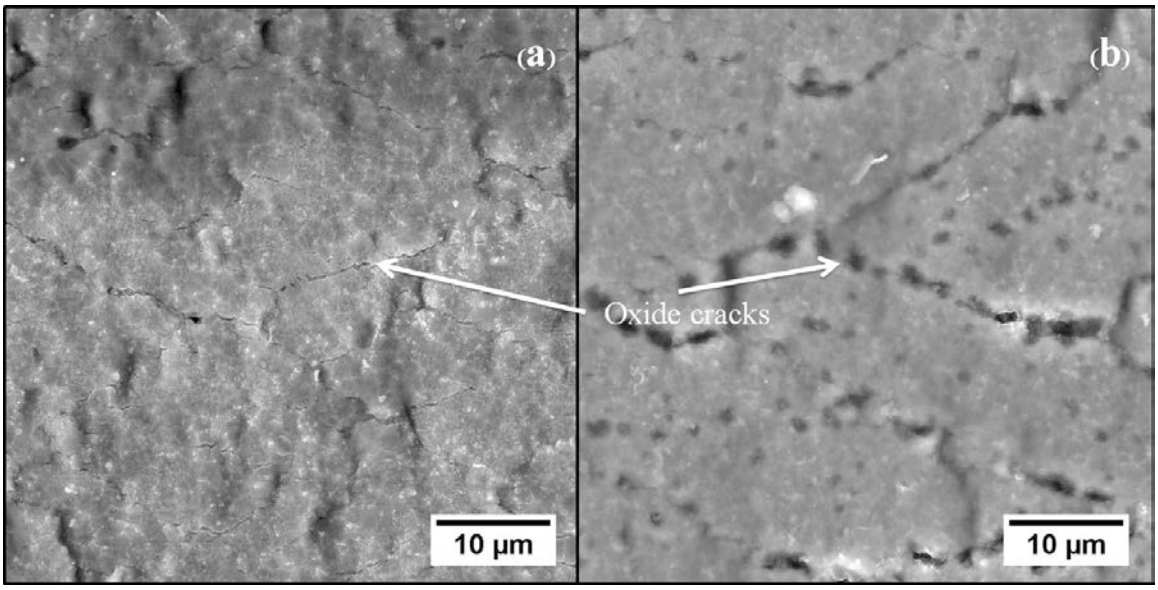

Figure 5-14 SEM images showing damage on the surface of Gen II NiAl/617 specimens after creep in He-CO/CO_2=1320 at 800°C. The stress/strain conditions were (a) 75 MPa/139h/15% and (b) 15-75 MPa/120h/ε=16%. The stress axis is vertical and in the plane of the page. The duration reported is total test time.

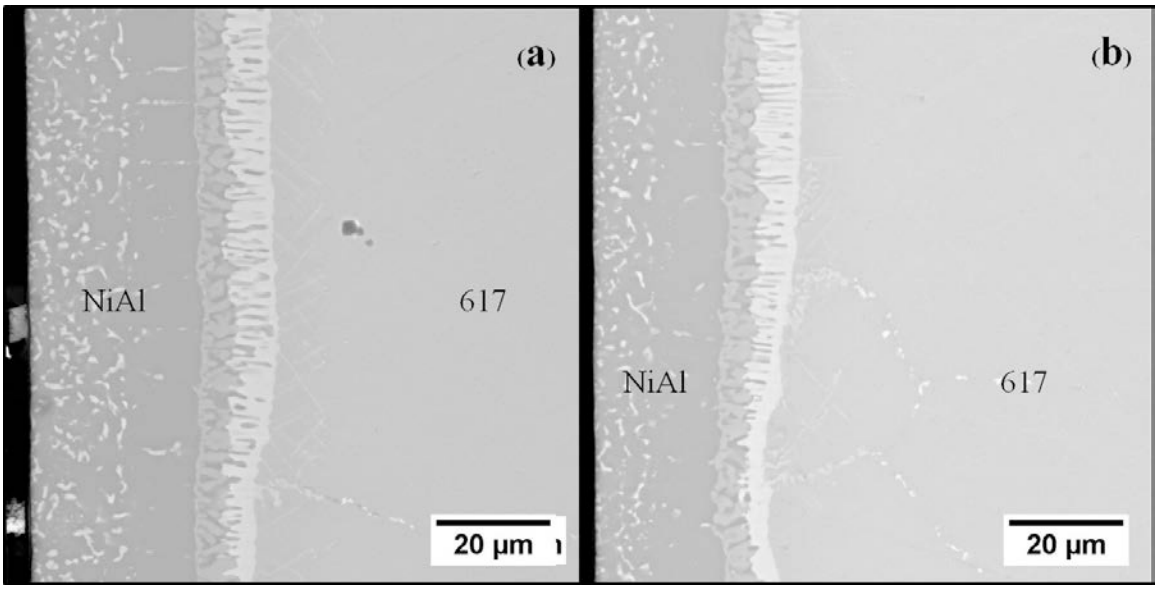

Figure 5-15 Cross-sectional SEM images showing no cracking on Gen I NiAl/617 specimens after creep in He-8ppm O_2 at 800°C. The stress/strain conditions were (a) 10-50 MPa/513h/ε=3% and (b) 50 MPa/215h/ε=3%. The stress axis is vertical and in the plane of the page. The duration reported is total test time.

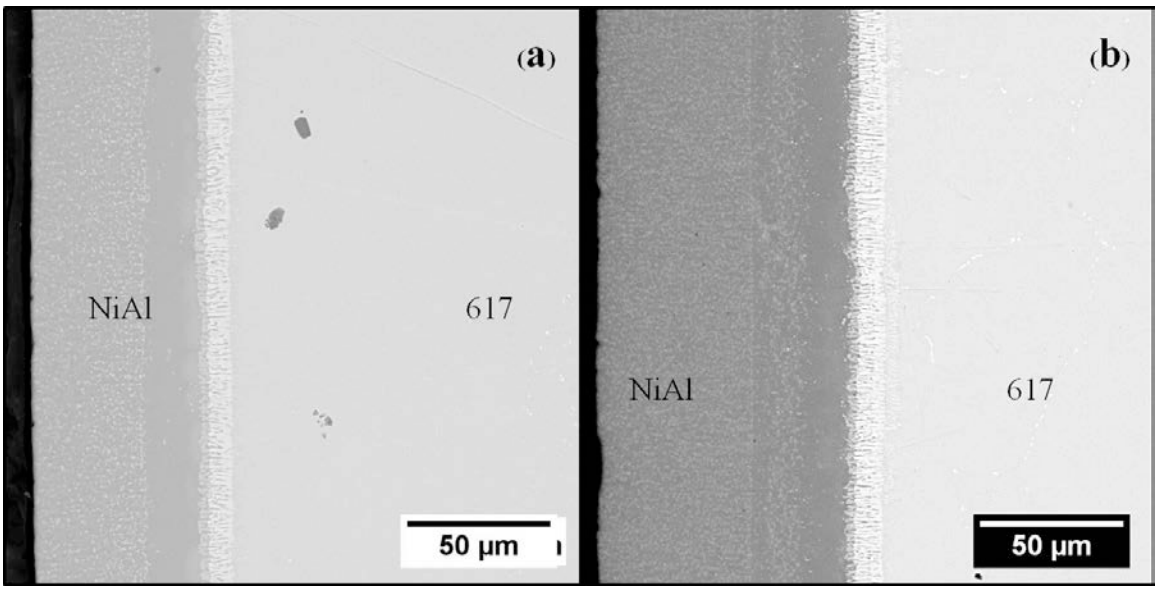

Figure 5-16 Cross-sectional SEM images showing no cracking on Gen II NiAl/617 specimens after creep in He-CO/CO_2=1320 at 800°C. The stress/strain conditions were (a) 75 MPa/139h/15%, and (b) 15-75 MPa/120h/ε=16%. The stress axis is vertical and in the plane of the page. The duration reported is total test time.

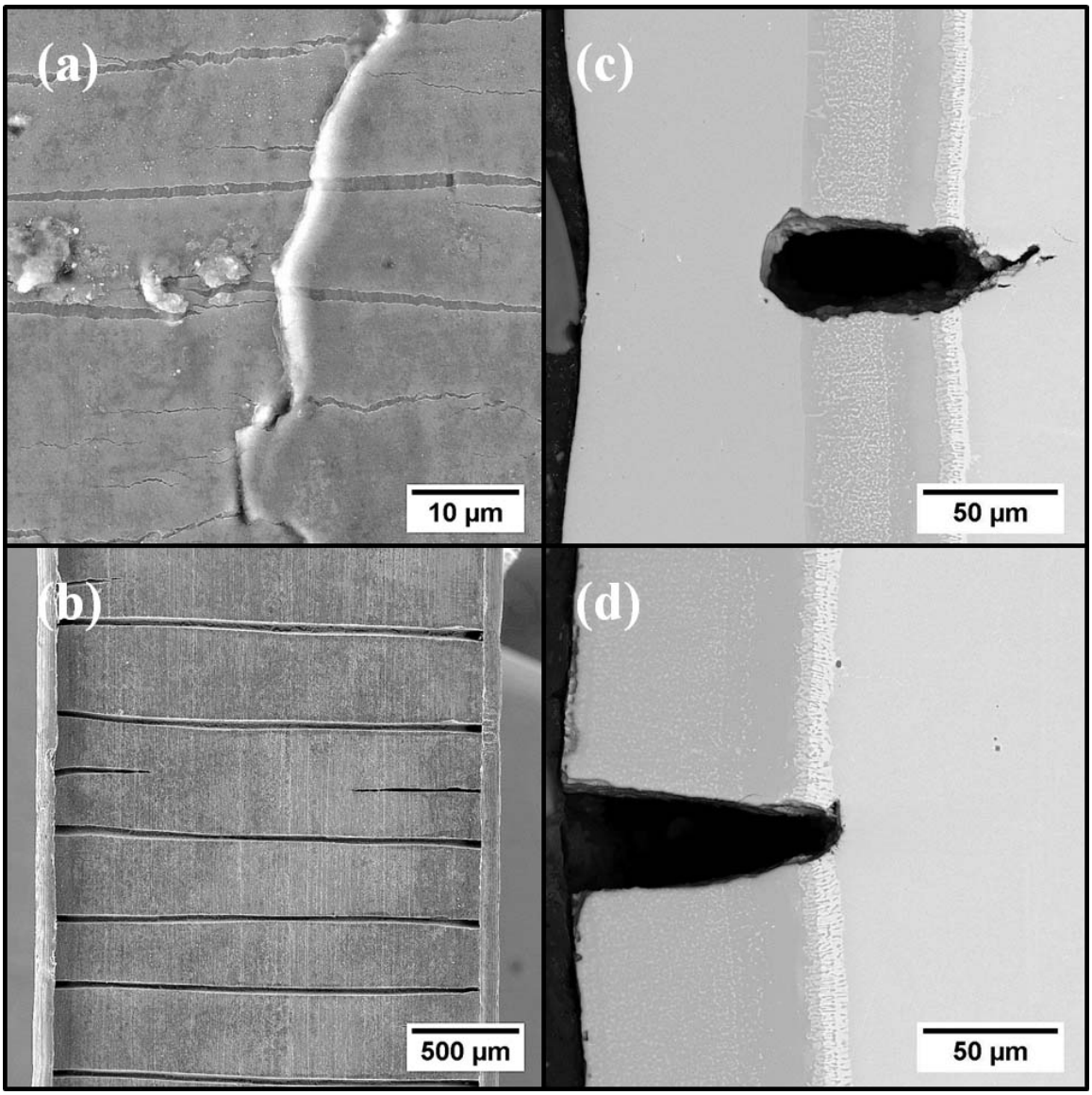

Figure 5-17 SEM images of crept FeCrAlY/NiAl/617 specimens showing damage on (a) the wider surface that is aluminized and clad, (b) narrower surface that is aluminized only, with accompanying cross-sectional views (c) parallel to the narrower surface, (d) parallel to the wider surface. The wider surface shows grain uplifts in the cladding whereas the narrower surface shows cracks in the aluminized-only layer. The test conditions are 75 MPa/109h/ε=16%/He-0.1ppmO_2. The duration reported is total test time.

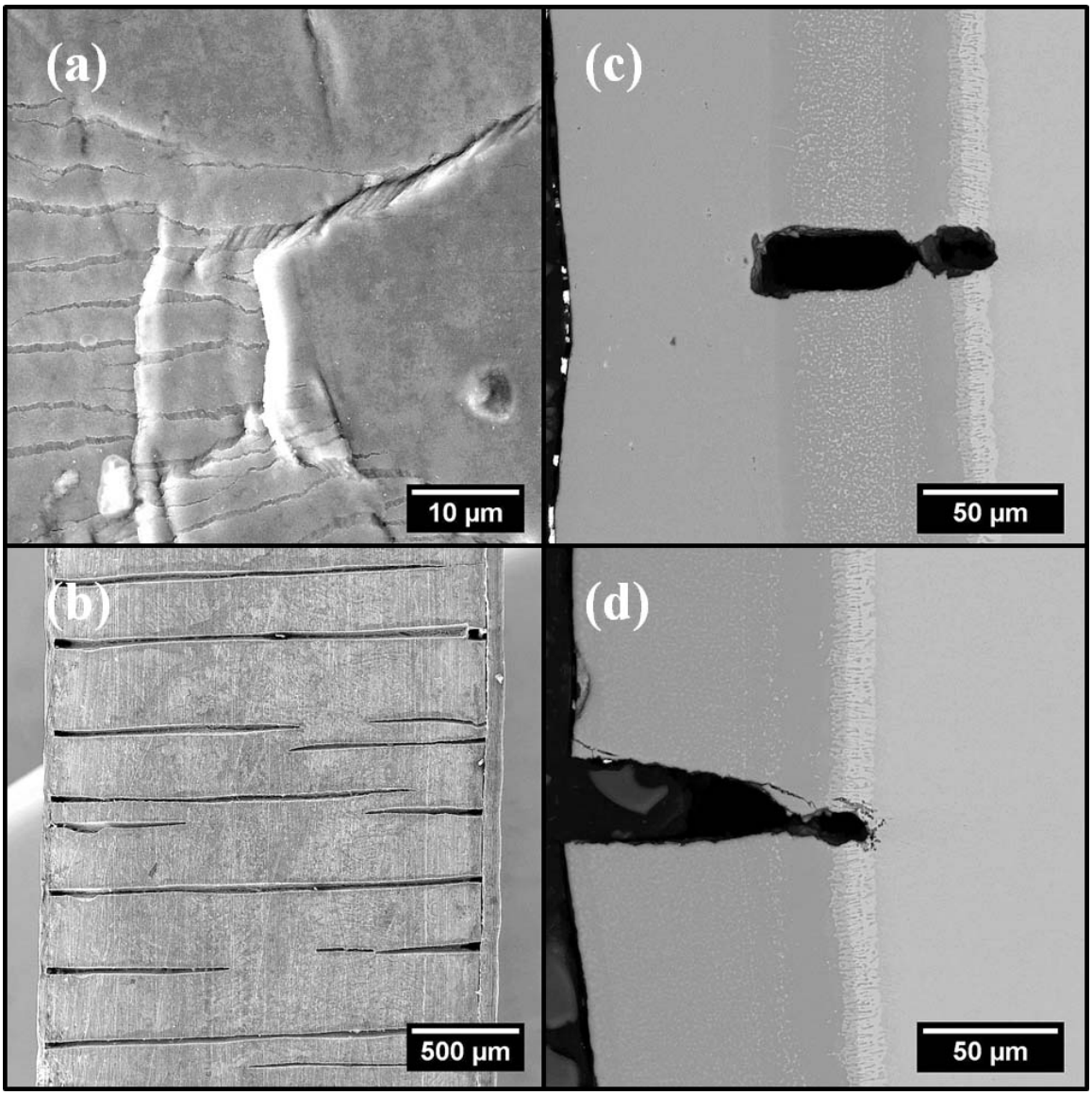

Figure 5-18 SEM images of crept FeCrAlY/NiAl/617 specimens showing damage on (a) the wider surface that is aluminized and clad, (b) narrower surface that is aluminized only, with accompanying cross-sectional views (c) parallel to the narrower surface, (d) parallel to the wider surface. The wider surface shows grain uplifts in the cladding whereas the narrower surface shows cracks in the aluminized-only layer. The test conditions are 15/75 MPa/140h/ε=16%/He-CO/CO_2=1320. The duration reported is total test time.

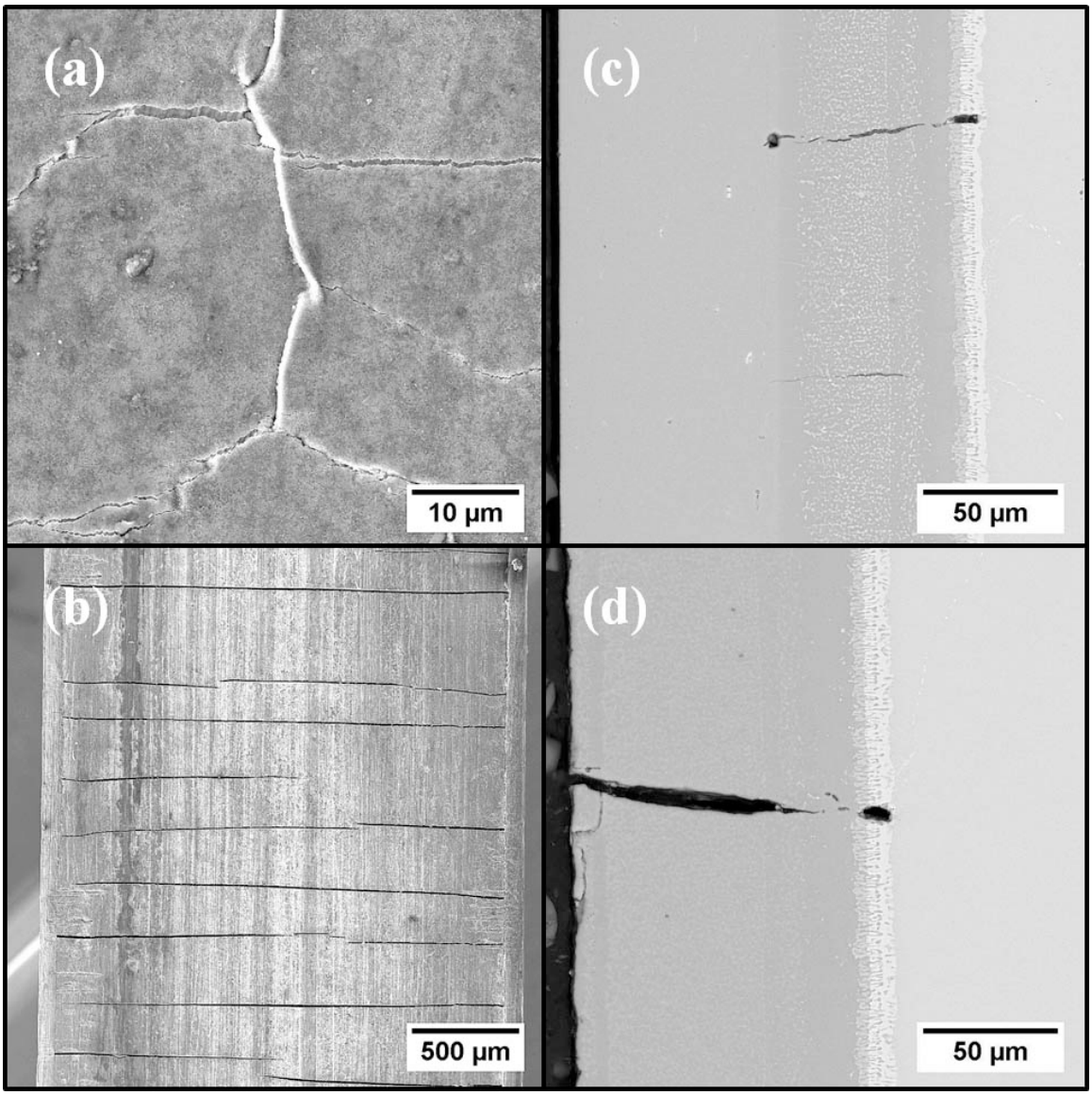

Figure 5-19 SEM images of crept FeCrAlY/NiAl/617 specimens showing damage on (a) the wider surface that is aluminized and clad, (b) narrower surface that is aluminized only, with accompanying cross-sectional views (c) parallel to the narrower surface, (d) parallel to the wider surface. The wider surface shows grain uplifts in the cladding whereas the narrower surface shows cracks in the aluminized-only layer. The test conditions are 50 MPa/120h/ε=4%/He-CO/CO_2=1320. The duration reported is total test time.

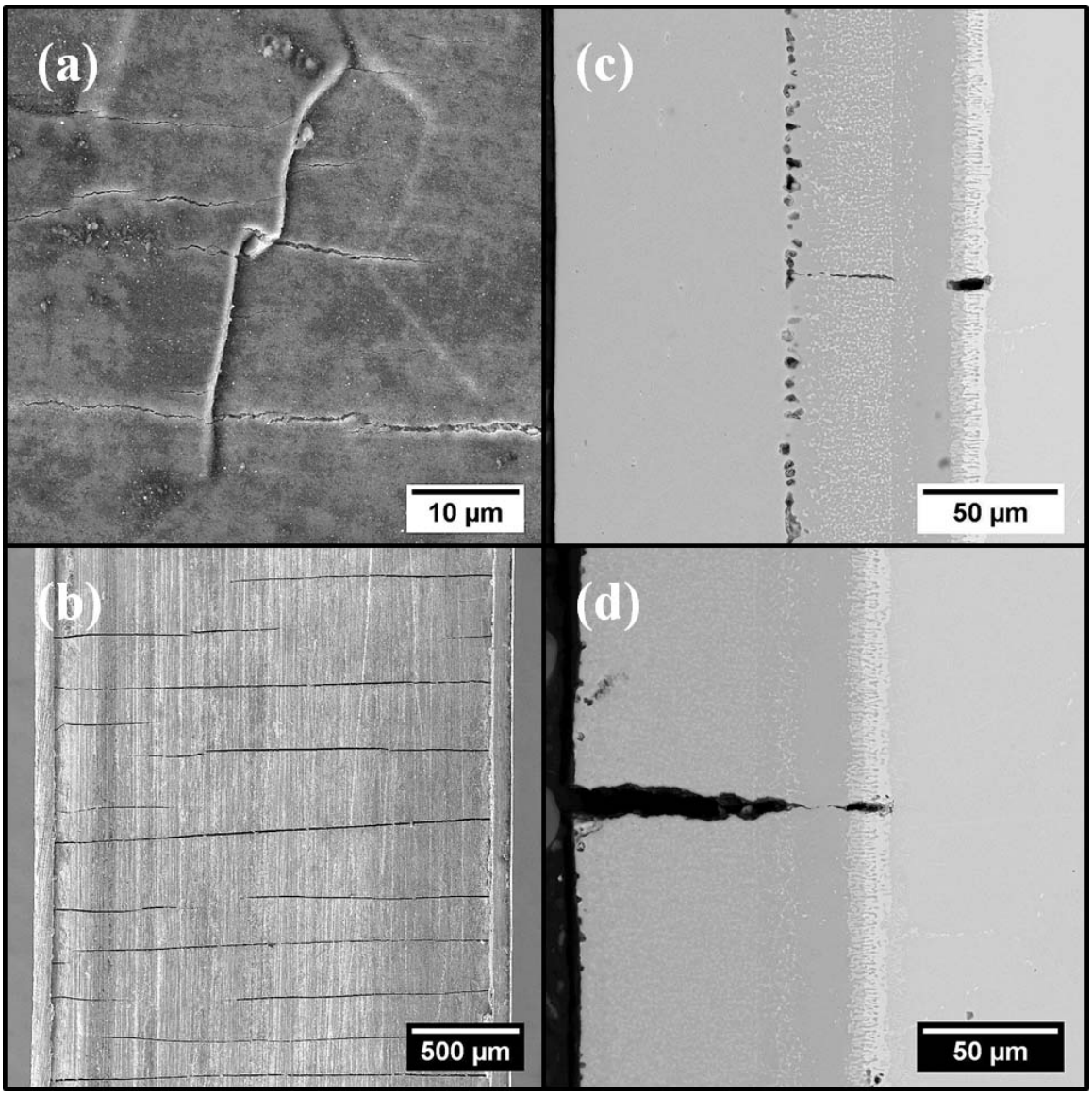

Figure 5-20 SEM images of crept FeCrAlY/NiAl/617 specimens showing damage on (a) the wider surface that is aluminized and clad, (b) narrower surface that is aluminized only, with accompanying cross-sectional views (c) parallel to the narrower surface, (d) parallel to the wider surface. The wider surface shows grain uplifts in the cladding whereas the narrower surface shows cracks in the aluminized-only layer. The test conditions are 10/50 MPa/213h/4%/He-CO/CO_2=1320. The duration reported is total test time.

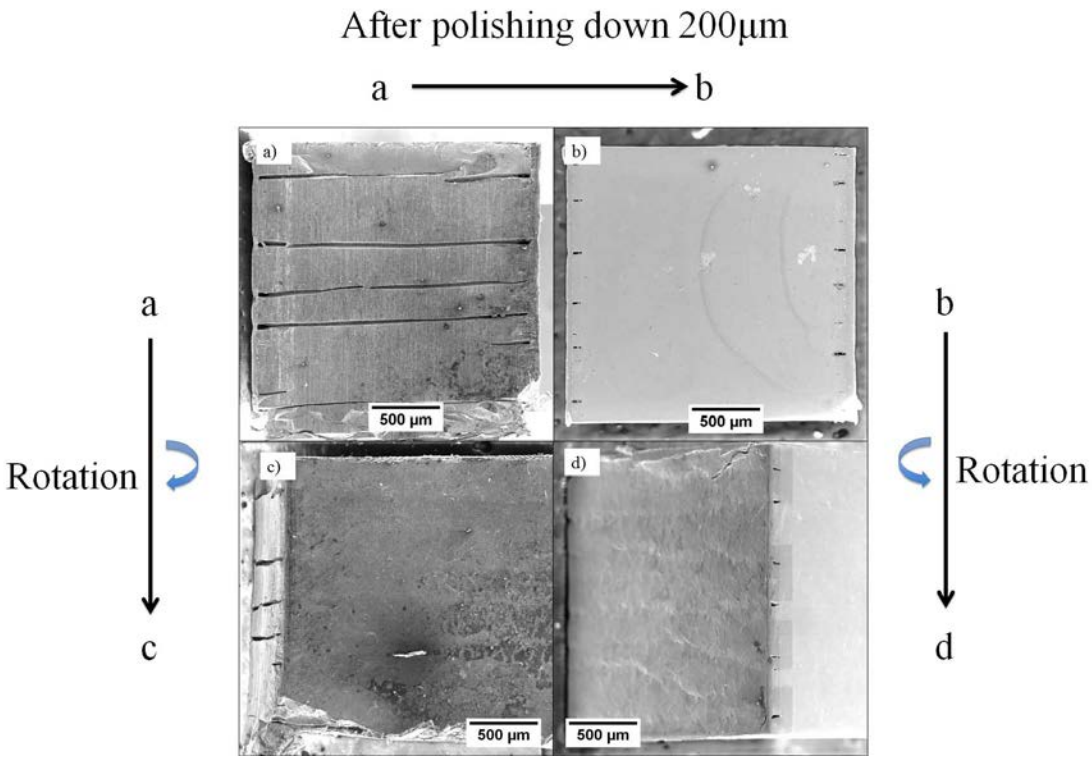

Figure 5-21 SEM images of FeCrAlY/NiAl/617 after cyclical creep (15/75 MPa, 140h) to 16% strain showing that the NiAl cracks wrap around the specimen. The duration reported is total test time.

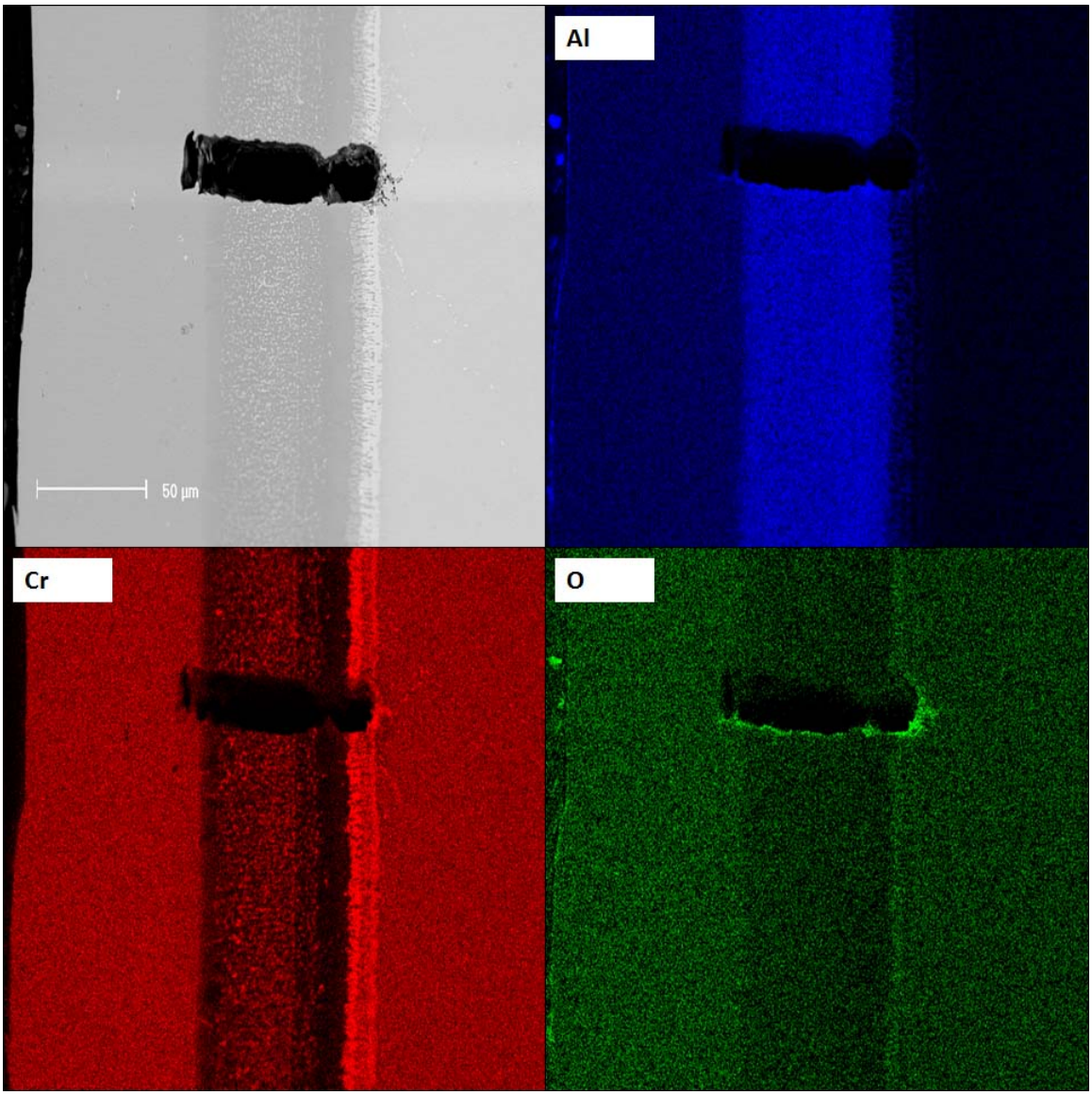

Figure 5-22 EDS elementals maps taken from a cross-section parallel to the stress axis of clad-aluminized 617 after cyclic creep (15/75 MPa/140h/ε=16%). The region corresponds to clad surfaces. The duration reported is total test time.

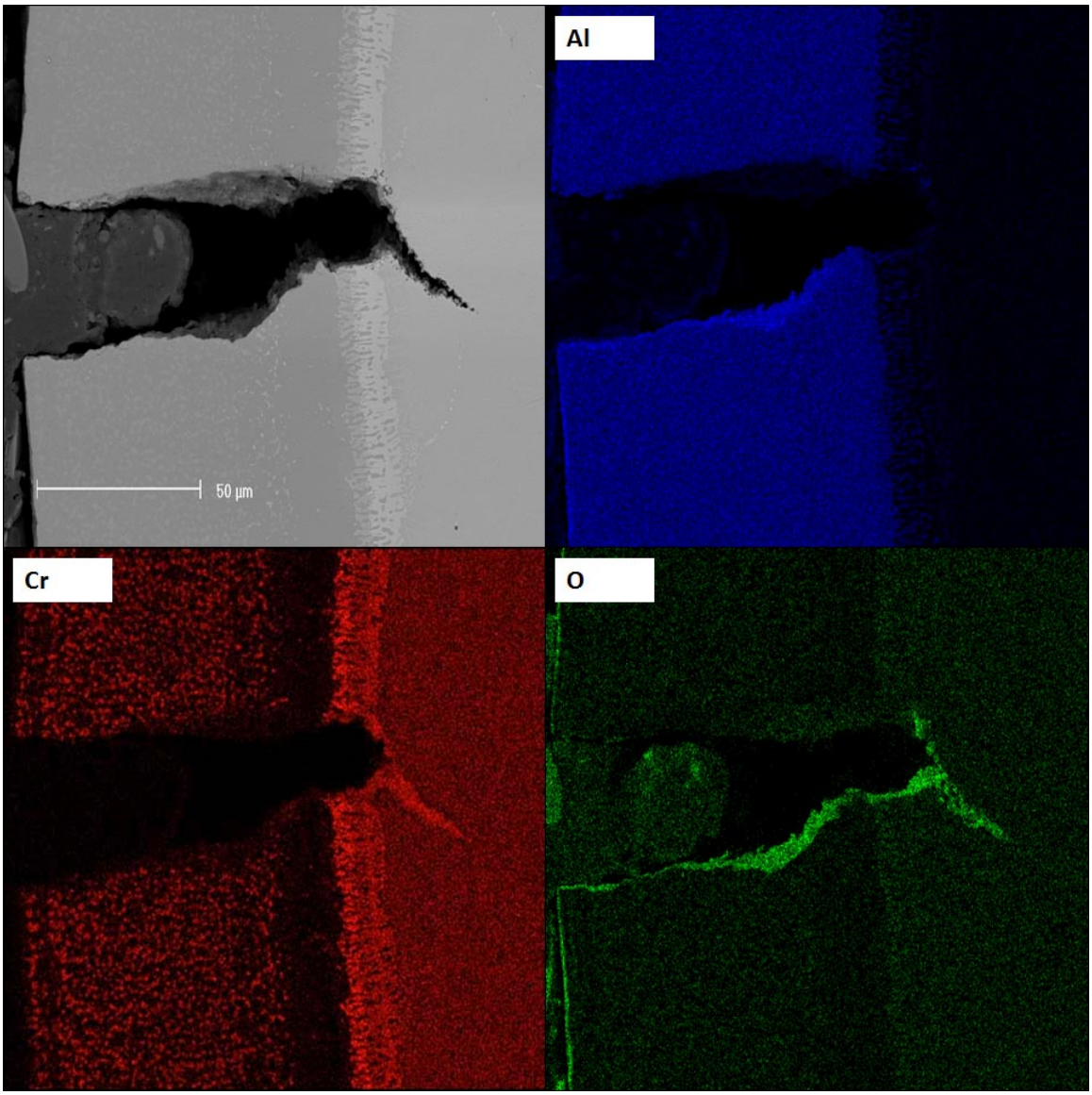

Figure 5-23 EDS elementals maps taken from a cross-section parallel to the stress axis of clad-aluminized 617 after cyclic creep (15/75 MPa/140h/ε=16%). The region corresponds to aluminized-only surfaces. The duration reported is total test time.

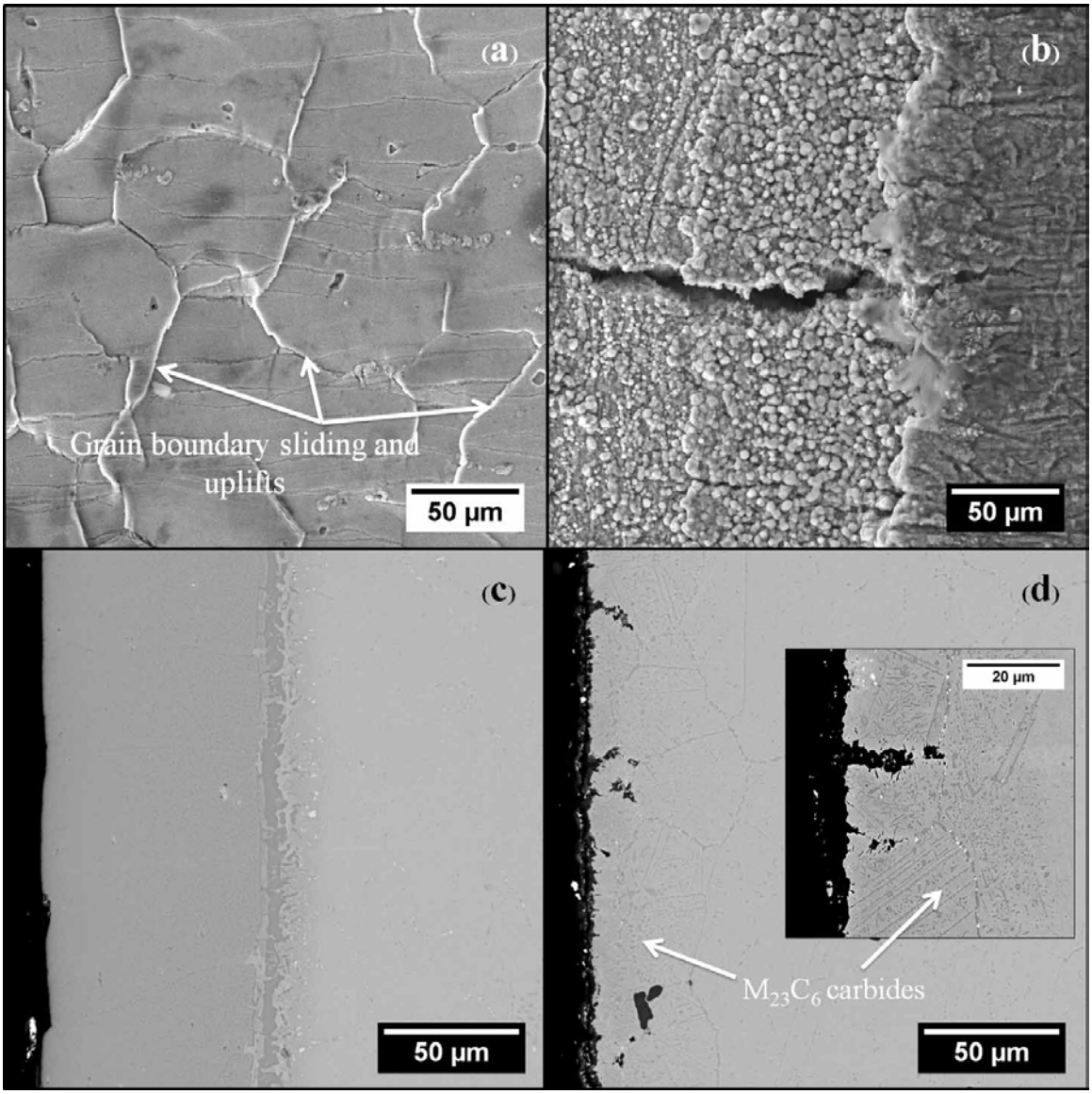

Figure 5-24 SEM images of FeCrAlY/617 specimens showing damage on the (a) wider surface that is clad, and (b), the narrower surface that is bare 617(b), as well as cross sectional views (c) parallel to the narrower surface (c), and (d) parallel to the wider surface. The wider surface shows grain uplifts in the cladding whereas the narrower surface shows environmental attack in the exposed 617. The stress/strain conditions were 15-75 MPa/167h/ε=14% in a carburizing environment (He-CO/CO_2=1320). The stress axis is vertical and in the plane of the page. The duration reported is total test time.

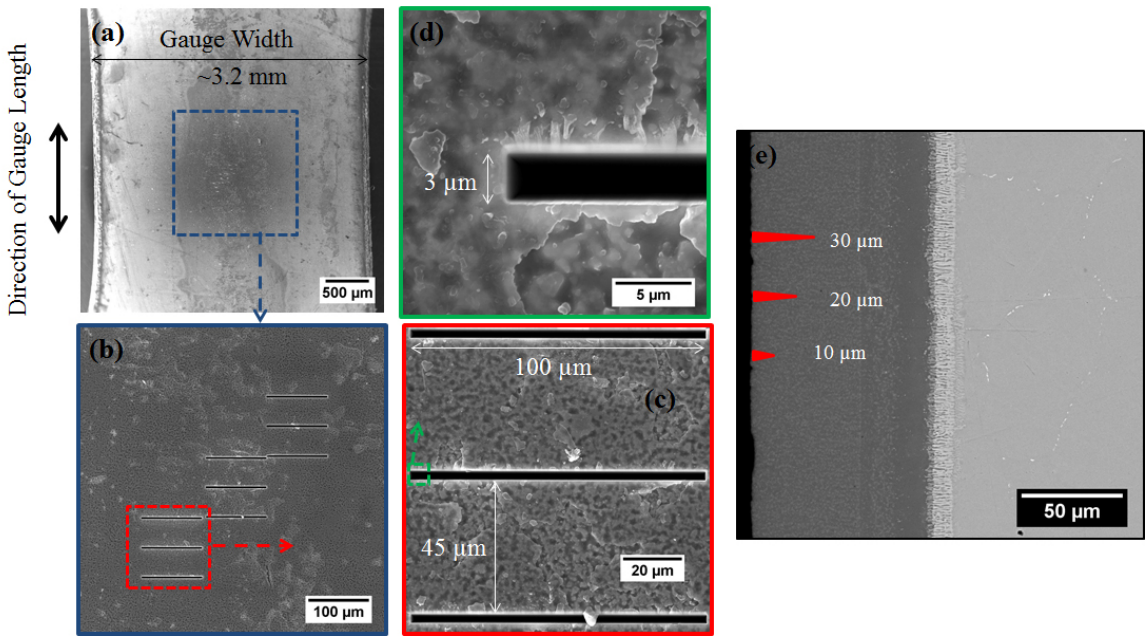

Figure 5-25 SEM images showing FIB notches used to investigate crack propagation in the aluminized layer of Gen II NiAl/617. Three sets of implanted notches with each set having 3 different depths as schematized in (e) to provide a larger specimen area for post-experiment analysis.

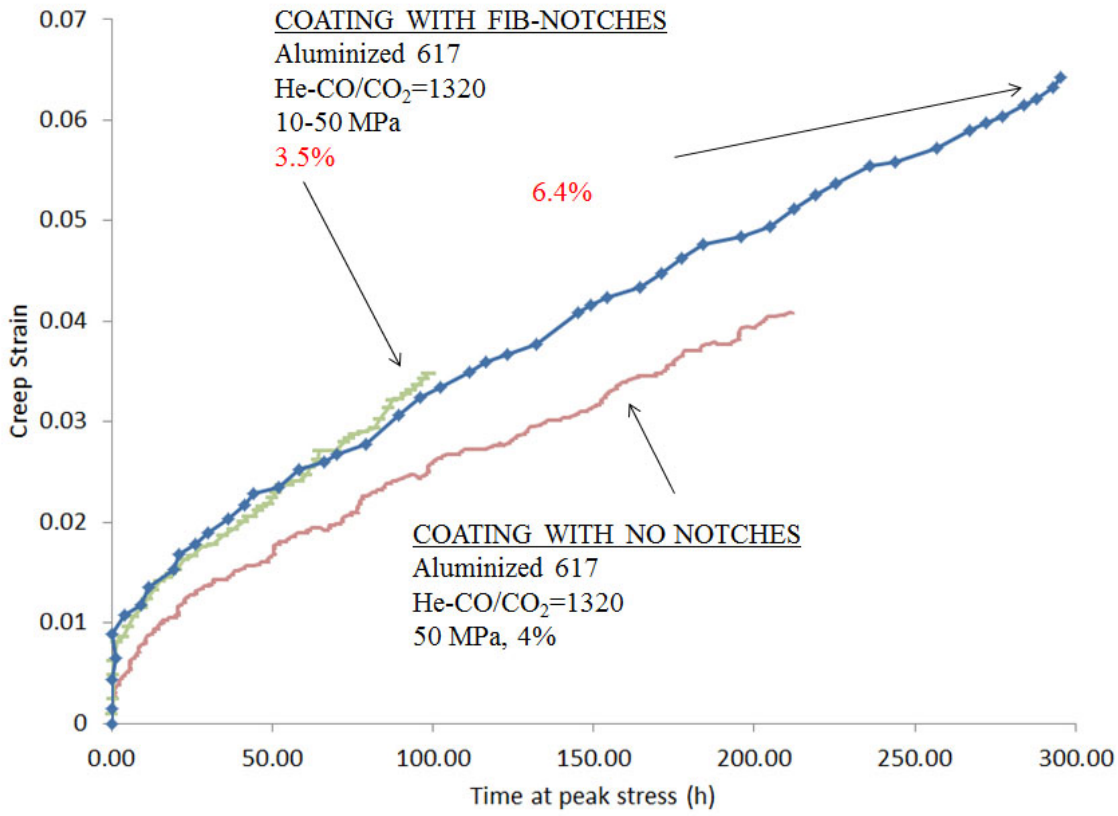

Figure 5-26 Curves of interrupted cyclic creep of NiAl/617 with and without notches indicating that the presence of the localized notches does not affect the creep rates (slope of linear part of curve). Note that the creep strains are reported as a function of time at peak stress. The total time at exposure is reported in the text, and is equivalent to twice the time at peak stress.

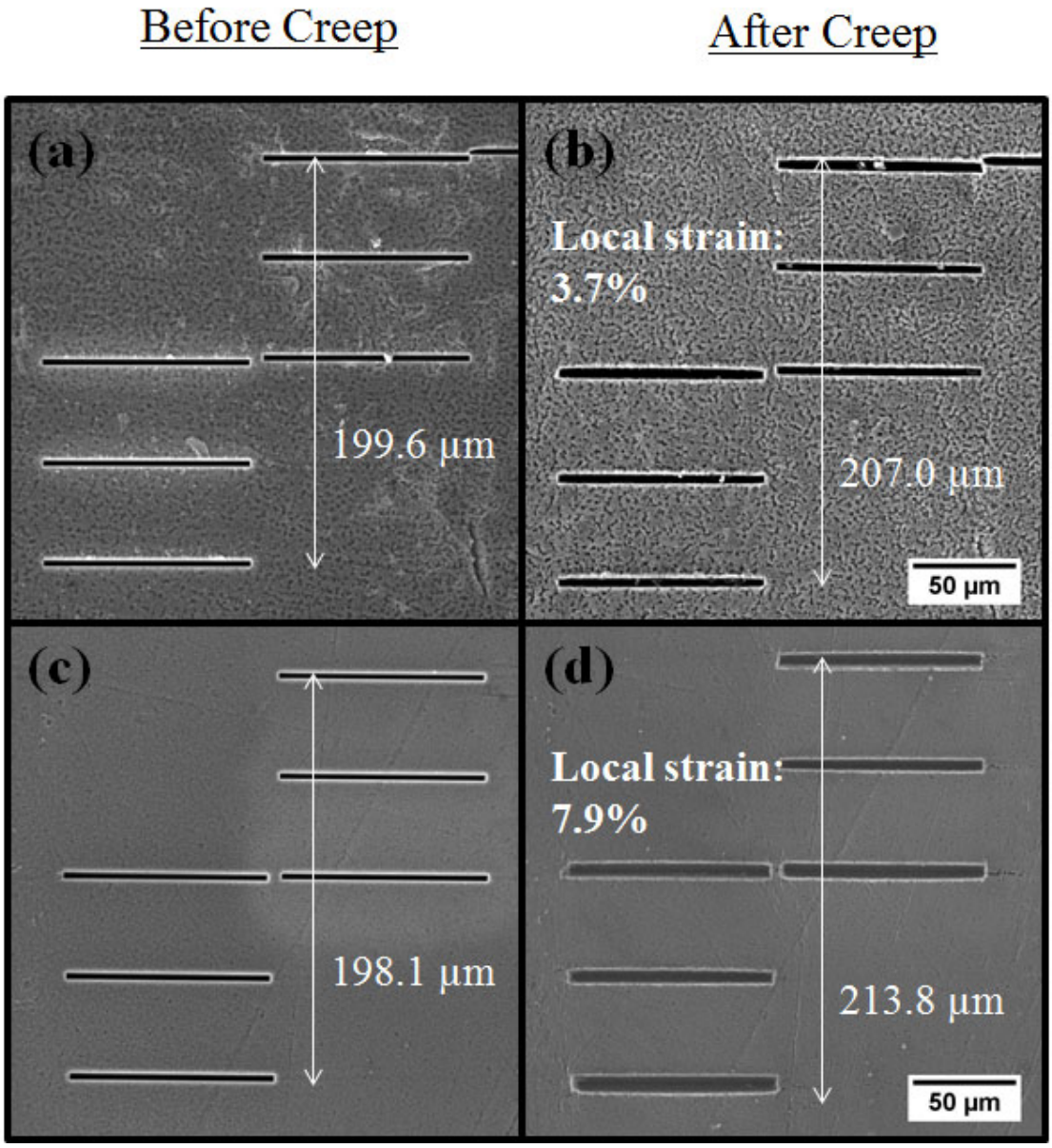

Figure 5-27 SEM images (low magnification) showing the determination of local strain after cyclic creep (10-50 MPa) at 800°C in a carburizing environment (He-CO/CO_2=1320) and subjected to 198h/3.5% strain (a,b) and 594h/6.4% strain (c,d). The stress axis is vertical and in the plane of the page. The duration reported is total test time.

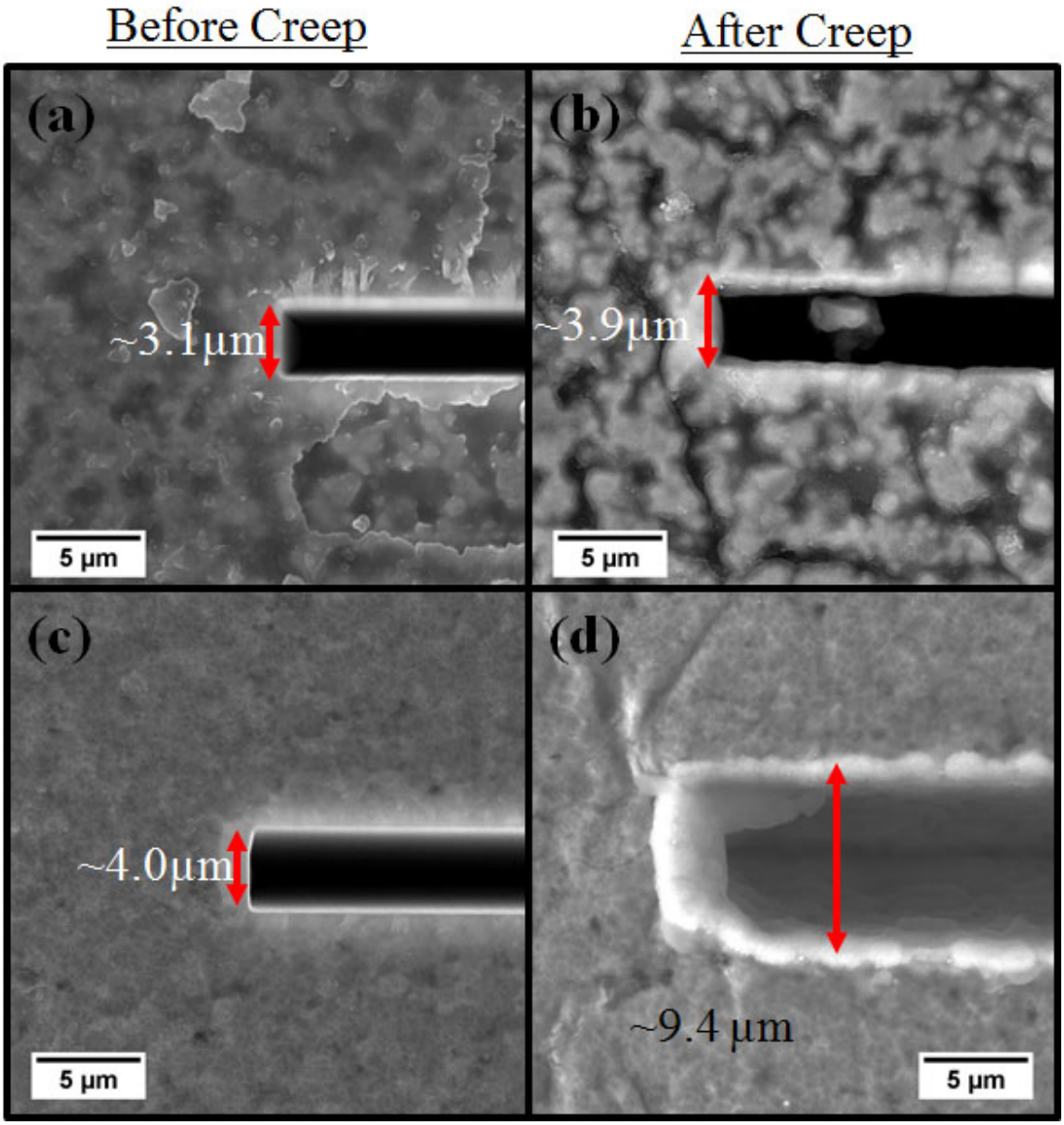

Figure 5-28 SEM images (high magnification) showing the dimensional changes on the individual notches after cyclic creep (10-50 MPa) at 800°C in a carburizing environment (He-CO/CO_2=1320) and subjected to (a,b) 198h/3.5% strain and (c,d) 594h/6.4% strain. Note the significant dimensional change in the notch opening after higher strains (c→d compared to a→b). The stress axis is vertical and in the plane of the page. The duration reported is total test time.

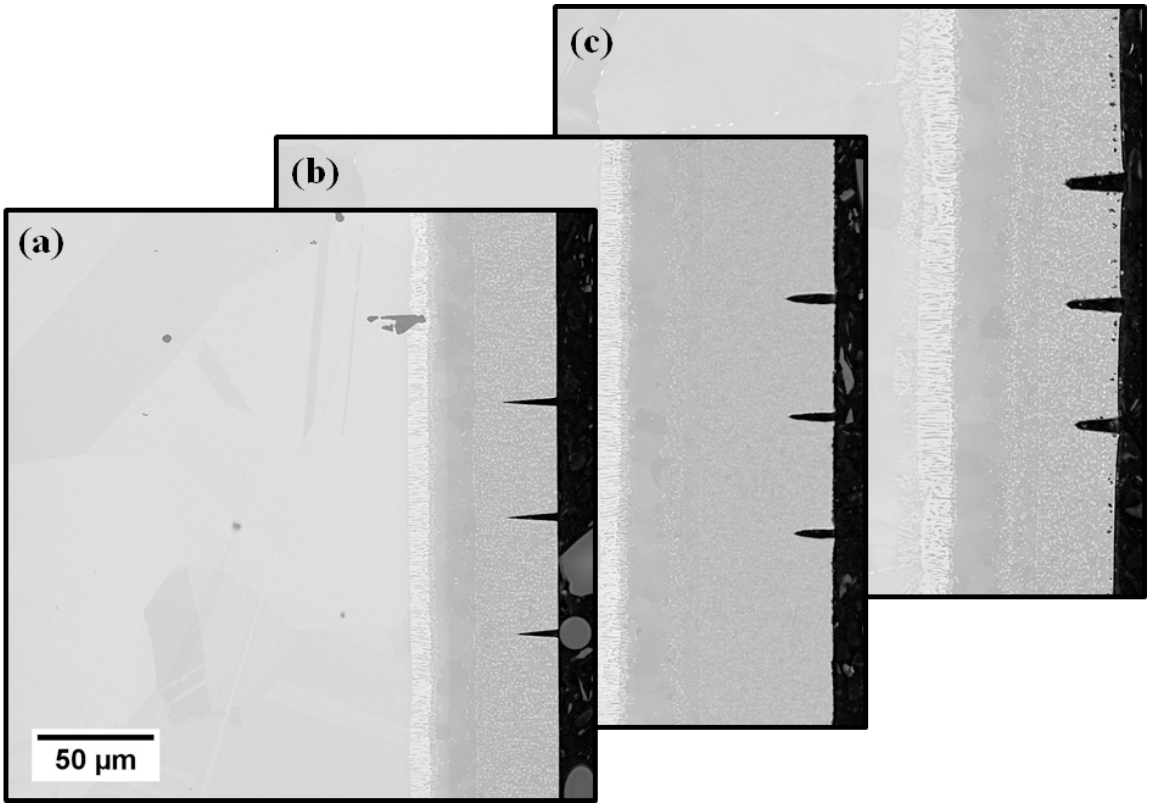

Figure 5-29 SEM images (high magnification) showing the three notches on the untested coupon (a), and those having undergone cyclic creep (10-50 MPa) at 800°C in a carburizing environment (He-CO/CO_2=1320) and subjected to 198h/3.5% strain (b) and 594h/6.4% strain (c). The stress axis is vertical and in the plane of the page. The duration reported is total test time.

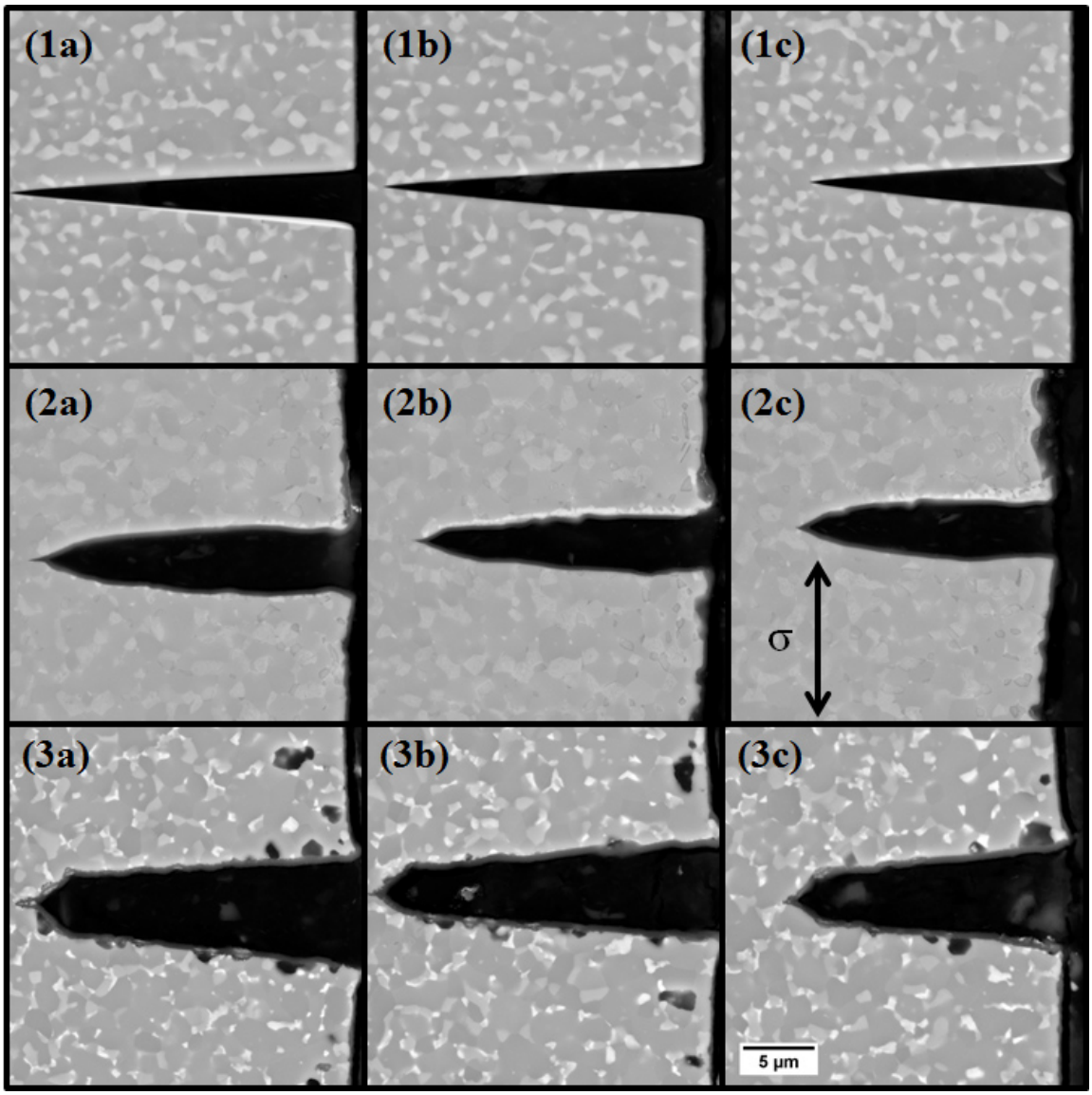

Figure 5-30 SEM images (low magnification) showing the three notches on the untested coupon (1), and those having undergone cyclic creep (10-50 MPa) at 800°C in a carburizing environment (He-CO/CO_2=1320) and subjected to 198h/3.5% strain (2) and 594h/6.4% strain (3). Note the penetration of the oxide at the notch root in (2) and the effect of microstructure in the neighborhood of the tip oxidation as seen in (3). The stress axis is vertical and in the plane of the page. The duration reported is total test time.

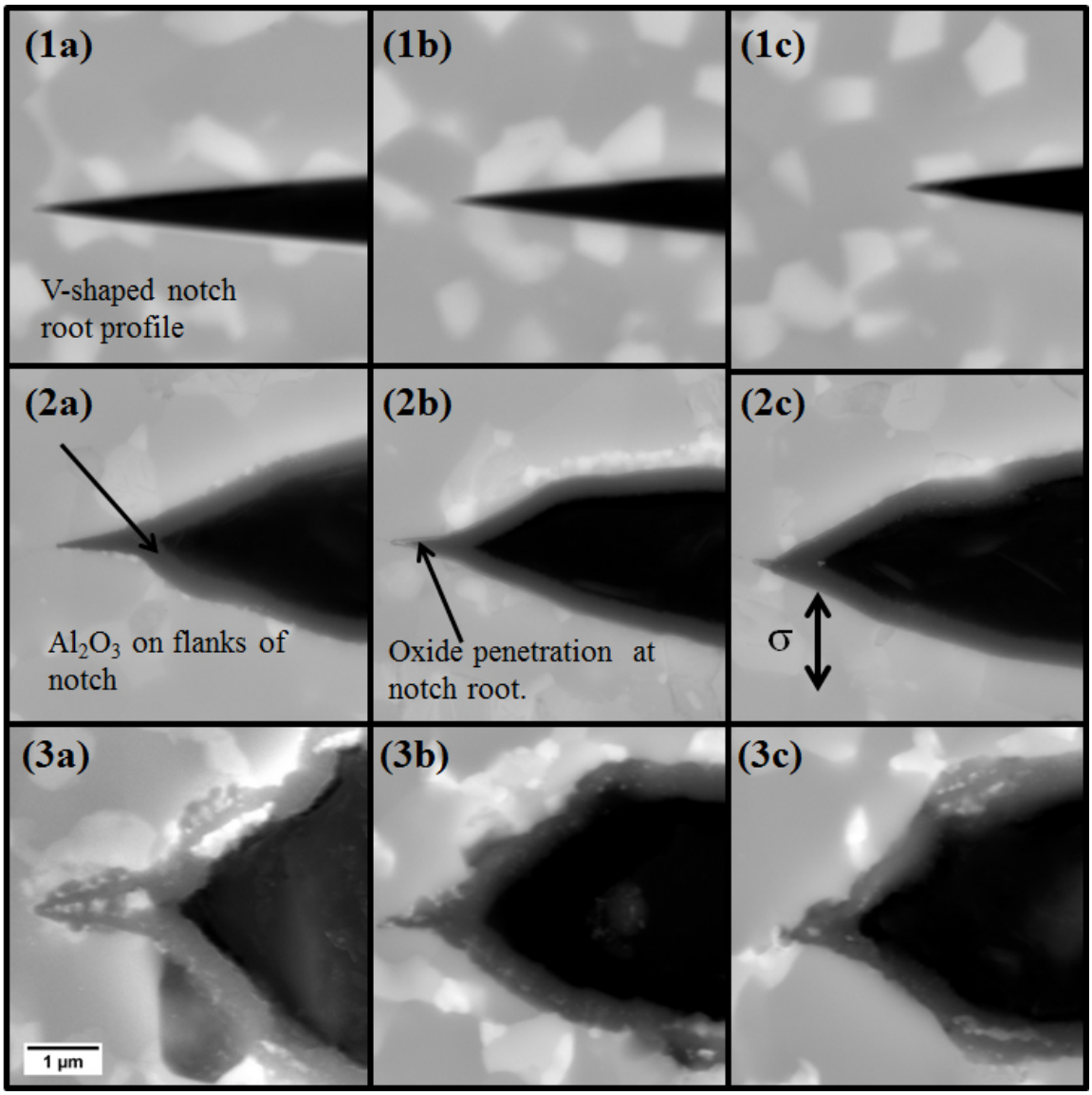

Figure 5-31 SEM images (high magnification) showing the three notches on the untested coupon (1), and those having undergone cyclic creep (10-50 MPa) at 800°C in a carburizing environment (He-CO/CO_2=1320) and subjected to 198h/3.5% strain (2) and 594h/6.4% strain (3). Note the penetration of the oxide at the notch root in (2) and the effect of microstructure in the neighborhood of the tip oxidation as seen in (3). The stress axis is vertical and in the plane of the page. The duration reported is total test time.

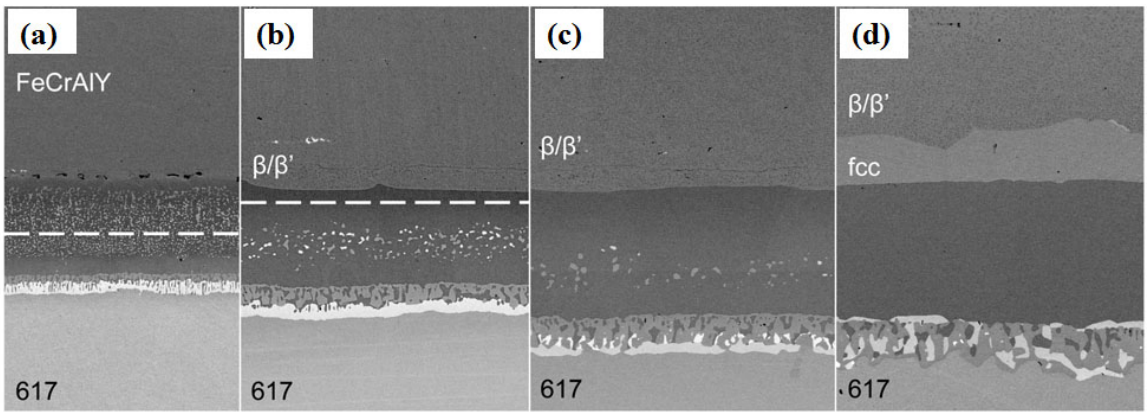

Figure 5-32 SEM images of Gen II clad + aluminized 617 (a) as clad and after 1000°C heat treatment for (b) 24h, (c) 100h and (d) 500h. The dashed lines in (a,b,c,d) indicate the approximate boundary between Al-rich NiAl and Ni-rich NiAl. The heat treatment of interest for dissolving the precipitates is ~24h.[18]

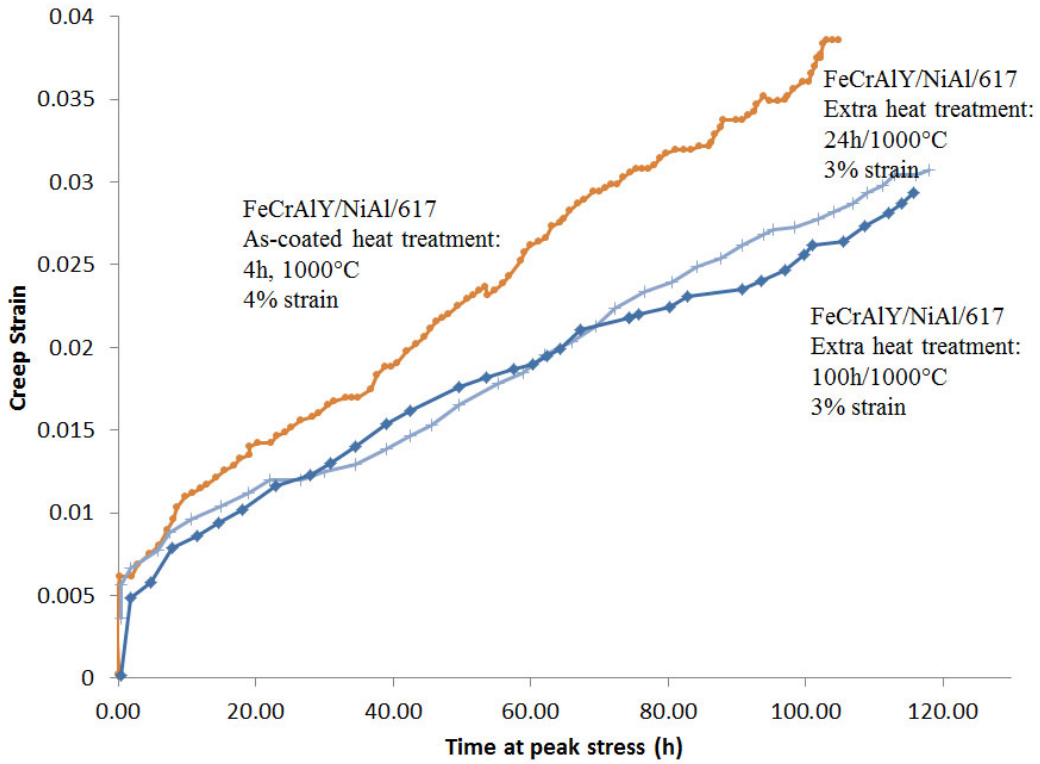

Figure 5-33 Curves of cyclic creep of FeCrAlY/NiAl/617 in carburizing/oxidizing environments interrupted after nominal strains of 3% and 4%. The specimens that received extra heat treatment have a lower creep rate.

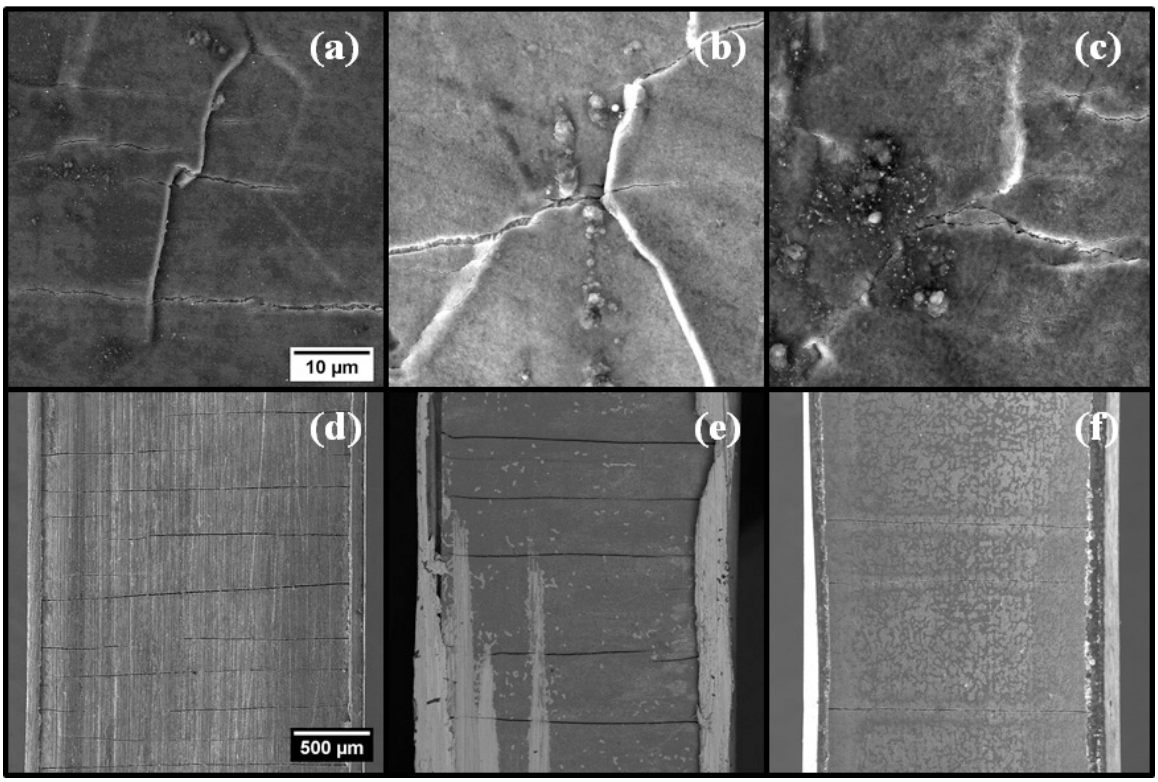

Figure 5-34 SEM images of crept FeCrAlY/NiAl/617 specimens showing surface damage on wider surface that is aluminized+clad (a,b,c) and narrower surface that is aluminized only (d,e,f). Even though the cracks in the NiAl layer still exist, they have been reduced significantly by the additional heat treatment. The stress axis is vertical and in the plane of the page.

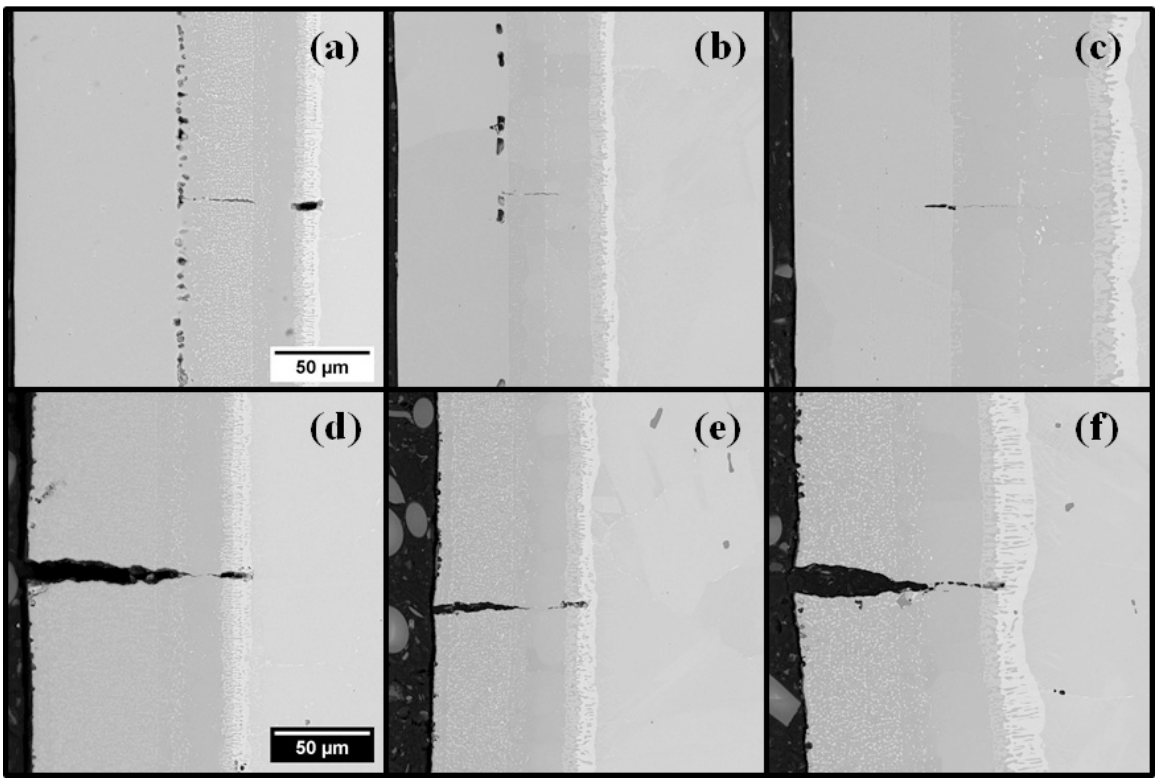

Figure 5-35 SEM images of crept FeCrAlY/NiAl/617 specimens showing internal damage parallel to the narrower aluminized-only surface (a,b,c), and parallel to the wider aluminized+clad surface (d,e,f). Even though the cracks in the unclad NiAl layer still exist, additional heat treatment has almost eliminated the cracks in the clad NiAl layer. The stress axis is vertical and in the plane of the page.

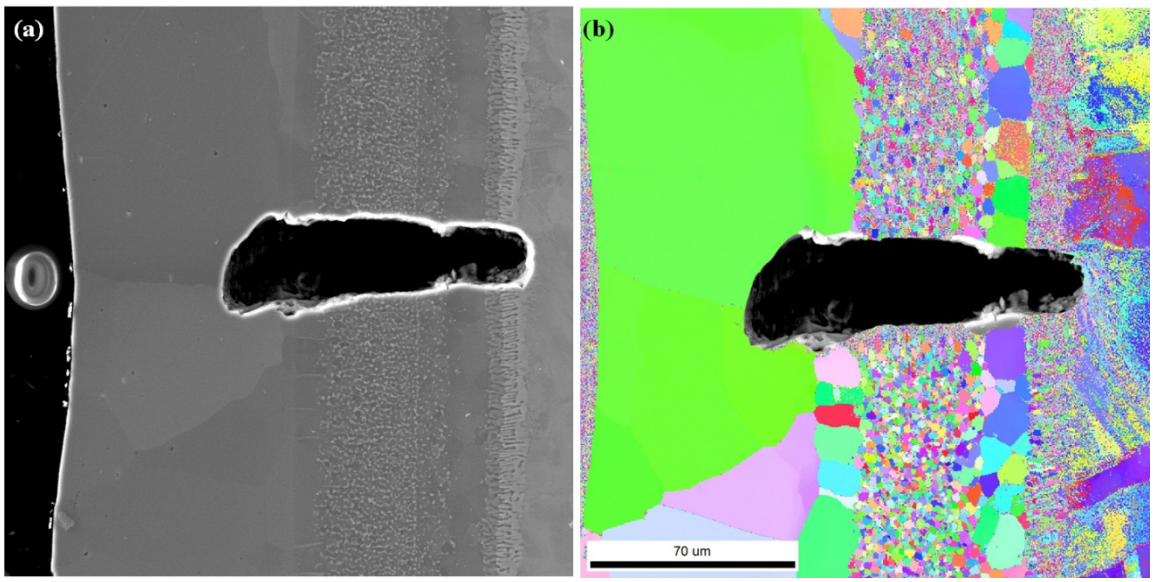

Figure 5-36 (a) Microstructure close to a void formed after high stress/strain cyclic creep tests of the clad-aluminized 617 and (b) corresponding EBSD map. The grain size and thickness of the FeCrAlY cladding are comparable and the precipitate-rich region in NiAl has smaller grains than the surrounding areas. The stress axis is vertical and in the plane of the page.

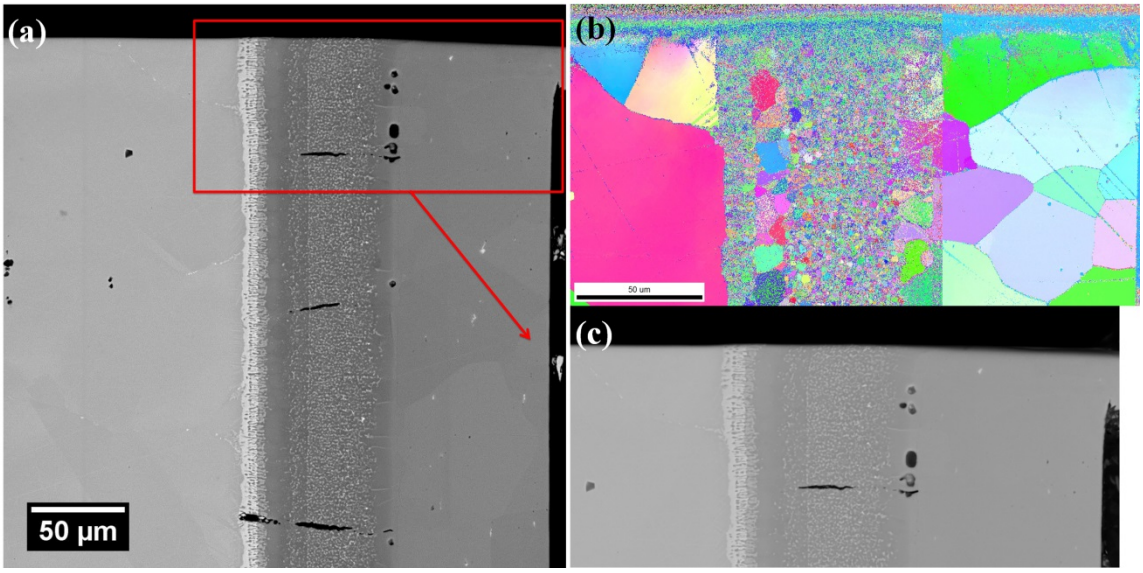

Figure 5-37 EBSD characterization of region close to a crack that formed after low stress/strain cyclic creep tests of the clad-aluminized 617. The grain size and thickness of the FeCrAlY cladding are comparable and the precipitate-rich region in NiAl has smaller grains than the surrounding areas. The crack seems to initiate farther away from pores and in the precipitate-rich region in NiAl. The stress axis is vertical and in the plane of the page.

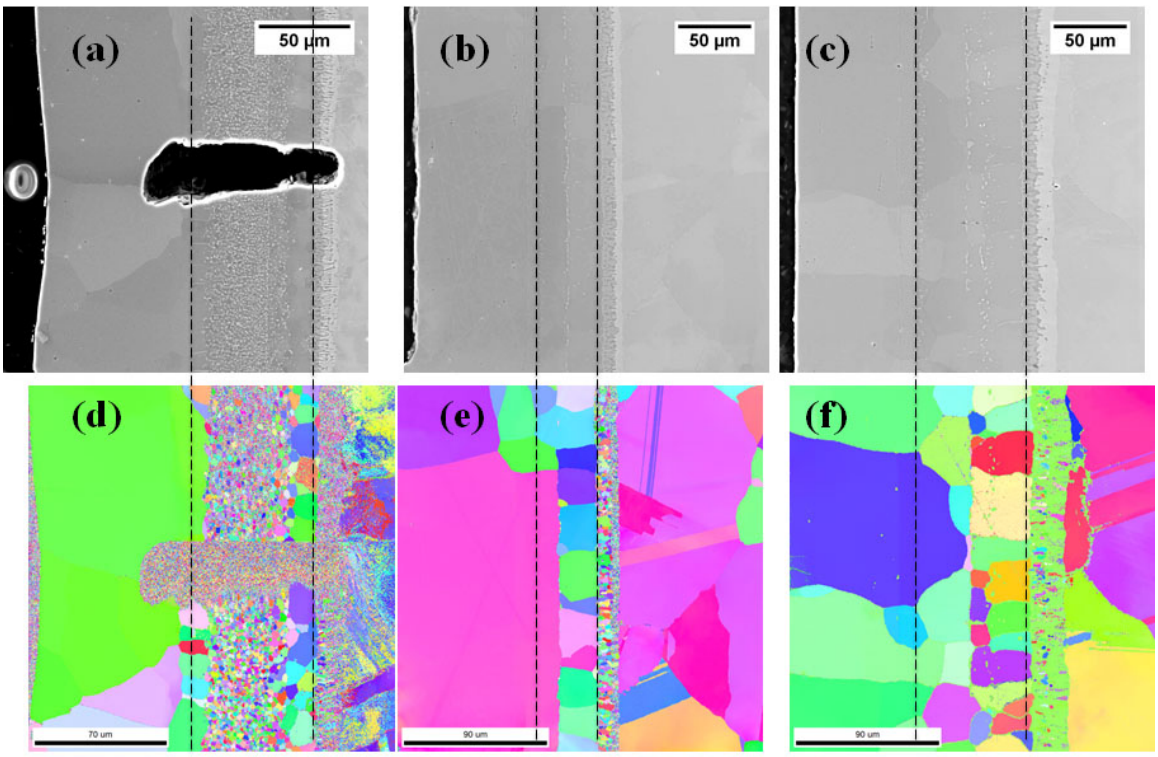

Figure 5-38 SEM images with corresponding EBSD grain maps of FeCrAlY/NiAl/617 specimens crept at 800°C in a carburizing/oxidizing environment showing the NiAl region (between the dashed lines). The different heat treatment conditions before creep were (a) 4h/1000°C/Ar for as-coated specimen, (b) as-coated + 24h/1000°C, and (c) as-coated + 100h/1000°C. The creep conditions of the specimens at 800°C were: (a) 15-75 MPa/ε=16%/110h, (b) 15-75 MPa/ε=3%/118h, and (c) 15-75 MPa/ε=3%/117 h. NiAl precipitates in the presence of cladding disappear with additional heat treatment. The stress axis is vertical and in the plane of the page. The duration reported is total test time.

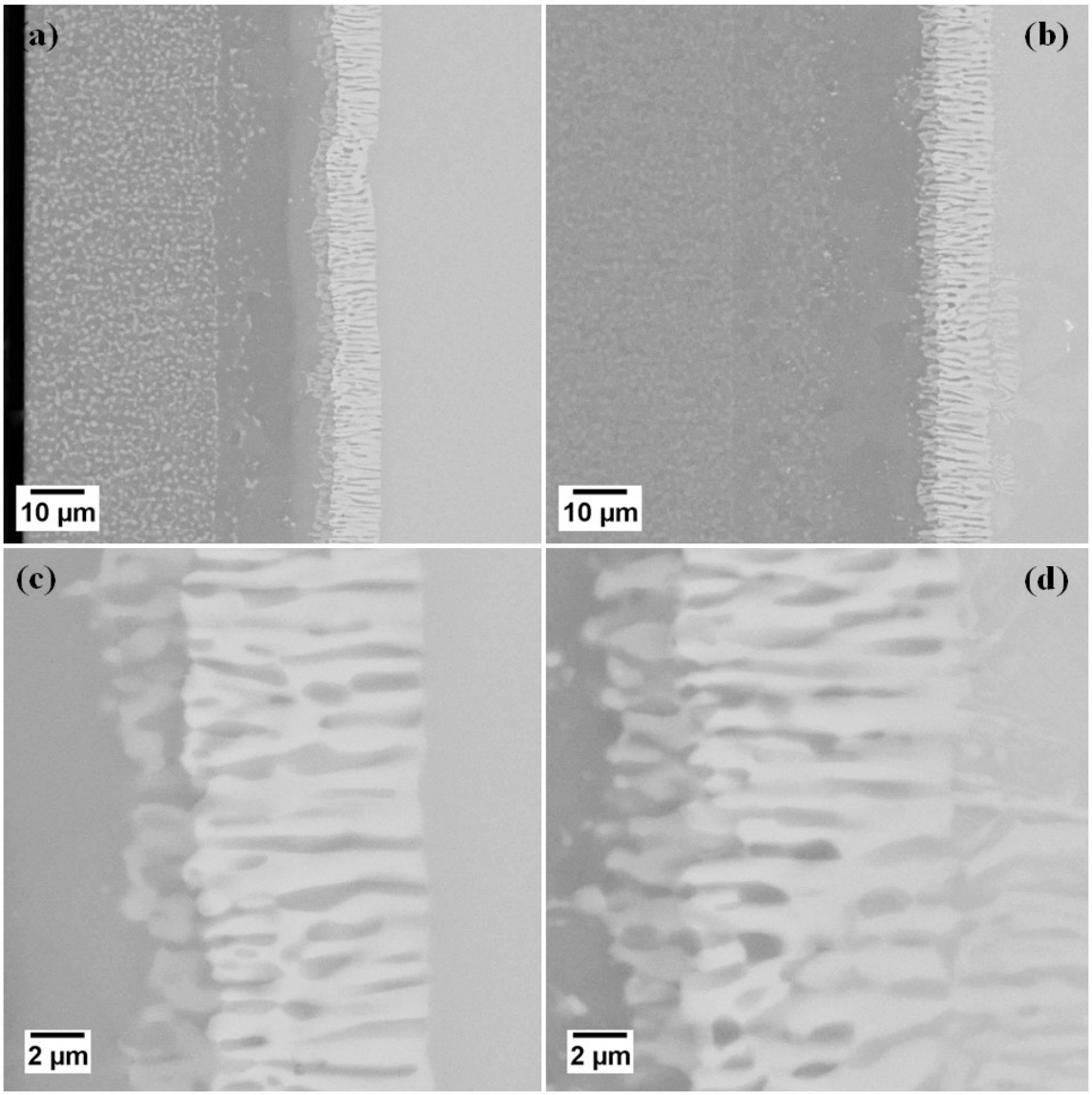

Figure 5-39 SEM images of untested NiAl/617 (a,c) and NiAl/617 after creep conditions of 15-75 MPa/16% (b,d). Note the integrity of the IDZ zone of brittle carbides and sigma phases shown in c and d. The stress axis is vertical and in the plane of the page.

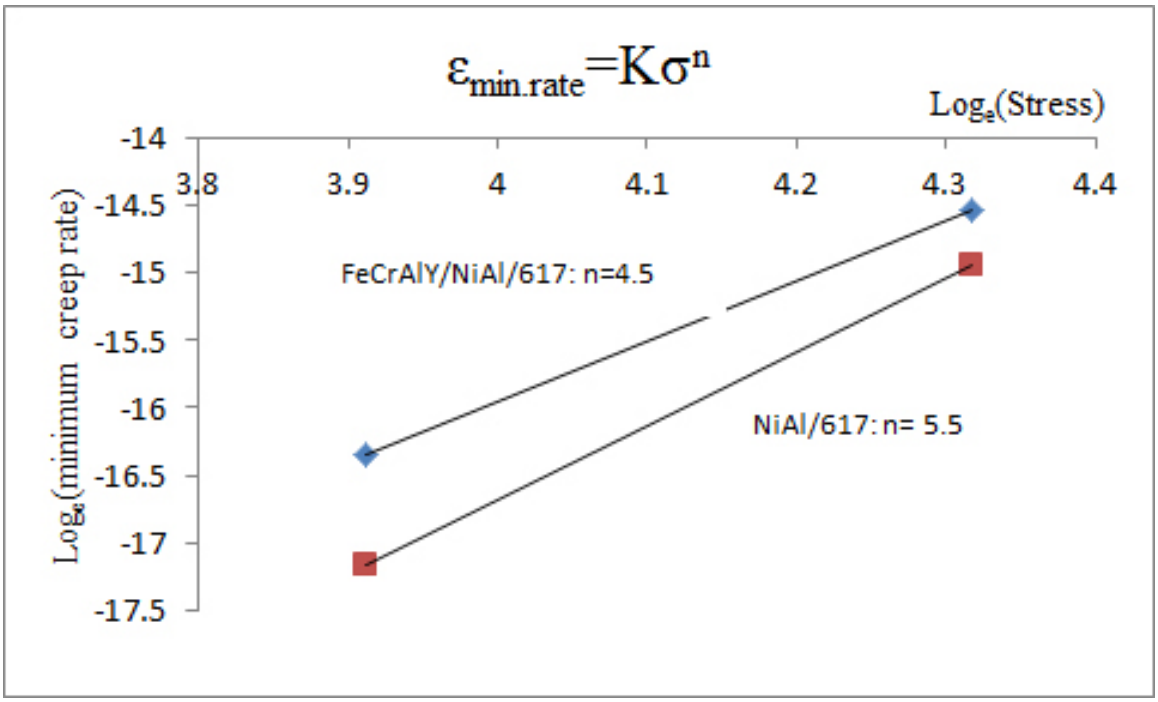

Figure 5-40 Approximation of creep strain rate dependence on stress for the coating layers (NiAl/617 and FeCrAlY/NiAl/617) used in this research work.

CHAPTER 6
CONCLUSIONS AND FUTURE WORK

6.1 Conclusions

The conclusions from the static and cyclic creep studies of Alloy 617 with and without barrier layers at 800°C in impure helium environments are the following:

1. Based on the observations of surface and near-surface damage of Alloy 617 during creep, surface Cr_2O_3 formed in He-CO/CO_2=1320 (low pO_2 and presence of carbon activity) is less protective than the scale formed in He-≤0.1ppm O_2 (high pO_2). Carburization also plays a role in the embrittlement of the surface regions, hence rendering internal corrosion more extensive in He-CO/CO_2=1320.
2. Mechanical loading and particularly cyclic loading accelerates the extent of damage on Alloy 617, but the type of surface damage does not change.
3. There is no observable effect of environment on creep deformation as long as the damage accumulation is limited to the surface and near-surface regions of the alloy.
4. NiAl and FeCrAlY coating layers are effective in preventing environmental attack on the underlying Alloy 617 by favoring the formation of slow-growing α-Al_2O_3 that is more protective than the naturally-forming Cr_2O_3.
5. Absence of surface cracks on NiAl in NiAl/617 and FeCrAlY in FeCrAlY/NiAl/617 may be due to lack of surface roughening/undulation on the coating surface during the cycling of load.
6. The addition of cladding on aluminized 617, while promoting a more efficient formation of α-Al_2O_3, is the source of cracking in the sandwiched NiAl layer during creep.

6.2 Recommendations for future work

The work in this dissertation has made a contribution to high-temperature mechanical and corrosion studies by examining the nature of environmental attack on surface and near-surface regions of Cr_2O_3-forming Alloy 617 during early creep and to present methods of mitigating this damage by use of Al_2O_3-forming coatings. Further study is recommended to address several important questions arising from this work, but which were outside the scope of the present investigation.

One important finding was that the compositional difference of the two gas environments determined the type of near-surface damage but did not affect the bulk creep deformation behavior of Alloy 617. The creep studies in this work were interrupted at nominal strains before failure and the damage was limited to the near-surface region in order to easily differentiate the effects of environment. Inferring the long term degradation of Alloy 617 in impure He environments cannot be done by examining only near-surface environmental effects produced during the short-time tests conducted in this research. Longer tests, though not practical in a laboratory setting, will still be required. This is especially true since previous research on the effects of environment on long-term creep behavior of Alloy 617 have not been conclusive. There is need to conduct longer creep studies to investigate the long-term effect of impure helium environments on creep behavior, especially in the tertiary stage, where bulk void formation and grain boundary sliding are expected to compound the surface damage accumulation. This will provide more insight on the synergy that might exist between the different stages of creep and environment – two time-dependent phenomena that are difficult to isolate.

Another finding was that despite the large creep strain accumulation on the NiAl/617 system, the aluminide layer did not suffer any cracks from the surface or the interdiffusion zone. It was also shown that in the likelihood that there were pre-existing-defects in the coating layer, no initiation or propagation of cracks occurred. Longer studies with static creep tests conducted to failure are necessary to examine the behavior of the barrier layer where more time would be allowed for possible crack initiation. It is likely that failure would be initiated in the bulk of the substrate during prolonged creep if the environmental attack on the substrate continued to be suppressed, and if the aluminide layer remained ductile at temperature for much longer exposure times. Another

possibility is that crack initiation from the interdiffusion zone could occur and render the underlying substrate vulnerable to the environmental attack. All these possibilities could be explored in long exposure creep tests on the order of 5000-10,000 hours in duration.

A major challenge in providing a more mechanically stable dual coating system was the cracking of NiAl when sandwiched between FeCrAlY and 617. The source of the cracking was associated with the cladding since the aluminized-only 617 specimens were crack-free after creep in similar conditions. The study of this phenomenon in the present work was complicated by the inability to clad all surfaces of the gauge section of the creep specimens, as was possible for the aluminizing-only specimens. A different method of cladding – perhaps by ion plasma deposition or low pressure plasma – could be pursued either on the same rectangular configuration or on tubular specimens. Subsequent creep studies on these new coating/substrate specimens would ensure uniform state of stress around the specimen.

REFERENCES

1. Hoffelner, W., *Materials for the Very High Temperature Reactor (VHTR): A Versatile Nuclear Power Station for Combined Cycle Electricity and Heat Production.* CHIMIA International Journal for Chemistry, 2005. **59**: p. 977-982.
2. Allen, T.R., et al., *Materials challenges for Generation IV nuclear energy systems.* Nuclear Technology, 2008. **162**(3): p. 342.
3. Harvego, E., *Evaluation of Next Generation Nuclear Power Plant (NGNP) Intermediate Heat Exchanger (IHX) Operating Conditions*, in *Nuclear Energy*2006.
4. Murty, K. and I. Charit, *Structural materials for Gen-IV nuclear reactors: Challenges and opportunities.* Journal of Nuclear Materials, 2008. **383**: p. 189-195.
5. Hsu, S.-S., *The effects of fatigue, hold time and creep on crack growth in high temperature environments—Ni □ Cr □ Co alloy.* Scripta Metallurgica et Materiala, 1991. **25**(5): p. 1143-1148.
6. Natesan, K., et al., *Materials behavior in HTGR environments*. Office. 2003: Division of Engineering Technology, Office of Nuclear Regulatory Research, US Nuclear Regulatory Commission.
7. Nickel, H., F. Schubert, and H. Schuster, *Evaluation of alloys for advanced high-temperature reactor systems.* Nuclear Engineering and Design, 1984. **78**: p. 251-265.
8. Adharapurapu, R., et al., *Chromia-Assisted Decarburization of W-Rich Ni-Based Alloys in Impure Helium at 1273 K (1000 °C).* Metallurgical and Materials Transactions A, 2011. **42**(5): p. 1229-1244.
9. Klöwer, J. and U. Heubner, *Carburisation of nickel-base alloys and its effects on the mechanical properties.* Materials and corrosion, 1998. **49**(4): p. 237-245.
10. Kumar, D., et al., *High-Temperature Oxidation of Alloy 617 in Helium Containing Part-Per-Million Levels of CO and CO_2 as Impurities.* Metallurgical and Materials Transactions A, 2011. **42**: p. 1245-1265.
11. Quadakkers, W.J. and H. Schuster, *Corrosion of high temprature alloys in the primary circuit helium of high temperature gas cooled reactors. - Part I: Theoretical background.* Materials and Corrosion/Werkstoffe und Korrosion, 1985. **36**: p. 141-150.
12. Shankar, P. and K. Natesan, *Effect of trace impurities in helium on the creep behavior of Alloy 617 for very high temperature reactor applications.* Journal of Nuclear Materials, 2007. **366**: p. 28-36.
13. Young, D.J., *Simultaneous oxidation and carburisation of chromia forming alloys.* International Journal of Hydrogen Energy, 2007. **32**(16): p. 3763-3769.
14. Hollenberg, G.W., et al., *Tritium/hydrogen barrier development.* Fusion Engineering and Design, 1995. **28**(0): p. 190-208.

15. Jo, T.S., S.H. Kim, and Y.D. Kim, *Microstructural changes of aluminized Alloy 617 during high-temperature aging.* Surface and Coatings Technology, 2011. **205**(20): p. 4743-4749.
16. Castillo, R. and K. Willett, *The effect of protective coatings on the high temperature properties of a gamma prime-strengthened Ni-base superalloy.* Metallurgical and Materials Transactions A, 1984. **15**(1): p. 229-236.
17. Evans, A.G., D.R. Clarke, and C.G. Levi, *The influence of oxides on the performance of advanced gas turbines.* Journal of the European Ceramic Society, 2008. **28**(7): p. 1405-1419.
18. Clark, E.A., *Surface Engineering of Nickel Alloys to Form a Stable Alpha Alumina Barrier Layer at T≤1000°C*, 2013, University of California, Santa Barbara.
19. Kumar, D., *Mechanisms of Oxidation of Alloy 617 in He-CO-CO2 Environment with Varying Carbon and Oxygen Potentials*, 2010, The University of Michigan.
20. Was, G.S., et al., *NEUP 09-678 Quarterly Progress Report Y4Q2.* 2013.
21. Levi, C.G., et al., *NEUP 10-963 Final Report.* 2014.
22. Hosier, J.C. and D.J. Tillack, *Inconel Alloy 617: A New High-Temperature Alloy.* Journal Name: Metals Eng. Quart. 12: No. 3, 51-5(Aug 1972).; Other Information: Orig. Receipt Date: 31-DEC-72, 1972: p. Medium: X.
23. Ren, W. and R. Swimdeman, *A Review Paper on Aging Effects in Alloy 617 for Gen IV Nuclear Reactor Applications.* Journal of Pressure Vessel Technology, 2009. **131**: p. 024002.
24. Mo, K., et al., *High Temperature Aging and Corrosion Study on Alloy 617 and Alloy 230.* Journal of Engineering for Gas Turbines and Power, 2011. **133**: p. 052908.
25. Mankins, W.L., J.C. Hosier, and T.H. Bassford, *Microstructure and Phase Stability of Inconel Alloy 617.* Metallurgical Transactions, 1974. **5**: p. 2579-2590.
26. Takahashi, T., *Analysis of Precipitated Phase in Heat Treated Inconel Alloy 617.* Transactions of Iron and Steel Institute of Japan, 1978. **18**(4): p. 221.
27. Kihara, S., et al., *Morphological Changes of carbides during creep and their effects on the creep properties of inconel 617 at 1000 C.* Metallurgical and Materials Transactions A, 1980. **11**: p. 1019-1031.
28. Graham, L., *Corrosion of metallic materials in HTR-helium environments.* Journal of Nuclear Materials, 1990. **171**: p. 76-83.
29. Menken, G., et al., *REVIEW OF THE GAS/METAL INTERACTIONS IN HTR HELIUM UP TO 950°C.*, in *Gas-Cooled Reactors Today, Proceedings of the Conference. Volume 4: Papers, Discussion, Closing Address, Corrigenda.*1982, British Nuclear Energy Soc, London, Engl: Bristol, Engl. p. 185-190.
30. Natesan, K., A. Moisseytsev, and S. Majumdar, *Preliminary issues associated with the next generation nuclear plant intermediate heat exchanger design.* Journal of Nuclear Materials, 2009. **392**: p. 307-315.
31. Nieder, R. and W. Stroter, *Long-term behavior of Impurities in an HTR primary circuit.* VGB Kraftwerstechnik, 1988. **68**(7): p. 671-676.
32. Burnette, R.D., *Primary coolant chemistry at Peach Bottom HTGR and implications on large HTGR design.* Transactions of the American Nuclear Society, 1978. **28**: p. 686-686.

33. Quadakkers, W.J., *Corrosion of High Temperature Alloys in the Primary Circuit Helium of High Temperature Gas Cooled Reactors. Part II: Experimental Results.* Materials and corrosion, 1985. **36**(8): p. 335-347.
34. Krompholz, K., J. Ebberink, and G. Menken. *Gas Metal Interactions and Depletion Effects in Helium-Cooled Process-Heat HTRs*. in *Metallic Corrosion. 8 th International Congress on Metallic Corrosion, 1981*. 1981.
35. Christ, H.J., et al., *Mechanisms of high-temperature corrosion in helium containing small amounts of impurities. I. Theoretical and experimental characterization of the gas phase.* Oxidation of metals, 1988. **30**: p. 1-26.
36. Brenner, K.G.E. *TERNARY DIAGRAMS FOR THE CHARACTERIZATION OF METALLIC CORROSION IN HIGH-TEMPERATURE REACTORS*. in *Gas-Cooled Reactors Today, Proceedings of the Conference. Volume 4: Papers, Discussion, Closing Address, Corrigenda.* 1982. Bristol, Engl: British Nuclear Energy Soc.
37. Brenner, K. and L. Graham, *The development and application of a unified corrosion model for high-temperature gas-cooled reactor systems.* Nucl. Technol.;(United States), 1984. **66**.
38. Christ, H.J., et al., *High temperature corrosion of the nickel-based alloy Inconel 617 in helium containing small amounts of impurities.* Materials Science and Engineering, 1987. **87**(0): p. 161-168.
39. Quadakkers, W.J., *High temperature corrosion in the service environments of a nuclear process heat plant.* Materials Science and Engineering, 1987. **87**(0): p. 107-112.
40. Cabet, C., et al., *High temperature reactivity of two chromium-containing alloys in impure helium.* Journal of Nuclear Materials, 2008. **375**: p. 173-184.
41. Krompholz, K., et al., *Fracture mechanics investigations on high-temperature gas-cooled reactor materials.* Nuclear Technology, 1984. **66**(2): p. 371-9.
42. Schnaas, a. and H.J. Grabke, *High-temperature corrosion and creep of Ni-Cr-Fe alloys in carburizing and oxidizing environments.* Oxidation of Metals, 1978. **12**: p. 387-404.
43. Kurata, Y., T. Kondo, and Y. Ogawa, *Creep and rupture behavior of a special grade Hastelloy-X in simulated HTGR helium.* Nucl. Technol.;(United States), 1984. **66**.
44. Huchtemann, B., *The effect of alloy chemistry on creep behaviour in a helium environment with low oxygen partial pressure.* Materials Science and Engineering: A, 1989. **120-121**: p. 623-626.
45. Grabke, H. and I. Wolf, *Carburization and oxidation ☆*. Materials Science and Engineering, 1987. **87**: p. 23-33.
46. Ledjeff, K., A. Rahmel, and M. Schorr, *Oxidation and Carburization of High Alloyed Materials for Cracking Tubes - Part 2: The Carburization Behaviour in Oxygen and Carbon Containing Atmospheres with High Carbon Activity.* Materials and Corrosion, 1980. **31**(2): p. 83-97.
47. Rouillard, F., et al., *Oxidation of a chromia-forming nickel base alloy at high temperature in mixed diluted CO/H2O atmospheres.* Corrosion Science, 2009. **51**(4): p. 752-760.

48. Schütze, M., *Mechanical properties of oxide scales.* Oxidation of Metals, 1995. **44**(1-2): p. 29-61.
49. Wolf, I. and H.J. Grabke, *A study on the solubility and distribution of carbon in oxides.* Solid State Communications, 1985. **54**(1): p. 5-10.
50. Shindo, M., W.J. Quadakkers, and H. Schuster, *Corrosion behaviour of high temperature alloys in impure helium environments.* Journal of Nuclear Materials, 1986. **140**: p. 94-105.
51. Rapp, R.A., *Kinetics, Microstructures and Mechanism of Internal Oxidation - Its Effect and Prevention in High Temperature Alloy Oxidation.* Corrosion, 1965. **21**(12): p. 382-401.
52. Sherby, O.D. and P.M. Burke, *Mechanical behaviour of crystalline solids at elevated temperature.* Progress in Materials Science, 1967. **13**: p. 323-390.
53. Ashby, M.F., *A first report on deformation-mechanism maps.* Acta Metallurgica, 1972. **20**(7): p. 887-897.
54. Ashby, M. and B. Dyson. *Creep damage mechanics and micromechanisms*. in *International Conference on Fracture, ICF6*. 1984. New Delhi (India).
55. Schubert, F., et al., *CREEP-RUPTURE BEHAVIOR OF CANDIDATE MATERIALS FOR NUCLEAR PROCESS HEAT APPLICATIONS.* Nuclear Technology, 1984. **66**(2): p. 227.
56. Roy, A.K., M.H. Hasan, and J. Pal, *Creep deformation of Alloys 617 and 276 at 750–950°C.* Materials Science and Engineering: A, 2009. **520**: p. 184-188.
57. Cook, R., *Creep properties of Inconel-617 in air and helium at 800 to 1000C.* Nuclear technology, 1984. **66**: p. 283-288.
58. Sharma, S., et al., *Oxidation and creep failure of alloy 617 foils at high temperature.* Journal of Nuclear Materials, 2008. **378**: p. 144-152.
59. Kim, W.-G., et al., *Creep oxidation behaviour and creep strength prediction for Alloy 617.* International Journal of Pressure Vessels and Piping, 2010. **87**(6): p. 289-295.
60. Rahmel, a., H.J. Grabke, and W. Steinkusch, *Carburization - introductory survey*. Materials and Corrosion, 1998. **49**: p. 221-225.
61. Ennis, P.J., W.J. Quadakkers, and H. Schuster, *Effect of selective oxidation of chromium on creep strength of Alloy 617.* Materials Science and Technology, 1992. **8**(1): p. 78-82.
62. Shida, Y., H. Fujikawa, and Y. Sawaragi, *The oxidation and carbon transfer behaviour of Ni-27Cr-5Mo-5W based alloys in an impure helium atmosphere at high temperature.* Corrosion science, 1993. **34**: p. 1157-1171.
63. Nickel, M., et al., *Qualification of metallic materials for application in advanced high temperature gas-cooled reactors.* Nucl. Technol.;(United States), 1982. **58**.
64. Bhanusankararao, K., et al., Trans. Indian Inst. Met., 1991. **44**(3): p. 255.
65. Sadananda, K. and P. Shahinian, *Crack Growth Behavior in Alloy 718 at 425°C.* Journal of Engineering Materials and Technology, 1978. **100**(4): p. 381-387.
66. Swanson, J.W. and H.L. Marcus, *Oxygen transport during fatigue crack growth.* Metallurgical Transactions A, 1978. **9**(2): p. 291-293.
67. Yun, H., et al., *The effect of high temperature reactor primary circuit helium on the formation and propagation of surface cracks in alloy 800 H and inconel 617.* Journal of Nuclear Materials, 1984. **125**: p. 258-272.

68. Viskari, L., et al., *Intergranular crack tip oxidation in a Ni-base superalloy.* Acta Materialia, 2013. **61**(10): p. 3630-3639.
69. Viskari, L., S. Johansson, and K. Stiller, *Oxygen influenced intergranular crack propagation: Analysing microstructure and chemistry in the crack tip region.* Materials at High Temperatures, 2011. **28**(4): p. 336-341.
70. Tawancy, H.M. and N.M. Abbas, *Mechanism of carburization of high-temperature alloys.* Journal of Materials Science, 1992. **27**: p. 1061-1069.
71. Jang, C., D. Lee, and D. Kim, *Oxidation behaviour of an Alloy 617 in very high-temperature air and helium environments.* International Journal of Pressure Vessels and Piping, 2008. **85**: p. 368-377.
72. Rodriguez, P. and K. Bhanu Sankara Rao, *Nucleation and growth of cracks and cavities under creep-fatigue interaction.* Progress in Materials Science, 1993. **37**: p. 403-480.
73. Ellison, E.G., *Review paper: a review of the interaction of creep and fatigue.* ARCHIVE: Journal of Mechanical Engineering Science 1959-1982 (vols 1-23), 1969. **11**: p. 318-339.
74. Kumar, D. and G. Was, *Mechanism of decarburization of alloy 617 at 1000◦ C in helium containing CO and CO2 as impurities.* Proc. Materials Research Society (Boston, USA, 5–8 December, 2009. **1125**: p. 2-7.
75. Wu, Q., et al., *Microstructure of Long-Term Aged IN617 Ni-Base Superalloy.* Metallurgical and Materials Transactions A, 2008. **39**(11): p. 2569-2585.
76. Ren, W. and R.W. Swindeman, *A Review of Alloy 800H for Applications in the Gen IV Nuclear Energy Systems*, in *ASME 2010 Pressure Vessels and Piping Conference: Volume 6, Parts A and B*2010, ASME. p. 821-836.
77. Gulsoy, G., *Mechanism of Internal Oxidation of Alloy 617 in Controlled Impurity Helium Environments At High Temperatures*, 2014, The University of Michigan.
78. Kumar, D., C.J. Torbet, and G.S. Was, *A facility for conducting high-temperature oxidation experiments of alloys in helium environments containing part per million levels of impurities.* Measurement Science and Technology, 2009. **20**: p. 095708.
79. Giannuzzi, L.A. and F.A. Stevie, *A review of focused ion beam milling techniques for TEM specimen preparation.* Micron, 1999. **30**(3): p. 197-204.
80. Tryon, B.S., *Multi-layered ruthenium-containing bond coats for thermal barrier coatings*, 2005, University of Michigan: Ann Arbor. p. 154-154 p.
81. Cotell, C.M., et al., *The influence of grain-boundary segregation of Y in Cr2O3 on the oxidation of Cr metal.* Oxidation of Metals, 1990. **34**(3-4): p. 173-200.
82. Giggins, C.S. and F.S. Pettit, *The oxidation of TD NiC (Ni-20Cr-2 vol pct ThO2) between 900° and 1200°C.* Metallurgical Transactions, 1971. **2**(4): p. 1071-1078.
83. Tsai, S.C., A.M. Huntz, and C. Dolin, *Growth mechanism of Cr2O3 scales: oxygen and chromium diffusion, oxidation kinetics and effect of yttrium.* Materials Science and Engineering: A, 1996. **212**(1): p. 6-13.
84. Gaskell, D.R., *Introduction to the thermodynamics of materials*. 2003, New York: Taylor & Francis. xv, 618 p.
85. Natesan, K. and P.S. Shankar, *Uniaxial creep response of Alloy 800H in impure helium and in low oxygen potential environments for nuclear reactor applications.* Journal of Nuclear Materials, 2009. **394**: p. 46-51.

86. Mino, K., *Effect of Simulated HTR Helium Atmosphere on Creep Rupture Properties of Nickel-Base Wrought Alloys.* Tokyo 135-91. Trans. Iron Steel Inst. Japan, 1983. **23**: p. 815-823.
87. Hänsel, M., C.A. Boddington, and D.J. Young, *Internal oxidation and carburisation of heat-resistant alloys.* Corrosion Science, 2003. **45**(5): p. 967-981.
88. Simkovich, G., et al., *Transport in nonstoichiometric compounds*. NATO ASI series. Series B, Physics ;v. 129. 1985, New York: Plenum Press. x, 563 p.
89. Gulsoy, G. and G.S. Was, *Surface oxidation of Alloy 617 in low oxygen partial pressure He–CO–CO2 environments at 750–850°C.* Corrosion Science, 2015. **90**(0): p. 529-534.
90. Wagner, C., Beitrag zur Theorie des Anlaufvorgangs, 1933. **B41**: p. 25-41.
91. Schnaas, A. and H.J. Grabke, *Changes in material properties of austenitic CrNiFe-alloys by carburization.* Materials and Corrosion, 1978. **29**(10): p. 635-644.
92. Christ, H.-J., et al., *Mechanisms of high-temperature corrosion in helium containing small amounts of impurities. II. Corrosion of the nickel-base alloy inconel 617.* Oxidation of Metals, 1988. **30**: p. 27-51.
93. Cabet, C., et al., *High temperature corrosion of structural materials under gas-cooled reactor helium.* Materials and Corrosion, 2006. **57**: p. 147-153.
94. Rouillard, F., et al., *Oxide-layer formation and stability on a nickel-base alloy in impure helium at high temperature.* Oxidation of Metals, 2007. **68**: p. 133-148.
95. Tolpygo, V.K. and D.R. Clarke, *On the rumpling mechanism in nickel-aluminide coatings: Part II: characterization of surface undulations and bond coat swelling.* Acta Materialia, 2004. **52**(17): p. 5129-5141.
96. Pollock, T.M., et al., *Oxide-Assisted Degradation of Ni-Base Single Crystals During Cyclic Loading: the Role of Coatings.* Journal of the American Ceramic Society, 2011. **94**: p. s136-s145.
97. Schneider, K. and H.W. Grünling, *Mechanical aspects of high temperature coatings.* Thin Solid Films, 1983. **107**(4): p. 395-416.
98. Meetham, G.W. and M.H.v.d. Voorde, *Materials for high temperature engineering applications*. Engineering materials. 2000, Berlin ; New York: Springer. ix, 164 p.
99. Prescott, R. and M.J. Graham, *The formation of aluminum oxide scales on high-temperature alloys.* Oxidation of Metals, 1992. **38**(3-4): p. 233-254.
100. Osthoff, W., et al., *Creep and relaxation behavior of Inconel-617.* Nucl. Technol.;(United States), 1984. **66**.
101. El-Magd, E., G. Nicolini, and M. Farag, *Effect of carbide precipitation on the creep behavior of Alloy 800HT in the Temperature Range 700 ° to 900 °.* Metallurgical and Materials Transactions A, 1996. **27**: p. 747-756.
102. Miracle, D.B., *Overview No. 104 The physical and mechanical properties of NiAl.* Acta Metallurgica et Materialia, 1993. **41**(3): p. 649-684.
103. Nychka, J.A., et al., *Surface oxide cracking associated with oxidation-induced grain boundary sliding in the underlying alloy.* Acta Materialia, 2004. **52**(5): p. 1097-1105.

104. Dryepondt, S., Y. Zhang, and B.A. Pint, *Creep and corrosion testing of aluminide coatings on ferritic–martensitic substrates.* Surface and Coatings Technology, 2006. **201**(7): p. 3880-3884.
105. Osgerby, S. and B.F. Dyson, *Modelling creep properties of coated superalloys in air and aggressive environments.* Materials Science and Engineering: A, 1989. **120–121, Part 2**: p. 645-650.
106. Nicholls, J.R., *Designing oxidation-resistant coatings.* JOM Journal of the Minerals Metals and Materials Society, 2000. **52**(1): p. 28-35.